Modelling, Implementation and Validation of Polymeric Planar Spring Mechanisms

by

Haroon-Ur-Rashid
MPhil., M.Sc., M.Sc.

Submitted to the University of Warwick
in partial fulfilment of the requirements
for the degree of
Doctor of Philosophy

School of Engineering

November 2014

THE UNIVERSITY OF WARWICK

Abstract

This thesis explores, by means of modelling and physical experiments, variant designs for triskelion devices, a type of planar flexure mechanism widely considered for use in micro-probe suspensions and, more recently, force transfer artefacts. The accurate measurement of low force is challenging problem that has wide range of force related applications. A lot of attention has been paid worldwide during last decade within and beyond the National Metrology Institutes (NMIs) to measuring low forces. A major concern is how to provide traceability for micro- to nanonewton level forces that is highly reliable and could be used for real machine calibration. The current consensus is that this process requires special secondary standards and novel artefacts to transfer such standards to working systems. The latter provides the motivation for this thesis, which makes the following main contributions.

A published linear elastic model has been considerably enhanced and generalised to enable the study of a wide range of variants from the one widely-used design of triskelion device. Triskelion and tetraskelion software programs implement this new model, providing a new tool for computing forces, moments, stress, strain, axial stiffness and torsional stiffness for devices before their fabrication. It has been used to explore widely the sensitivity of the devices to changes in design parameters such as suspension leg geometry and 'elbow' angles.

To provide essential physical verification of the practicality of a linear model, a low-cost technique has been developed for making small triskelion test samples. This was used with a new test-rig configuration to measure polymeric triskelion devices under loads in the 1 mN to 1N region with deflections up to around 1 mm. Experiments have determined the onset and characteristics of non-linear spring behaviour in typical devices and have verified the general predictions from the new model.

The overall conclusion to be drawn is that at large deflection the spring characteristics follow a cubic law (stiffening). However, during the initial stages of the deflection the linear term dominates over a range that is quite sufficiently wide for practical use as force test artefacts. The polymeric test devices performed well, behaving reasonably closely to predicted values in the linear (model) region. The promising results indicate its prospects for use in low force technology in the future.

Acknowledgements

I would like to take this opportunity to thank to my supervisor Professor Derek Chetwynd for his support and encouragement during my period of research. The suggestions and commitment to this challenging research work have been highly valuable in perfecting the thesis.

I am very grateful for discussions I had especially related to nano-force secondary standards with Professor Richard Leach and Dr Christopher Jones of National Physical Laboratory (NPL).

I would also like express my gratitude to Dr Xiaping Liu and Dr Ken Mao for their encouragements and discussions.

A special thanks to Dave Robinson for fabricating the samples of triskelion and tetraskelion force artefacts and his help with the progress of my experimental work. I am also grateful to Graham Canham for taking the pictures of these samples.

This work was funded by the Engineering and Physical Sciences Research Council (EPSRC) CASE Studentship Program (Ref: 08002602) in conjunction with NPL.

Finally, I would like to thank my family and friends who always supported and encouraged me.

Declaration

Statement of Originality

I declare that this thesis is presented in accordance with the regulations for the degree of Doctor of Philosophy. It has been written and composed by myself. The work presented in this thesis is my own research work, except where noted. Information derived from the published or unpublished work of others has been acknowledged in the text and a list of references is given.

No part of the research work presented in this thesis has previously been published by the author. This thesis has not been submitted for a degree at any other university.

Haroon-Ur-Rashid

PhD Candidate

MPhil. Computer Science, University of Aberystwyth, UK

M.Sc. Computer Science, University of Aberystwyth, UK

M.Sc. Physics, Punjab University, Lahore, Pakistan

List of Abbreviations

AFM	atomic microscope
AM	additive manufacturing
BIMP	Bureau International des Poids et Mesures
C-MAR	cantilever microfabricated array of reference springs
CMS-ITR	centre for measurement standards-industrial technology research institute
CMM	coordinate measuring machine
CNC	computer numerical code
CS	centre symmetric
CGPM	General Conference on Weights and Measures
CIMP	Committee for Weights and Measures
DAFM	dynamic atomic microscopy
DoF	degree of freedom
DS	diagonal symmetric
ECB	electromagnetic compensated balance
FSM	force standard machine
IPK	International Prototype of Kilogram
KRISS	Korean Research Institute of standard and science
LEN	lateral electrical nanobalance

LFB	low force balance
MEMS	microelectromechanical systems
MSL	microstereolithography
NMIs	National Metrology Institutes
NIST	National Institute of Standards and Technology
NPL	National Physical Laboratory
NFC	nano-force calibrator
PTB	Technische Bundesanstalt
RP	rapid prototyping
SL	stereolithography
TSFA	triskelion force artefact
TTSFA	tetraskelion force artefact

Symbols used in numerical experiments

b	beam length [m]
w	beam width [m]
t	beam thickness [m]
a_ℓ	arm length [m]
h_r	arm radius [m]
α_i	angle between the arm and x-axis of triskelion suspension (i = 1, 2, 3) and tetraskelion (i = 1, 2, 3, 4) force artefacts in the local frame of reference [radian]
β_i	outer angle between the x-axis and beam of triskelion (i = 1, 2, 3) and tetraskelion (i = 1, 2, 3, 4) suspension in the global frame of reference [radian]
θ_x	rotation about x-axis of hub of the triskelion and tetraskelion force artefacts [radian]
θ_y	rotation about y-axis of hub of the triskelion and tetraskelion force artefacts
F_z	force along z-axis [N/m]
M_x	moment along x-axis [Nm]
M_y	moment along y-axis [Nm]
k_z	axial stiffness along z-axis [m]
λ_x	torsional stiffness along x-axis [Nm/rad]
E	Young's Modulus [pascals]

Terminology used in chapters 4 to 9

TSFA-60	triskelion force artefact with elbow 60 °
TSFA-90	triskelion force artefact with elbow 90 °
TSFA-120	triskelion force artefact with elbow 120 °
TSFA-180	triskelion force artefact with elbow 180 °
TTSFA-CS-90	tetraskelion force artefact, centre symmetric with elbow 90 °
TTSFA-DS-90	tetraskelion force artefact, diagonal symmetric with elbow 90 °
TTSFA-CS-135	tetraskelion force artefact, centre symmetric with elbow 135 °
TTSFA-DS-135	tetraskelion force artefact, diagonal symmetric with elbow 135 °
TTSFA-CS-180	tetraskelion force artefact, centre symmetric with elbow 180 °
TTSFA-DS-180	tetraskelion force artefact, diagonal symmetric with elbow 180 °
CS1-60	classic triskelion sample with elbow angle with elbow 60 °
CS2-60	classic triskelion sample with elbow angle with elbow 60 °
CS1-90	classic triskelion sample with elbow angle with elbow 90 °
CS2-90	classic triskelion sample with elbow angle with elbow 90 °
CS1-120	classic triskelion sample with elbow angle with elbow 120 °
CS2-120	classic triskelion sample with elbow angle with elbow 120 °
ABS1-60	angle-beam sample with elbow angle with elbow 60 °
ABS2-60	angle-beam sample with elbow angle with elbow 60 °
ABS1-90	angle-beam sample with elbow angle with elbow 90 °

ABS2-90	angle-beam sample with elbow angle with elbow 90 °
ABS1-120	angle-beam sample with elbow angle with elbow 120 °
ABS1-120	angle-beam sample with elbow angle with elbow 120 °
CS1-CS-90	classic tetraskelion sample, centre symmetric with elbow angle 90 °
CS2-CS-90	classic tetraskelion sample, centre symmetric with elbow angle 90 °
CS1-DS-90	classic tetraskelion sample, diagonal symmetric with elbow angle 90 °
CS2-DS-90	classic tetraskelion sample, diagonal symmetric with elbow angle 90 °
ABS1-CS-90	angle-beam tetraskelion sample, centre symmetric with elbow angle 90 °
ABS1-DS-90	angle-beam tetraskelion sample, diagonal symmetric with elbow angle 90 °

Dedication

This thesis is dedicated to my father Raja Muhammad Azam Khan Kayani (Late), mother Surya Begum, Uncle Raja Amir Alam Kayani, aunt Taj Begum, and my son Mamoon-Ur-Rashid Kayani & daughter Ruhi-Ur-Rashid Kayani.

Contents

List of Tables

List of Figures

Chapter 1

Introduction

This chapter introduces the needs and ideas for low force measurement and the subsequent need for low force artefacts. It then identifies limitations in the current understanding of low force technology leading to the aims, objectives, and scope of this thesis.

1.1 Background: General need in force metrology

The past two decades have seen many advancements in micro and nano technology. New devices are being produced which can create very small forces in the micro to nano-newton scale and require new calibration methods. The growing interest in nanomechanics is greatly demanding the accurate measurement for determining the mechanical property micro- and nano-devices down to nanonewton level [29], [30], [31]. These types of application have great importance in metrology and are becoming essential for micro to nano level for small force calibration. The biophysicists have also been seen to characterising small forces down to subpiconewton that are associated with cells and molecules to study the role of forces and mechanical properties that can effect biological processes [32], [33], [34].

Nowadays the atomic microscope (AFM) is an important tool for investigating the surface property with atomic resolutions. The AFM may detect a small force by measuring deflection of an AFM cantilever with a laser to determine topological an information such as height, length, and shape [35]. AFM plays an important role in studying the surf topography of material and measuring intermolecular forces [35], [36], [37]. Instrumentated indentation techniques are very common, and are used to determine both hardness and the

elastic modulus of bulk materials [38]. This technique is also referred to as nanoindentation when used at small forces and depths. The interaction forces between biological molecules and Casimir force is also measured by an AFM [39], [40].

Dynamic atomic microscopy (DAFM) is also a most important and powerful tool in nanotechnology, used to measure topography and physio-chemical properties of organic and inorganic material at nano length scale, manipulation and fabrication of functional nanostructures. An example of a vibrating micro cantilever with a nanoscale tip when interacts with a sample via long and short range force that has several distinct eigenmodes and tip sample forces that are non-linear. Further improvement in imaging contract or reduction in imaging forces are afforded by the modes are worthy testament to the importance of cantilever dynamic in DAFM [41], [42].

The role of contact probes in metrology is essential for dimensional and other measurements. Force metrology is crucial in many industries that have increasing concern with smaller and ultimately these are relying only on AFM etc. Force measurements are most essential in micro- and nano-technology,atomic force microscope (AFM), coordinate measuring machine (CMM), material testing aerospace, aviation industry, car industry, safety engineering, energy production process, power plants, medicine, biomedicine, chemical industry micro-CMM which are creating great demand for tracing micro- to nano-newton forces [43] [44].

The most intuitive method for force calibration is by deadweight. This is still used for maintaining traceability within the millinewton to meganewton range([45]). However, for smaller forces at the end of the low force balance scale, handling difficulties and independent testing issues lead to a high relative uncertainties in deadweight measurement. Hence, dead-weights are impractical for low force calibration. A new route required to calibrate the low force that will be discussed in chapter 2.

Researchers at National Institute of Standards and Technology (NIST), National Physical Laboratory (NPL), Korean Research Institute of standard and science (KRISS),

Physikalich-Technische Bundesanstalt (PTB), centre for measurement standards-industrial technology research institute (CMS-ITRI) and other institutions are attempting to develop technology and implement it in the working range 1 nN to 10 μN to measure low forces. They have also developed low force facilities [46], [47], [48], [49], [50], [9], [51], [52], [53], [54], [55], [56] which will be reviewed in the second chapter.

1.2 Scope of the thesis

Section 1.1 has highlighted some of the many physical principles that could be applied to small-scale force sensing. It has also made it evident that very few are mature enough and technologically sufficiently controllable to have practical relevance in force transfer artefacts within the next few years. This is especially the case for upper parts of the ranges of the low- force secondary standards being implemented by National Measurement Institutions (NMIs) in the 2000-2020 period. Given also the perception that the upper range is one of most pressing industrial needs, NPL appear fully justified in declaring that the other programs from 2005 would follow only an elastic device as a force transfer artefact for use with their low force balance (LFB).

Moreover, NPL is committed to a generation of designs based on their already demonstrated triskelion micro-probe suspension (figures 1.1) [50], [57]. There are inevitable downsides to any such decision. The triskelion geometry (as will be discussed later) is mechanically suspect because it is a compromise to allow convenient micro fabrication. It will possibly show an undesirably high levels of non-linearity in its spring constant and fairly poor constraint of some parasitic motion modes. Very likely, such effects will be sensitive to various geometrical parameters. There appears to be virtually no discussion of design variants and optimization in the open literature. Even if a computer model were to be used for such optimization, there is a pressing need for experimental data with which to verify them. This thesis provides a first step in addressing the needs of institutions and the overall aim of the study.

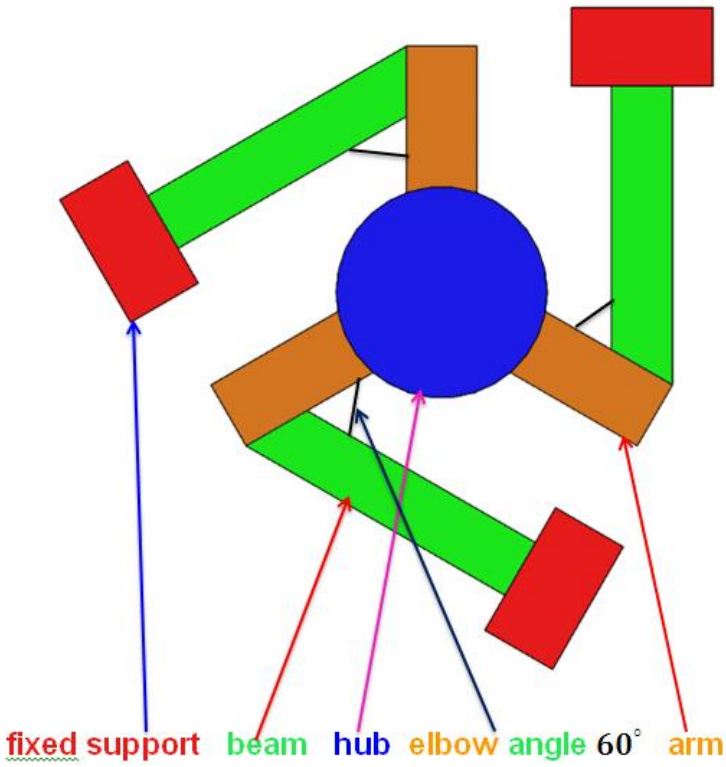

Figure 1.1: The classical triskelion suspension for a micro probe, layout with elbow angle 60 °.

1.3 Aims and objectives of the research work

The overall aim of this study is to improve the understanding and practice of micro calibration by means of triskelion force artefacts and the measurement of small forces that could interact between a secondary standard and working instruments. It is concerned first with calibration at a national level, and later with a low-cost effective, robust design for direct industrial use.

In order to achieve the above aims, the following major research objectives have been identified:

- Studying and reporting on of force sensing methods.
- Development of enhanced linear clastic model for variant design of triskelion artefacts.
- Development of triskelion and tetraskelion software programs.
- Exploring a low-cost approach for fabrication of triskelion and tetraskelion force artefacts.

- Development of test-rig method to measurement of low forces in the range up to around 1 Newton and displacements of up to of 1mm.

1.4 Layout of the thesis

Chapter 2: Needs and capabilities in low-force technology

This chapter reviews the measurement of small forces in the micro- to nano-newton range that is becoming a very important field of research within in micro- and nanotechnology, nanoindenters, AFM, micro-CMMs and so on. The generation and measurement of small forces have many applications in the various fields of technology. This chapter specifically presents force sensing methods and the capability for small force metrology in the NMIs and other institutions.

Chapter 3: Linear Elastic Model for triskelion suspension

This chapter starts with a brief overview of some fundamental elastic beam theory. Following this, a novel contribution of this chapter is the development of an enhanced linear elastic model for triskelion suspension in order to predict the stiffness of triskelion force artefacts. Unlike published examples, it has capability to set independently all potential significant design parameters, such as elbow angles and can allow any number and distribution of n suspension beams around the centre of the hub of force artefacts. The new linear elastic model for triskelion force artefacts will be used to investigate changes in the elbow angles of the triskelion force artefacts, the stabilities and stiffness of platform centre (hub).

Chapter 4:- Implementation of linear elastic model; Numerical experiments and data analysis

This chapter presents the development of the triskelion software program to implement the enhanced linear model. However, the computed results of the triskelion software program could be compared to some published data from another study (indirect validation) before proceeding to simulate results from geometries of trial designs. It specifically explores the variation in the angle at the elbow of the suspension beams. It is clear that artefacts of

these types must become non-linear with increasing deflection, so the validity of the simple model under different parameters needs full investigation.

Chapter 5:- Triskelion polymeric force artefacts; Specification and design

This chapter describes the use of polymeric triskelion force artefacts for the first time. The use of polymeric force artefacts has the commercial capability to exploit polymers in a mass production scale for triskelion force artefacts and the possibility to offer a low-cost approach that is highly useful for industries. The low-cost approach could bring a revolution in the use of polymers in the design of triskelion force artefacts, just like precision injection moulding in the commercial market.

Chapter 6:- Experimental analysis of stiffness; Classic triskelion force artefacts

This chapter covers the specification, design and use of the best bespoke method for testing the stiffness of triskelion force artefacts. The validation testing results of classical triskelion force artefacts were carried out using the triskelion software program. The results of classic triskelion force artefacts force artefacts were also presented in this chapter. A non-linearity is deducted from whole range of experiments of classic triskelion force artefacts and angle-beam triskelion force artefacts that follows a best cubic fit. This allows analysis for the range of validity of the enhanced linear elastic model for triskelion force artefacts. The concept of non-linearity was detected for the first time from the experimental result of classic and angle-beam triskelion force artefacts and was not seen in any scientific published research papers.

Chapter 7:- Experimental analysis of stiffness; Angle-beam triskelion force artefacts

This chapter presents specification, design and fabrication using a low-cost approach for measurements of planar angle-beam suspensions that are introduced for the first time for force artefacts. Experimental results of angle-beam are compared with validated results of the triskelion software program. Like classic triskelion force artefacts, non-linearity was also detected for the angle-beam force artefacts that also follows best cubic fit and allows better range of performance as compared to the classic force artefacts.

Chapter 8:- Tetraskelion force artefacts; specification, design, experimental analysis of stiffness and numerical investigations

This chapter describes the extended research work for the design of tetraskelion force artefacts. Two type of polymeric tetraskelion force artefacts (four legs) for classic and angle-beam tetraskelion force artefacts were fabricated. It was observed in the experimental research work that all the tetraskelion force artefacts belong to the triskelion force artefacts family and become significantly stiffer because they were kinematically constrained. This new idea is slightly counter-intuitive, being a trade-off between individual stiffness and a number of additional support legs which leads to better practical performance compared to three legs. The new polymeric tetraskelion force artefacts models and experimental technique was developed and used for the preliminary investigation of these points. The polymeric tetraskelion force artefacts were developed for the first time for practical testing and have never been published in any scientific research papers. Moreover, a new tetraskelion software program was developed by upgrading the triskelion software program to predict the stiffness of tetraskelion force artefacts before their fabrication and validation.

Chapter 9:- Best choices of triskelion and tetraskelion force artefacts for industrial applications

This chapter discusses the potential use of triskelion and tetraskelion force artefacts for commercial use. Their performance and working ranges in the linear region of the graphs plotted from the experimental data are described. The numerical experiments are also extended to explore the best variant design of triskelion and tetraskelion force artefacts or micro probe suspensions.

Chapter 10:- Conclusion and future recommendations

This chapter presents the conclusions for future research drawn from the research work presented in this thesis. The importance of a low-cost approach for commercial production and the best variant design for triskelion and tetraskelion micro probe suspension or force artefacts are also highlighted in this chapter.

Chapter 2

Needs and capabilities in low-force metrology

2.1 Introduction

This chapter highlight the essential standard capabilities for low force metrology developed in various NMIs in the world. The current challenges are the base units (kg, m, s) of SI systems. The NMIs are motivated by the needs for small force standards and have started to explore new methods and techniques of calibration for SI-traceable force. The primary standards of force are derived from the unit of the Newton using base units of SI systems.

The realisation of an SI unit, 'newton' (or a fraction of it) in terms of base unit will involve complex and delicate instrumentation (often called a 'secondary standards'). Such systems are impractical for almost any direct calibration, necessitating the development of intermediate (interfacing) devices: force transfer artefacts. Hence, the exploration of various methods and modelling techniques are carried out in this chapter for new design of "force transfer artefacts". This is the starting point for the development of the research work presented in this thesis.

Furthermore, this chapter discusses force-sensing methods, which could be used for low force technology in the future.

2.2 Scope of low force measurement

Advances in research have made possible the traceability of force at the macro to nano level. The twentieth century has seen a rapid increase in the demands of scientific study and a jump in the sensitivity of instruments to measure very small forces. For example, in bioscience the detachment force using a bio-membrane probe is measured in the ranges 10^{-2}pN and 100pN [58]. Also the mechanical force realization based on flux quantization in the pico-Newton range is proposed by [59], [60]. More generally, the use of soft materials (polymers and cells etc.) in research or industry situation risks distortion or damage unless probe forces are carefully controlled. The twentieth century has also seen major growth in highly miniature systems and true micro electro mechanical systems (MEMS) involving a wider range of materials and manufacturing procedures, e.g., the need to monitor and control forces on gripper of micro-robots and other micro-mechanical processes). The surface characterisation tools needed for such applications and for high precision macroscopic products (optics and bearings, etc) therefore often involve smaller and smaller forces in order to deliver necessary performance; consider for example, the stylus profilometer, and micro CMM, micro and nano-hardness testers, micro- and nano-tribometers as well as probe microscopy mentioned in chapter 1. It might further be noted that pharmaceutical and some other sectors often rely on weighing very small doses of powder, with a need to control to below a milligram mass ($\sim$ 10 μN weight).

The scientific and technical situations just discussed to cover, perhaps, forces from a large fraction of a newton to nano-newton, with likely growth in the use of even smaller ones where at least pico-newton resolution is needed. This is clearly to wide to cover by one method and a series of techniques with overlapping ranges will be required. There then arise a major challenges over how traceable force metrology can be archived for them.

The newton derives in the SI system from the kilogram, which is extremely difficult to realise even in a best standards laboratories to precision much better than (1×10^{-9}). 1μN relates to 0.1 mg (1×10^{-7} kg) which on interpolation would, therefore, only be traceable to at best 1%. Fortunately, nano-science and ultra-precision technology are providing plausible solution routes and several National Metrology Institutes (NMIs) are working

actively on them. Generally there are at least two stages involved. First, a high-specialised traceable secondary standard is needed, which focuses directly on small forces. Following this, there needs to be adequate means of transferring information from secondary standards to working devices within laboratories and factories.

This thesis takes the assumption that one of the most important ranges of low-force measurement for the next few years covers broadly from 1 μN to around 100 mN. It is chosen for several reasons. First, it is highly relevant to mechanical characterisation and micromanipulation for already established, economically important industries. Second there is good evidence that NMIs will be able to provide reasonable traceable reference instruments for this vision. There is likely to be a stable market for simpler small instruments and transfer artefacts that at low cost can either fully calibrate or at least diagnose out-of-specification conditions on user instruments. Before proceeding to consider the latter, it is helpful to review the capabilities of typical NMIs and to consider the range of sensing principles that might be applied.

2.2.1 Traceability and fundamental force concepts in metrology

Traceability

"Traceability is defined as the property of a measurement result whereby the result can be related to a reference through a documented unbroken chain of calibrations, each contributing to the measurement uncertainty" [61], [45].

or

"Traceability may also be defined as an unbroken record of documentation (documentation traceability) or an unbroken chain of measurements and associated uncertainties (metrological traceability)" [1].

Measurements are made everywhere in the world, in houses, schools, colleges, universities, industries and international laboratories. It is very difficult to find the exact relationship between the actual and measured value if the observations vary with time, since this may perturb the reference scale. The variation in the measurement processes are controlled by repeating the observations made during precision measurements of any parameter, but

rare changes exist that were found to be identical under the same conditions. The variation in the measurement process occurs, which may be caused by many factors, such as standards, work pieces, instruments, persons and procedures and environment [62]. The methods to estimate the uncertainty in measurement should be need rigorously. The approach to uncertainty of fundamental concept of traceability described in [63], [64], [65] is highly encouraged and considered to be essential in the engineering experiments. As an example figure 2.1, considered here deliberately from outside our immediate context that shows a common path for a calibrated thermometer [1]. The other example is measurement of the surface profile using stylus instrument. The stylus instruments are commonly used for a measurement of topography by measuring the displacement of stylus as it traverses the surface [45].

Fundamental force concept in conventional metrology

Force is a derived unit in the SI, which means that primary standards of the force are derived from the fundamental definition of force by using three basic units kilogram (kg), mass (m), and second (s). One newton is defined as the force required to accelerate a mass of one kg at a rate of one meter-$(\text{sec})^{-2}$. 1kg is defined as the mass of primary kilogram, a platinum-iridium cylinder stored in Paris. The weight of a body is a gravitational force acting on a body and measured in kg as mass [66]. Conventionally, the force is measured by using strain gauges, load cells, resonance structured, electric balances, force transducers, piezoelectric crystal and pressure. For a known acceleration due to a gravity, the downward force generated by the earth field can be calculated. This is the basic principle that works behind the deadweight standards machines [67], [68].

The forces on the micro and nanotechnology scale are measured by using different principles as compared to measurement of macro scale forces. The uncertainty increases of the scale of masses are reduced for deadweight methods. A mass of 1kg may be measured with a standard uncertainty of 1 μg (1 part in 10^9) [45]. Small masses (0.5mg) are calibrated at

NIST. The handling of such small masses becomes difficult and their relative uncertainties increases inversely proportional to the decrease in mass [69].

2.2.2 Low force traceability in metrology

The low force measurement is becoming essential in the national metrology institutes (NMI). In order to meet the demand of traceable micro to nano-newton force, NMIs worldwide are working together to extend the range of traceable force measurement further down to the nano-Newton level [70], [71], [72], [29], [73], [74], [47] . These NMIs have developed their own small force facilities based own designs and operating principles. Each NMI has realised diverse paths of calibration for small force facilities for primary realisation and dissemination routes. A variety of artefacts and methods have been developed by them.

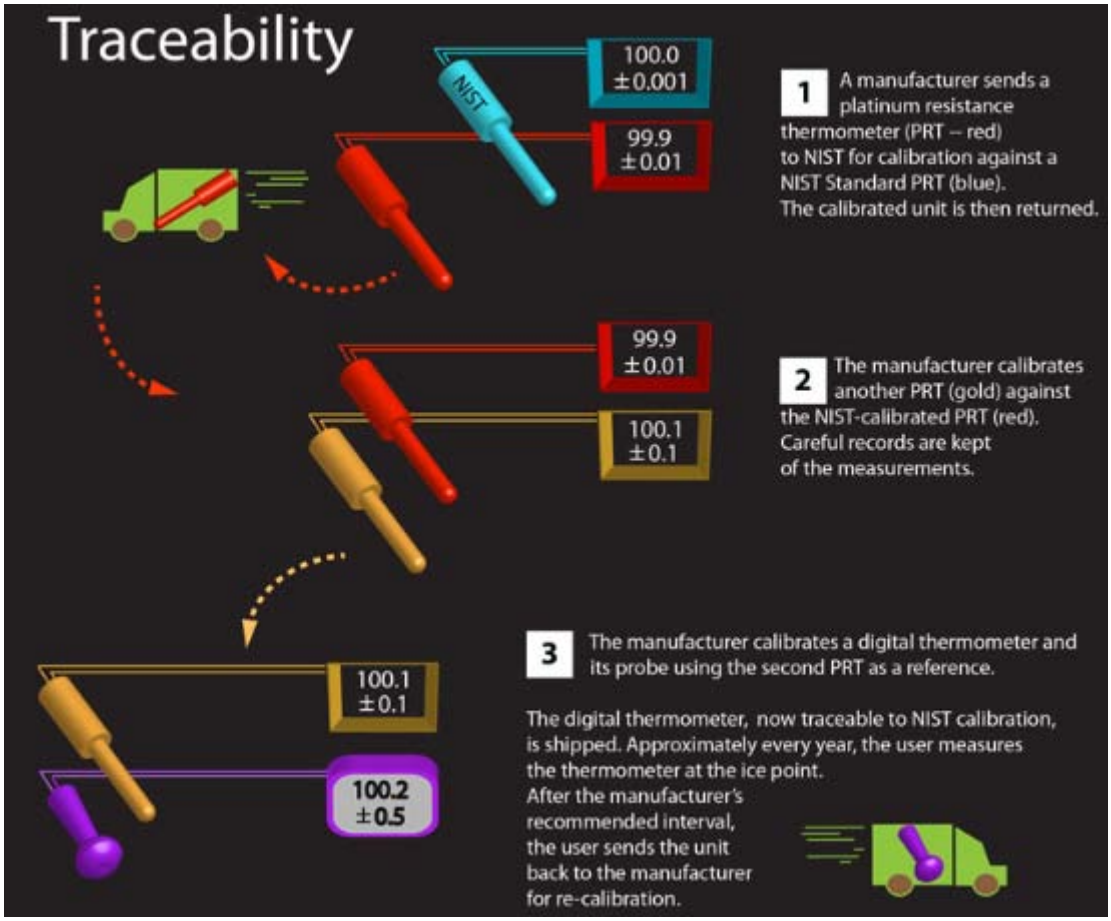

Figure 2.1: A common traceability path(from [1])

.

The small force standards are still in a nascent stage. First an informal study pilot comparison program was organized by the NMIs, who have small force facility and standards. The comparison study program among four NMIs, KRISS, NIST, NPL and PTB [75]. The primary realisation of a small force in the pilot study program is divided into two types: electrical force-based and mass-based methods. Both NPL and NIST facilities realise traceable forces based on electrostatic methods through electrostatic balance principle and traceability is derived from international system of units SI (i.e. meter, capacitance & voltage, while KRISS and PTB primary standards are realised based on deadweight principles by using high-precision mass comparators. The calibration procedures employed by them are not standardised yet and deviate from those used in the macro-force metrology such as standardised procedure described in ISO 376 [76].

In this pilot study comparison programm, it was decided by consensus of the participants not to adhere to the existing macro-force protocols. They agreed that comparison would be performed for the measurement of spring constant and force sensitivity for each of a set of five piezoelectric cantilevers. The pilot study comparison programm was conducted among NMIs from February 2008 to February 2010. The results of calibration capability are in agreement, suggesting that their small force facility are equivalent within their reported uncertainties. The detail of the reported uncertainties may be seen [77]. It was concluded by the authors that for future comparison a more rigorous technical protocol should be developed and adopted.

2.3 Standards and capabilities for small force metrology

Rapid scientific progress the during the 1990 in fields such as micro-systems, computing, low- noise electronics and other precision technologies meant that by around 2000 major national laboratories could seriously contemplate the design and implementation of traceable secondary standards targeted specially at small force calibration. Notably, and briefly as summarized below, the NMIs in the UK (NPL), the USA (NIST), Germany (PTB), (KTISS) and Taiwan (CMS-ITRI) have been contributing in this field [78], [48], [79], [80], [81], [82], [83], [10], [53], [**?**].

2.3.1 Low force measurement at NPL

The United Kingdom NPL, an internationally leading NMI, is playing active role to develop a facility for low force measurement. The low force balance was designed and developed at NPL with the collaboration of University Warwick and Technical University Eindhoven (2002-2005) [84], [85]. At NPL, and commonly elsewhere, small-force metrology (nanometrology) is considered the retain of facilities that inform it are, therefore, texture measuring instruments, such as NPL's Nanosurf 4 (primary profile measuring instrument) [86], topography measuring instruments [49], the development of primary balance in 1930 [87], micro-Newton thrust balance [88], nanoidentation instruments [89], micro-coordinate metrology probe based on a patented noncontact vibrating sensor [50], [90] novel comb drive for calibration of AFM cantilever [91] and micro-electromechanical device for lateral force calibration [3].

Low force Balance

The NPL has developed an instrument (figures 2.2 and 2.3) to provide force traceability in the micro to nano Newton range 1nN to μN. The low force balance(LFB) [48], [78] uses electrostatic forces, which tend to be small and so more easily controlled in this context. The NPL system, designed in collaboration with Eindhoven University of Technology, Netherlands and University of Warwick, has superficial similarity to precision electronic balance. A dielectric plate is suspended between pairs of electrodes by a very soft linear translation flexure mechanism. This motion is measured by a traceable multi-path laser interferometer. The basic principle of low force balance is summarised by

$$F = \frac{1}{2}V^2\left\{\frac{dc}{dz}\right\} \tag{2.1}$$

where F is force exerted, V is the applied voltage and $\frac{dc}{dz}$ the rate of change of capacitance per unit distance in the direction of motion.

When an external force is applied to the flexure system via small platen, it deflects and

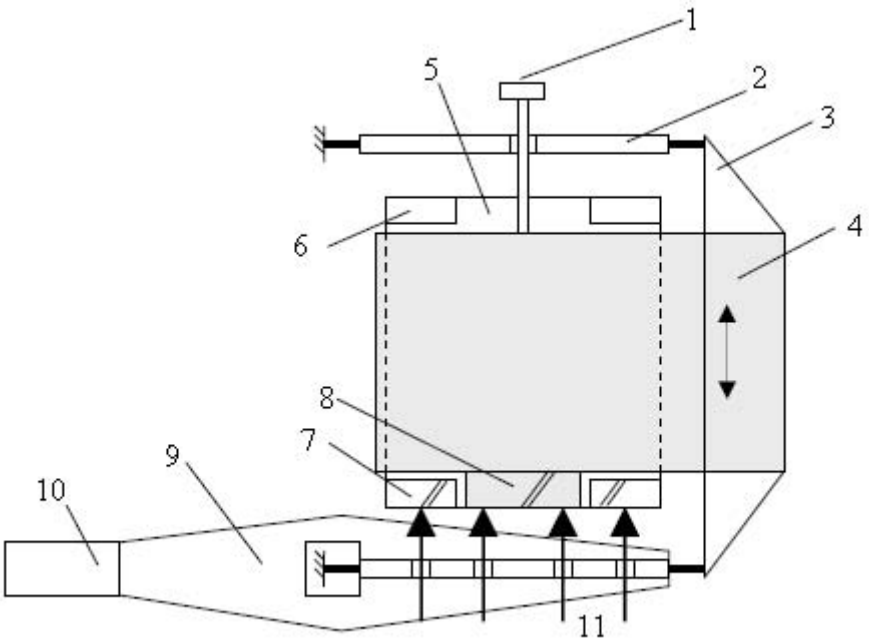

Figure 2.2: Schematic of NPL low force balance components: (1) platen and strut, (2) leaf spring, (3) parallelogram body, (4) dielectric, (5) capacitor plate, (6) spacer, (7) reference mirror, (8) moving mirror, (9) cantilever, (10) counterweight, and (11) laser beams (from [84]).

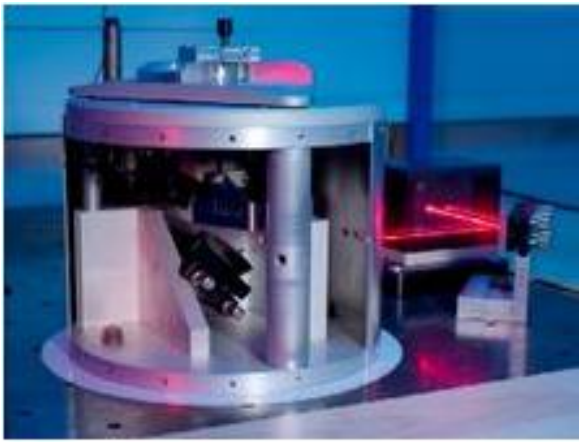

Figure 2.3: Picture of NPL low force balance (from [2]).

displaces both flexure and dielectric, this defection is measured by the interferometer, and used to modify the voltage in the capacitors to create a defection nulling back force. Thus the exerted force is calculated from the value of V and $\frac{dc}{dz}$. The measurement is traceable to the metre and ampere.

2.3.2 Electrical Nanobalnce

A novel comb-drive device was developed at NPL to calibrate the AFM cantilever spring constant. One example, the nanobalance device is shown in figure 2.4 that requires it operation in vacuum [91]. A vertical asymmetric in the fields is produced in the pairs of comb device that levitates a landing stage against an internal electric field. The spring constant value traceable to SI unit is calculated from the measurement of the driving electric signal and resultant deflection. Then for end-users, the device becomes a passive, calibrated, elastic device without requiring any more connections or possible disturbance by interacting fields. The authors reported a value of landing stage centre-point spring constant, 0.195 $Nm^{-1} \pm 0.01$ Nm^{-1}, that can provide calibration of AFM in the range $0.03 Nm^{-1}$ to 1 Nm^{-1}. The other example of a similar technique is seen at NPL, the Lateral Electrical Nanobalance (LEN) that was designed to measure the lateral forces such friction in AFM [3].

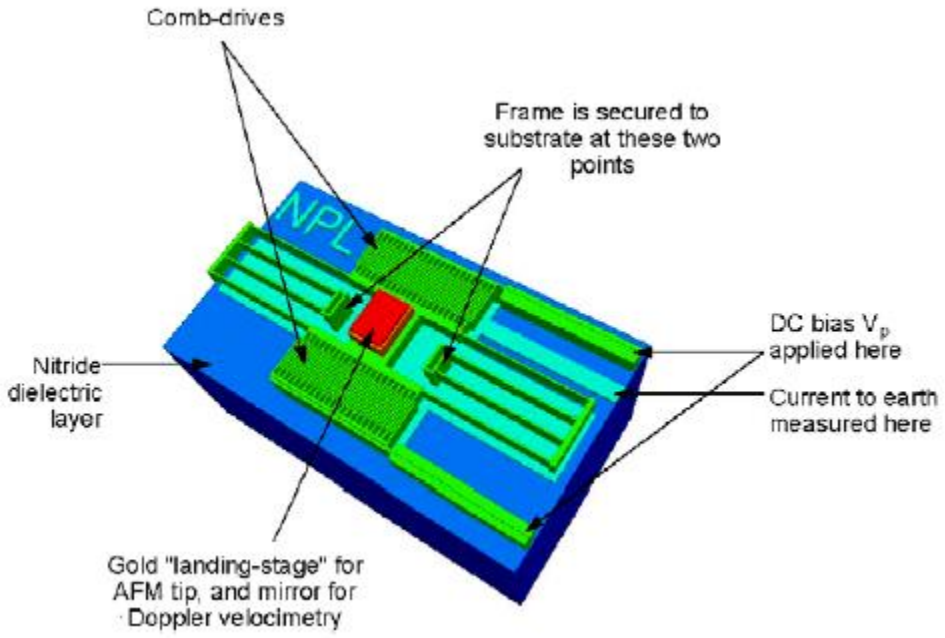

Figure 2.4: (Three-dimensional computer model of the electrical nanobalance device. The area shown is 980 μm 560 μm. Dimensions perpendicular to the plane have been expanded by a factor of 20 for clarity (from [3]).

2.3.3 Low force measurement at NIST

The researchers at NIST are actively playing a role for SI traceability of low force measurement and testing of forces in the range below 10^{-3}N. The block diagram of SI traceability

in the NIST small force laboratory is show in figures 2.5. The hierarchy in NIST for small force metrology is based on a combination of *length, capacitance and voltage* below than 10^{-5}N [47]. The NIST has realised traceable force standards below 20μN (electrostatic force balance (EFB)) [47]. The EFB is derived from electrical units to provide force tracebility to the AFM and instrumented indentation [92]. A piezoresistive cantilever is calibrated by using EFB at NIST. This type of cantilever acts as a force transfer artefact when assessing the thermal calibration method by comparison [25].

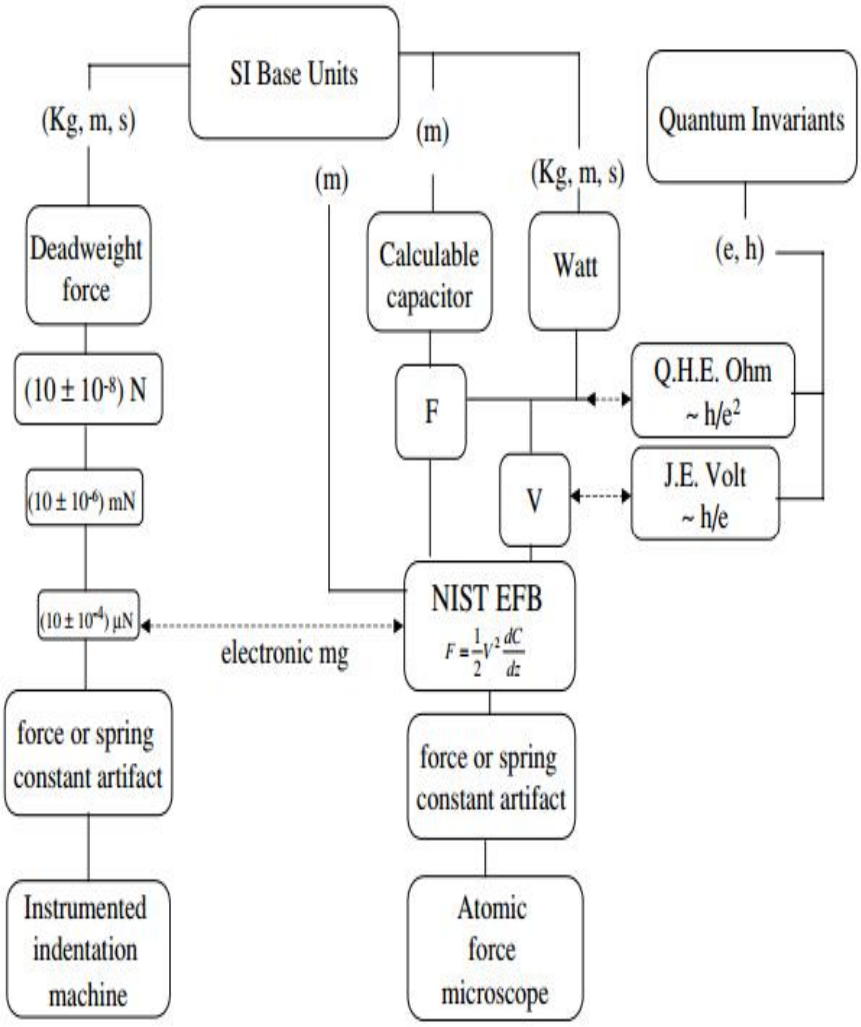

Figure 2.5: SI traceability in the NIST small force metrology laboratory (from [4]).

Electrostatic force balance

The NIST has developed a electrostatic force balance after a series of design iterations [79], [80], [93], [94], [4].The current version is shown in the figure 2.6. The figure shows that electrostatic force balance has been assembled on an optical table, which is designed free standing vacuum chamber. The electric force balance is mounted on an optical table with three legs that are protrude from the chamber floor through flexible bellows that terminate in blank flanges. The electric force balance operates in the air, or with another inert gas and the vacuum chamber operation eliminates air currents that could perturb compliant suspension. Both index of refraction in the interferometer and die electric constant gap in the capacitance are eliminated by the operation of vacuum a chamber. The electric force balance consists of an electrostatic force generator that acts along a vertical z-axis (aligned with local gravity) [79].

Forces are produced when a voltage is applied to the pairs of nested coaxial cylinders. The high voltage cylinder is fixed and inner ground cylinder is free to translate along z-axis, which can vary the degree of overlap between the cylinders. The electric force F is generated along the vertical z-axis for a given applied voltage.

$$F_z = \frac{1}{2}\left\{\frac{dc}{dz}\left(V_1^2 - V_2^2 + 2V_s(V_1 - V_2)\right)\right\} \tag{2.2}$$

where F is force, $\frac{dc}{dz}$ is capacitance gradient, V_1 is the voltage applied to the outer electrode before loading,V_2 is the voltage applied to the outer electrode after loading and V_s is the potential difference between the electrodes.

The source of uncertainty from the potential difference between electrodes is diminished by the procedure of reversing the direct voltage across the plates [93].

As reported at IMEKO World Conference in 2006, the agreement between electrostatic and deadweight force measurements in the range 200 μN is to within 13.3 nN that is greater than k=1 and less than k=2 uncertainty bounds on each measurements [94]. Later, on the spring constants of the array of cantilevers made from single crystal silicon (1 0 0) were

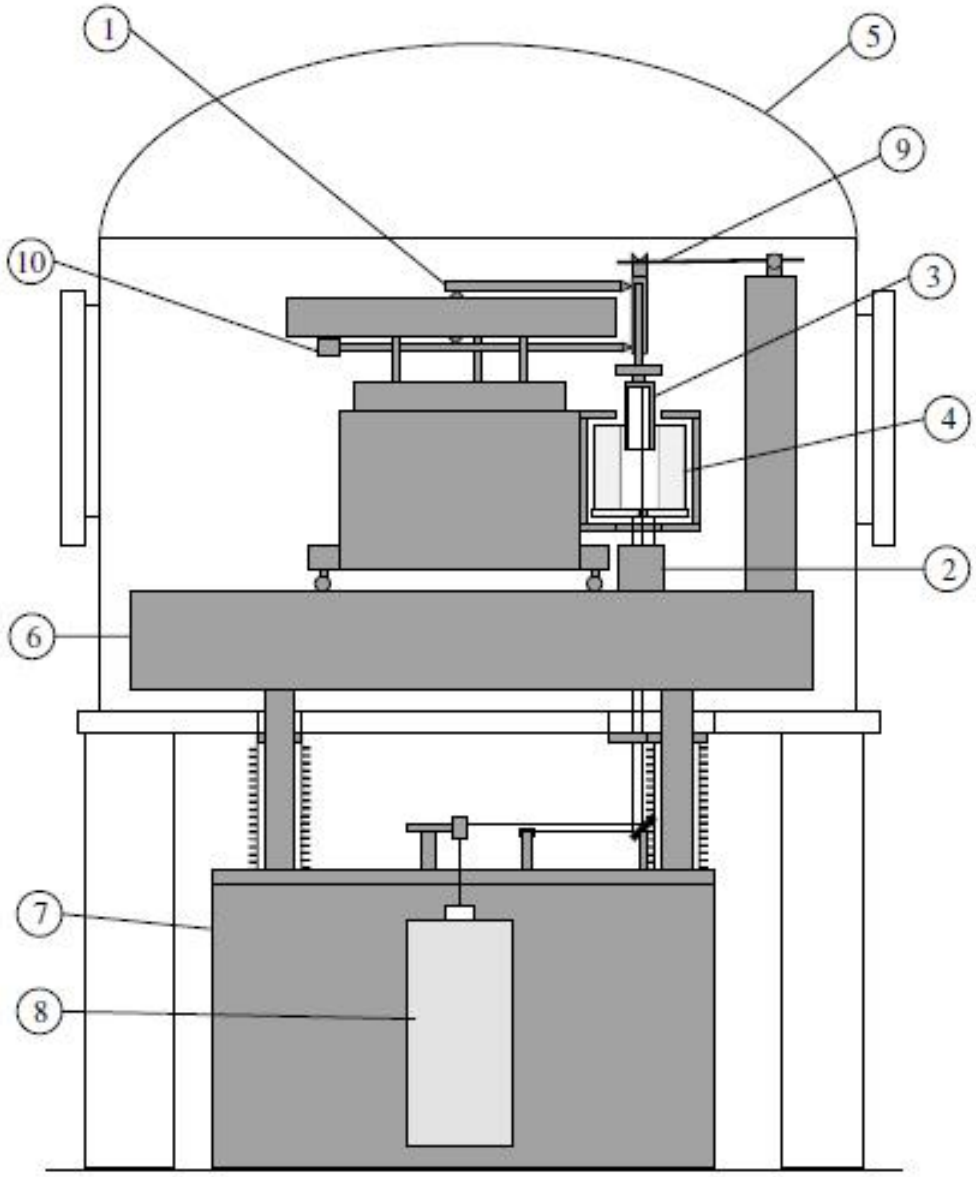

Figure 2.6: Schematic of NIST EFB components: (1) parallelogram balance, (2) differential plane mirror interferometer, (3) main inner electrode (cross-section), (4) main outer electrode (cross-section), (5) vacuum chamber, (6) optical table, (7) granite foundation block, (8) heterodyne laser light source, (9) mass lift and (10) counterweight (from [4]).

estimated through an electrostatic force balance in the range 0.02 Nm^{-1} to 0.1 Nm^{-1} and uncertainty of better than 2% reported. The agreement was confirmed between measured stiffness values and estimated stiffness from using resonance frequency measurements [25].

2.3.4 The low force measurement at PTB

The PTB has developed different weighing and mass comparators with an automatic weight exchange facility. The weighing principle of mass comparators used at PTB for realisation of mass scale and high-precision determination are summarised in table 34 [81].

The PTB developed devices are categorised into three types of device. The first type is for force calibration that covers that ranges from 10mN to 10N. The force calibration device mimics the operation of a conventional dead weight machine using electromagnetic compensation balances, which have a range of either 1200g ($\approx$ 12N) [82], or 210g($\approx$2N) [95], [96], [97] in order to calibrate the transducers in accordance with ISO 376. The incorporated feedback controls the mechanical forces of balance and is able to stabilise the force down to $\pm$ 1 μN level.

The second type of devices coveres the mid range from 50μN to 500mN forces, for which the PTB has developed micro-force measuring device (MFMD), which uses a mass comparator of 41g ($\approx$ 800mN) capacity with 0.2mg ($\approx$ 0.2μN) resolution. It is used for determining the stiffness and force sensitivity of AFM cantilever, such as vibration sensor and cantilever type sensor [95], [98].

The third type are called nano-force calibration devices and have in the range 1 to 180μN with approximately 1nN resolution.

Force compensation balance

The PTB developed a compensation balance (1mN to 5N), which is consists of a piezoelectric adjustment unit and precision compensation balance shown in figure 2.7. The force The force transducer under calibration is hold from above by an adjuster comprised of a screw for coarse positioning and piezoelectric actuator for fine motion. As the fine adjustment

Table 2.1: Data of the balances and mass comparators used at PTB for the realization of the mass scale and for high-precision mass determinations (selection), (Max: maximum capacity, d: scale interval, S: standard deviation, S_{rel}: relative standard deviation in relation to the usable maximum capacity).

Weighing principle	Range of nominal values	Max/d	S	S_{rel}
Electronic comparator balance with full electromagnetic force compensation	1 mg.....5 g	5 g / 0.1 μg	0.3 μg	6×10^{-8}
Mass comparator with automatic weight exchange facility, 4 positions	10 mg.....100 g	111 g / 1 μg	1.2 μg	1.2×10^{-8}
Vacuum mass comparators with automatic weight exchange facility, 6 or 8 positions (prototype balances)	100 g.....1 kg	1 kg / 0.1 μg	0.3 μg	3×10^{-10}
Mass comparator with automatic weight exchange facility, 4 positions	2 kg..... 10 kg	10 kg / 10 μg	20 μg	2×10^{-9}
Mass comparator with automatic weight exchange facility, 4 positions	20 kg..... 50 kg	64 kg / 0.1 mg	0.4 mg	8×10^{-9}
Mechanical, equal-armed beam balance	100 kg..... 200 kg	200 kg / 20 mg	0.2 g	1×10^{-6}
Mechanical, equal-armed beam balance with automated acquisition of measured data	500 kg..... 5000 kg	5000 kg / 60 mg	0.6 g	1.2×10^{-7}

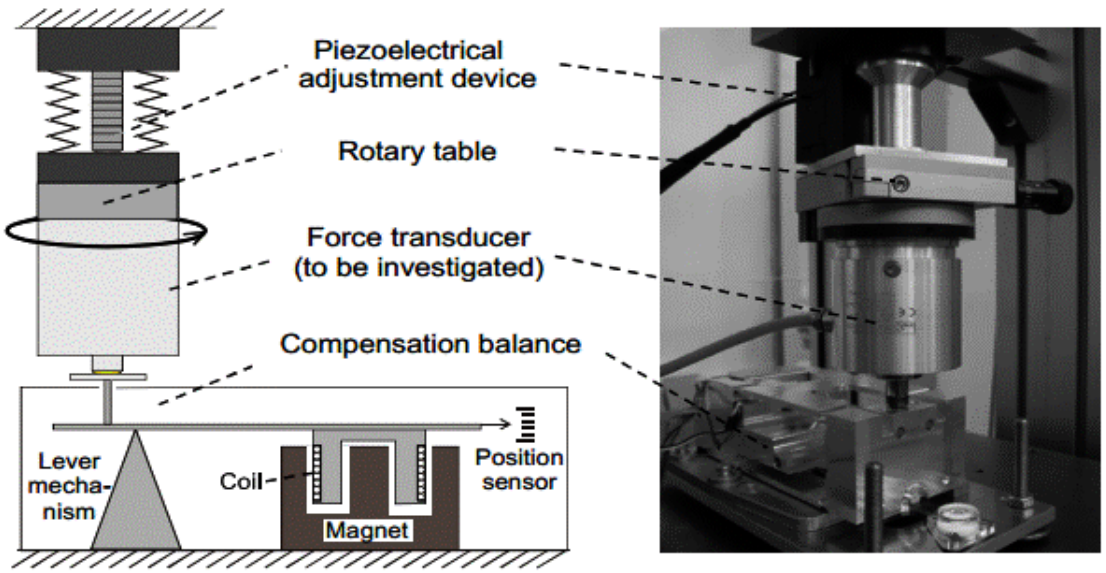

Figure 2.7: Measuring Facility with rotary table (from [5]).

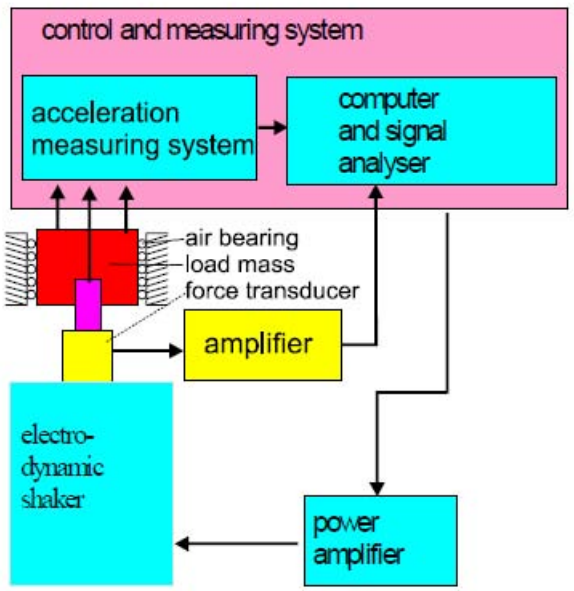

Figure 2.8: Facility for dynamic force calibration (from [6]).

device moves downwards then the force transducers push the load receptor of balance downward. The movement of the lever arm is recorded by the position sensor and balance automatically changes the current through a coil connected to the lever arm. A force is

produced by the action of the current carrying coil in a magnetic field and the position sensor resettled to its initial position. Due to the variation of piezoelectrically produced translation and force balance could be loaded in compression with different forces that are recorded by the balance. The piezoelectrical adjustment device allows a maximum displacement of 100 μm with a resolution of 1 nm and linearity deviations below 20 nm.This procedure enables the balance calibration at regular intervals against a weight of 10N [5].

The second type of compensation balance developed in 2006 was more reliable and can be used for force standard machine having range of few newtons and resolution of single micro-newton [97], [96]. The above mentioned types of force machine, which use electromagnetic balances with a range of 2 or 12N respectively for reaction force compensation of force transducers to facilitate the calibration and measurements of force transducer with range from 1mN to 10N.

Later another a new device was developed at PTB called the electromagnetic compensated balance [99], which has a highly stable and linear scale for the force and can be used for a force standard machine.

Moreover, to measure the forces in the range below 10^{-5}N with resolution of 10^{-12}N, PTB developed another method [7], [100], which uses a mechanical system, thus reducing stiffness.

Facility based on electrodynamic shaker system

A new calibration facility based on an electrodynamic shaker system was developed at PTB in 2003 for calibrating forces up to 10kN shown in figure 2.8 and used to determine to dynamic properties of measuring instruments. The dynamics force measuring instruments cover static and dynamic measurements. Static procedures are used to study the effects such as linearity, hysteresis, creep, repeatability and rotation etc. Dynamic measurements are performed to fix the differences between static and dynamic characteristics. This approach appear to be scalable to the needs of sub-newton measurements. It was not possible

to calibrate the force transducer beyond the 1 kN loads that are used in the automobile industry, robotic, material testing and force transducer [6] [81].

Electrostatic system for measuring micro- and nano-forces

Another high precision facility was developed at PTB for micro- and nano-force measurement. A disc-pendulum with electrostatic stiffness reduction allows a force measurement in the range less than 10^{-5}N with a force resolution of 10^{-12}N [7], [100]. Figures 2.9 and 2.10 show a conductive disc-pendulum (2) suspended between two parallel plates (3, 4) on the frame (9), which act as parallel plate capacitors. The stiffness of the pendulum could be adjusted by applying a voltage on the capacitors. Both plates (3, 4) and frame (9) are jointed to the base plate (1). The voltage u_1 and u_2 are applied on the disc-pendulum(2) & plate (3) and disc-pendulum (2) & plate (4).

The details of the mathematical model of electrostatic system for stiffness compensation method, principle, description of measuring set-up, thermal noise and seismic noises are well demonstrated by the author. In brief micro- to nano-forces in the range 10^{-5} with a resolution of 10^{-12} are presented. The theoretical model analysis predicts forces $F_n \approx 10^{-10}$N and relative uncertainty 0.8%, which corresponds to a force resolution of $\delta F_n = 8\times10^{-13}$N. Further, when the Josephson effect is used for voltage realisation with $\frac{\delta u}{u} \approx 10^{-8}$, this resolution could be improved to $\delta F_n = 1.5\times10^{-14}$N.

Force standard machine for measuring forces from 100μN to200mN

The new force standard machine (FSM) developed at PTB for the range 100μN to 100mN is shown in figure 2.11 and 2.12. Basically this machine is based on the comparison of a force transducer with the indication of an electromagnetic compensated balance (ECB). One core component of the FSM is the nano-positioning table(NPT) [101], [8]. The ECB stands on a table platform, which has advantage for the balance change that could adjust the force range. The NPT is capable of ensuring a wide positioning range of 7 mm along with an absolute position of 4nm. A suitable controller is used for interaction between the servomotors and piezoelectric actuators. The table also facilitates an internal incremental linear encoder for measuring position and the sensor has a resolution 2 nm.

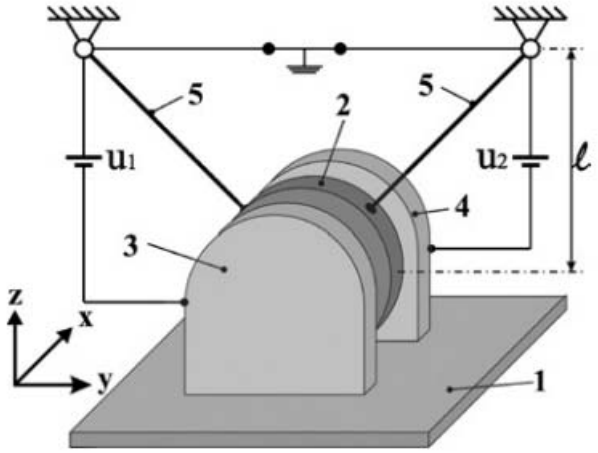

Figure 2.9: Electrostatic system for stiffness reduction1: base plate; 2: conductive disc-pendulum; 3, 4: external conductive plates; 5: suspension by a thin conductive wire) ($\ell \approx$0.3 m) (from [7]).

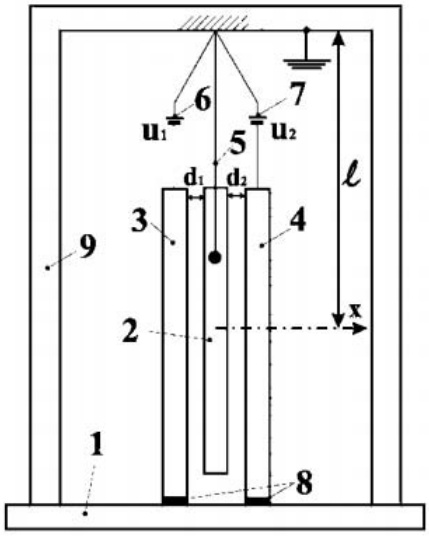

Figure 2.10: Lateral view of the electrostatic system for stiffness reduction1: base plate; 2: conductive disc-pendulum; 3, 4: external conductive plates; 5: suspension by a thin conductive wire; 6, 7: voltage sources; 8: electric insulation layer; 9: frame fastened to base plate ($d1 \approx d2 \approx 10^{-4}$m) (from [7]).

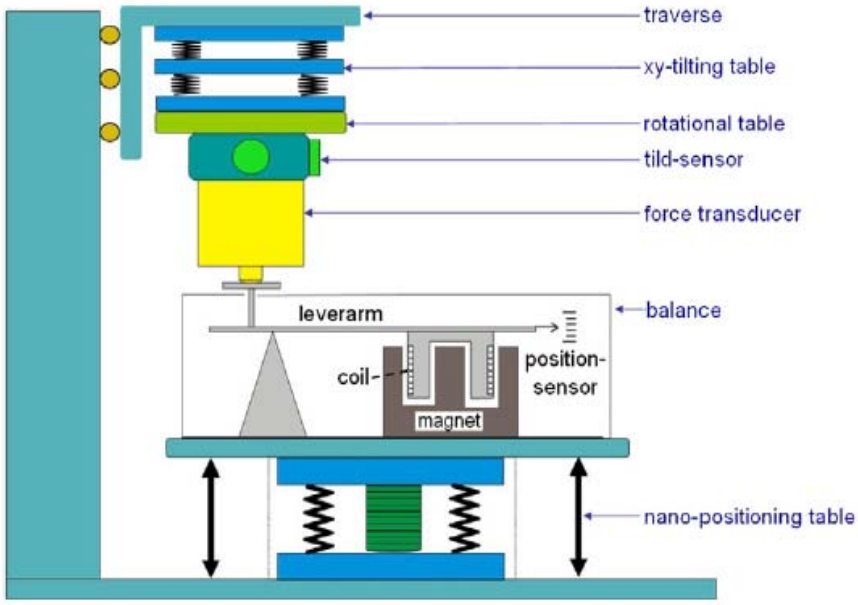

Figure 2.11: Construction principle of the new FSM. The ECB is located on a platform mounted on a NPT and can thus be driven against the force transducer. The transducer itself hangs on a rotational and tilting table for precise adjustment. The tilt table can be changed in x and y direction, whereby the tilt angle is measured by two appropriate tilt sensors. The rotational table allows a rotation of 360 degree. All hanging components are mounted on a vertical moveable traverse. (from [8]).

Figure 2.12: Photograph of the new FSM. In the lower part one can see the NPT and the balance, surrounded by a foil to reduce thermal influences. Above the balance, the transducer, with the adapter mounted on the rotational and tilt table (from [8]).

The two positioning concepts enable the movement of the table with wide velocity range i.e. (positioning range of 7 mm could be drive in 70s).

For designing the force range 100 μ to 100 mN, an EBC with a nominal range is used and has has a readability of 1 μg and standard deviation of 3 μg. The data data filters are switched internally and the balance can read with frequencies between 50 to 100 Hz The pressing of transducer causes its lever to move down figure 2.11. The position sensor located on the opposite side of the lever detect the position change cause by the transducer. The current though a coil mounted below the lever also increases through the internal controller of the balance, because the coil is also surrounded by the magnet which causes the coil to produce a magnetic field that is repelled from the static field of a permanent magnet. The produced deflection is compensated for by lowering the balance lever. Thus for high mass/force, the higher current and Lorentz force produced by the coil. Due to this effective result, the weighing pan is always kept at the same position. The coil current is controlled by balancing a wheatstone bridge arrangement for the transducer. A wheatstone bridge receives a current of coil through a resistor. Finally, the voltage signals are tuned and transferred to the balanced. Furthermore, the transducer may be adjusted by using a rotational and tilt table to set it perpendicular to weighing pan. The new FSM is capable of producing forces in the range 0.1 to 200 nN in accordance with ISO 376 standard.

2.3.5 The low force measurement at KRISS

The force standards, applications and traceability from the macro and micro level have been developed at KRISS. The KRISS has developed a small force facility that focuses on smaller force ranges of 500 nN to 100 μN. KRISS has also developed various device such as nano-force calibrator (NFC) using a precision comparator of 5g ($\approx$ 50mN) capacity with 0.1μg ($\approx$1 mN resolution for providing traceable calibrations to determining the spring constants and force sensitivities of various AFM cantilevers and micro-force sensors in the range 0.01 Nm^{-1} to 100 Nm^{-1}. KRISS has also claimed that the relative uncertainty of such a calibration is better than 1%. They have used several calibration methods for the comparison of the spring constants of various AFM cantilevers including the NFC method [83], [10].

An extensive study of calibration using various AFM cantilevers with spring constants in the range 0.06 to 42 Nm^{-1} was made using NFC. KRISS handcrafted a set of weights ($0.05, 0.1, 0.2$, and 0.5mg) from thin gold wire and made an uncertainty analysis. They claimed that NFC can calibrate AFM cantilevers traceable to SI with an uncertainty of better than 1%. The relative standard uncertainty of the smallest mass artifact, 0.05mg, reaches up to 0.4% (0.2 μg), which is the largest component of uncertainty in the calibration [10].

Conventional weighing balance

The low force measurement standards established at KRISS are of the deadweight type traceable from the mass standard. They cannot examine a standard below 1mg [9]. The mechanical modelling, micro-weighting device and the principle of force sensing using null balance are explained in [9]. The industrial experts prefer to use null balance for forces of high precision in order to overcome the limitations of real loadcells. Their force calibrator (NFC) consists of a micro-balance and nano-stage [9]. The schematic diagram of micro-weighing system is shown in the figure 2.13; it uses a high-precision comparator 5g($\approx$ 0.1 μg) capacity with 0.1μg($\approx$ 1nN)n resolution.

The device consists of a parallel spring and mechanism for amplifying displacement. When an object is placed on the weighing pan, the vertical force pushes the spring down and displacement of the spring is transferred by the flexible link, which rotates the lever arm about a flexure hinge. The rotation of the lever arm causes the coil to move. An optical position sensor is used to detect the displacement. The position sensor controls the electromagnetic transducer and increases the force until the position errors becomes zero. At this stage the applied force equals that from the current fed though the coil (electromagnetic force compensation). The device was designed for resolution of 1.0 mg and range over 100 g. Settling time was less than 1s figure 2.13.

Nono-force calibrator

The NFC consists of a commercial electromagnetic balance. For accurately tracing the spring constant, a nano-stage with integrated displacement sensor is used. Figure 2.14 is

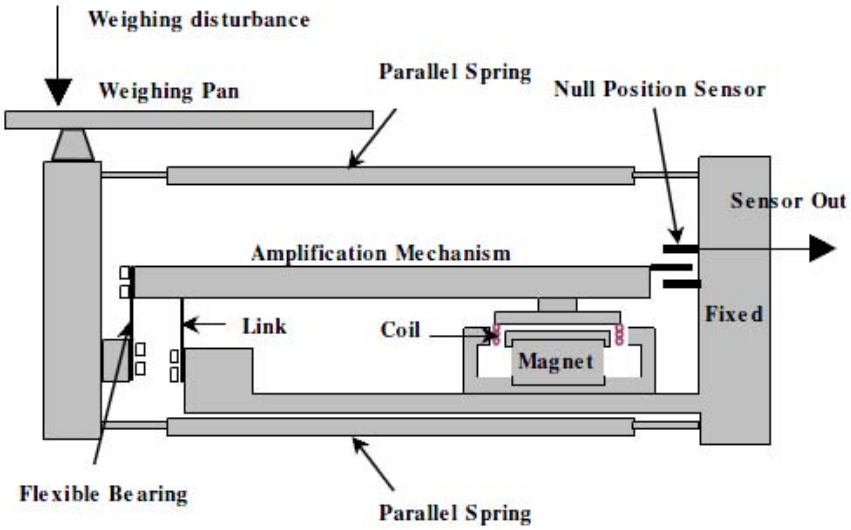

Figure 2.13: A conventional micro-weighing device: the electro-mechanical system.(from [9]).

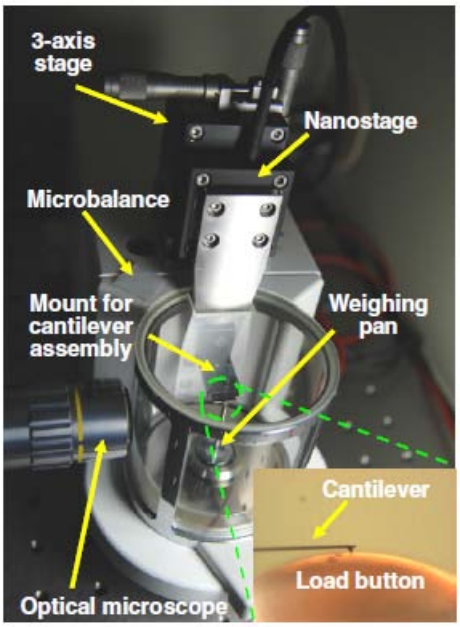

Figure 2.14: A photo of the nano force calibrator (NFC) consisting of a commercial microbalance, a three-axis stage, a nanostage and so on. The cantilever pressing the load button is shown in the inset(from [10]).

for calibration and figure 2.15 shows schematic setup for the calibration of spring constant. The NFC could perform well for characterising the levers even for a small force ($\approx$

500 nN). The relative uncertainty of spring constant calibration in this method is better than 1% based on calibration results and uncertainty analysis [10].

Quantum-base mechanical force realistion

The KRISS researchers have introduced a new concept of controllable ultra-low force realisation that is based on macro-scopic phenomenon as shown in figure 2.16 [11], [102], [103]. A ten micron sized annulus is mounted on a micro cantilever with ultra-small spring constant ($k = 10^{-4}$ to 10^{-5} Nm^{-1}). An external magnetic field $\mathbf{B_{ext}}$ is applied perpendicular to the annulus. The magnetic flux ϕ through the annulus below a super conducting temperature is quantised in the units of flux quantum that is equal $\frac{\hbar}{2e}$ ($\hbar$ is Planck constant and e is elementary charge).

The resultant magnetic moment m is an integral multiple of magnetic momentum for a single flux quanta m_q, which has component depending on the number n of the trapped flux quanta. A step force is exerted on the cantilever through interaction between the quantised magnetic flux and calibrated magnetic field gradient $\frac{d\boldsymbol{B}}{dz}$. The discrete forces steps are measured by monitoring the displacement of the cantilever using an optical interferometer. The minimum step force $\boldsymbol{F_q}$ is

$$\boldsymbol{F_q} = m_q \frac{d\boldsymbol{B}}{dz} \tag{2.3}$$

The step force was estimated of 184fN for a 50nm thick N_b annulus which has inter and outer radii 5μm and 10μm respectively for the gradient of 10Tm^{-1}.

2.3.6 The low force measurement at CMS-ITRI

Only a few publications have been seen about the activities of researchers in CMS-ITRI in Taiwan. But the authors Sheng, J.C. et al. claimed that their research team has developed micro-force measurement facility below 10μN during an IMEKO conference session. They drew attention to the practical applications of their established techniques, such as a Nano universal testing machine for force measurement below 1 N (force range $\leq$ 500 mN, extension range $\leq$ 150 mm and test material used: spider slik, polymer materials & thin film), calibration of nano-indention system (force range $\leq$ 500μm, cantilever stiffness

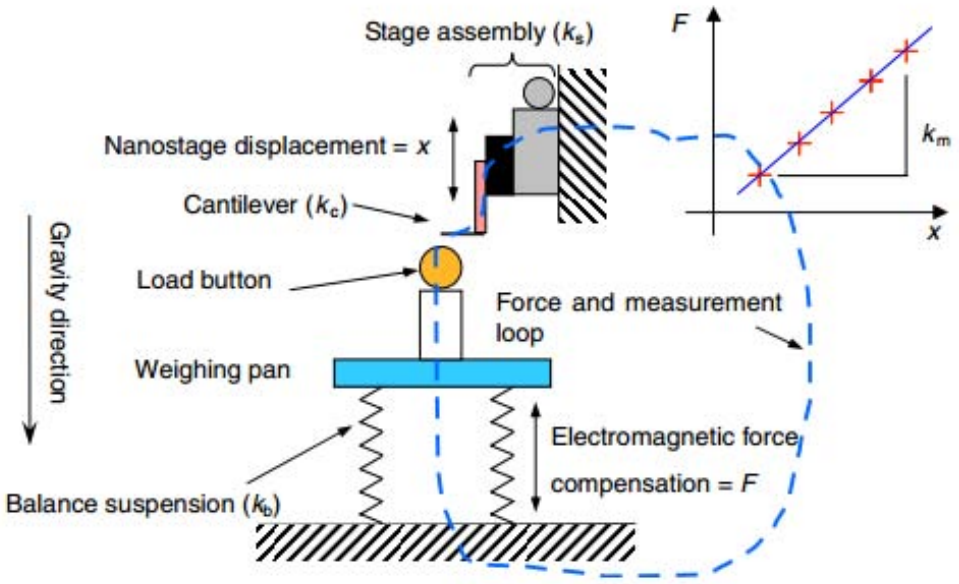

Figure 2.15: A schematic diagram of the calibration setup using the nano force calibrator (NFC) (from [10]).

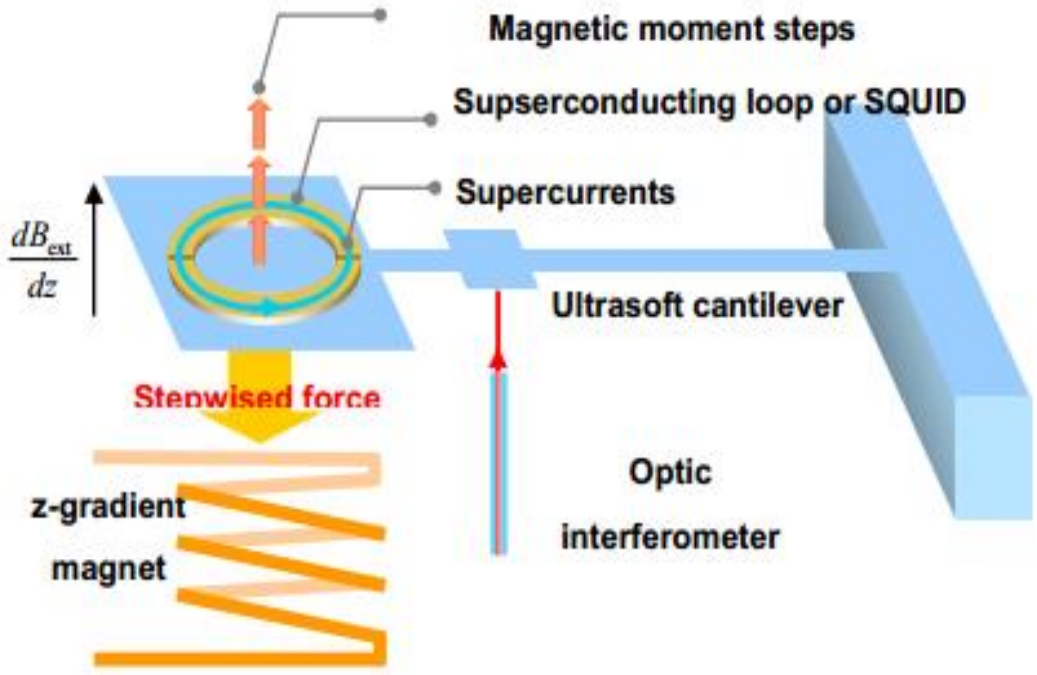

Figure 2.16: Schematic diagram of traceable picoNewton force realization based on flux quantization in a superconducting annulus (from [11]).

measurement 0.5 Nm^{-1} $\sim$ 10 m^{-1} & uncertainty 20% (k=2), microbalance (Mettler Toledo UMT5) and electrostatic force balance. Their established facilities also include a torsion pendulum balance to measure what they called the horizontal gravitation force below 50 nN that contain integrated radiation pressure base on damping for force measurement and flexure stage with electrostatic sensing and actuating (vertical force range below 200μN, with monolithic flexure stage and compensation electrostatic force) [53], [104], [55], [56].

2.4 Current challenges for the base units of SI

The measurement of micro to nanonewton forces is becoming essential in research, industry, worldwide national intuitions and academic intuitions at this time of flourishing biotechnology because wide ranges of forces are required and there is great demand for them to be related to their applications. The biophysicists are also characterising small force further to subpiconewton, associated with molecules and cells, to investigate mechanical to properties and role of forces that could influence biological processes. These measurements are becoming more and more precise and current levels of measurement uncertainty will be a problem in the near future. Therefore, preparations are being made to redefine the kg in SI system [105], [32], [34], [33].

Weighing problem of small masses in metrology

Dead weights are usually used for maintaining the force traceability in the millinewton to meganewton range [48]. The lowest traceable force realised by a deadweight standard machine is around 1N. Researchers and metrologists are exploring new facilities for force calibration from millinewton even to a micronewton, e.g. by placing calibrated mass artefacts on sensors to calibrate them or by using the down-slope component of gravity acting on an object that placed is on an inclined plane to generate small force [106]. This approach has some restrictions if the sensor is small and it becomes difficult to load a weight directly on to the sensor. Hence uncertainty of calibration depends how a weight is placed accurately at right position onto sensor. The other restriction is that the lowest mass available commercially is 1mg ($\approx$ 10μN) and all world NMIs provide a calibration facility only for a mass above 1mg. But below 10μN handling difficulties and contamination produce higher relative uncertainties in weight measurement, e.g., 2mg

($\approx 20\mu$N) could be made practically from a length of fine gauge wire of length $\approx$ 10mm [107]

Another approach currently being developed at PTB and KRISS is to use primary standards in combination with based on dead weights mass comparators (mass balances) discussed already in the previous section. [96], [97], [10], [108].

New challenge for base unit (kg) of SI system

The classical methods of calibrating forces derived from the kg standard do not apply to the sub-millinewton regime. The newton derives in SI system from kilogram, which is extremely difficult to realise, even in a best standards laboratories, to precision of the nano traceable metrology of level. A lot of scope is seen for micro- to nano-newton level forces, which are highly reliable and may be used for real machine calibration.

The apparatus required to make such measurements must have metrology traceability to realise the SI unit of force. The low force measurement makes huge demands and a relevant system must be traceable to tiny masses smaller than a milligram for realisation of SI unit of force. The instability of small masses means that the artefact range scaling down from kilogram (kg) to nano force presents challenging targets in terms of instability and traceability [109].

During the 24^{th} meeting in 2011, the General Conference on Weights and Measures CGPM and the International Committee for Weights and Measures (CIPM) agreed to revise the units of SI with a view to it continuing to meet the needs of science, technology, and commerce in the 21^{st} century [12].

2.4.1 Conventional definition of kg in SI System

The kg is still defined in terms of a material artefact, namely the international prototype of kilogram (IPK) kept at the Bureau International des Poids et Mesures (BIPM) [110]. The third verification of national prototypes of the kilogram (NPK) against the IPK in the period 1989 to 1991 confirm the relative mass changes being in the order of 50μg during

a period of about 100 years [12]. The unknown changes in the mass unit also influence the base unit, because the definition of ampere is related to the kg. Similarly, the other definition of mole and candela also depend on the kg (figure 2.17).

2.4.2 Proposed changes to base unit of SI system

The proposed changes by CGPM and CIPM to the SI can be summarised as follows [12], [111].

- Define all existing base units of SI in terms of well-recognized fundamental or atomic constants, such as the Planck constant h, see figure 2.18.
- The values of all these constants are fixed to an exact significant number (with zero uncertainty), such as for the speed of light in vacuum, $c = 299\ 792\ 458$ metre per second.
- Formulate and define all seven base units of SI in a uniform manner.
- Prepare specific sets of instructions (i.e. "mise en pratique") and explain how each base units can be practically realised based on recommended top-level procedure.

Planck's constant h, the ampere in terms of the electronic charge e, the kelvin in terms of Boltzmanns constant k, and the mole in terms of the Avogadro constant NA would be used for a new definition of the kilogram.

2.4.3 Redefinition of base units of SI system

The Consultative Committee for Mass is (CCM) is currently working to redefine the kg. Several methods are under the consideration that could be realised in the future by different primary methods, e.g. the Avogadro method (also know as " crystal density method"), "watt balance" using primary mass standards and how NPK or other secondary mass standards of NMI can be linked to the primary mass standards via Planck constant "h" figures 2.17 and 2.18 [12], [112].

2.4.4 Proposed new definition of base units of SI system

The new definition of the kilogram as currently proposed has its magnitude is set by fixing the numerical value of the Planck constant $h = (6.62606\text{D}\times\ 10^{-34}\ \text{m}^2)\ \text{s}^{-1}\text{kg}$, or in derived

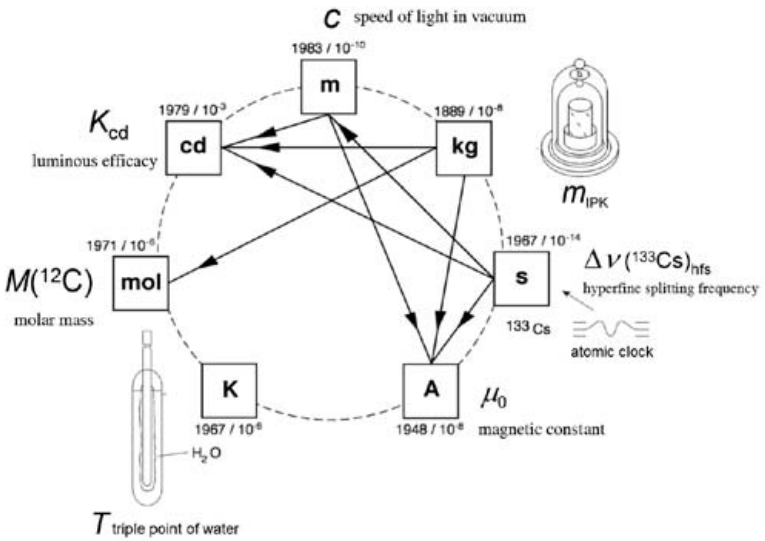

Figure 2.17: The seven base units and their relationship in the current SI (from [12]).

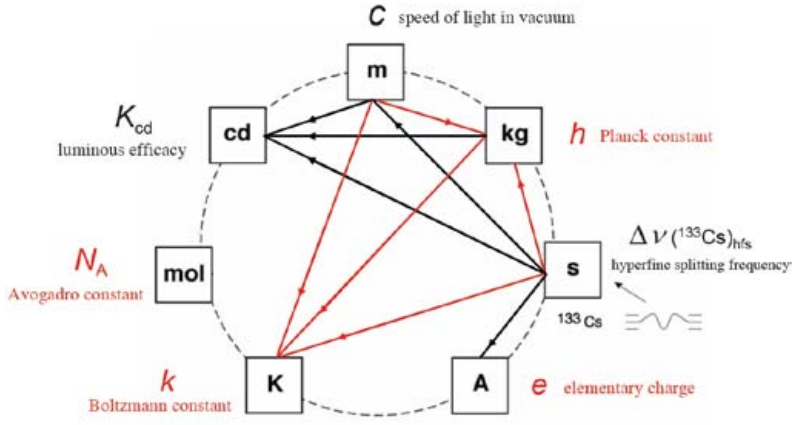

Figure 2.18: Figure 2. Definition of and relationship between the seven base units in the proposed new SI. In the new SI all base units will be defined in terms of fundamental or atomic constants. The changes to the current SI, and the new relationships, are marked in red. The black arrows denote relationships that remain unchanged in the new SI (from [12]).

units J s. D stands for digits that are added to the numerical value at the time when the definition of the kg will be adopted. The value of the Planck constant is decided by

nature, and its numerical value is set by this definition and other units, second and the metre are defined separately. Therefore, the effect of this equation is used to define the new unit of kg [12].

The most important aspect of the redefinition of any unit is its continuity. The new defined unit would be of the same size as the previous unit to a high degree so that the results of past measurements remain the same. In order to realise the new unit the unavoidable discontinuity shall be smaller than or at least comparable to the uncertainty. Hence, the new definition of the kg requires a measurement of the Planck constant in the present SI system to determine the numerical value to be used. Another important aspect considered is whether the future new definition would be practically realized with a sufficiently small uncertainty. Experts in mass metrology who meet in the Consultative Committee for Mass and Related Quantities (CCM) estimate that the uncertainty for the realisation of the kilogram should not be larger than 2 parts in 10^8, for legal requirements in metrology. A "mise en pratique" will be developed by the CCM which will specify how the new definition could be realized in practice. The existing difficulty has to be addressed in terms of how to ensure the uniformity of mass calibration in the future [109].

The uncertainty for the determination of the Planck constant is expected to be around about 2 parts in 10^8. It has been already stated above, the Planck constant could be directly determined with a watt balance or indirectly, via the definition of the Rydberg constant. Watt balance experiments purely rely on the equivalence of mechanical and electrical energy and also on the use of two macroscopic quantum effects i.e. (the Josephson effect and the quantum Hall effect).The watt balance approach has the advantage that it could be carried out by a single laboratory [105], [113].

It has been reported by other researchers that while the new definition of the kg requires as reliable evaluation of the Planck constant h, the published values of h are not in agreement within their uncertainties [114]. To solve this problem METAS has developed a new watt balance in strong collaboration with specialised partners coming from high technology industry, universities and research institutions. The preliminary experimental results were

judged very promising and should allow one in the future to reach the expected relative uncertainty of a few parts in 10^8 [115], [116], [117], [109].

2.4.5 Low force artefacts

Transfer artefacts are considered to be one of the most essential elements in the hierarchy of SI measurements for disseminating national standards to industrial standards or instruments at lower levels of the hierarchy. Direct transfer of force standards to the target instruments is incomplete without transfer artefacts due the immobility of standards or target instruments. This is why, in most cases, one needs devices or standard reference materials that are capable of delivering force from the standard to the target. Transfer artefacts in conventional force metrology are based on a load-cell technology. When they are loaded, they then act like an elastic spring element. On loading, they can read the resistance changes that are proportional to the applied load of the strain gauges attached on the spring element. The deadweight standard machines maintained by NMIs ensure relative uncertainties of a few parts in 10^5 of top-grade load-cells, which are known as "transfer standards". There are available standards above the newton level. Therefore, NMIs are seeking to develop new low-force transfer standards along with low-force primary standards [75].

The first machine that falls into the category commonly called coordinate measuring machines (CMMs) was developed by Ferranti, LTD., of Dalkeith, Scotland (Ogenden 1970) shown in figure 2.19. The initial Ferranti development was an inspection machine that has movement facility along x and y-axis (610 mm & 381 mm) respectively. It was used for production inspection accuracy 0.025 mm and resolution of 0.012 mm.

While many physical principles might be exploitable for nano force transfer in the long term (section 2.6), NMIs are also seeking technologies that could be developed rapidly into relatively robust and wrt-effcetive transfer standards for at least the millinewton to micronewton range. There is believed to be more urgent commercial need to cover this range. So far, all published proposals are based upon various types of spring.

Figure 2.19: Ferranti coordinate measuring machine (from [13]).

One major line of research builds on the probe technology for micro-coordinate measuring machines.

The first development of CMMs was started in 1968 at Mitutoyo with the design of an x-y measuring instrument. It was used for measuring the cases of household electric appliances. Thus the probe can perform the measurement that was previously performed by various devices such as height, gauges, calipers, roundness-measuring equipment, surface plates and micrometers. Later, in 1973, Carl Zeiss of the Germany introduced the first CMM with three dimensional measuring probe head and made probing (scanning) possible.

Further advances in CMMs, since 1985 have improved its accuracies and other features such as programming and data analysis have been expanded [13]. During the 1990s, various research and commercial groups were observing the growth in micro- and nano-applications and considering whether small, super-precision versions of the CMM could be devised and used under practical conditions. But alongside other major challenges it was soon realized that delicate surfaces need to be addressed via probes offering not just high-precision but very low contact forces and access into very small recessed features. In this way a new field

of research into micro-probes opened up and much of the best, extensive early work was performed in the Netherlands.

Pril developed one of the first designs for a higher precision mechanical micro probe for a coordinate measuring machine during his PhD Studies at the University of Eindhoven [14]. In 2008 Bos another PhD student at the University of Eindenhoven [118], redesigned Pril's Probe as shown in figure 2.21 and presented new design of gripper [119], [118]. The basic suspension shown in figure 2.20 for the probe system consists of three slender rods (acting of beams) with three effective degree of freedom (3-DOF), translation along the x-axis and rotations about the x-axis and y-axis. Strain gauges are attached to the slender rods to measure indirectly the displacement of the tip. Experiments performed with strain gauges showed hysteresis was often caused by connection of strain gauges to the base material [119].

Pril's original design for the micro probe was adopted by Bos, IBS and NPL [120], [121], [118], [122], [123]. NPL renamed it as "Triskelion" (triskelion simple means three legged, from the Greek) micro probe. The original Pril and Bos designs for the probe always arranged slender rods in a circular pattern with 120 degree offsets (the elbow angle between each arm and slender rods always was 60 degree). NPL versions were made as small metal fabrications, but they latter introduced a microfabricated version, actually with metallic beams although produced using typical silicon processing routes. Note that NPL adopted the geometry with 60 degree elbow, proposed by Prill. IBS has also adapted Pril and Bos designs with 60 degree elbow. The professional competitive environment for commercial purposes has been seen between IBS and NPL for advancement for micro probe work such as Isara 400, and vibrating micro probe, [124], [125].

The extensive research work for triskelion micro probe has been performed at the University of Eindhoven, NPL, METAS [14], [118], [126], [127], [128], [129], [130], [131], [132], [120], [50], [121], [133], [134]. The research work for micro probe was also carried out at other intuitions [135], [136], [137], [138], [139], [140], [141], [142], [143], [144], [145], [146], [147]. While significant to the design and application of micro probes, these sources contribute nothing original in terms of suspensions relevant to this thesis and are not

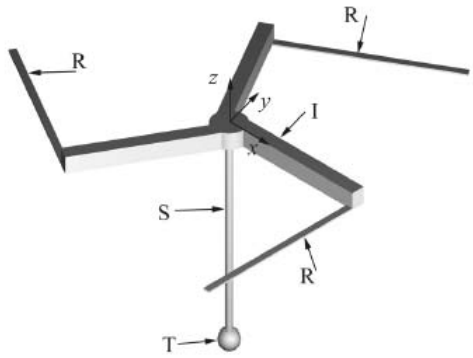

Figure 2.20: The probe tip (T) and the stylus (S) are suspended to the probe house by three slender rods (R) tangentially touching an intermediate body (I).The free ends of the rods are to be connected to the probe house (from [14]).

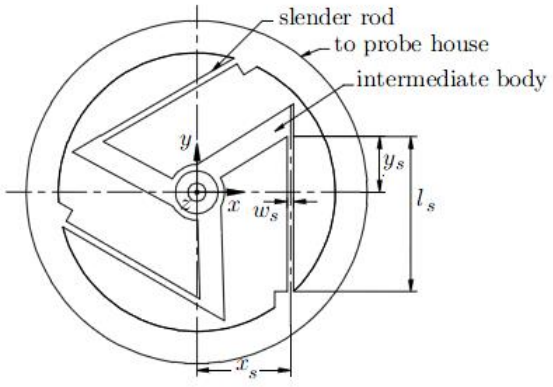

Figure 2.21: Dimensions of the suspension from [14]).

further discussed.

Jones at the University of Warwick in 2012 [148] also adopted microfabricated triskelion force artefacts again with 60 degree elbow angle only. These were fabricated at Cranfield University and demonstrated with some success.

Moreover, micro probes are usually intended as x-y-z sensors of movement at a stylus tip and all the planar suspensions implement this as at the free end of a stylus rod that is connected to a flexure with a z-translation and two rotations. Triskelion (or even diaphragm) designs do this pretty well, where roughly equal effective stiffness at the tip in each active

axis is desirable and, in principle, attainable. However, for a force transfer artefact we would ideally want (but cannot have by these methods) a pure z-translation having a single degree of freedom device. The implications of varying this pattern for the detailed design of triskelion transfer artefacts seem not to have been published or discussed in the literature available in the public domain.

2.4.6 3D micro probe system

A new tactile 3D micro probe with optical detection was developed and published in 2011 [15]. The system design is shown in figure 2.22 and 2.23. The mechanical design of the probe system was altered to allow exchange of the stylus separately from the flexure elements. Metal membranes were used in the new system design instead of silicon membranes that were used in the old system and the function of these membranes was to lock the parasitic movements to optimise for isotropic forces. While discussing the membranes/design (suspension), several key points were identified by the authors:

- Stiffness is controlled by altering the thickness or width of the elements (beams).
- The suspension must provide the tip with a stable resting position and movement relative to the probe system's housing.
- The optimisation of the membranes is required for small isotropic probing forces.
- The natural frequency must be higher than few hertz to reduce the free oscillation of the flexure elements and probe tips.
- The membranes should be stiffened against parasitic movements.
- The equivalent mass should be small because it directly affects the probing forces.
- Elastic flexure hinges should be made from non-creeping material and breaking resistance should be considered.

The authors also presented their overviews of past micro probes shown in figures 2.24 and 2.25. Figure 2.24 (a) shows the first system design with a silicon membrane [16]. The sensor elements were removed and deflection was detected from the backside. The anisotropic stiffness of the membrane was determined to be approximately 200 N m^{-1} in

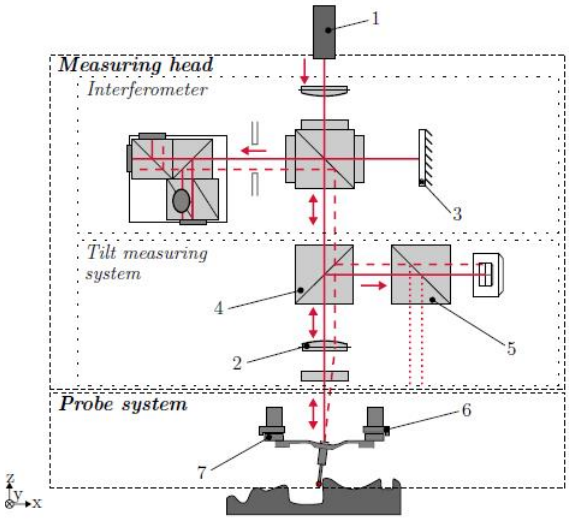

Figure 2.22: Functional principle of the 3D microprobe system: (1) fibre coupling, (2) focus lens, (3) reference mirror, (4) neutral and (5) polarizing beam splitter, (6) probe mount system and (7) plug. from [15]).

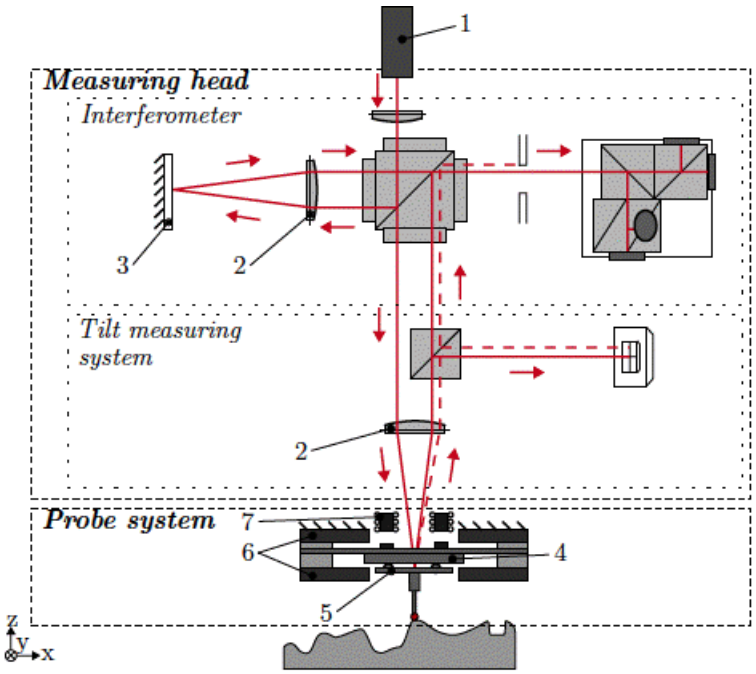

Figure 2.23: New system design for the 3D microprobe system: (1) fibre coupling, (2) focus lens, (3) reference mirror, (4) probe mount system, (5) plug, (6) overload protection and (7) weight force compensation and force generating unit from [15]).

the $x-$ and y-direction and 5200 N m^{-1} in the z-deration.

Another design is shown in figure 2.24 (b) and (c), which clearly indicates the flexure elements (three beams) are arranged symmetrically with 120 degree angle offset position with three degree of freedom, rotations about x, & y-axis and translation movement in z-direction. Measurements were made that this arrangement have nearly equal stiffness for all probing directions [17], [149].

Further, the flexure element in figure 2.24 (c) was adapted to minimise parasitic rotations

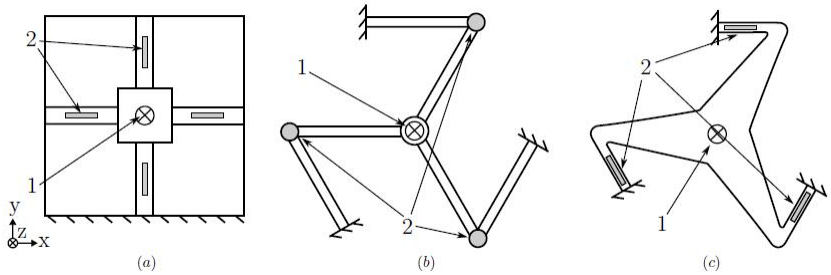

Figure 2.24: Designs for the suspension system: (1) stylus, and (2) sensor elements. (a) Full or cross-shaped boss membranes [16]). (b) IBS Triskelion probe [17]): Invar membrane with capacitive sensors. (c) Gannen-XP [18]): silicon membrane with piezoresistive sensing elements.

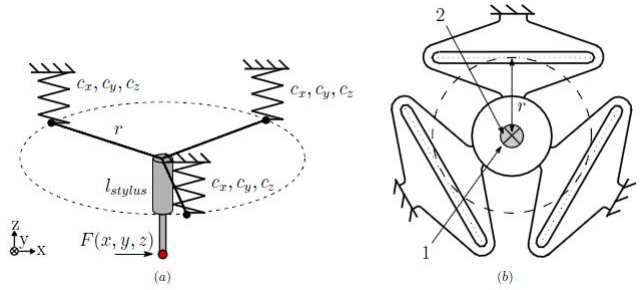

Figure 2.25: Assumptions and result of the membrane design. (a) Substituted mechanical system. (b) Design: (1) stylus, (2) bending area from [15]).

about z-axis figure 2.25 (b) which could occurs over a few degrees when the flexure element moved out of the xy-plane. The new microprobe system design possesses great potential for micro- and nanometrology, with respect to the possibility of exchanging the stylus without the flexure elements. This distinct feature is introduced in this system, which is capable of enabling the absolute roundness calibration of the probing sphere. This is main reason that

concept of new approach is a promising for 3D measurements, which include sphere form deviation corrections.

2.5 Force sensing methods

Studies of behaviour, as potential force transfer artefacts, of planar flexure mechanisms such as triskelions is the core topic of this thesis. Further discussion is deferred to chapter 3. Prior to that, it may be useful to review other force generating principles that might offer rival solutions for direct ranges of the force transfer.

2.5.1 Dead wight forces production

The earth's gravitational field acting on an object of finite mass is commonly used method for force production (a dead weight). The net downward force produced by a weight in the earth's gravitation field is given as

$$F = mg\left(1 - \frac{\rho_a}{\rho_m}\right) \tag{2.4}$$

where ρ_a is air density, ρ_m is mass density, m is mass and g is gravitational acceleration.

The force produced in equation 2.4 is in newton. From the outcome of international comparisons, the relative uncertainty of measurement produced by dead weight standard machines is stated by National Measuring Institutes as below $1\times\ 10^{-5}$. Dead weights are used for maintaining the force traceability in the mN to MN range [150], [151]. This attempt to lead the needs rather than present a series of sperate statements in sperate sentences. For the force below 10 μN, well within the low force balance scale, there will be higher relative uncertainty in weight measurement due to difficulties of handling, contamination etc. Dead weights are not considered suitable for use as low-force transfer artefacts [45].

KRISS handcrafted and calibrated microweights, a set of mass artefacts of masses 0.05 mg, 0.1 mg, 0.2 mg and .5 mg to achieve SI-traceability in force measurements during calibration of compliant cantilever. The relative uncertainty of the smallest mass artefact 0.05 mg was reported to be 4% (2μg), that has been seen as the largest component of

uncertainty in the cantilever calibration [10].

The Laboratorie National d'Essais (LNE) in France has produced a set of artefacts in the range 0.1 to 0.9 mg with aiming to calibrate the sensitivity of mass comparators []. LNE reported the standard uncertainty of the smallest mass of 0.1 mg was 0.06 μg [152]. PTB also reported that a high-precision mass comparator are used to calibrate the spring constant of compliant V-shape cantilevers [108].

Low force standards based on deadweights approach is useful and reliable down to 0.5μN($\approx$ 0.05mg) via extension of mass standards. However, the increased levels of careful technique required implies that it becomes impractical for routine industrial or shop-floor use at considerably higher forces (masses).

2.5.2 Resonance method: nanoguitar

Since mechanical resonance is affected by direct stresses in a vibrating system, resonance frequency modification can be used to sense applied forces. One variant proposed for calibrating scanning force microscopes is know as nanoguitar [19].

A conventional scanning force microscope was set up operating in vacuum, with its tip pressed against the platform of the device, a cantilever. A fine wire 'String' is attached to the free end of the beam an held in tension. Changes of tip sample interaction force lead to proportional changes in the resonance frequency of the string (figure 2.26). The experimental setup of apparatus is show figure 2.27. Vibration in the wire was excited electromechanically (Lorentz force) and its frequecy detected by Doppler vibrometry. Optical sensing must be used to minimise disturbance of wire. It is a major challenge to obtain a good frequency signal from a wire. An exciting vibration in the wire (done by the Lorentz force) and detecting the frequency (which must be done optically for minimum disturbance, with doppler vibrometry being used) is challenging at this scale. The other two serious drawbacks may be seen in this method: the optical integration of resonant frequency and Doppler vibrometery and oscillation, which are generated by using the

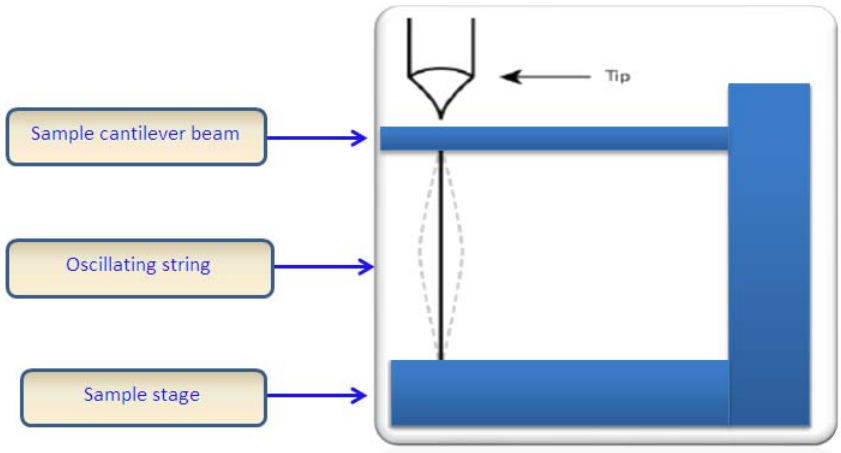

Figure 2.26: Schematic setup of the string force sensor- the nanoguitar (from [19]).

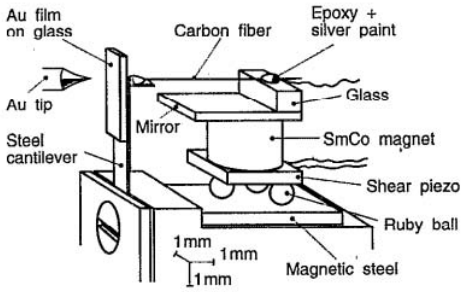

Figure 2.27: Drawing of the prototype force sensor. Example of an actual experimental set-up showing sheer piezo for tension adjustment and magnetic for actuation of Lorentz oscillations (from [19]).

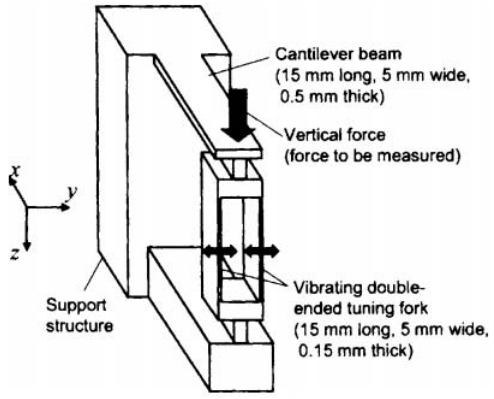

Figure 2.28: Schematic diagram of a double-ended tuning fork resonance force sensor (from [20]).

Lorentz force.

The method used add complexity and cost, leading to a large physical system. The author reported a force of 0.1 nN could be archived. This novel idea is not practical because the system only generates forces one direction and can't easily used on the low force balance or with most target instruments.

2.5.3 Resonance method: tuning fork

The use of a double-ended tuning fork(DETF) as a unique approach for a high sensitive sensor is presented by [20] and shown in figure 2.28. When a vertical force is applied to the cantilever, the resonance frequency of the DETF beam changes due the change in axial force. DEFT resonators are monolithically fabricated and this process can reduce clamping loss and improve the force sensitivity. The beams of the DEFT are vibrated by an external electromagnet and amplitude is measured with laser Doppler Velicometery. The monolithically fabricated system has experimentally achieved minimum detection limit of 19 μN and amplitude of 1nm, with a theoretical maximum value of 0.45 N. This limit is rather high for practical with a low force balance.

A simulation of the DETF is presented in [153]. The finite element method was used to design the resonator and is applied for detection of two axial angular vibrations as gyro-sensor. The sensor design presented cannot be adapted for a transfer artefact due to noise levels, device fabrication and oscillation driving modes.

2.5.4 Casimir forces

A remarkable prediction of quantum electrodynamics made by Casimir in 1948 [154], is that a small force attractive force exists between two parallel, closely spaced conducting plates in vacuum. Practical measurement of Casimir forces have been demonstrated, [155], [156]. The Casimir force arises from electromagnetic fluctuations and can be described in terms of virtual photons. The energy density decreases as the plates are moved closer and the

Casimir force [155] in a vacuum is give by

$$F_c = \frac{\hbar A \pi^2}{240 L^4} \tag{2.5}$$

where $\hbar$ is Planck constant, c is velocity of light, A is surface area of plate and L is distance between two mirrors. The magnitude of Casimir force depends on the boundary of in face geometry.

The practical measurement of Casimir forces was carried out [156] and [40] in μm range (0.6 to 6μ and 0.1 to 0.9μm). The interesting diagram in , can exploit serval feature required for transfer artefact but could not interface to the system. The Casimir forces suffer the same drawbacks as Van der Waals interaction experiments [157] (see section 2.5.6). These experiments have several feathers similar to the required for a transfer artefacts, but they could not interfaced with a low-force balance or typical instruments.

The demonstration made in [158] for a silicon cantilever (Cr/Au coating) milled have better sensitivity for Casimir force detection. Future study could enable the minimum forces of the order of tens of attonewton for cantilevers with attached metal coated sphere required for measuring the sensitive Casimir forces. It may be that this type of cantilever could be used for transfer forces at very low end of range. The issue of roughness measurement, demonstrated in [159], [160] become insignificant to measurement of the Casimir forces.

A MEMS-Based Force Sensor was developed [161], which is capable of measuring forces as small as 10^{-15}N. A novel micromachined torsional oscillator with an interferometric position-sensing mechanism has been used in the force sensor. The sensitivity and unique features of micromachined torsional oscillators allow measurement that would be extremely complicated using any other technique, such as the observation of the Casimir effect and deviation of the Newtonian gravity at distances below 1μm. Experimental results with device and theoretical analysis led to new constraints on Yukawa modifications of Newtonian gravity at short distances. Measurements of the Casimir force between two metallic surfaces with a resolution two orders of magnitude better than previous experiments were

reported by the authors.

Another advancement is a force sensing micromechanical beam and an electrostatic actuator that was integrated on a single chip for demonstrating the Casimir effect between two silicon components (micromachined) on the same substrate. This new scheme has opened the possibility of exploiting the Casimir force using lithographically defined components of non-conventional shapes [162].

The possibilities of the Casimir expulsion effect was presented in[163], which can be the basis of quantum motors, which can be in the form of a special multilayer thin film with periodic and complex nanosized structures. These motors could be the base of transportation, energy and many other systems in the future [163].

Furthermore, KRISS has developed a facility [164] to generate forces in the piconewton range based on flux quantization in superconducting annulus and thence on a microcantilever. The forces generated by this methods are too small for current needs of a transfer artefact. However, the possibility exits to improve the design of flux quantization in the superconducting annulus for future force transfer artefacts operating extremely small forces.

2.5.5 Radiation pressure and momentum

The electromagnetic wave carries both energy and momentum. The expression between the energy $\triangle E$ and momentum $\triangle p$ when a plane electromagnetic wave is completely absorbed or reflected ($0 \leq R \leq 1$) is given as [165]

$$\triangle p = \frac{\triangle E}{c}(1+R) \tag{2.6}$$

For a perfect absorbing surface, R = 0 the equation (2.6) reduces to,

$$\triangle p_a = \left(\frac{\triangle E}{c}\right) \tag{2.7}$$

For perfect reflecting surface, R = 1 the equation (2.6) becomes,

$$\triangle p_r = 2\left(\frac{\triangle E}{c}\right) \tag{2.8}$$

The general expression of radiation pressure and force for reflectivity ($0 \leq R \leq 1$) is given by

$$P_{rad} = \left\{\frac{2I(1+R)}{c}\right\} \tag{2.9}$$

$$F_{rad} = \left\{\frac{2I(1+R)}{c}P_{rad}\right\} \tag{2.10}$$

For perfectly reflective surface $R = 1$, therefore, the expression for force from equation 2.9 is given as,

$$F_{rad} = 2\left(\frac{P_{rad}}{c}\right) \tag{2.11}$$

By way of illustration, a practical experiment using household bulb of $15W$ can generate a force of 10 nN. The model presented in equation 2.11 is considered to be the best option for generation of a nanoNewton force for a low force balance using a high reflectivity mirror and laser power in the milliwatt region.

The stability of optical levitation by radiation pressure was studied in 1974 [166]. The experimental evidence for passive (or intrinsic) optical cooling of a micromechanical resonator was reported in 2004 [167]. It used cavity-induced photothermal pressure to quench the brownian vibrational fluctuations of a gold-coated silicon microlever from room temperature down to an effective temperature of 18 K. Thus heating effects may be big for ultra-precision metrology applications.

The practical use of radiation pressure has been shown at PTB for their torsion pendulum facility that is capable of nanoforce generation [168].

2.5.6 Van der Waals forces

Van der Waals forces are weak electric forces that attract neutral molecules to one another in gases, liquids, and solids. An AFM was used study a wide variety of sample (plastics, gases, metals and biological samples such as walls of cells and bacteria) and exploit the Van der Waals forces between closely adjacent surfaces [169]. The mathematical mode predicted Van der Waals forces, F_{vdw} = 114mN & 139nN for silicone rubber (S_iO_2) and polyester (polydi-methylsiloxane, Dow-corning, HII) [169].

Hence these forces have useful magnitude only for very small separations so it is difficult task to use Van der Waals forces in a force transfer artefact. The first experimental evidence for dry adhesion of gecko setae being from Van der Waals forces was demonstrated by Autumn K. et al. . MEMS technology was used to fabricated a cantilever for adhesion measurement. The perpendicular forces were measured by using a probe with 1.75 Nm^{-1} and 390 nms^{-1} retraction speed. Moreover, traceability of Van der Waals interaction require the determination of the Hamaker constant in ultrahigh vacuum, which varies depending on the interacting surfaces and level of accuracy available.

The major problem for the AFM base method is determination of a force-distance relation for the AFM probes. Parametric tip models and force relation for Hamaker constant, a topic of great interest of AFM force measurement [170].

2.5.7 Step forces in protein unfolding

With the recent advancements in various innovative experimental techniques and equipment have been developed, which may be used to probe the physical properties of biostructures from the micro down to the pico-scale [21]. Some of experimental techniques are shown in figures 2.29 and used for conducting biomechanical tests in a single molecules and single cells. The available imaging techniques for such tests are shown in figure 2.30. The folding and unfolding of a single protein molecule appears to be a promising technique for generating low range forces. This topic has been extensively studied using AFMs [171], [22], [172]. Each unfolding event is characterised by a certain force but that force is not symmetric on refolding corresponding dispalcement for example one example is “by straching and relaxing

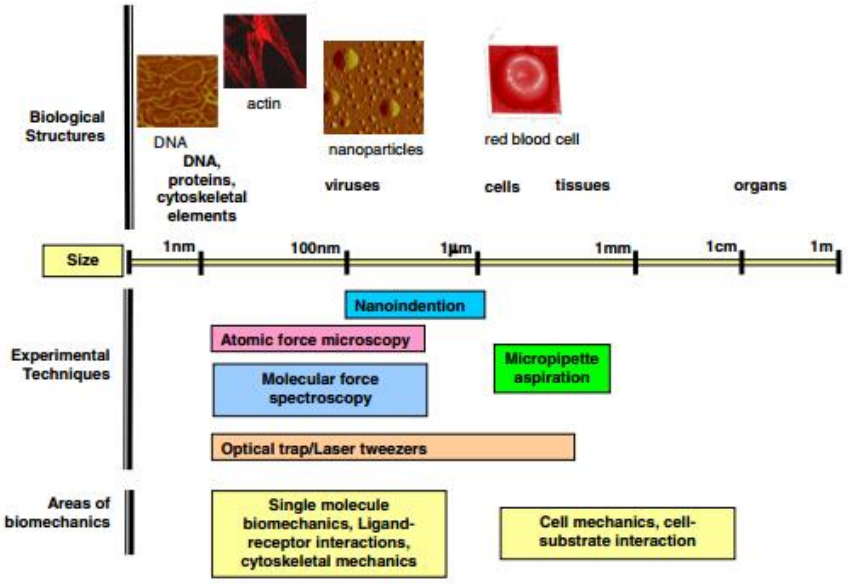

Figure 2.29: Imaging techniques that can be used to observe physical, biological and biochemical changes occurring in biological structures during biomechanical tests of cells and biomolecules (from [21]).

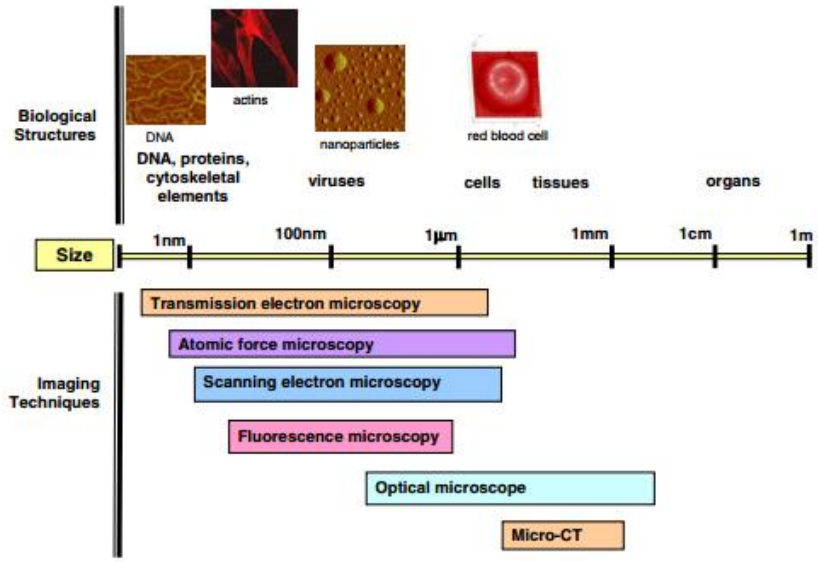

Figure 2.30: Experimental techniques for conducting mechanical tests in single cell and single molecule biomechanics (from [21]).

tenascin, a large hysteresis is seen i.e. the forward force has a sawtooth pattern, where as the relaxation trace is featureless (no force peaks). This is because the system is not at equilibrium during the time scale of the experiment (milliseconds) and refolding is very

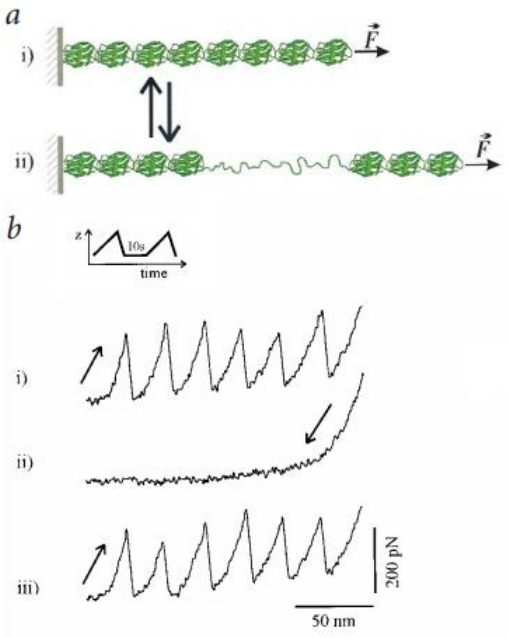

Figure 2.31: (a) The unfolding of protein domains by an external force, (b) The characteristic saw tooth pattern for extension (from [22]).

slow (seconds); in addition the refolding rate is very sensitive to the applied force" as shown in figure 2.31.

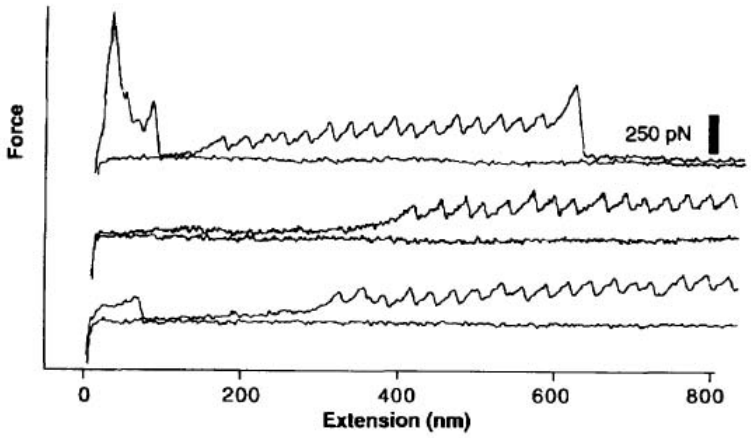

Figure 2.32: Force extension curves obtained by stretching titin proteins show periodic features that are consistent with their modular construction (from [23]). The ex1ension curve in the spacer region preceding the saw-tooth is not well defined and would likely hinder traceability.

An AFM tip was used to investigate the mechanical properties of titin. Individual titin molecules were repeatedly stretched, and the applied force was recorded as a function of the elongation. The forces required to unfold individual domains from 150 to 300 piconewtons

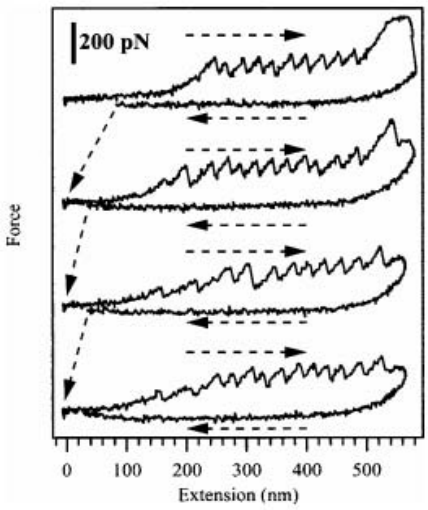

Figure 2.33: Four consecutive force spectra on a single molecule of the protein titin using a small cantilever. All force spectra were acquired at a pulling rate of 3039 mm/s, which is an order of magnitude faster than previously performed with conventional cantilevers (from [24]).

range depended on the pulling speed shown in figure 2.32 [23]. A small cantilever (10μm long and with spring constant 23 Nm^{-1} was also used at resonant frequency of 23 kHz. The force versus extension curves for four consecutive "pulls" of a single molecule of titin showed a consistent force at each cycle that is shown in figure 2.33 [24].

The folding and unfolding technique has been extensively studied, which reveals significant problems, such as hysteresis, repeatability, and speed rate effects during folding and unfolding; the process is not uniform [173], [174], [175], [176]. Currently these issues do not provide much promise for using unfolding and folding technique for low force calibration.

2.5.8 Elastic element methods

The most commonly used method for force generation is by using an elastic element method with know spring constant. For a very small forces this often draws on the concept of the AFM, and is based on the elastic deflection of a micro-cantilever. Many modern commercial AFM offer some (non-traceable) force metrology in terms of nano-indentation and pull-off force capabilities based on their standard cantilevers.

The elastic element, such as cantilever, is deflected by a test force. This deflection is measured by a traceable sensor such as an external interferometer. The spring constant can be determined by using a traceable force such as from an electrostatic balance. The magnitude of other forces can then be determined. AFM cantilevers of appropriate specification for this purpose can be modelled and designed. Small, very thin ones with low values of spring constant are manufactured for measurement of forces down to nano or even piconewton levels. The second stage of operation relies on the internal spring constant when applied to the target instrument. The cantilever's spring constant is highly dependent upon its composition [45].

Given the difficulties of calibration at a very small scale, in most reported work the spring constants of AFM cantilevers are determined indirectly from geometric properties length, width, and thickness) and Young's modulus of the cantilever material. To determine the spring constant of a cantilever directly, a well known force is required at a known position along the cantilever and the resultant displacement is measured. The spring constant of a cantilever depends on the beam theory parameters (length l, width w, and thickness t). The spring constant of a uniform rectangular beams is relatively easy to model by linear theory [177]. On imposing a force F_e at its end, the small vertical defection, z, at the end of cantilever will be,

$$z = \left(\frac{L^3 F_e}{3EI}\right) \tag{2.12}$$

where E is Young's modulus, $L, w, \& t$ are length, width and thickness of the cantilever and I is the second moment of area is given by

$$I = \left(\frac{wt^3}{12}\right) \tag{2.13}$$

Thus, the spring constant at the end of rectangular beam is

$$\begin{aligned} k_e &= \left(\frac{F_e}{z}\right) \\ &= \left(\frac{Ewt^3}{4L^3}\right) \end{aligned} \tag{2.14}$$

The spring constant determined by its geometry parameters is potentially inaccurate due to a combination of uncertainties. Numerous methods are described in [178], [179]. for calculating the spring constant but uncertainties in (especially) thickness and Young's modulus can cause great uncertainty in k_e, often to 10% or (perhaps more under potential nano force conditions).

Thermal methods for determining the spring constant have been proposed in [180], [92]. They are based on standard physics but are independent of both the shape and the constituent material of the cantilever. However, the accuracy of the thermal method was reported as 5% and 5-10% respectively [180], [92]. The three other problems pointed out in [45] for thermal methods are:

1. The higher vibration modes cannot be neglected.
2. The modes are accessible only within bandwidth limitations of experiments.
3. The method to measure the deflection always involves inclination rather than pure displacement.

Temperature dependence of factors such as the Johnson noises limit and Young's modulus cannot be neglected. The other factor, $\frac{1}{f}$ noise, becomes dominant in the piezoresistive cantilevers when applied voltage increases to the bridge. A cause of noise is due to many sources, such as from contacts or carrier trapping at the surfact defects. When voltage is applied to the bridge, the out put signal increases and it may be seem to operate with a voltage as high as possible for better results. However, for given $\frac{1}{f}$ noise, the signal to noise relation flattens out after certain voltage. The minimum deflection were seen 10Hz to 1kHz is lower because the output of the detector increases linearly with bridge supply voltage [181].

The resonance frequency of the first eigenmode of the microfabricated silicon cantilever is dependent on the Young's modulus, spring constant, and temperature dependance of the geometric dimensions, which is weak and can be ignored in comparison to the temperature dependance of the Young's modulus. The temperature dependence of Young's modulus is due to the anharmonic effects of the lattice vibrations [177].

2.5.9 Passive type array of cantilevers

It has been proven possible to calibrate AFMs by the use of reference cantilevers. Prototype cantilevers array were designed and developed at NIST [25]. Their design consists of seven rectangular cantilevers of varying length (figure 2.34), microfabricated from single silicon crystal(1 0 0), covering nominal estimated spring constants in the range 0.2 to 0.2 Nm^{-1}. Variations in resonance frequency of less than 1% were reported, which indicates an improvement over available reference cantilevers in the commercial market. The spring constants were verified on the NIST electrostatic balance, which has been found suitable for calibrating such cantilevers in an SI traceable way. The devices are passive and their uncertainty is higher than active type cantilevers. Such passive devices are not useful for primary transfer artefacts, but may well have a role lower down the traceability chain.

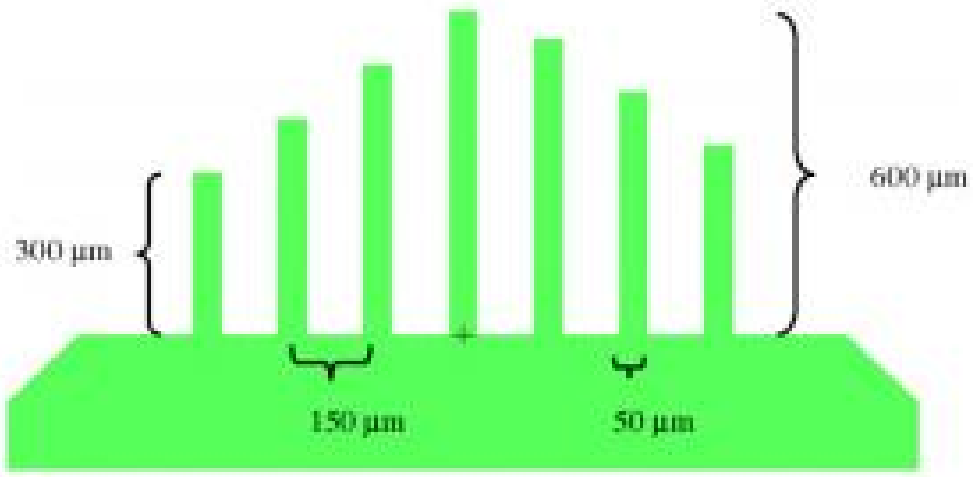

Figure 2.34: Experimental prototype reference cantilever array plan view (SOI device level) (from [25]).

2.5.10 Active type single cantilever

An active cantilever approach was reported in [181], fabricated using standard micromaching techniques. This device was manufactured on a single piezoresistive strain element with an on-board simple detection scheme and can be used to calibrate the target instruments. Vertical resolution of 0.1 $\AA$ (rms)in a range 10 Hz to 1 kHz bandwidth was claimed by the author. A research team at PTB created piezoresistive cantilevers of two types, type

A (length, 13 mm and width, 1 mm) and type B (length, 5 mm and width, 0.2 mm). The cantilever carries of a probe tip at its free end. A applied force is measured using a piezoresistive strain gauge at the cantilever suspension. Two-leg and single-leg probes have been produced. These prototypes were fabricated by using silicon bulk micromachining technology and their stiffnesses were found in a range of 0.66 Nm^{-1} and 7.7 Nm^{-1}. The authors claimed a highly linear relationship between gauge output voltage and the probing force in the μ N range. These devices were said to be good for calibration use in nanoindentation and surface texture work.

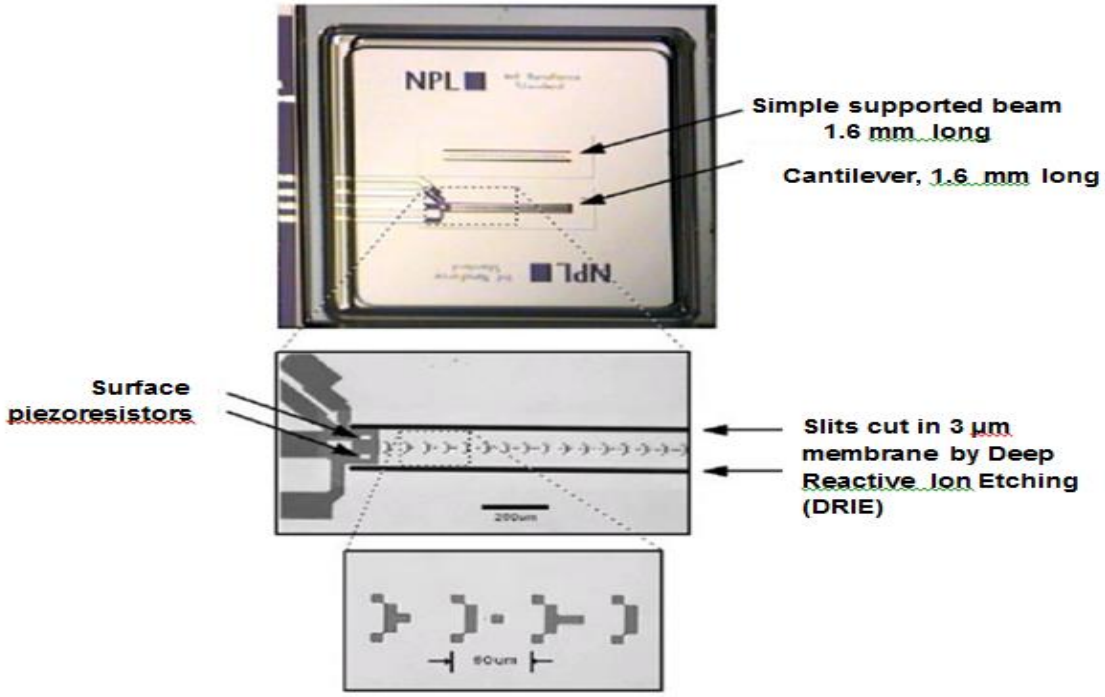

Figure 2.35: Optical micrographs of the cantilever microfabricated array of reference springs (C-MARS). Note the binary length scale formed from 10 μm surface oxide squares (from [26]).

NPL has also developed artefacts that could be used as reference artefacts for traceable AFM calibration with a microfabricated array of reference springs (C-MAR) [26]. The larger cantilevers are marked with fiducial points on a scale that consists of arrows made of squares $10 \times 10\mu$m and separated by 60μm from the next arrow. The device is shown in figure 2.35.

C-MAR devices could be used for calibration of AFM cantilevers to measure nano and picoNewton forces. The spring constants for C-MARS devices are found in a range 25Nm^{-1} to 0.03Nm^{-1}. The spring constants at the end of cantilevers were determined by several approaches: Sader's method ($k_e = 4\pi\kappa_{sader}\, mf^2$, $\kappa_{sader} = 0.2427$, m, mass of the cantilever and f, fundamental frequency); Euler-Beroull theory ($k_e = \frac{Ebt^2}{4L^3}$, where L, b, t are length, width and thickness of the cantilever) and Finite element analysis.

2.5.11 Fluid flow, surface tension and capillary forces

The fluid flow may be considered for generating of small forces. Deflection of fluid stream by a target requires a change in the fluid momentum and so on generate a force on that target. This would be possible for low force metrology only if liquid has a low density and flow rate.

A method of actuation for AFM cantilevers in fluids by using acoustic transducer at radio frequency 100-300MHz has been demonstrated [182]. The dynamic method used for actuation of the atomic force microscope cantilever in a fluid is not suitable to use in low force facility.

Elsewhere, a model system was developed, consisting of two thin glass cylinders of radii 50μmm immersed vertically in a liquid and at a liquid/air interface. The magnitude of the weak capillary forces experimentally measured by means of a torsion microbalance were reported in the ranges 4×10^{-7} to10^{-9}N. However, there are some factors that may be seen in this model system such as, surface geometry, surface chemistry, and humidity, which could not easily be controlled for use in a force transfer artefact [183].

2.6 Conclusion

This chapter has established the context for the development of small force standards and facilities at various NMIs. The extensive study of various methods, approaches, and designs have highlighted that Pril's design of micro-probe suspension would be considered a good starting point for the development of novel linear elastic triskelion force artefacts. Pril published design is limited, with 60 degree elbow angle, and little information about this design has been published. A serious question arises of why all subsequent published and

commercial designs for triskelion style micro-probe suspensions have focused only a Pril's 60 degree elbow angle configuration? More recently Jones also adopted the Pril's design for force artefacts without indicating that triskelion designs were considered.

Therefore, the next chapter will highlight the novel development of an enhanced linear elastic model for triskelion force artefacts that fully parameterised and can investigate the variant designs for triskelion force artefacts and for triskelion micro probe suspensions. It will be used to explore the best designs for triskelion force artefacts and triskelion micro-probe suspension. No such such analysis has previously been seen in published journals or in the public domain.

A general survey of physical principles capable of generating or measuring small forces reveals several that long-term potential for various ranges of force artefact. However, all require major technical challenges to overcome before they might be considered for practical for commercial applications. It seems inevitable that more immediate metrological needs will depend on using variants of springs as force transfer artefacts. The rest of this thesis therefore concentrates only on this approach.

Chapter 3

Linear elastic modelling for triskelion force artefacts

3.1 Introduction

Elastic defections have been applied in fine instrument mechanisms and precise mechanics for more than three hundred years. Robert Hooke and Edme Marriott were the first to recognise the basis of linear elasticity [184] [185]. Flexure mechanisms are produced through successive connections of rigid bodies and flexure elements operating in the linear elastic ranges. Flexures produce predictable, repeatable motion and provide precise displacement upon application of an applied force. Today's flexure mechanisms in various forms are used at the limit of precision in, for example, devices such as balances, probe microscopes, coordinate measuring machines, x-ray equipment, optical scanners, optical interferometers and many types of mechanical measuring instruments.

This chapter consists of three parts. First it covers some basics of beam theory, its implications for ligament design and pseudo-kinematic analysis of triskelion force artefacts. The second part describes development of an enhanced linear elastic model for triskelion force artefacts, which extends previous work by the capability of varying the elbow angles and following any number $n = 3, 4, 5...$ of suspension beams around the central platform (hub). This form, relating to published design, discussed in chapter 2, will here be called the classical suspension beam model. The third part discusses an analytical triskelion

angle-beam suspension model that is an alternative approach to the linear elastic model for triskelion force artefacts. Implications, limitations of linear elastic model, specifics requirements of triskelion force artefacts and their non-linearity are also included in the third part of the chapter.

3.2 Basic elasticity and simple beam theory

Micro and nano-force triskelion artefacts need to be designed to be suitable for micro-fabrication. This implies a planar structure involving elements of relatively simple geometric forms. The ligaments that act as the flexing elements between a static base and a moving measuring platform will be thin structures with locally rectangular cross-sections. In fact, all designs considered here will have flexures that are simple rectangular prisms. They can therefore can be modelled reasonably well as uniform rectangular beams. Subject to its usual restrictions underpinning the theory (small deflections and negligible shear), a simple elastic beam theory provides a good prediction for deflection (e.g. [184], [186]) and will be used as the basis for all the models used in this chapter.

The fundamental model element used is a uniform cantilever beam of uniform rectangular section with dimensions ℓ, w, and t, as shown in figure 3.1. The clamped end is fixed at the origin of a co-ordinate frame with its x-axis along the beam length and its z-axis being out of the plane of the beam. The 'free' end is subject to three orthogonal forces and three moments corresponding to the six possible independent displacements, rotations and end-slopes (tilts or twists) of the end. They will model its connection to the other components when combined with Newton's third law of motion. Simple beam theory supplies the small-amplitude out of plane deflection and slope (i.e.δ_z and θ_y). For example, end deflection due to an applied moment is

$$\delta_M = \left(\frac{\ell}{2EI_y}\right) M_y \tag{3.1}$$

where parameters ℓ, E, $I_y = wt^3/12$, and M_y are the length of the beam, Young's Modulus, second moment of area of the beam cross-section, moment generated along y-axis of beam. There are four possible actions associated with a force F_z or moment M_y.

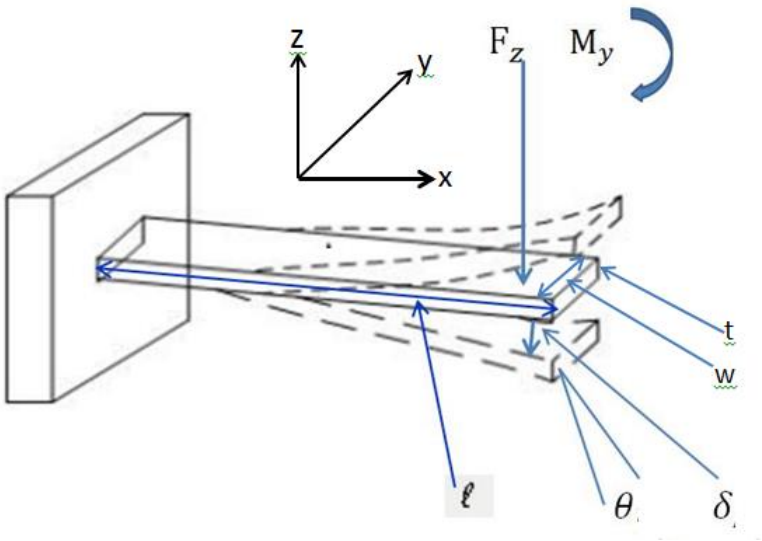

Figure 3.1: A generic end-loaded cantilever.

$$\delta_{M_y} = \left(\frac{\ell^2}{2EI_y}\right) M_y \tag{3.2}$$

$$\theta_{M_y} = \left(\frac{\ell}{EI_y}\right) M_y \tag{3.3}$$

$$\delta_{F_z} = \left(\frac{\ell^3}{3EI_y}\right) F_z \tag{3.4}$$

$$\theta_{F_z} = \left(\frac{\ell^2}{2EI_y}\right) F_z \tag{3.5}$$

The in plane behaviour with δ_y and θ_z is similar to the equations (3.1) to (3.4), except the roles of breadth and depth are transposed, $I_z = \frac{w^3 t}{12}$. These equations are not, therefore, given here in detail.

Behaviour in the x-axis derives from the tension and torsion rather than the bending. Along the beam

$$\delta_z = \left(\frac{\ell}{AE}\right) F_x \tag{3.6}$$

where $A = wt$ is the cross-section area of the beam. Torsion of a rectangular beam is given by the well-known approximation

$$M_x \simeq \left(\frac{\theta_x G w t^3}{3\ell}\right)\left[1 - \left(0.63\frac{t}{w}\right)\left(1 - \frac{t^4}{12w^4}\right)\right] \tag{3.7}$$

where G is shear modulus.

For small amplitudes, all elementary effects may be combined by linear superpositions. The x-axis terms remain effectively independent. However equation (3.1) and (3.3) may be added to give the full out of plane displacement δ_z and equation (3.2) and (3.4) must be used to give θ_y. The same procedure is needed to reveal δ_y and θ_z.

Each of these equations define an elemental stiffness; either linear F/δ, rotational (torsional) stiffness M/θ, or a cross-stiffness (either M/θ or F/θ) or the equivalent compliance as constant of proportionality. These are directly exploited in the matrix formation of device models. Note that, as done here most texts tend to present the equations in compliance form (i.e. assuming force is casual) except for beam torsion. Although most designers would tend to think more intuitively in stiffness terms for a force transfer artefact, the internal logic of the model equations can be shown more simply in the compliance form.

3.3 Implications for ligament design

We want a flexure mechanism to show a strong perpendicular motion in one axis (or possibly in a few axes), the intended or design direction. It is commonly desirable to have quite low stiffness in this axis. In all other axes, unintended parasitic motions arising from the imperfect geometry, stray forces, etc must be small or (preferably) negligible. Clearly, sensitivity to parasitic forces and moments is reduced by high stiffness in the corresponding axis. Hence, relative stiffness can be a useful guide in design. Unfortunately, there are very many combinations that might occur, so discussion and any consequent design insights for ligaments commonly focus on two cases.

A bending ligament in a flexure mechanism can be visulised by the kinematic equivalent shown in figure 3.1 a pinjointed rod with added return springs. One basic case treat J_1 as

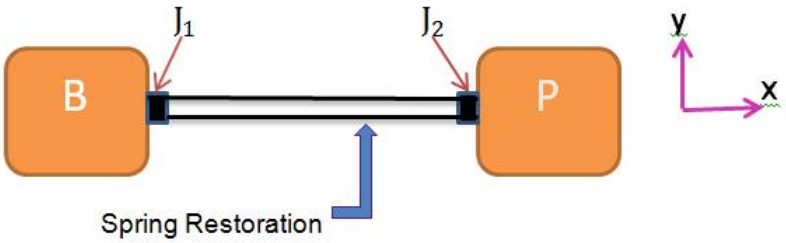

Figure 3.2: A rod attached to rigid support (base and platform).

pin J_2 rigid, so that P both translates and rotates.

One case is cantilever shown figure 3.1 in which are subject to end force, as describe by equation (3.4). The end slope is fixed with respect to the deflection and, in this sense, its motion approximates to that of a rod pinned at one end. For example, equation(3.4) and (3.5) show that $\delta_F = (2\ell/3)\theta_F$, which is similar but slightly different to the small angle motion of the rod, where $\delta_R = \ell\theta_R$.

The second case is one that occur very regularly in flexure mechanisms [184], [186] when the beam ends remain parallel under out of plane deflection. This corresponds to J_2 in figure 3.1 being a pin-joint, with P also constrained by a prismatic (sliding) joint. Setting $\theta_y = 0$ and solving equation (3.1) to (3.4) shows that the moment must be applied is defined by deriving force with

$$M_y = \left(\frac{\ell}{z}\right) F_z \tag{3.8}$$

and then

$$\begin{aligned} \delta_{zp} &= \left(\frac{\ell^3}{12EI_z}\right) F_z \\ &= \left(\frac{\ell^3}{Ewt^3}\right) F_z \end{aligned} \tag{3.9}$$

The primary design motion of a ligament is its out of plane deflection and in plane deflections should be suppressed. The relationship between I_z and I_y with in equations (3.8) and (3.9) or equation (3.4) show that the relative stiffness of these axes is

$$\begin{aligned} \frac{k_z}{k_y} &= \left(\frac{\frac{Ewt^3}{\ell^3}}{\frac{Ew^3t}{\ell^3}}\right) \\ &= \left(\frac{t}{w}\right)^2 \end{aligned} \tag{3.10}$$

For a desired z-motion device, we might take a criterion such as that cross-deflection is $< 1\%$ of the demand deflection under the influence of similar force magnitudes. Even this fairly severe condition only needs $w > 10t$. Most real parasitically coupled forces (e.g. from a misaligned drive) might only be a fraction of the drive force and smaller ratio could suffice. Even with apparently small cross-sections, axial displacement behavior is rarely an important consideration. From equation (3.6), (3.8), and (3.9) for more severe case of a parallel motion ligament,

$$\frac{k_x}{k_z} = \left(\frac{\ell}{t}\right)^2 \tag{3.11}$$

Torsion about the x-axis is more difficult to relate, say to a design deflection because it is a sheer effect and closed form equations only approximate for a thin rectangular section. A few fairly crude approximations nevertheless provide some guidance. For many common materials Poisson's ratio is about 1/3 and so analytically we have $G = E/2(1+\nu) \sim 3E/8$. Provided $w > t$ by a factor of at least a few, the shape correction term in equation (3.8)will not below unity. We might then consider

$$\lambda_x \simeq \left(\frac{3E}{8\ell}\right)\left(\frac{wt^3}{3}\right) \simeq \left(\frac{Ewt^3}{8\ell}\right) \tag{3.12}$$

Thus, comparing with parallel motion case of equation (3.8)

$$\frac{\lambda_x}{k_z} \simeq \left(\frac{Ewt^3}{8\ell}\right)\left(\frac{\ell^3}{Ewt^3}\right) \simeq \left(\frac{\ell^2}{8}\right) \tag{3.13}$$

This ratio is not dimensionless and so, while indicating a variable for tuning purposes, it is not easy to use intuitively for real design. It broadly suggests that any concerns about θ_x parasitics are best met by using a longer ligament with a robust cross-section.

One possible for this parasitic would be to consider a force driven system in which the line of application is offset by ℓ_a from the ligament axis in the y-direction, i.e. an Abbe offset. This causes an x-axis torque $T_a = F\ell_a$ and parasitic z-deflection in the line of the force of $\delta_a = \theta_x \ell_a$, then using equation (3.18)

$$\frac{\delta_a}{\delta_z} = \left(\frac{T_a \ell_a}{\lambda_x}\right)\frac{k_z}{F} \sim \left(\frac{8{\ell_a}^2}{\ell^2}\right) \tag{3.14}$$

Interestingly, this is independent of material and cross-section, except to the extent that they were implicit in the approximations. To keep the excess deflection of this parasitic for single ligament below 1%, an Abbe offset ℓ_a must be restricted to around $\ell/30$.

Complete flexure mechanisms use several ligaments in order to control constrained motion and this tends to reduce sensitivity to parasitics. Nevertheless, there is some desire, within the limits imposed by specific design constraints to choose larger values for ℓ and w/t. There is considerable scope for tuning design stiffness because different geometric parameters appear with different power laws. Note, for example, that stress, strain and maximum elastic deflection are independent of w, but the stiffnesses are not.

3.4 Pseudo-kinematic analysis of triskelion flexure

Although there may not always be a simple, or unique, one-to-one correspondence it is often helpful to consider how the operation of flexure mechanism might be represented by a kinematic mechanism (corresponding to a set of rigid bodies coupled by ideal frictionless joints) to which springs have been attached [184], [186]. In particular, such a pseudo-kinematic model allows the idea of kinematic mobility to be used to examine whether a design is likely to be effective in delivering the design-intended degree of freedom.

The degree of freedom (DoF) of a mechanism indicates how many translations and rotations of the platform of a mechanism relative to its base can be independently manipulated. It corresponds to the number of simple actuators required to fully assert the position and orientation of the platform within its workspace. DOF is also the minimum number of displacement sensors needed fully to describe a spring-loaded mechanism used

as part of a sensing system. Generally DoF is a design specification, as are the particular axes about which those freedoms act. Clearly, $0 \leq \text{DoF} \leq 6$.

The kinematic mobility (M) of a mechanism is simply the net count of the number of freedoms contributed by all the rigid no of constraints contributed by all the joints connecting these members. The mechanism base is assumed fixed, contributing no freedoms. Mobility is a highly useful parameter for checking design consistency, but it has no power to prove a design correct. Clearly if M exceeds the intended DOF, there is a problem because of uncontrolled freedoms (under constraint). If $M \leq$ DOF (over constraint) the mechanism may not assemble properly and may tend to seize at certain points in the workspace. However, over constraint is sometimes used deliberately. Thus, $M =$ DoF implies a structure but does not guarantee it because there could be a combination of over and under constrained subsystems. There are many variant ways of computing mobility.

Parallel kinematic mechanisms, which are closed loop systems in which several subsystems or "legs" contribute to the motion of a single platform by direct connection between it and the base. First consider the i^{th} leg separately as an open mechanism, which includes the platform, with N_i links and J_i joints that individually contributes C_{ij} constraints: Then this system has mobility

$$M_i = 6N_i - \sum_{i=1}^{J_i} C_{ij} \tag{3.15}$$

Now consider all the legs together. For the whole mechanism, the M_i are summed for the N_i legs except that platform becomes a single rigid link, so we must remove its six freedoms for each leg, and then give back six freedoms for the platform itself. Hence

$$M = \sum_{i=1}^{N_i} M_i - 6(N_i - 1) \tag{3.16}$$

An appropriate kinematic equivalent of a ligament based flexure mechanism can be explored by considering the likely relative stiffness in different freedoms when a cantilever is used to connect a platform to a rigid base. The first two columns of table (3.1) summarize this

Table 3.1: Equivalent for model in figure 3.2

Motion at P	Nature + Source	Model as figure 3.2
δ_z	Easy, bending	J_1 revolute along y-axis, J_2 rigid
δ_y	Stiff, bending	J_1 revolute along z-axis, J_2 rigid (+ stiff spring)
δ_x	Very stiff, axial	$J_1, (J_2)$ rigid (in x-axis)
θ_x	Fairly easy, torsion	$J_2(J_1)$ revolute along x-axis, $J_1(J_2)$ rigid
θ_y	Easy coupled to δ_z	$J_1(J_2)$ revolute along y-axis, $J_2(J_1)$ rigid
θ_z	Stiff, coupled to δ_y	$J_1(J_2)$ revolute along z-axis, $J_2(J_1)$ (+ stiff spring)

information for six independent motions of a typical ligament design.

A kinematic equivalent of ligament flexure element can be established by considering a rigid rod with spring-loaded idealized joints to the base and platform (figure 3.2). This type of joint will depend on the boundary conditions and the intended function. The spring systems are not important to the present discussion. They can be thought of as within joints (e.g. a torsion-spring on a revolute axis) or as applied at other points on the rigid rods. The only requirement is that they hold the design position of the unloaded ligament (linear characteristics are assumed).

From the relative stiffness in different motion axes, we can summarize the reasoning for various models of J_1 and J_2. Note here that in combination the condition on δ_x, δ_y, and δ_z mean that the lengths are fixed there are no prismatic (sliding) joints in the modelling. They δ_x rotation of P is kinematically the same whether J_1 or J_2 is chosen (but not with both, when free axial rotation of the rod could occur). In physically terms, it feels slightly preferable to place is at J_2, the active end of the link.

Table (3.1) takes the platform position and orientation as that of cantilever end. It also considers displacement as primary with slopes as coupled effects, but it is equally valid to reverse this relationship. The third column identifies a kinematic joint J_1, that could be placed between the base and a rigid rod to generate similar behavior. For some rotational motions it might be equally logical to move the joint to the junction between rod and platform, identified by J_2.

In most cases, δ_z is likely to be desired design freedom. The basic kinematic equivalent is then simply a rod connected to base by a revolute R joint with its axis aligned along the y-direction. Noting the relative low stiffness in torsion, it will sometimes be more sensible to model the ligament with an additional revolute along the x-axis, either combining the two into a universal U joint at the base or placing one at each end (an RR configuration). When ligaments are built in to a complete close-loop mechanism, there must be joint freedoms between it and the platform. Again considering the relative stiffness in table (3.1), it is most likely that an RR system both parallel to the y-axis or an RU (equivalently UR) system would be most representative of the conditions.

The use explicit of this technique is deferred until specific devices are being discussed. However, note here that a triskelion micro-probe is by definition intended as a 3 DoF (x, y, z) system at the probe tip. With a rigid probe arm this becomes a $(z,\ \theta_x,\ \theta_y)$ system at the triskelion hub (platform). Using this pseudo-kinematic model the triskelion itself has four active bodies, the platform and three ligaments treated as UR legs, giving an overall mobility of -3 (six-over-constraints). Nevertheless it works well over very small displacements (evidence here).

3.5 Linear elastic model for triskelion force artefacts

Previously, published all research papers are focussed on Pril's design [14] that is limited to the fixed geometry with elbow angle $60\,^\circ$. Implications of Pril's design were not published.

3.5.1 Motivation: The need for new models

The literature survey in the chapter 2 has revealed that triskelion probe suspensions of Pril design [14] could be used for the development of linear elastic model for force artefacts. Indeed, exactly this approach was followed by Jones [148]. The force transfer artefacts would for the near future rely on elastic systems based on a conventional planar triskelion flexures. These were first time used by [148] for nano-force transfer artefacts. All published analysis of triskelion suspensions has been based on system for co-ordinate measuring micro probe that employ micro-fabrication for triskelion springs. It is based on simple linear elastic analytical model for triskelion micro probe [14]. The basic kine-

matic model is shown in figures 1.1 2.20 and 2.21 is limited by considering a mostly fix geometry (with only a few actively variable design parameters). It has later been used in [120], [118], [123], [122], [187], [121] although changes of notation have confused rather than clarified its proper use.

The basic triskelion suspension figures 2.20 and 2.21 study by Pril consists of a hub with rigid three arms that are joined by thin beams (leaf springs) to an outer fixed frame. Both arms and beams have uniform rectangular section. When the displacement is imposed on the hub of the micro-probe, it results in deformations in the outer beams. To maintain static equilibrium, the sum of forces and sum of moments required the beams must balance those applied extremely at the hub. Pril's analytical model was based on beam theory and also provides a means to estimate the spring constant of the force artefact for design purposes.

Previous models have encompassed only a single compact maximally symmetric configuration with three identical legs and an internal elbow angle between the arm and the beams of 60 °. Such features are directly encoded within the published models.

We are interested here in the potential use of triskelion-like flexures as reference springs, which differ from micro-probe by not including a ball tip stylus and having a different ideal degree of freedom. The redesigned triskelion-like flexure is not limited to elbow angle 60 °, such as shown in figures 3.3 and 3.4.

3.5.2 Critique for triskelion suspensions

The critique has identified the following concerns:

1. All published research work seems to addresses only the specific geometric configuration limited to 60 ° [118], [188], [189], [121], [57], [187] and has been based on co-ordinate measuring micro-probe. It is all been derived from a simple linear elastic analytical model of the triskelion micro-probe suspension design [14].

2. The triskelion suspensions for micro probes are generally treated as approximating 3-DoF mechanisms but applications such as reference springs would prefer 1-DoF

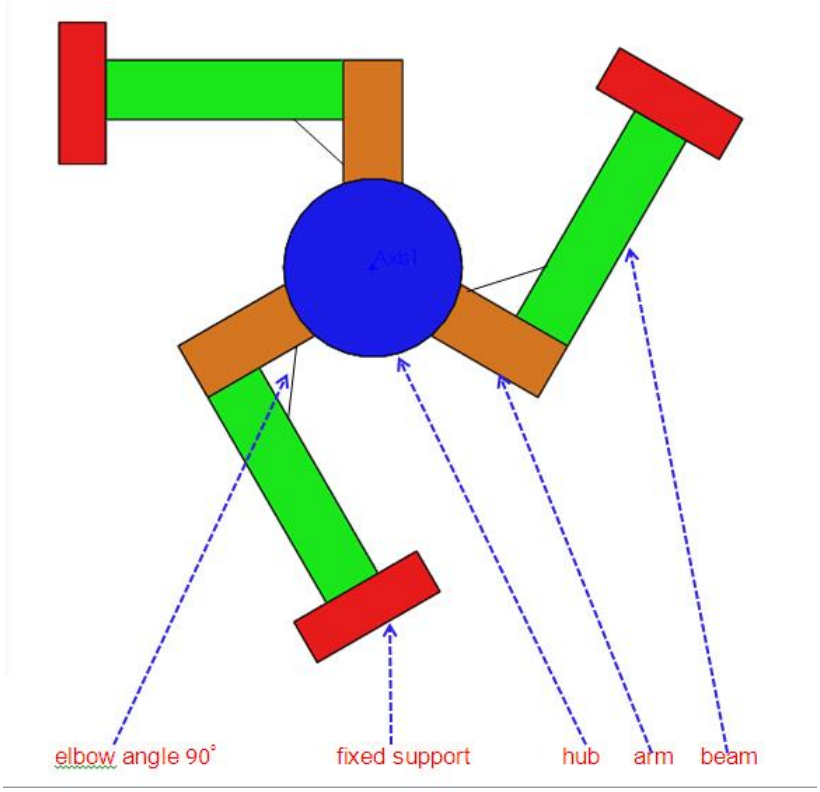

Figure 3.3: The classic triskelion suspension: (a) layout of 90 ° elbow angle.

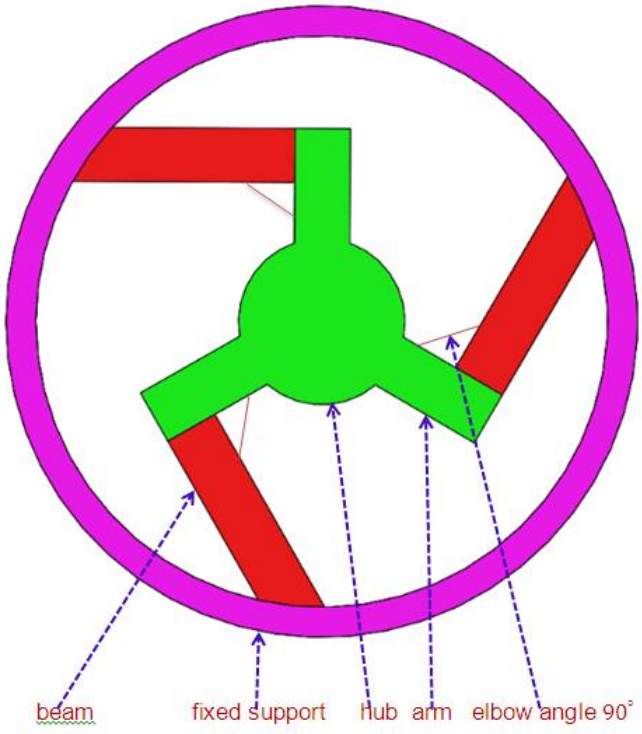

Figure 3.4: The classic triskelion suspension: (b) further model simplification.

operation (although these are the theoretical reasons for not closely achieving 1-DoF in a triskelion suspension).

3. The standard 60° elbow angle triskelion suspension is clearly practically useful for the design of triskelion force artefacts .

4. Hence, investigation is required to explore a range of variant conditions to establish applicability of currently used design values and seek potential superior geometries to enhance modelling for the design in optimization in industrial applications of triskelion and similar flexure systems. A new more general model based is therefore needed.

5. The approach adopted here preserves most of the ideas introduced by Pril [14], significantly enhancing the model to encompass all potential design parameters explicitly, especially allowing different elbow angles and non symmetrical leg distribution for wider investigation of artefact designs. It is set up to be immediately applicable for versions od suspension with more than three legs. It therefore directly uses transformation matrices to build the system from vector descriptions designed in convenient local co-ordinates frames.

6. The research work presented in this thesis pay considerable attention to redesigns at other than 60° elbow angles for triskelion force artefacts. However, the implementation of enhanced linear elastic model for variant designs triskelion suspensions has been carried out in chapter 4 by developing triskelion and tetraskelion software programs. Hence the secret of elbow angle was disclosed for the first time by performing numerical experiments that are also discussed in chapter 4, 8 and 9 in this thesis.

3.6 Enhanced Linear elastic model for variant triskelion suspensions designs

The development of enhanced linear elastic model for the variant designs of triskelion suspensions is presented in this section.

3.6.1 Hub motion and displacement at the arm

The approach for the enhanced linear elastic model for variant designs of triskelion suspension has drawn upon Pril's design for probe suspension [14]. Considering first the basic geometrical layout, and referring figure 3.5, we initially take an arm of the length a projecting from the hub centre to be aligned to the $x-$axis of the reference frame; i.e. its tip is at $\mathbf{a} = (a \quad 0 \quad 0)^T$. A fully formal, and so adaptable, method for locating the position where suspension beam meets any general platform arm is to use matrix transformation. The real device has three arms disposed around the platform at angles α_i to a reference direction. The arms remain in the plane of the device, so a simple rotation matrix transformation expresses the position vector for the tip of any arm relative to original x-axis as

$$\boldsymbol{a_i} = \begin{pmatrix} \cos(\alpha_i) & -\sin(\alpha_i) & 0 \\ \sin(\alpha_i) & \cos(\alpha_i) & 0 \\ 0 & 0 & 1 \end{pmatrix} \boldsymbol{a} \tag{3.17}$$

Assuming all arms are of equal length,

$$\boldsymbol{a_i} = \begin{pmatrix} a\cos(\alpha_i) & a\sin(\alpha_i) & 0 \end{pmatrix} \tag{3.18}$$

Here all arms are assumed to be in the xy-plane of the platform, but this approach allows extension into z-axis. This approach might be thought overly complicated and distracting for some present applications. Hence Pril's original model built in all such geometry implicitly, causing potential confusion by over-simplicity. It dealt only with the symmetrical case where $\alpha_i = -\pi/6, -5\pi/6$ and $\pi/2$. The present formulation allows to be added by specifying additional α_i for use in the rotation matrix at equation 3.17. To provide a working platform (or target area) and to allow mechanical clearance, real devices will have a hub region (usually circular) from which the arms project before meeting the beam elements of the main flexure, figure 3.5.

For computational convenience, the model is constructed such that a specified rigid-body motion is applied to the hub with force and moment vectors required to cause it then being reported. A global reference frame is established at the centre of the un-deflected

hub, with its z-axis normal to the plane of the hub representing the expected direction for action as force transfer artefact. The radius of the hub is h_r and the rigid arm projected by a_ℓ, giving an effective rigid lever of length $a = (r_h + a_\ell)$ from the centre. The beam has length ℓ, width w and thickness & t that is jointed with arm. Young's modulus, E,and modulus of direct shear, G are required parameters assumed constant to compute spring constant

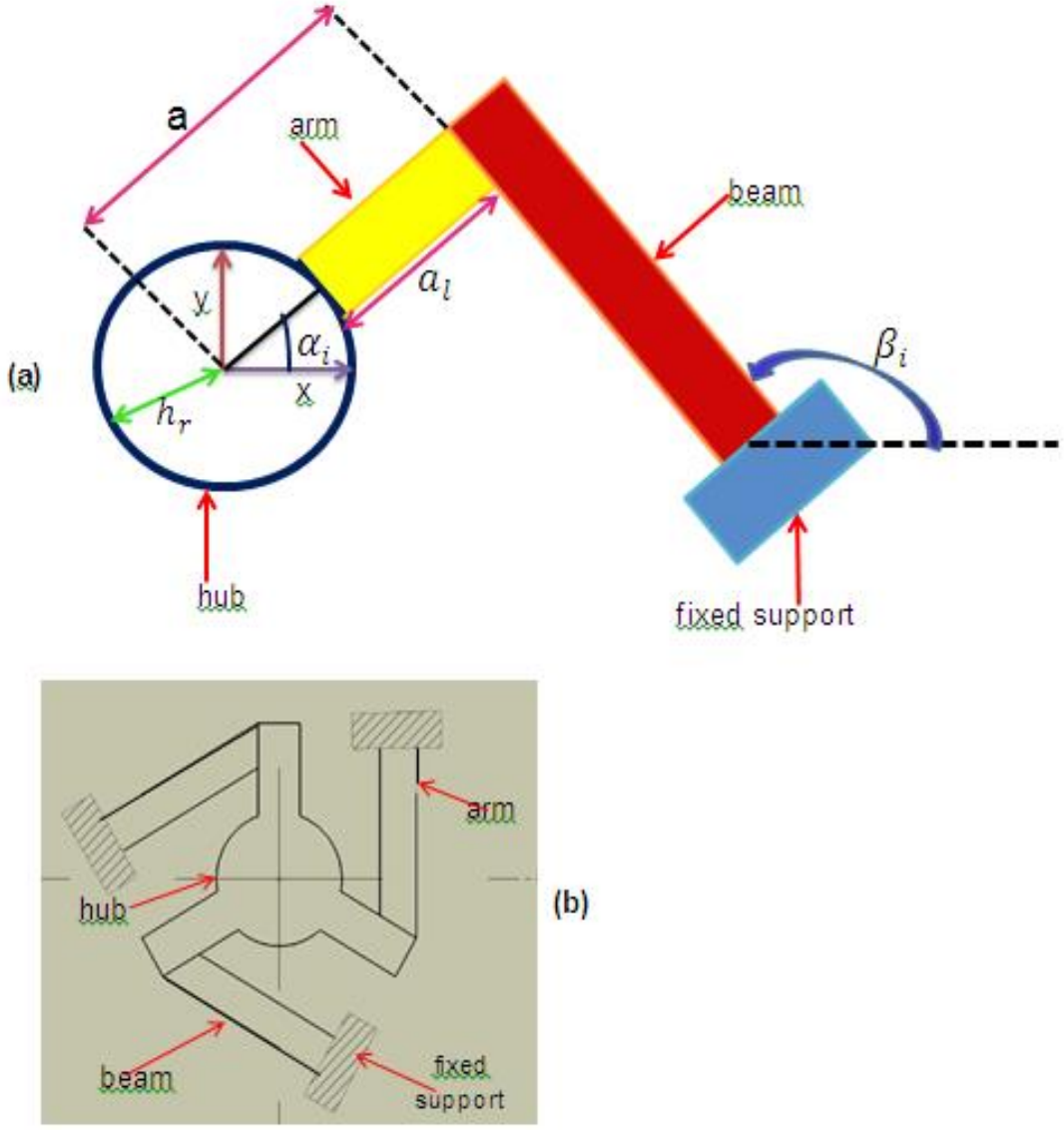

Figure 3.5: Geometric parameters of a typical suspension system (a), and the classic triskelion suspension layout (b).

k and stiffness. The desired model outputs are in terms of moment, $M = (M_x, M_y, M_z)^T$, force, $P = (P_x, P_y, P_z)^T$, normal stress σ_n, and normal strain ε_n.

Several assumptions are built into the basic model.

1. Platform and arms are rigid bodies.
2. Suspension ligaments ideal elastic beams rigidly coupled to the base and to the ends of the arms.

Displacement at the platform center, edge and arm are represented by D_{po}, D_{pb} and $D_{pa1,2,3}$ respectively.
The second input vector is

$$\boldsymbol{D_{p_o}} = \begin{pmatrix} x & y & z & \theta_x & \theta_y & \theta_z \end{pmatrix}^T \tag{3.19}$$

Ideally, the force would be exactly along z and only the displacement would be in the z-axis. Inputs on the θ_x and θ_y element reflect hub tilt that might occur through misalignment of the test forces. The other three elements are usually force to zero, assuming plausible misalignment could have negligible affect on the most stiffly constrained axes of the triskelion. An intermediate approach allows us to define explicitly any set of i arm at angle α_i. Then the displacements at the tip are

$$\boldsymbol{D_{pa_i}} = \begin{pmatrix} 1 & 0 & 0 & 0 & 0 & 0 \\ 0 & 1 & 0 & 0 & 0 & 0 \\ 0 & 0 & 1 & a_{y_i} & -a_{x_i} & 0 \\ 0 & 0 & 0 & 1 & 0 & 0 \\ 0 & 0 & 0 & 0 & 1 & 0 \\ 0 & 0 & 0 & 0 & 0 & 1 \end{pmatrix} \begin{pmatrix} x \\ y \\ z \\ \theta_x \\ \theta_y \\ \theta_z \end{pmatrix} \tag{3.20}$$

where a_{xi} and a_{yi} are the components of $\mathbf{a_i}$.

The arm tips experience the same direct translations and rotations as the hub plus extra transformations arising from lever effects with the rotations (equivalent to vector cross-products). Thus, for the current design, ideally $x = y = \theta_z = 0$ and the model

equations can force three zeros because they have only second order effects that linear models can't handle. Hence elements 1, 2, 6 of $\mathbf{D_{pa_i}}$ are now overwritten with zeros in practical implementation of the model.

3.6.2 Transformations to beam co-ordinates

The local frame for each ligament is set with its z-axis parallel to that of the global frame and its x-axis along the long axis of the beam. The i^{th} beam has its x_i-axis oriented at angle β_i to the x-axis in the global frame. Computing the forces for suspension beams from basic elastic theory is easiest in this body-fixed frame. The arm deflection can easily be transformed to an end deflection of the beam expressed in the local frame figure 3.6.These transformations are purely rotations about z-axis giving

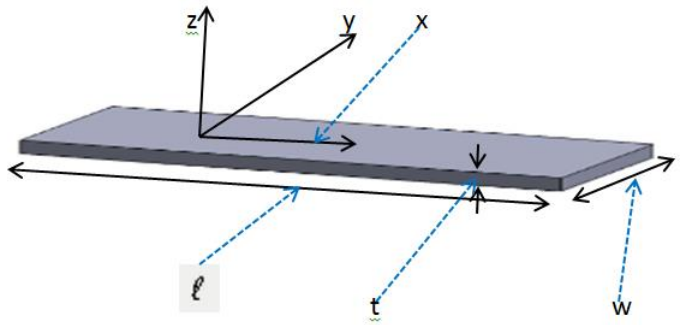

Figure 3.6: Single beam of triskelion suspension model.

$$\boldsymbol{D_{pb_i}} = R_{\beta_i}\boldsymbol{D_{pa_i}} \tag{3.21}$$

or

$$\boldsymbol{D_{pb_i}} = \begin{pmatrix} \cos(\beta_i) & +\sin(\beta_i) & 0 & 0 & 0 & 0 \\ -\sin(\beta_i) & \cos(\beta_i) & 0 & 0 & 0 & 0 \\ 0 & 0 & 1 & 0 & 0 & 0 \\ 0 & 0 & 0 & \cos(\beta_i) & +\sin(\beta_i & 0 \\ 0 & 0 & 0 & -\sin(\beta_i) & \cos(\beta_i) & 0 \\ 0 & 0 & 0 & 0 & 0 & 1 \end{pmatrix} \begin{pmatrix} \boldsymbol{D_{pa_i}} \end{pmatrix} \tag{3.22}$$

where β_i is the orientation of the local x-axis in the reference frame for the i^{th} beam and R_{β_i} is rotational matrix (6×6), transforming translation and rotations simultaneously.

3.6.3 Forces and moments

We assume all suspension beams are the same. This is the case in all published designs extremely likely to remain as ideal in all envisaged applications, for which the symmetry is design requirement. The assumption significantly simplifies the notation and derivation, while the extension to the fully general case follows a similar path is fairly obvious fashion. Each is represented as a uniform cantilever subject to loads and moments applied to its free end so as to cause specified end deflections end slopes there. The generalised end force $P_i = (F_i M_i)$ with $F_i = (F_x, F_y, F_z)^T$ and $M_i = (m_x, M_y, M_z)^T$ can be obtained by using the stiffness matrix give

$$\boldsymbol{P_i} \quad = \quad (K_{sa})\, \boldsymbol{D_{pb_i}} \tag{3.23}$$

For a cantilever, the suspension beam element stiffness matrix, K_{sa}, collects together elementary components discussed in appendix A.1 and simplifies to

$$K_{sa} \quad = \quad \frac{Ewt}{l} \begin{pmatrix} 1 & 0 & 0 & 0 & 0 & 0 \\ 0 & \frac{w}{l}^2 & 0 & 0 & 0 & \frac{w^2}{2l} \\ 0 & 0 & (\frac{t}{l})^2 & 0 & \frac{t^2}{2l} & 0 \\ 0 & 0 & 0 & k_{44} & 0 & 0 \\ 0 & 0 & -\frac{t^2}{2l} & 0 & \frac{t^2}{3} & 0 \\ 0 & \frac{w^2}{2l} & 0 & 0 & 0 & \frac{w^2}{3} \end{pmatrix} \tag{3.24}$$

where $k_{44} = \frac{Gt^2 w}{E}[\frac{1}{3} - 0.21\frac{t}{w}(1 - \frac{t^4}{12w^4})]$

From Newton's third law, there will be an equal and opposite force on the end of the platform arm. It needs to be re-transformed into the reference co-ordinate frame in order to relate it to the 'input' platform displacements to give

$$\boldsymbol{P_{pa_i}} \quad = \quad -R_{\beta_i}^{-1} \boldsymbol{P_{p_m}} = -R_{\beta_i}^{-T} \boldsymbol{P_{p_m}} \tag{3.25}$$

Observed from the centre of the hub, P_{pa_i} will appear with simply translated force components while the moment components will involve the moments of force components about the centre as well as the directly imposed ones. Formally and generally, this can be done by a translation matrix encoding vector cross-perpendicular with a_i. However, the practical constraints already imposed mean that only three components P_{pa_i} are active in the model; these for F_{z_i}, M_{x_i} and M_{y_i}. These are easily expressed as individually and summed at the centre. The overall effects of the ligaments observed at the centre are Hence summing over all the arms, taking the moments at the platform centre gives

$$\boldsymbol{F_{z_p}} = \sum_{i=1}^{3} \left(F_{z_i}\right), \tag{3.26}$$

$$\boldsymbol{M_{x_p}} = \sum_{i=1}^{3} \left(M_x + F_{z_i} \sin \alpha_i\right), \tag{3.27}$$

and

$$\boldsymbol{M_{y_p}} = \sum_{i=1}^{3} \left(M_{y_i} + F_{y_i} \sin \alpha_i\right) \tag{3.28}$$

Equations 3.26, 3.27, and 3.28 are collected into vector form as $\mathbf{P_p} = \left(0,\ 0, F_{z_p},\ M_{x_p},\ M_{y_p},\ 0\right)$

The generalised force that must be imposed on the platform to cause the specified displacements is, by Newton third law $\mathbf{F_{p_o}} = \left(\mathbf{P}^T,\ \mathbf{M}^T\right)$ or simply

$$\boldsymbol{F_{p_o}} = -\boldsymbol{P_p} \tag{3.29}$$

3.6.4 Stress and strain on the suspension beam

The axial stress at the on lower surface commonly dominates consideration of the safe loads for beams applications. In the triskelion suspension there could significant contributions from other stress components, e.g. shear from torsion or any tensile/compressive force along the beam which would add or subtract directly. Nevertheless, using σ_n for the simple form remains a useful indicator for design. It is also a dominant effect in generating surface strain that might be measured by applying strain gauges to the suspension beams for use

in micro-probe or force sensors applications. The direct stress along x-axis at the beam surface is [184], [186] and [190],

$$\sigma_n(x) \quad = \quad \left\{ \frac{[BM](x)t}{2I_x} \right\} \tag{3.30}$$

where $[BM](x)$ is the bending moment at distance about x. For the end loaded cantilever approximation used here for the suspensions, the dominate bending moment can be expressed in terms of the reactions at the base, $F \simeq F_z$ and $M \simeq -M_y$, as

$$[BM](x) \quad = \quad (xF - M) \tag{3.31}$$

where x is measured from the base. The expression for strain at the same point is

$$\varepsilon_n \quad = \quad \left(\frac{\sigma_n(x)}{E} \right) \tag{3.32}$$

where E is Young's modulus of the beam. Clearly, the maximum stress and strain are computed as an indicator of reliable operation, but values at other x might be relevant to sensing because of limitations M where strain gauges can be placed in practice.

3.7 Pseudo-kinematic consideration of the suspension beams

The triskelion platform hub displaces through bending of the suspension beams perpendicular to the plane of the beams, but is effectively constrained from translation in the plane of the beams. The platform will be able to rotate slightly under a combination of axial twisting and bending action in the beams. The end slopes in the cantilever model of suspension might be totally constrained to map to the end deflections, but in most practical situations they will have some degree of independence. The third platform rotation about z is heavily constrained. To this extent, the small displacement behavior of the triskelion flexure shows three degree of freedom.

In pseudo-kinematic terms, a triskelion flexure with 'rigid' platform and mounting arms is closely a parallel kinematic device based on three identical subsystems. It will have four active links (three suspension beams, and one platform). As discussed in section 2.1, the

most obvious rigid and ideal joint equivalence to the ligament suspension will provide it with 3 U-joints about x_i and y_i axes and 3 R-joints about y_i axes (figure 3.7). Hence, the mobility is

$$M = (6N_{act} - 5J_1 - 5J_2) = ((6 \times 4) - (5 \times 3) - (4 \times 3)) = -3 \tag{3.33}$$

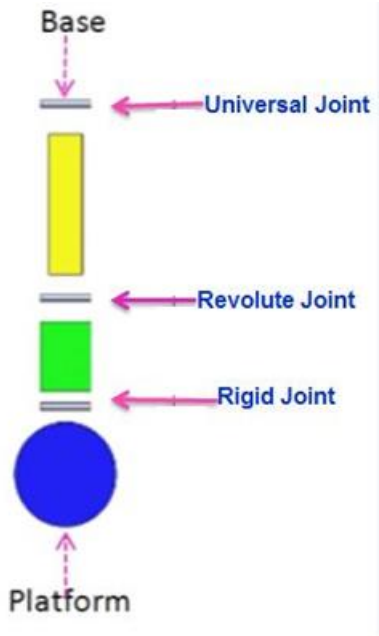

Figure 3.7: Pseudo-kinematic 'map' for one suspension leg of a classic triskelion design.

The negative value indicates that system is overconstrained, implying that, generally, it would not be possible to assemble this device from kinematic components without internal strains and that any device assembled is unlikely to run smoothly in the manner envisaged. Of course, monolithic devices automatically have all their elements geometrically compatible, making it easy to produce overconstrined designs. As demonstrated by successful micro-probe design, elastic (monolithic) triskelion suspensions can be constructed readily and they can show (experimentally) reasonably developed degrees of freedom. The mobility model suggests that six over constraints are unaccounted for. One explanation might be that the joint modelling is inadequate. For instance, assuming spherical joints at the platform gives three 1S, 1U sub-systems and $M = 3$. However, it is hard to reconcile the behavior of an S-joint with how the suspension beam attaches to either base or platform. In any case, this configuration allows a trivial axial rotation: effectively an artificial freedom

has been generated mathematically in an attempt to reconcile the mobility. It seems more likely that the degree of over constraint is about right but other physical factors compensate. The planar construction means that (ideally) the initial motion introduces strain into the over-constrained axes at a rate governed by small changes in cosine of an angle nominally zero. Even the slight elasticity in the heavily constrained axes might be enough to accommodate such small initial effects without obvious signs of poor behavior. However, a substantial stiffening spring action would then be expected as deflection increases.

If we take a definition of triskelion flexure to include that it has the platform and three identical legs, because the net freedom/constraint in each leg must be the same, its overall mobility must be a multiple of three (equation 3.16). The ideally designed 1 DOF triskelion for a force transfer artefact can't be archived in a planar device without breaking the symmetry and arguably not at all since even if an M =1 set of constraints is created their direction of action will not be truly independent. We might consider a triskelion-like design with different numbers of legs in an attempt to achieve different, favorable force responses. For example the four-legged tetraskelion might be considered intuitively to offer better protection against undesirable platform tilt; in pseudo-kinematic terms simply adds another suspension beam to the triskelion. If this is contained within the single plane of the device, its stiff axes coincide with the pervious existing ones and it is not clear that it sensibly offers more than the three pseudo-kinematic freedoms seen with each of the suspension legs.

Perhaps, once it starts to move, there is more scope for different smaller deflections to accommodate the motion over constraints and so a model might be proposed is which arms extending from the hub also act or beam elements. Now, pseudo-kinematic equivalent for each suspension limb treats the two beams in series as having two links with 2U, 1R joints (figure 3.8), there are now seven active links and so overall mobility becomes

$$M = ((6 \times 7) - (5 \times 3) - (4 \times 6)) = 3 \tag{3.34}$$

which matches the observed degrees of freedom. (Recall, though that mobility agreement is never a 'proof' of a proper design!).

Triskelion-like devices might also use more complex individual suspension elements to change the effective mobility. Of particular interest here, because it matches this analysis and easy to make in planar form, is a design in which the whole limb from base to hub has the same thickness, for convenience, this design will be called an "angle-beam" flexure throughout this thesis. This is equivalent to introducing a small rigid secondary platform to isolate two suspension cantilevers.

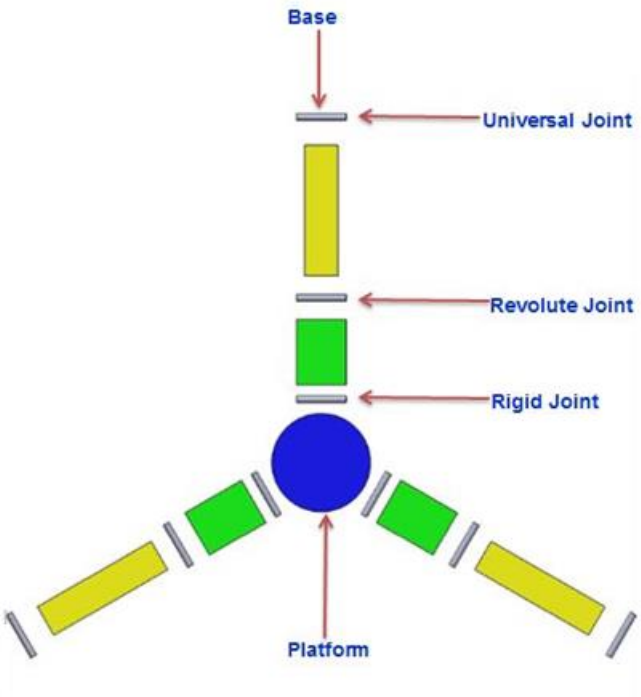

Figure 3.8: Pseudo-kinematic equivalence for 'angle-beam' triskelion flexure.

3.8 Analytical model for triskelion angled-beam suspension

As identified in section 3.7, there is significant potential in investigating angled suspension beams for use within triskelion-like devices. Therefore, the linear model discussed in section 3.2 should be expended to cover this more general situation: the simple beam is clearly a special case where one side of the angled suspension beam has zero length (or equivalently, that the elbow angle goes to 180 °). The approach adopted here will follow an unpublished strategy of Chetwynd, by creating an alterative stiffness matrix that can be used within

the framework of the analytical model already discussed.

It has already been established that, for the small deflections relevant to elastic deflections of the transfer artefacts, the constraints on three degrees of freedom are so stiff that their motion can be neglected in a first order model. For compact treatment, these terms have been omitted from the sparse vectors matrix equations developed in appendix A.1, and the stiffness matrix given at equation 2.24 to give a reduced 3×3 formulations that captures all the major features.

The small-amplitude behaviour is described by simple linear beam theory using the primitive equation for individual terms, equations (3.1) to (3.8).

Consider a first a cantilever modelled for the three significant deflection/stiffness modes (other deflections negligible). Each beam has length ℓ, width w, thickness t, a constant cross-

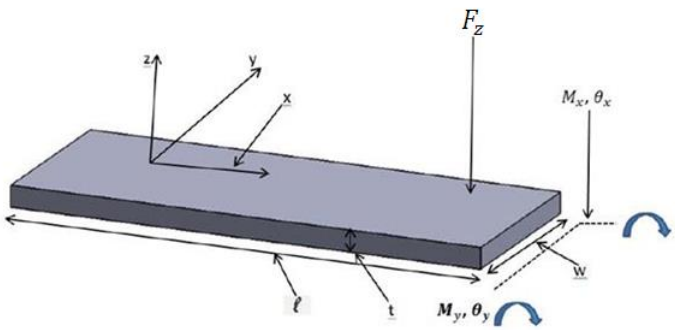

Figure 3.9: Basic cantilever model.

section $A = wt$ and moment of area $I = (wt^3/12)$ shown in figure 3.9. Then superposing the significant displacement axes in the compliance configuration, we have

$$\begin{pmatrix} \theta_x \\ \theta_y \\ \delta_z \end{pmatrix} = \begin{bmatrix} \lambda_x^{-1} & 0 & 0 \\ 0 & \lambda_{yy}^{-1} & \lambda_{yz}^{-1} \\ 0 & \lambda_{yz}^{-1} & k^{-1} \end{bmatrix} \begin{pmatrix} M_x \\ M_y \\ F_z \end{pmatrix} \tag{3.35}$$

where the stiffness are

$$k_z = \left(\frac{3EI}{\ell^3}\right), \tag{3.36}$$

$$\lambda_{yy} = \left(\frac{EI}{\ell}\right), \tag{3.37}$$

$$\lambda_{yz} = \left(\frac{2EI}{\ell^2}\right), \tag{3.38}$$

and

$$\lambda_x \simeq \left[\frac{4IG}{\ell}\left(1 - 0.63\frac{t}{w}\right)\right] \tag{3.39}$$

This is the essential structure that underlies the linear triskelion models that derive from [14] and [187]. The matrix in equation(3.35) is readily identified as a partition of that in equation(3.24)

The angled planar suspension can be modelled by treating it as two free bodies with a built-in connection between them at the elbow figure 3.10. The same approach can be applied for any elbow angle, β. For design purposes (and in earlier discussion) the elbow angle is conveniently taken as the "internal" one, whereas to be consistent in the use of right-hand frames analysis and model building better uses ϕ as shown in figure 3.11

.

Appropriate geometrical and Newton 3rd Law compatibilities are applied at the elbow to represent the connection. Then the behavior of BE (figure 3.10) is that of a simple uniform beam subject to effective end-loading at E. While having different stiffness from the (possibly) different length, EP also under goes simple beam bending subject to the end loading at P. However, its bending deflections are superimposed on a rigid body motion defined by the z-motion and slope/twist at E. For an actual force system imposed at P, the force system active at E is just the reaction when EP is treated as an independent cantilever. Equation (3.39) neglects the small higher-order term and is adequate providing w is just a few times larger than t.

Each section, BE and EP, is treated in its own body-fixed frame as a beam acting under the conditions described by equation (3.35); these frames both have x-axis along their sections, while their z axes are parallel. For notational convenience, compliance matrix in

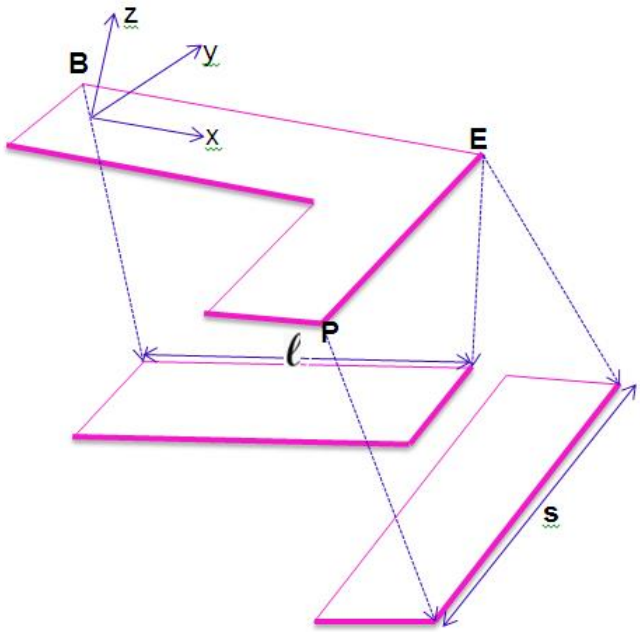

Figure 3.10: Two separated bodies of the suspension beam (shown for a angle 90 °).

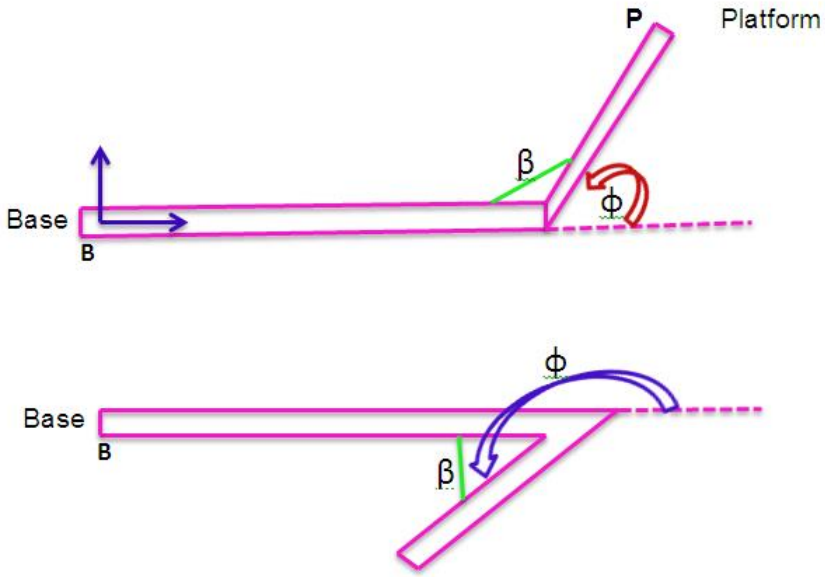

Figure 3.11: Relationship between β and ϕ, illustrated for 'internal' angles of around 120 ° and 60 °.

each of these frame will here be expressed in the several form

$$\left[\lambda^{-1}\right] = \begin{bmatrix} \lambda_A^{-1} & 0 & 0 \\ 0 & \lambda_T^{-1} & \lambda_C^{-1} \\ 0 & \lambda_C^{-1} & k^{-1} \end{bmatrix} \tag{3.40}$$

The model manipulations required to describe and combine the behaviour of these beams all reduce to rotations on the z-axis or to cross-product-like operation related to moments.

Expressing all the terms in the BE-frame, the end E of beam BE is subject to the same generalised forces as are applied to the platform, via a series of Newton's 3^{rd} law interactions (i.e. it supplies all the reactions needed to treat EP as a cantilever with it fixed end at E). Additionally, the angled lever arm EP causes Newton 3^{rd} law moments from the end-force at P in both the x-axis and y-axes. Thus, deflection at E founded by equation (3.35) for this augmented load,

$$\begin{pmatrix} \theta_{xE} \\ \theta_{yE} \\ \delta_{zE} \end{pmatrix} = \left[\lambda^{-1}\right]_{BE} \begin{pmatrix} M_x + F_z \sin(\phi) \\ M_y - F_z \cos(\phi) \\ F_z \end{pmatrix} \tag{3.41}$$

or

$$\begin{pmatrix} \theta_{xE} \\ \theta_{yE} \\ \delta_{zE} \end{pmatrix} = \left[\lambda^{-1}\right]_{BE} \begin{bmatrix} 1 & 0 & s\sin(\phi) \\ 0 & 1 & -s\cos(\phi) \\ 0 & 0 & 1 \end{bmatrix} \begin{pmatrix} M_x \\ M_y \\ F_z \end{pmatrix} \tag{3.42}$$

where s length of section EP. Measuring the displacement of P in the body frame for BE, the rotations at E are merely transmitted by the rigid-body motion of EP, but the angled lever arm contributes additional displacements from both twists, $\theta_{xE} s \sin(\phi)$ and $-\theta_{yE} s \cos(\phi)$. Then the overall deflection of P from rigid body displacement of EP is, in the BE-frame,

$$\begin{pmatrix} \theta_x \\ \theta_y \\ \delta_z \end{pmatrix}_{P,RB} = \begin{pmatrix} \theta_{xE} \\ \theta_{yE} \\ \delta_{zE} + \theta_{xE} s \sin(\phi) - \theta_{yE} s \cos(\phi) \end{pmatrix} \tag{3.43}$$

or

$$\begin{pmatrix} \theta_x \\ \theta_y \\ \delta_z \end{pmatrix}_{P,RB} = \begin{bmatrix} 1 & 0 & 0) \\ 0 & 1 & 0 \\ s\sin(\phi) & -s\cos(\phi) & 1 \end{bmatrix} \begin{pmatrix} \theta_{xE} \\ \theta_{yE} \\ \delta_{zE} \end{pmatrix} \tag{3.44}$$

Note that x and y-axis translations at P will have $\theta^2/2$ relationships with s and the twists, so remaining negligible for the small θ conditions already implicit in these models.

Considering the independent bending behavior of EP in its local (axial) frame, We have at P

$$\begin{pmatrix} \theta_A \\ \theta_T \\ \delta_{EP} \end{pmatrix} = \left[\lambda^{-1}\right]_{EP} \begin{pmatrix} M_A \\ M_T \\ F_{EP} \end{pmatrix} \tag{3.45}$$

It is clear by observation that these forces and deflections can be expressed in the body frame for BE as

$$\begin{pmatrix} M_x \\ M_y \\ F_z \end{pmatrix} = \begin{pmatrix} M_A\cos(\phi) - M_T\sin(\phi) \\ M_A\sin(\phi) + M_T\cos(\phi) \\ F_{EP} \end{pmatrix} \tag{3.46}$$

$$\begin{pmatrix} \theta_x \\ \theta_y \\ \delta_z \end{pmatrix} = \begin{pmatrix} \theta_A\cos(\phi) - \theta_T\sin(\phi) \\ \theta_A\sin(\phi) + \theta_T\cos(\phi) \\ \delta_{EP} \end{pmatrix} \tag{3.47}$$

Noting that these expressions are governed by the same simple rotation matrix transformation and that for such orthogonal transformations the inverse is equal to the transpose, we obtain directly

$$\begin{pmatrix} \theta_x \\ \theta_y \\ \delta_z \end{pmatrix} = [R_\phi]\left[\lambda^{-1}\right]_{EP}[R_\phi]^T \begin{pmatrix} M_x \\ M_y \\ F_z \end{pmatrix} \tag{3.48}$$

where

$$[R_\phi] = \begin{pmatrix} \cos(\phi) & -\sin(\phi) & 0 \\ \sin(\phi) & \cos(\phi) & 0 \\ 0 & 0 & 1 \end{pmatrix} \tag{3.49}$$

Superposing this bending motion onto the 'rigid body' motion for EP then gives

$$\begin{pmatrix} \theta_x \\ \theta_y \\ \delta_z \end{pmatrix} = \left[[\delta_\wedge] \left[\lambda^{-1}\right]_{BE} [\delta_\wedge]^T + [R_\phi] \left[\lambda^{-1}\right]_{EP} [R_\phi]^T \right] \begin{pmatrix} M_x \\ M_y \\ F_z \end{pmatrix} \tag{3.50}$$

where

$$[\delta_\wedge] = \begin{pmatrix} 1 & 0 & 0 \\ 0 & 1 & 0 \\ s\sin(\phi) & -s\cos(\phi) & 1 \end{pmatrix} \tag{3.51}$$

The equation (3.50) defines a singe enhanced compliance matrix that can be evaluated *a priori* from the design parameters. It is expressed in the BE-frame, a body-fixed frame of the suspension limb aligned axially at the junction with the base. The compliance matrix developed in section 3.3 is also in a body-fixed frame of this type. Thus the new compliance matrix can be expanded into full (6×6) format by adding rows and substituted directly in place of the simpler matrix used within the previous model.

3.9 Implications and limitations of the linear model

3.9.1 General needs for small force transfer artefacts

The triskelion design has been adopted for the first practical micro-fabricated nano-force artefacts partly because the previous modelling of designs for micro-probes gave added confidence that useful performance can be achieved. However, these linear models are clearly incomplete and can be expected, at best, to predict performance over only a limited range of applicability. This chapter section explores a source of non-linearity that may

become significant in the real artefacts.

The microprobe requirements are significantly different to those for a high-quality force transfer artefact. Most obviously, a microprobe is required to respond to three orthogonal displacements at the attached tip, each having a similar range (maybe 10 μm). These displacements are then manifest (via the probe arm lever) as a $z-$translation and two orthogonal rotations of the planar triskelion platform. The effective linear stiffness at the probe tip should be approximately equal in all three axes, hence specifying platform torsional stiffness for the $x-$ and y-axes. The system is intended to have three degrees of freedom (DoF). In contrast, the force transfer artefact should respond primarily to a force (not a displacement) applied directly to the platform. An ideal artefact would exhibit a design-specified stiffness in one translational axis (say, z-axis) while having very high stiffness in all others. It would be a 1 DoF system.

A more functionally specific way to consider the artefact stiffness is that the inherent sensors (whatever sensing principle happens to be used) should show sufficiently low sensitivity to any reasonable level of misalignment of the applied force. If the force is nominally applied along z and centrally on the platform, we might define maximum shifts in x and y and tilts about the $x-$ and $y-$axes for which there is no metrologically significant change in the output signal. As the device, and its target instruments are small and confined, fairly large relative alignment errors should be tolerated, perhaps up to, say, 250 μm and 50 mrad (i.e. visually detectable region of 0.5 mm diameter or a misalignment of 1 mm over a 20 mm length). If costs and sensor technology allow multiple sensing points (e.g. strain gauges as used on the micro-probes, where a minimum of three is essential to function), then it may be plausible and sensible to compute and correct for parasitic platform motions. Nevertheless, it is still good practice to select a mechanical design to reduce the degree of correction that would be needed.

There is urgent need to specify the operational limits on the $z-$stiffness of force artefacts for given applications. This requires for example considering whether low values might upset the stability of some target instruments (specially if they have finite stiffness within

a tip positioning control loop). High stiffness would be unsuited to operation in which the artefact is deliberately displaced bodily to impose a force on the target a mode considered by NPL for the low force balance [48]; it would place excessive demand on practical control and stability.

Consider first asserting force by bulk movement of the artefact when operating on the LFB. We do not require extreme accuracy in the applied displacement because the target system and artefact themselves report on the actual setting. However, we do need smooth motion at very high resolution. Expensive manipulators such as Digital Piezo-Translator(DPTs) [191], [192], [193], [194], [195] can readily control to 1 nm. Even some lower cost manual systems can be smoothly adjusted by skilled operators to maybe 10 nm equivalent positioning. The most sensitive artefacts that might be calibrated using the current LFB should presumably be stepped at something like 1 nN intervals for good testing of linearity. This implies stiffness of below 1 N/m even for the high-performance manipulators. It would well be argued that such fine calibration justifies the high manipulator cost and 10 nN nominal stepping will suffice on most occasions, suggesting that 1 N/m $z-$stiffness would be acceptable. Even at the upper end of the LFB capability, when an artefact might have target range of, say, 100 μN to 20 mN, it may be difficult to use this mode at a stiffness above about 100 N/m.

Now consider calibrating an AFM. Many AFMs have a z-range restricted to the order of 10 μm or less. The elastic displacement of the artefact caused by tip contact (which must be accommodated by the AFM $z-$axis) should be limited to, say, 1 μm. A tip force of 1 μN would be regarded as 'heavy', but it is not implausible. Again, an artefact stiffness of around 1 N/m is implied, but could probably be increased somewhat. Finally, consider indenter instruments [191], [196], [197]. Nano-indenters might impose up to 100 mN with nN resolution, or perhaps be set for five times those values. A micro-indenter is likely to have resolutions in the tenths of mN and is outside the realistic scope of microfabricated artefacts but nevertheless needs some form of calibration device. The effective stiffness of the force control loop for such instrument is not generally published, but is probably at least of the order of 1 kN/m. If the artefact is significantly less stiff than this, then its

deflection might not be accommodated by the indenter without compromising the latter's own force assertion. A whole family of different scaled transfer artefacts will be needed to cover even this brief collection of applications.

Viewed simply, increasing the platform arm length of a triskelion increases the displacement and hence, the cantilever reaction force for a given platform rotation, i.e. it increases the torsional stiffness seen at the platform. This is favourable for the artefact application. However, other cantilever deflections are also induced. For example, if the beam were perpendicular to the arm (a 90 ° elbow angle), the dominant effects of a tilt directly along that arm would be from a combination of the normal beam bending and axial torsion through the angle of platform tilt. In this particular geometry (not that adopted in micro-probe or proposed force artefacts) arm length tends to be beneficial to tilt stiffness and might also reduce the onset of non-linearity under tilt errors by making the normal beam beading term more dominant. However, other elbow angles can lead to more complicated combinations at the end of beam, with more potential for non-linearity.

The restoring moment from thin leg arises principally from the axial torsion and suspension end force. Then, from equation (3.24) and (3.35) and approximating at equation(3.12) for pure tilt condition when $\theta_x = \theta$ and $\delta_z = a\theta$,

$$\frac{M_{total}}{\theta} \quad = \quad \lambda \simeq \frac{Ewt^3}{\ell}\left(\frac{1}{8} + \frac{a^2}{\ell^2}\right) \tag{3.52}$$

where ℓ is length of beam and a is length of arm. Thus we don't expect a major contribution from arm length of the beam. It starts to dominate once $a > 1.5\ell$, but this implies less compact devices that might have other disadvantages. Derivation of equation (3.52) is given in appendix A.2.

Dynamic performance could also be of concern. For example, taking an artefact platform of around 2 mm square and 100 μm thick, made of a silicon-like material (density $\sim$ 3 mg/mm^3, we have a typical lumped mass of around 1 mg. Even for a 1 N/m vertical stiffness, the first mode resonance (which will be in the measurement axis) will be around 1000 rad/s or 170 Hz. This should be high enough to avoid dynamic operational problems

with the majority of target systems, but might be within the control bandwidth of some AFMs, etc.

3.10 Kinematics and parasitic motion

It is argued in section 3.4 that the approximate pseudo-kinematic model for the classic triskelion design treats the suspension beams as UR links. The overall device mobility would then be M = −3, which is notably over-constrained. It is further argued that introducing angled-beam cantilevers in place of the 'rigid' platform extension arms would bring the system closer to a kinematically 'correct' device. Its mechanically stability is, however, of potential concern, because all the links of the equivalent kinematic system lie in one place, both variants of the triskelion represent what a robot designer or mechanism analyst would call a 'singular condition', something to be avoided because it tends to lead to either a locked-up or an uncontrollable state. 'Singularity' is used in this context because the Jacobian matrices describing the variations of drives and outputs become singular or zero at such positions.

Despite these criticisms, there is plenty of evidence from micro-probe applications that triskelion flexures can function well as precision devices. One reason is that elasticity can add short-range pseudo-freedoms in 'constrained' axes, so reducing the equivalent kinematic over-constraint and preventing lock-up. Also, the spring forces inherent to flexures can add stability at 'uncontrolled' joints. Broadly, the argument for the present geometry is as follows. The projection of the suspension arms into the platform plane varies as cosine of their rotation, and so for small deflections there is little in-plane induced change of length to generate the constraining forces. This suggests, however, that fairly severe non-linear elastic behaviors could build up at quite modest platform displacements. Normally, the over-constraint of a flexure would lead us to expect that its actual stiffness would be higher than that predicted by basic linear models and that it would act as a stiffening spring. The evidence from micro-probes suggests there might not be too much over-stiffening over practically useful ranges.

In common with all published versions of triskelion models, the analysis in this thesis contains inherent assumptions because it is based on simple (linear elastic) beam theory. These assumptions are well known and need not be examined in detail here. In almost all examples of structural engineering deflections are restricted for practical reasons to levels that make the approximations extremely effective. However ligament flexures are an exception by regularly breaking the guidance that $z-$deflection should be less than the beam thickness. This introduces new concerns, not well documented, that, while still working fully and respectably in the elastic region, this change in geometry from the starting ideal might provide another source of non-linearity in the spring rate of flexure. This will be discussed further in the next section.

The previously published versions of the triskelion model also has (probably, in part, by passing through several hands) absorbed a fairly complex notation accompanied by a tendency to lay out the mathematical terms in different ways at different places. Some of the complexity arises from extracting simplified forms of general formulae, where it may tend to hide that specific restrictions have been applied. Associated with this, the co-ordinate frames used appear at first somewhat arbitrary, but some are actually chosen to simplify (implicitly) the algebraic expressions for the specific triskelion geometry. They are not always ones that have an immediate resonance with readers or users of the model. For example, the body-fixed frame for the cantilever has, unusually, its y-axis along the beam. There is inconsistency in the text and figures of the [187], which may be just typographical, including the appearance of a left-handed frame. For the benefit of future applications, it was judged well worth the modest extra effort required to completely redraft the algebraic description in a simpler consistent notation when introducing new features here and to provide an implementation closely aligned to that notation.

The linear-elastic matrix stiffness model is inherently incapable of expressing any effects of interaction between deflections along or about different body-frame axes or higher-order effects on any single axis. Some such effects could, in principle, be captured by matrix-based quadratic forms, but there are questionable levels of cost-benefit. First, if second-order effects are significant it becomes increasingly likely that some of the assumptions of

simple beam theory will be violated (e.g., neglecting shear, small deflections relative to overall size). Second, matrix elements concerned with deflection interactions are not known a priori and so either a closed-form geometric approximation or an iterative scheme must be used, both adding new uncertainty sources. There appears to be no justification for pressing for perusing such approaches unless there is clear experimental evidence of need for them in dealing with real applications. Currently there is no such evidence.

3.11 Spring non-linearity in force artefacts

Consider a perfect kinematic version of the triskelion in which the suspension arms are rigid rods carrying a revolute and a universal joint. Any 'vertical' motion of their ends (i.e., of the platform support points) shortens the projection of their length into the original plane, implying that the platform must move laterally to accommodate it. But, the three arms require platform motions in different directions. Thus, the system would ideally lock (through kinematic over-constraint) in its null position. (Of course, real devices could not be perfectly rigid and some motion is likely to occur). For a beam, the axial effect equivalent to shorting length of the rods projection into its original plan is know as curvature of shorting [198]. For a beam truly fixed at both ends, any transverse deflection must be associated with the build up of axial (tensile) forces, so stretching it to a length that fits the curved shape into the required space. Note that such axial forces will tend to pull the beam into a straighter shape, so an alternative reading is that complete constraint increases the lateral stiffness beyond the predicted value.

The axial shortening of the curved beam is calculated formally by integrating the projection of the local slope along the beam. It is completely ignored in basic texts, but is covered briefly in advanced textbooks on structures or strength of materials [198]. For a pinned rod of length ℓ having an end deflection δ, the effective displacement along the original axial direction is $(\ell - (\ell^2 - \delta^2))$, which for small δ reduces to $(\delta^2/2L)$. For a transversely-loaded cantilever and closely-related forms such as the double-built-in shallow-S leaf-spring, the equivalent axial shift - sometimes known as curvature shortening is $(0.6\delta/\ell)$. The linear model ignores such effects.

If the triskelion platform moves in a z-translation without any externally imposed tilts, then the symmetry means that ideally it will have no in-plane translations. However, the movement causes each suspension arm to bend, resulting in them having equal curvature shortening. Maintaining a continuous physical path from the base to the platform z-axis then requires a combination of other relative motions. The elbow angle between the platform arm and the beam axis could expand through a small degree of (elastic) rotary freedom or, effectively a variant, the beam could bend in-plane to open the projected angle. A z-rotation of the platform will generate a displacement at the end of its arms that directly compensates for a component of the axial shortening; this would still require slight rotary freedom at the arm-beam joint.

If tilt is imposed on the platform, with no overall z-motion, the arm ends will not necessarily displace the same amount and the component of the twist accommodated by end y-rotation of each of the beams will generally differ, as, therefore, will their in-plane curvature shortening. Since any bending causes a shortening from the default ('zero') position, there will still be a tendency for platform rotation. The overall effect is considerably more complex than for simple z-motion and is likely to lead to small in-plane shifts of the platform centre from the z-axis. On at least some of the suspension beams a component of the platform twist must be matched by both an end-slope in the design bending axis and a twist about the longitudinal axis. The latter is relatively compliant in typical designs , but generally the overall stiffness will vary according to the relative orientation of the beam to the imposed twist. Under tilt, the in-plane projections of the arms will also shorten, generally requiring additional bending of the suspension beams in their stiff planes, and so increasing overall device stiffness. Recall here that, unlike the microprobe, the force artefact will ideally respond only to a z-stimulus: this point might be an indicator of need for divergent design strategies.

A simple way to visualize to how the second-order shortening effects will influence things is to consider the xy-projection of the path through the beam and platform arm. It forms a triangle with the straight line from the beam base to the z-axis. The length of the latter is fixed. The arm-projection will vary if there is platform twist, but remains at its original

length for pure translation. The beam-projection shortens always for any deflection. For any specific initial case, the triangle is solved for the fixed 'pseudo-hypotenuse' by the cosine rule, using some combination of the fix base-line,the arm and beam lengths and their included angle. As the beam shortens, we need small changes in this and other angles to maintain the triangle.

An unpublished design study by Chetwynd (2009) included an exploration of this projection triangle by use of spreadsheet calculations. It suggested that there is a slow-moving minimum in the need for the angle to change, dependent on the ratio, a/ℓ, of arm length. Hence it tentatively suggested that a ratio of around 2 is best for the 60° elbow used traditionally in a triskelion. However, most published designs have a ratio around 0.5. This raised, but could not adequately answer, the question of whether different elbow angles might give more linear stiffness characteristics in physically compact devices.

In terms of accommodating beam shortening by platform rotation, at least for platform translation, the beams should clearly be tangential, i.e., the included elbow angle, should be 90°. Also, longer platform arms reduce the rotation needed for a specific shortening. Smaller rotation leads to less need for lateral deflection of the suspension beam in order to maintain continuity (a square law relationship so valid even if the arm length is increased). Longer suspension beams suffer less curvature shortening for a given end deflection, again leading to less platform rotation.

If inherent platform rotations are likely to occur at magnitudes broadly similar to other second-order deflections (as is the case for dimensions and geometries being considered here), a criterion based on stabilizing the included angle is not necessarily best. While the cosine model effectively treats the projected lengths as rigid rods, a real device will presumably relax elastically to an intermediate value between all deflections, governed by the relative local stiffness. Over-constraint stiffening caused by platform rotation will arise from work done in a combination of expanding this angle and laterally deflecting (slope and linear) the suspension beam.

Depending upon the exact form of the arms projecting from the central platform, the best simple model for the junction to the suspension beam is probably the slightly conservative one that the arm and connection are locally rigid. Then there can be no local change to the included angle and all accommodation must be by in-plane bending of the suspension beam. For this model, we would impose in the plane of the device an end-slope equal to the platform in-plane rotation and an end-deflection equal to the change in projected radial length of the arm caused by that rotation.

From the reasons discussed earlier, there is no point in perusing these ideas further unless they are shown experimentally to be of practical importance. This emphasizes further need for experimental investigations of non-linear stiffness region of a variety of triskelion design; no such data exist in the public domain at the time of writing.

3.12 Conclusion

A novel contribution has been presented in this chapter for the development of analytical linear elastic model for triskelion force artefacts. The previously published linear models for micro-probe have some inconsistencies in notation, but build in some common approximations and force the use of highly pre-ordained design geometries. The new approach retains good features of earlier ones while introducing consistent, systematic use of conventions generally used in mechanism analysis. More importantly, it makes direct use of direct vector-matrix tools so that the model can deal with all potential design parameters; most important here are variation in 'elbow angle' and the number and or distribution of suspension legs. Extensive use of pseudo-kinematic concepts highlights the like types of non-linear stiffness behaviour, which is of great importance for applications to force transfer artefacts than to micro-probe. This leads to the proposal for 'angle-beam' design and second linear model is developed to analysis this family. Considerable discussion of the general needs for force transfer artefacts includes exploration of like patterns for non-linearity and some of outline strategies for modelling it. However, it is conclude that detailed work is not justified in the absence of practical data on the behaviour of real device (triskelion force artefacts). Hence this chapter provides means for imposed modelling of

designs and highlights the importance of gaining experimental data.

The implementation of an enhanced linear elastic model has been discussed in the next chapter for development of triskelion software program.

Chapter 4

Implementation of enhanced linear elastic model: Numerical experiments and data analysis

4.1 Introduction

This chapter presents the development of a triskelion software program that is purely dependant on the mathematical equations of the analytical linear model for a triskelion force artefacts. The newly developed program is not limited, as previous ones have been to studying the fixed geometry of the planar flexure artefact with a 60 ° elbow angle [120], [14], [118], [188], [148]. Because force artefacts have different requirements from and so many benefit from different designs, to micro-probe suspensions, research with new system is intended. The new search work is intended to explore the relative sizes, orientation of angles, etc. it is an important first stage, in combination with experimental studies in chapter 6, 7, and 8 towards discovering 'best designs' and minimizing the non-linearity of the triskelion force artefacts and micro-probe artefacts. The new concept of variable elbow angle has been incorporated into an enhanced linear elastic model to provide a flexible for triskelion software program for computing the behaviour of the suspension beams, forces F_z, moments M_x & M_y, stress σ_n, strain ε_n, stiffness constant k_z, and torsional stiffness λ_x of triskelion force artefact and the micro probe suspension artefact of

any elbow angle prior to their fabrication processes.

This approach has never previously been seen in the public domain or any scientific published paper for predicting the stiffness k_z and torsional stiffens λ_x or λ_y of triskelion force artefact or micro probe suspension artefact.

4.2 Implementation of enhanced linear elastic model

A robust program could be developed by using programming languages such as C, C++, fortran 95 and Java, but the MATLAB is a high-level language and provides an interactive environment for programming extensive computation tasks faster than other languages such as C, C++ and Fortran. The MATLAB is best for developing new complex mathematical algorithms and is very popular in machine learning. It is well-suited and widely used for prototyping before later commitment of a final procedure to a non-efficient language. Hence, it has been decided to use the MATLAB for developing a robust program.

4.3 Design variables of the triskelion software program

The design parameters used for the development of software program are divided into three categories.

1. Platform parameters. item Elbow angle β_i
2. Suspension beams parameters.
3. Material constant parameters.

4.3.1 Platform parameters

The platform consists of a hub radius h_r, which is assumed to be rigid, joined with three symmetrically designed arms, see figure 4.1. The centre of the hub is coincident with the centre of the xyz-co-ordinate frame for the whole device. The end-point of each arm is initially defined by a vector $\mathbf{a_i} = (a,\ 0\ ,0)^T$ aligned to the x-axis, which is then rotated about z-axis by $(\alpha_i, i = 1,\ 2,\ 3)$. Note that $a = r + \ell$. Each arm has length ℓ_a, width w_a and thickness t_a. The end-points of three identical arms are joined with three suspension

beams ($b_i, i = 1, 2, 3$). These beams behave as a cantilever that is clamped at the supporting ring and subject to the imposed forces and moments at free end. The α_i angles expressed in radians, used for triskelion force artefacts with various elbow angles are given in the table (4.1). These angles are consistent with those used in Pril's model (figure 2.20 and figure 2.21) in which one arm is aligned along the y-axis [14].

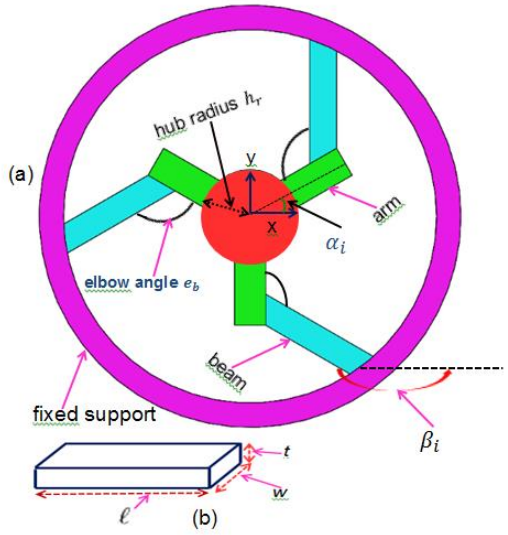

Figure 4.1: (a) The simplified classic triskelion suspension with elbow angle 120 ° and (b) dimensions of the outer three uniform beams.

4.3.2 Elbow angle β_i

The elbow angle, e_b is defined as the non-reflex angle between the arm of the rigid platform and the relevant beam. The elbow angles e_b for each artefact satisfy the follow relation.

$$e_b = |(\alpha_i - \beta_i)| \tag{4.1}$$

Elbow angles β_i angles are calculated from α_i angles in radians. These angles for various triskelion force artefacts are given in table (4.1).

4.3.3 Beam parameters

Three rectangular beams b_i of uniform cross-sectional area are attached to the rigid platform. Each beam has length ℓ, width w, thickness t and orientation angle ($\beta_i, i = 1, 2, 3$) with respect to the reference x-axis.

Table 4.1: Angles α_i and β_i for triskelion force artefacts

Triskelion force artefact ID	α_1	α_2	α_3	β_1	β_2	β_3
60°	$-(\frac{\pi}{6})$	$(\frac{\pi}{2})$	$-5(\frac{\pi}{6})$	$-(\frac{\pi}{2})$	$(\frac{\pi}{6})$	$5(\frac{\pi}{6})$
90°	$-(\frac{\pi}{6})$	$(\frac{\pi}{2})$	$-5(\frac{\pi}{6})$	$-2(\frac{\pi}{3})$	0	$2(\frac{\pi}{3})$
120°	$-(\frac{\pi}{6})$	$(\frac{\pi}{2})$	$-5(\frac{\pi}{6})$	$-5(\frac{\pi}{6})$	$-(\frac{\pi}{6})$	$(\frac{\pi}{2})$
150°	$-(\frac{\pi}{6})$	$(\frac{\pi}{2})$	$-5(\frac{\pi}{6})$	$-(\pi)$	$-(\frac{\pi}{3})$	$-5(\frac{\pi}{3})$
180°	$-(\frac{\pi}{6})$	$(\frac{\pi}{2})$	$-5(\frac{\pi}{6})$	$5(\frac{\pi}{6})$	$-(\frac{\pi}{2})$	$(\frac{\pi}{6})$

Table 4.2: Input parameters for the new model, with typical values.

S.No.	Parameter	Values & Unit
1	z	5×10^{-6} m
2	θ_x	1×10^{-3} rad
3	θ_y	1×10^{-3} rad
4	$a = (h_r + a_\ell)$	0.002 m
5	ℓ	0.004 m
6	w	0.001 m
7	t	0.0002 m
8	E	$2.5e^9$ pascal
9	G	1×10^9
10	α_1 , α_3 , & α_3	Table (4.1)
11	β_1 , β_3 , & β_3	Table (4.2)

4.3.4 Material constant parameters

The other two parameters, Modulus of direct shear G, and Young's Modulus E are taken to be constant. They are used in the input specification of the triskelion software program, with typical values given in table (4.2).

4.4 Triskelion software program

The triskelion software program has been developed by using the analytical elastic model. The MATLAB environment is a flexible means for developing complex algorithms and functions. The MATLAB workspace is also very useful for the type of modelling research work being presented in this thesis. The nomenclature of the input parameters to execute the program is given in table (4.2).

The whole program was written as a collection of functions, each with aim, pre-condition and post-condition to reflect one sequential step in the enhanced linear elastic model in chapter 3. The dependance diagram for triskelion program is shown in figure 4.2. The

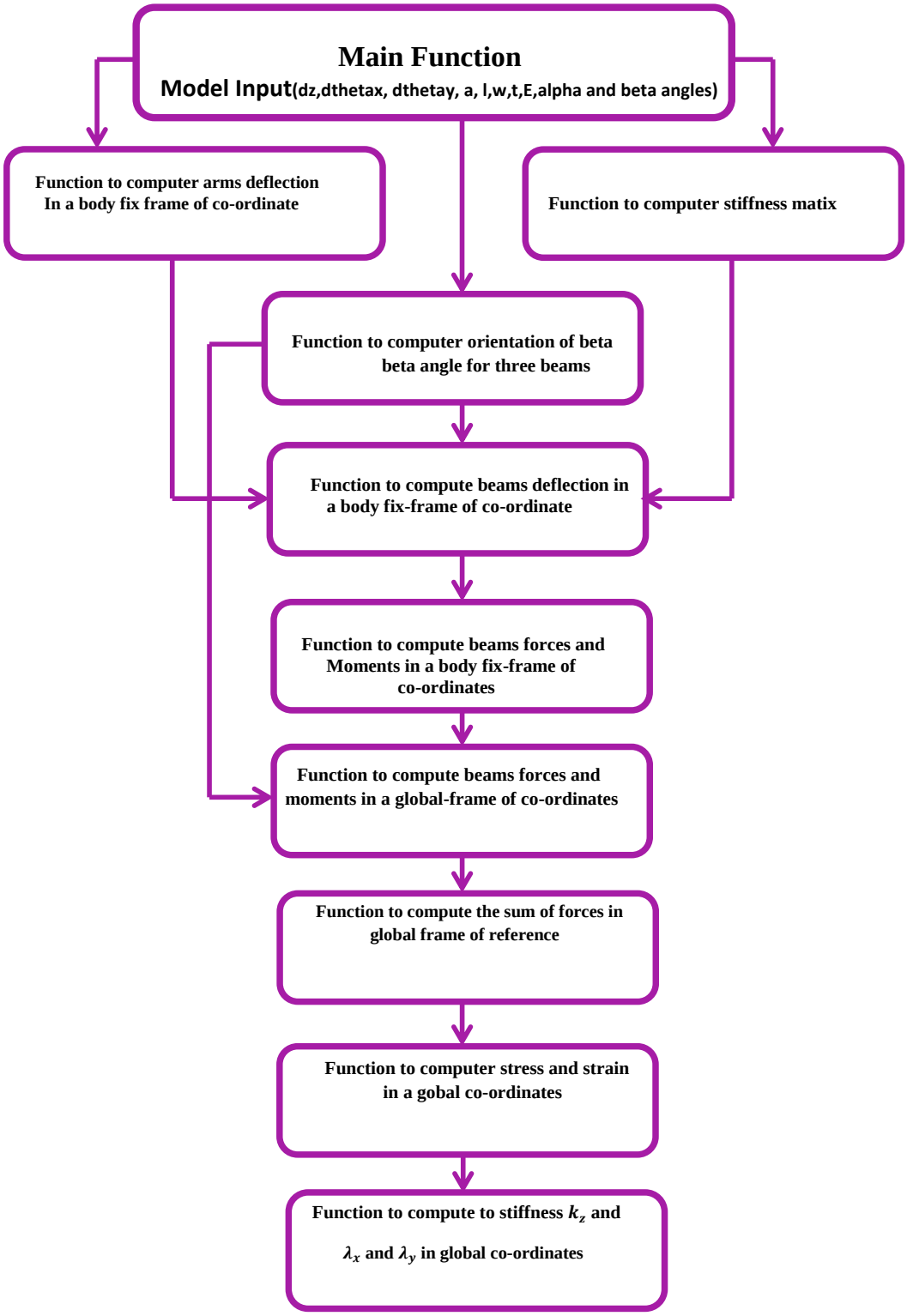

Figure 4.2: Dependency diagram for triskelion program

detail of the computational schema and codes for triskelion software program, have been described in the appendix C.

During the development phase, the execution of a function was tested by manually placing appropriate input parameters into the MATLAB interpretive workplace and then calling it, standing alone, from the workplace. The computed results were compared with the hand calculated results. The same procedure was adopted for every function of the triskelion software program.

At the last stage of the development, when all codes for all required functions were completed, the codes for the main function was written by defining all input parameters ($\delta z,\ \theta_x,\ \theta_y,\ a,\ l,\ w,\ t,\ E,\ \alpha_1,\ \ \alpha_2, \alpha_3,\ \beta_1,\ \beta_2,\ \&\ \beta_3$). Each function in the main program is called in the right order shown in the dependance diagram, figure 4.2.

The first three input parameters ($\delta z,\ \theta_x\ \&\ \theta_y,\ $) represent displacements externally imposed upon three degree of freedom of the platform; they are respectively a translation along the z-axis and small angle rotations about the $x-$ and y-axes. Note that for a force transfer artefact expects δz to be the desire input, with the rotations being parasitic motions. However, in the case of a microprobe, $x-y-z$ motions at the probe tip correspond directly to these inputs at the platform, since the model is linear, the actual choice of value for these parameters is of little consequence, but here value representative of typical applications are always used. The remaining set of input parameters define geometries of the platform, beam and material constant parameters, which are necessary for the execution of all functions that compute the enhanced linear elastic model. The triskelion software is considered to be a good tool for predicting the stiffness of force artefacts and micro probe suspension artefact over short deflection range prior to their fabrication processes.

4.4.1 Triskelion software program verification

Before starting the numerical experiments, the consistency and robustness of the triskelion software program was tested using a simple input values at the platform that can compared to physical arguments about the patterns of behaviour. The five trials were

1. The fist consistency trial was carried out by using input parameters $\delta z = 1 \times 10^{-5}$ and θ_x & $\theta_y = 0$, and values of other parameters as given in table 4.2. The program was computed for triskelion force artefacts with 60° elbow angle. Subsequently, this experiment was repeated for all other triskelion force artefacts and input specifications given in table 4.2, The same value of stiffness k_z was computed by the program in all cases by forcing $\theta_x = \theta_y = 0$, the platform undergoes pure z-translations and each of its arm moves the same distance. Thus the end of each suspension beam is subject only to, in its body-fixed frame, z-shift and y-rotation and these are identical for each beam. If the beam geometries and material remain the same, so does the associated stiffness matrix, consequently the end-force and end-moment. Hence the value of k_z remains same for all triskelion force artefacts, having different elbow angles if the design parameters are unchanged.

2. The second trial was carried out by having $\theta_x = 1 \times 10^{-3}, \delta z$ & $\theta_y = 0$ by keeping the same input values as above and a 60° elbow angle. The program responds M_x as finite and positive and $F_z = 0$. Similarly, trial was repeated for all triskelion force artefacts and input specifications given in Table (4.2) and the same result was found i.e. positive M_x and $F_z = 0$. This follows the physical expectation that pure rotation of the platform about the x-axis should require purely as x-axis moment (other than possible parasitic effects not accessible to a linear elastic model). However, the moment is not necessarily independent of the elbow angle because the tilting platform can induce torsional effects in the beams.

3. The third numerical experiment was carried out by using $\theta_y = 1 \times 10^{-3}, \delta z$ & $\theta_x = 0$ while other being the same as trial 2. The program reports M_y as finite and positive, $M_x = 0$ and $F_z = 0$ in all cases tested. This meet the physical expectation that by symmetry, the simple torsional behaviour of the platform should be the same on any axis.

4. The fourth numerical experiment was carried out by using θ_x *or* $\theta_y = 1 \times 10^{-3}$ and $\delta z = 0$ for all triskelion force artefacts by keeping the same value of parameters given in table 4.2. The program computes $M_x = M_y$ and $F_z = 0$ for all triskelion force

artefacts, which have different elbow angles. This test confirms that no unintended cross-axis twist effects have been introduced into the program

5. The final trial was carried out by using $\delta z = 1 \times 10^{-5}$ & $\theta_x = 1^{-3}$ and $\theta_y = 0$ but was otherwise the same as trial 4. The program computed the same value of F_z for all triskelion force artefacts, but with different values of M_x and $M_x = 0$. The parameter θ_x generates rotation about the x-axis in the plane of platform and hence the program predicts the different values of M_x for all triskelion force artefacts with different elbow angles. this test confirms there is no unexpected cross-talk between translational and rotational inputs.

All the above testing experiments confirm the robustness of the triskelion software program

4.5 Stiffness of triskelion force artefacts

Before using the new software to explore the effects of different choices for design parameters, it is useful to draw some general intuitive conclusions about their effects. The model treats each suspension beam as a cantilever subjected at its free end to three displacements, being in its body-fix frame translation along z-axis and rotations about x-and y-axes. These displacements depend, of course on the motion of the triskelion platform. For certain artefact geometries and some single platform motion, it is fairly easy to visualize the beam and the defection and draw conclusion about the parameters sensitivity more from one dominating term in the local stiffness matrix for the beam. Mostly, though, the defections combine in ways not easy to compare so directly and it is then that computer model adds value.

The ideal triskelion suspension has three torsional stiffness about any axis in its xy-plane that passes through the centre of the platform. We can, then, gain some insight by considering only the 2D behaviour of a cross-section. In the case of a force transfer artefact, the platform motion would ideally be a pure z-translation. We can then expect that the suspension beams will be dominated by displacements, expressed in their body-frame, of δz finite and $\delta\theta_x = \delta\theta_y = 0$. For such conditions the present model can be reduced to a 2D rigid platform with a simple spring at each side, as shown in figure 4.3.

Even if there is a small amount of platform tilt, the some stiffness term is likely to dominate.

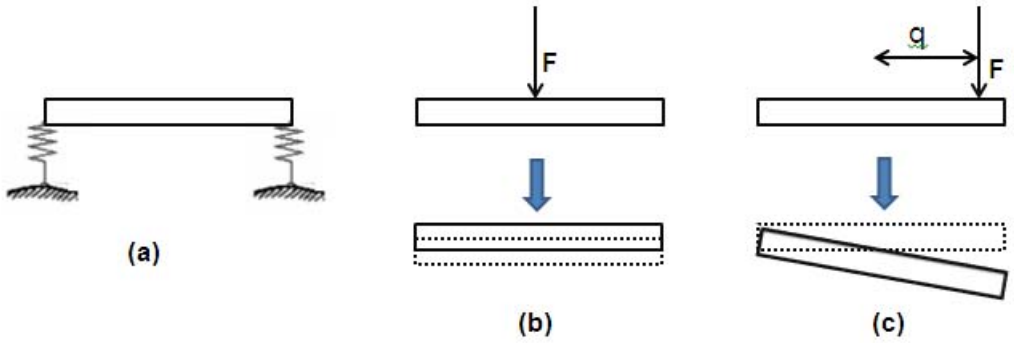

Figure 4.3: Simplified 2D model of platform and suspension, (a) concept, (b) effect of central load, (c) effect of offset load.

So both cases can be considered:

- Case-a, when a load is applied on the centre at the hub of the triskelion micro-probe.
- Case-b, when a load is applied at off set position at the hub of the triskelion micro-probe.

For note, however, that here is a potential ambiguity in the definition of "stiffness" for the force transfer artefact. Its operation stiffness is in the vertical axis, i.e.

$$k_z = \frac{F}{\delta_z} \tag{4.2}$$

but δ_z could rationally be defined as either the displacement at the centre of the hub or the displacement in the line of action of the force. Experimental evaluation with, say, micro-indenter tends to favour the later, but the model developed in this thesis use the former. the definition can diverge if the platform tilt is added to its z-translation. As seem in figure 4.3, the spring in this simplified model simply act in parallel for which we have in general

$$k_z = \sum_{i=1} k_{z_i} \tag{4.3}$$

where k_{z_i} is the stiffness of the i^{th} beam, which will here be close to the well known "shallow-S" deflection seen in simple ligament flexure mechanisms. We assume the beams identical and so far the simplified 2D model we have simply $k_z = 2k_{z_i}$.

4.5.1 Case-a: When a load is applied at the centre of the hub

When a load is applied at the centre of the hub (figure 4.3), the platform moves in pure translation, with, by symmetry, both springs taking half of the force and equal defections. expressing this more formally in term of forces and moments for static equisetum, we require

$$\sum_{i=1}^{3} (M_{xi} + F_{xi} \times r_{xi}) \quad = \quad 0 \tag{4.4}$$

$$\sum_{i=1}^{3} (M_{y=i} - F_{yi} \times r_{xi}) \quad = \quad 0 \tag{4.5}$$

$$\begin{aligned} F_z &= F_{z1} + F_{z2} + F_{z3} \\ &= \sum_{i=1}^{3} F_{zi} \end{aligned} \tag{4.6}$$

4.5.2 Case-b: When a load is applied at off set position at the hub

If a load is applied at off set position at the hub of the triskelion force artefact, then expression for the moment is given as

$$M \quad = \quad Fq \tag{4.7}$$

and where q is the magnitude of off set vector **q** of the line of action of the load from the centre, figure 4.3 (c). Because the platform acts as a rigid body, the vertical displacement at the line of the action of the force is found by and

$$\delta_c - \delta_o \quad = \quad q\theta \tag{4.8}$$

where δ_o is the vertical displacement at the centre-line and θ is the angle of platform tilt. Expressing the off-set force of a central force plus a moment, at static equisetum i.e. we have

$$\delta_o = \frac{F}{k_o}, \tag{4.9}$$

$$\theta = \frac{M}{\lambda} = \frac{Fq}{\lambda} \tag{4.10}$$

where k_o is the effective linear stiffness observed at the platform centre and λ is the torsional stiffness. These are functional specifications usually considered by the designer. Substituting equation into equation defines the displacement and effective stiffness along the line of force,

$$\delta_c = \frac{F}{k_c} = F\left(\frac{q^2}{\lambda} + \frac{1}{k_o}\right), \tag{4.11}$$

$$k_c = \frac{k_o\lambda}{q^2k_o + \lambda} \tag{4.12}$$

Physically, this simply indicates that translational effects of the two stiffness act in series (i.e. their compliances are additive). It also formalizes the intuition design that for a force artefact of specifical k_o torsional stiffness should be as practicable; it quantifies this deriver as dependent on q^2 (given a maximum allowed, or tolerated, offset).

The expression above can be compared to the results of the equilibrium force balance for the 2D platform in figure A, taking it to be of length $2a$ subject to end reaction forces F_A and F_b associated with support springs of stiffness $k_A = k_B = k$. Resolving vertically and taking moments about end A gives

$$F = F_A + F_B = (a + q)\,F \tag{4.13}$$

Hence,

$$\delta_A = \frac{1}{k}\left(\frac{a-q}{2a}\right)F, \tag{4.14}$$

$$\delta_B = \frac{1}{k}\left(\frac{a+q}{2a}\right)F \tag{4.15}$$

since the platform is rigid,

$$\delta_o = \frac{\delta_A + \delta_B}{2} = \frac{F}{2k}, \tag{4.16}$$

$$\theta = \frac{\delta_B + \delta_A}{2a} = \frac{qF}{2ka^2} \tag{4.17}$$

So, direct comparison to equation 4.9 & 4.10 shown that $k_o = 2k$ and $\lambda = 2ka^2$ and from equation 4.12, we have

$$k_c = 2k\left(\frac{a^2}{q^2+a^2}\right) = k_o\left(\frac{a^2}{q^2+a^2}\right) \tag{4.18}$$

A general interpretation of equation 4.12 is that measuring deflection solely in the line of action of the applied force cannot reveal the two stiffness uniquely if q is known. However, equation 4.18 shows that with this further assumption, which is not grossly unreasonable, a sensible estimate for k_o might be attained from a measured k_c.

For a force transfer artefact, we want k_c to be vary as little as passible from k_o because uncertainty in the stiffness reflects directly as uncertainty in the transfer calibration. For the small-scale systems that are the main concerns here, a might be only a few millimetres at most and it will probably be difficult to control q to better than around 0.5 mm in practice. Taking, for example, a as 2 mm and q as 0.5 mm, k_c deviates from k_o by about 6 %, but this rises rapidly as a reduces. Even allowing for the limitations of the modeling, there is clear motivation to design for relatively large a. Moving to 3D behaviour of triskelion, there is also motivation for seeking designs in which the interactions of different stiffness

terms (ignored here) lead to an increase in λ without (much)effect k_o. One open question is wether the choice of elbow angle has significant bearing on this aspect.

4.6 Numerical experiments for the triskelion force artefacts

Simply for convenience in the modelling process, the software program for the triskelion force artefact operates by imposing platform displacements and computing the forces and moments necessary to cause them; from this it relates the stiffness of the individual suspension elements to the over all stiffness of the device. The input parameter δz forces a translational motions along the z-axis and the other two parameters θ_x & θ_y cause rotational motion along the x-axis & y-axis respectively. The beam parameters length ℓ, width w, and thickness t, lead to controlling the stiffness k_z. If z-deflection of the suspension beams completely dominate the overall stiffness we have

$$k_z \quad \propto \quad \left(\frac{Ewt^3}{\ell^3}\right) \tag{4.19}$$

The torsional stiffness for a uniform rectangular cantilever is defined as

$$\lambda_x \quad = \quad \left(\frac{M_x}{\theta_x}\right) \simeq \left(\frac{KG}{\ell}\right) \tag{4.20}$$

where

$$K \quad \cong \quad \frac{w\,t^3}{3\ell}\left(1 - 0.63\left(\frac{t}{w}\right)\right) \tag{4.21}$$

and G is Poisson's ratio of the material used. or

$$\lambda_x \quad \propto \quad \frac{w\,t^3}{\ell}\left(1 - 0.63\left(\frac{t}{w}\right)\right) \tag{4.22}$$

If $t < w$ in equation (4.22). Indeed, given the broad approximations already invoked typical value of t and w in typical applications, it is not unreasonable to take the torsional stiffness as approximately to wt^3/ℓ. Both k_z and λ_x rise rapidly by increasing the value of t and ratio k_z/λ_x becomes maximum as $w \to t$. Increasing the length of beam reduces the stiffness k_z more rapidly than it does the torsional stiffness so radically increases k_z/λ_x. The new

research work is intended to explore the relative sizes, orientation of angles, etc. to seek better performance of the triskelion as force transfer artefact. For which we ideally want one degree of freedom (1-DOF). We will focus our attention on the parameters $a, \ell, w, \ \& \ t$ in the numerical experiments and observe how changes in these parameters can effect the computed values of spring constant k_z and λ_x. The extent to which results for different geometries match the predictions of the argument above, and simple beam theory, will provide same indication of which, if any, stiffness made dominates the triskelion behaviour. A five input specification of the triskelion software program polymer is given in table (4.2. The triskelion force artefacts with elbow angles $60\,^\circ, 90\,^\circ, 120\,^\circ, 150\,^\circ \,\&\, 180\,^\circ$ are shown in figure4.4.

4.6.1 Numerical experiments phase 1: Investigation of arm length a_ℓ

Five numerical experiments were carried out for all the triskelion force artefacts by using input specification given in table (4.2).

Relationship between a_ℓ and k_z

Five numerical experiments were carried out with displacement $z = 1 \times 10^{-6}$ m for input specification given in table (4.2) of the triskelion force artefacts with different elbow angles (table (4.1)). The only exception to these tabulated values was experimental independent variable, the arm length. It was set to 0.001m for the first test run and incremented by 0.001 m for the remaining numerical test run 2 to 5. The computed values of stiffness k_z at each elbow angle are shown in figure 4.5. All have same the value of stiffness k_z.

It is clear from this figure that the stiffness k_z of all triskelion force artefacts is independent of arm length for pure δz translational motion along z-axis effects the stiffness k_z. This is expected because arm-length interacts with platform tilt, not translation.

Relationship between a_ℓ and λ_x

Five numerical experiments were carried out with displacement only $\theta_x = 1 \times 10^{-3}$ for each input specification of triskelion force artefact given in table (4.2). These experiments have

both translational and rotational motion. The arm length was incremented by $0.001m$ for the remaining numerical run tests 2 to 5, as above.

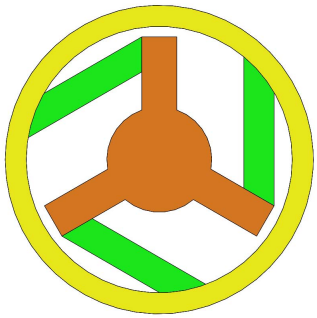

(a) TSFA-60

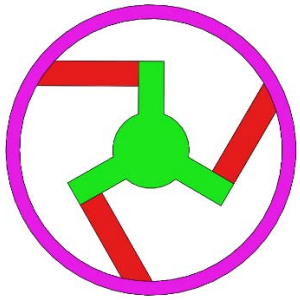

(b) TSFA-90

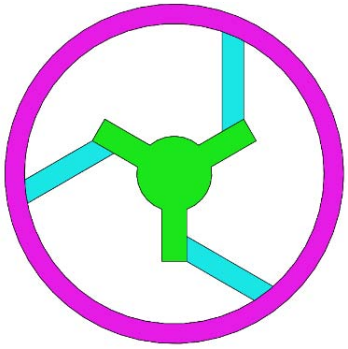

(c) TSFA-120

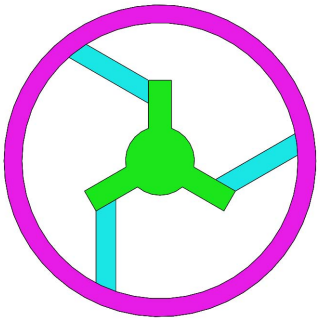

(d) TSFA-150

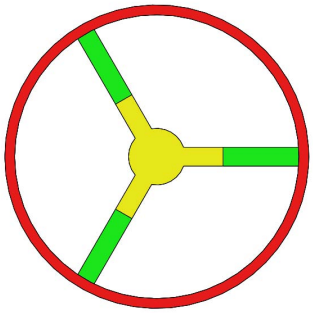

(e) TSFA-180

Figure 4.4: The triskelion force artefacts with elbow angles, (a) 60 °, (b) 90 °, (c) 120 °, (d) 150 ° and (e) 180 °.

Relationship between a_ℓ and λ_x

Five numerical experiments were carried out with displacement only $\theta_x = 1 \times 10^{-3}$ for each input specification of triskelion force artefact given in table (4.2). These experiments have

both translational and rotational motion. The arm length a_ℓ was incremented by $0.001m$ for the remaining numerical run tests 2 to 5, as above.

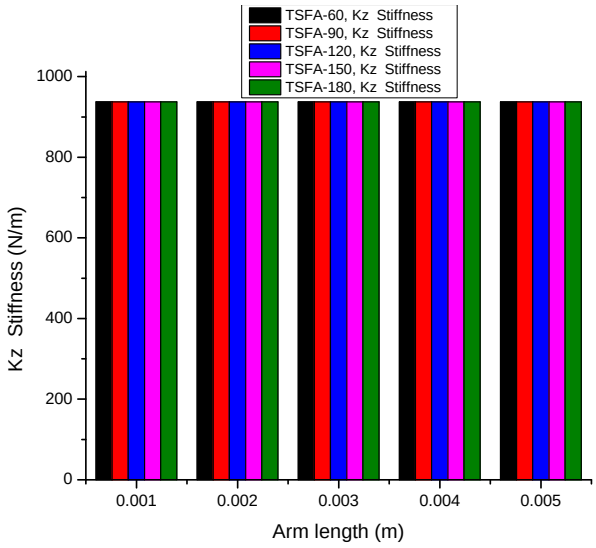

Figure 4.5: Graph for variable arm's length a_ℓ verses computed results for stiffness k_z of triskelion force artefacts with elbow angles $60\,^\circ, 90\,^\circ, 120\,^\circ, 150\,^\circ$ & $180\,^\circ$.

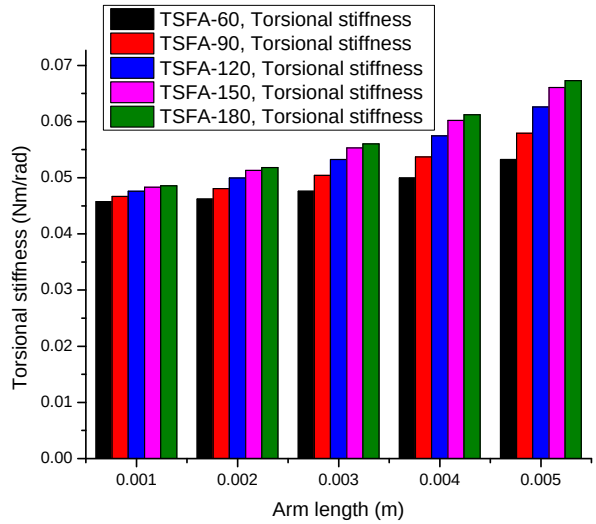

Figure 4.6: Graph for variable arm's length a_ℓ verses computed results for stiffness λ_z of triskelion force artefacts with elbow angles $60\,^\circ, 90\,^\circ, 120\,^\circ, 150\,^\circ$ & $180\,^\circ$.

The computed stiffness λ_x for all the triskelion force artefacts are shown in figure 4.6. It is clear from figure 4.6 that the torsional stiffness λ_x depends on beam length and the elbow angle of triskelion force artefacts. All the arm lengths, the triskelion force artefact

with elbow 60° has a lower value of torsional stiffness λ_x and the triskelion force artefacts with the elbow angle of 180° being highest value of λ_x. As we increase the length of the arm a_ℓ, the values of torsional stiffness λ_x also increases for all triskelion force artefacts and other effects are sumarised as follows:

- For a given tilt the vertical motion at the end of arms increases linearly with arm length (for small θ).
- Assuming, say, that vertical beam motion totally dominates the motion.
- Since the beam parameters are unchanged, the force at the end beam will also increase linearly with arm length a_ℓ.
- The the moment applied to the platform to generate these forces will depend on a. Hence, the torsional stiffness should increase with the square of the arm length a_ℓ.

4.6.2 Numerical experiments phase 2: Investigation of stiffness k_z and beam parameters

In phase 2, the relationship between the beam parameters $(\ell, w \,\&\, t)$ and stiffness k_z are investigated by carrying out experiments for each triskelion force artefacts with elbow angles $60^\circ, 90^\circ, 120^\circ, 150^\circ \,\&\, 180^\circ$ for the translational motion of the platform only.

Relationship between ℓ and k_z

The computed stiffness k_z for all triskelion force artefacts are shown in figure 4.7. All triskelion force artefacts have same value of stiffness k_z independent of the elbow angle if the beam parameters are unchanged. This is also expected of the linear model, because pure translation of the platform does not impose twists to the beam (see also section 4.6.1). The stiffness k_z also decreases for all triskelion force artefacts with the increase of beam length, closely following the inverse cube law of individual suspension beam subjected only to z-displacement.

Relationship between w and k_z

The computed stiffness k_z for all triskelion force artefacts is shown in figure 4.8. This stiffness k_z is independent on the elbow angle, as expected. It is clear from figure 4.8

that the value of stiffness k_z is increased by increasing the beam width, closely linearly as expected of an individual suspension under simple deflection.

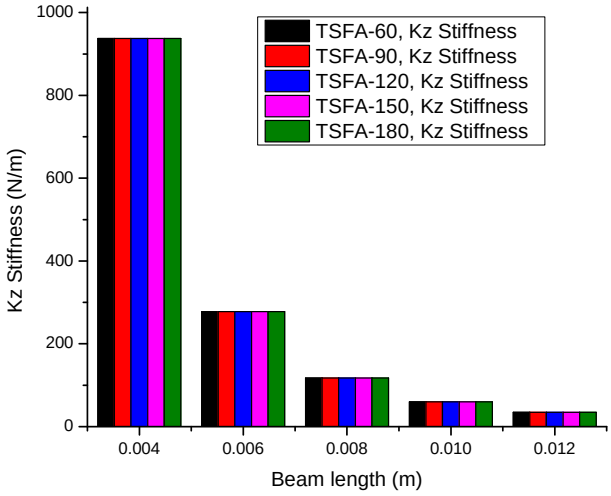

Figure 4.7: Graph for variable beam's length ℓ verses computed results for stiffness k_z of triskelion force artefacts with elbow angles $60\,°, 90\,°, 120\,°, 150\,°$ & $180\,°$.

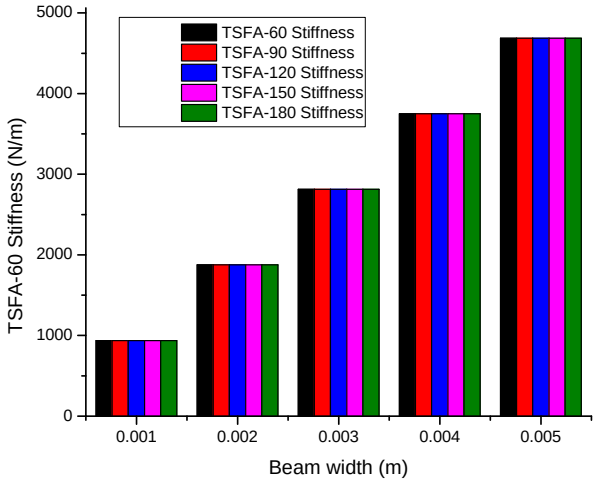

Figure 4.8: Graph for variable beam's width w verses computed results for stiffness k_z of triskelion force artefacts with elbow angles $60\,°, 90\,°, 120\,°, 150\,°$ & $180\,°$.

Relationship between t and k_z

The computed stiffness k_z for all triskelion force artefacts is shown in figure 4.9. All triskelion force artefacts have same and very low value stiffness k_z . It is clear from figure 4.9 that the value stiffness k_z also increases by increasing the value of beam thickness.

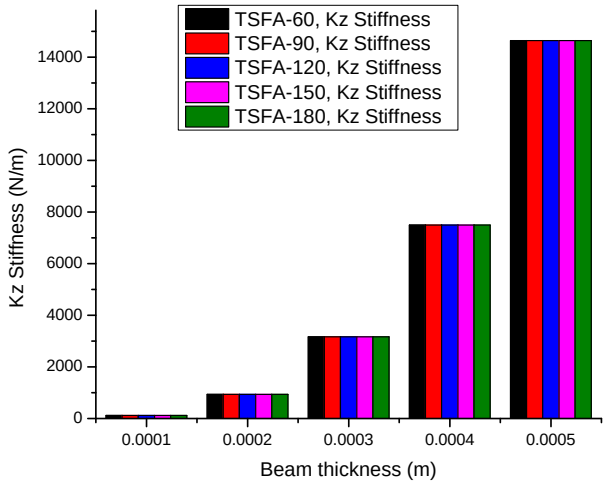

Figure 4.9: Graph for variable beam's thickness t verses computed results for stiffness k_z of triskelion force artefacts with elbow angles $60\,^\circ, 90\,^\circ, 120\,^\circ, 150\,^\circ \,\&\, 180\,^\circ$.

4.6.3 Numerical experiments phase 3: Investigation of torsional stiffness λ_x

In phase 3, the relationship between the beam parameters $(\ell, w \,\&\, t)$ and torsional stiffness λ_x are investigated by carrying out experiments for each triskelion force artefacts with elbow angles of $60\,^\circ, 90\,^\circ, 120\,^\circ, 150\,^\circ \,\&\, 180\,^\circ$ for both translational motion along z-axis and rotational motion x-axis of the platform.

Relationship between ℓ and λ_x

The computed torsional stiffness λ_x for all triskelion force artefacts are shown in figure 4.10. It is clear from figure 4.10 that the triskelion force artefact with elbow angle $60\,^\circ$ has a lower value of torsional stiffness λ_x and as we increase the elbow angle, the torsional stiffness λ_x also increases steadily but not linear. The value of torsional stiffness λ_z decreases if we

increase the beam length as expected. The sensitivity to the elbow angle is greater with shorter beams.

Relationship between w and λ_x

The computed torsional stiffness λ_x for all triskelion force artefacts is shown in figure 4.11. The torsional stiffness λ_x again varies slightly with elbow angles; it is consistently lowest for triskelion force artefacts with elbow angle $60\,^\circ$ and highest for those with elbow angle $180\,^\circ$. The torsional stiffness λ_x of all the triskeions also increases linearly with increasing the beam width as expected for both bending and torsion of suspension beams.

Relationship between t and λ_x

The computed stiffness λ_x for all triskelion force artefacts is shown in figure 4.12. The torsional stiffness λ_x increases rapidly by increasing the thickness of the beam and also increases sightly with the elbow angle of triskelion force artefacts. The relationship with thickness approaches the cube law expected for both bending and the torsion of an individual suspension beam.

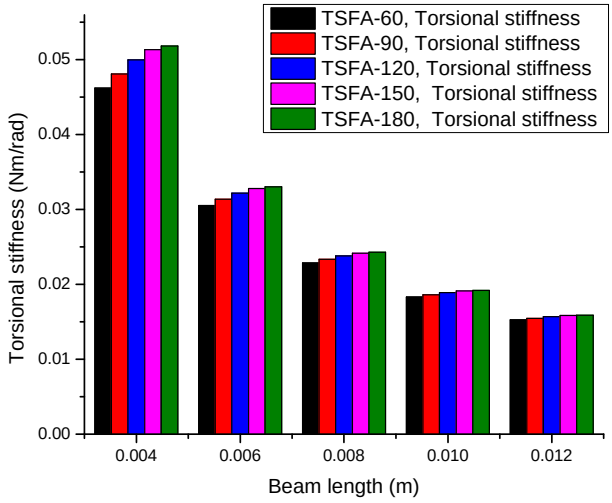

Figure 4.10: Graph for variable beam's length ℓ verses computed results for stiffness λ_z of triskelion force artefacts with elbow angles $60\,^\circ, 90\,^\circ, 120\,^\circ, 150\,^\circ$ & $180\,^\circ$.

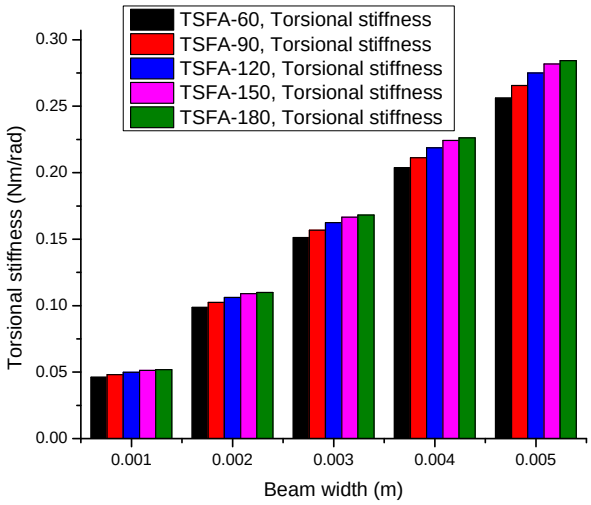

Figure 4.11: Graph for variable beam's width w verses computed results for stiffness λ_z of triskelion force artefacts with elbow angles $60\,^\circ, 90\,^\circ, 120\,^\circ, 150\,^\circ$ & $180\,^\circ$.

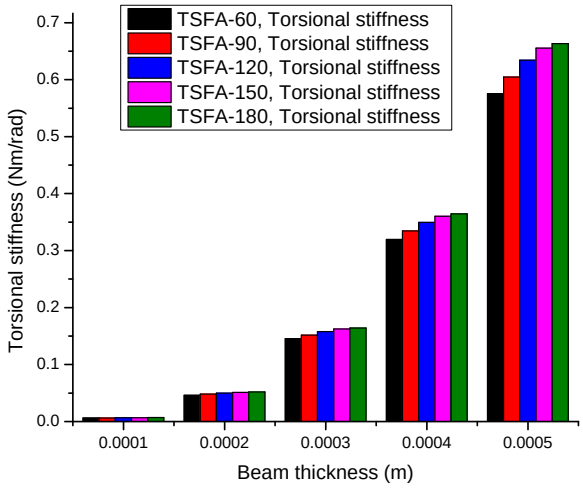

Figure 4.12: Graph for variable beam's thickness t verses computed results for stiffness λ_z of triskelion force artefacts with elbow angles $60\,^\circ, 90\,^\circ, 120\,^\circ, 150\,^\circ$ & $180\,^\circ$.

4.7 Discussion of computed results

The computed values of stiffness k_z and λ_x the input specifications given in the tables (4.1) and (4.2) for force artefacts with elbow angles $60\,^\circ, 90\,^\circ, 120\,^\circ, 150\,^\circ$ & $180\,^\circ$ are conveniently be summarised as follows:

1. As expected of a linear model, the computed values of stiffness k_z will not be affected by increasing the arm length a_ℓ of the platform or changing the elbow angle, for any triskelion force artefact with otherwise the same input specifications. The computed value of k_z is 937 N/m may be seen from figure 4.5.

2. The torsional stiffness λ_x (by symmetry representative of any tilt direction) increases gently with increase in the platform length, on top of a relatively large constant value figure 4.6. It also increases with a little elbow angle at all lengths tested. This value is more sensitive to the elbow angle at large arm lengths a_ℓ. The rate of increase with arm length a_ℓ follows closely a square law. A square law dependence on **a** would be expected if the behaviour from physical arguments was dominated by z-axial stiffness at the end of the arms. This compensations indicate that torsional effects in the suspension beams (which are expected to be largely independent of a_ℓ) dominate over translational ones for the geometries tested.

3. The computed values of stiffness k_z indicate that when increasing the length ℓ of the suspension beam, the stiffness decrease with a factor $(\ell + \triangle\ell)^3$ and is independent of the elbow angle, see in figure 4.7. The bending stiffness of an individual suspension beam will ideally vary as the inverse cube of its length, so seen this behaviour at the platform confirms that simple bending controls purely translational motions.

4. The computed stiffness λ_x also indicate that by increasing the length ℓ of the suspension beam, the λ_x values decrease by a factor $(\ell + \triangle\ell)$. This variation in the value of stiffness λ_x may be seen in figure 4.10.

5. The computed axial stiffness k_z increases linearly with the suspension beam width w, and is independent of the elbow angle for all triskelion force artefacts, as shown in figure 4.8. This is expected physically from the behaviour of individual suspension beams in simple bending.

6. The torsional stiffness λ_x also increases largely with the width of the suspension beam in all numerical testing experiments and is shown in figure 4.11 for all triskelion force artefacts. This is expected physically because both bending and torsional stiffness of the suspension beams depend (almost) lineally on this width. λ_x increases slightly with the elbow angle in all cases tested; this effect, the direct sharing between bending and torsional modes of the deflection.

7. The computed axial stiffness k_z indicates that by increasing the beam thickness t, the stiffness increases by a factor $(t + \triangle t)^3$, where $\triangle t$ is the increment in the beam thickness. As shown in 4.9, the axial stiffness is independent of the elbow angle. These results are consistent with physical behaviour in which only bending modes are present in the suspension beams; the linear model discounts possible cross-coupling of modes.

8. The computed torsional stiffness λ_x also increases with roughly by a factor $(t + \triangle t)$ as shown in figure 4.12. There is a small increase in stiffness with elbow angle in all cases. This near-cube relationship would be expected from both bending and torsion in the suspension beams, with sharing between those modes obviously varying with the elbow angles.

4.8 Conclusion

A new more flexible and a robust software program for modelling triskelion force artefacts has been presented in this chapter. It provides a critical new tool for predicting force, moments, stresses, strains, stiffness k_z and torsional stiffness for triskelion force artefacts and micro probes. Even with the simplest designs it can become difficult for designers to understand in detail how changes in geometry affect performance (e.g. the combined effects of bending and torsion at different elbow angles).

The results of all numerical experiments are in agreement with the beam theory and are precisely stated as follows:

- $k_z,\ \lambda_x \ \propto \ wt^3$
- $k_z \ \propto \ 1/\ell^3$

- $\lambda_x \propto 1/\ell^2$

Comparing these relationships to those for bending and torsion in the single beam, it appears that bending modes in the suspension beams dominate quite strongly the torsional one for the range of geometries considered. This makes it rather easier for the designer to make intuitions about the effects of changing the geometry. These results will be compared to 'linear' and 'non-linear' of a range of physical (polymeric) triskelion in later chapter 6, 7 and 8.

The new program uses an enhanced linear elastic model to investigate arbitrary dimensions, arm positions for investigation of elbow angles of triskelion force artefacts based on the stabilities and the stiffness of the platform.

Numerical experiments have been performed on a range of triskelion designs (all with three-fold symmetry about the z-axis) covering plat form arm length between 1 mm and 5 mm; suspension beam lengths 4 mm and 12 mm; width between 1 mm to 5 mm and thickness between 0.1 mm and 0.5 mm; elbow angles between 60 ° and 180 °. There appears to be no previous study of elbow angle in the public domain.

The restriction of the enhanced linear elastic model mean that it transfer pure z-translation of the platform only to the bending of the suspension beams (in the own xz-planes. Thus there is no dependence on the elbow angle or platform axes length for the z-translation stiffness. The model reports, as expected, behaviour on other dimensional parameters consistent with that of the individual beams. Because only axially-symmetric designs been studied, and it confirmed that the program reports the same stiffness in all direction of the platform tilt, only torsional stiffness about x-axis, λ_x is considered in detail. Consistently across all design, there is tendency for torsional stiffness to increase slightly with elbow angle. This effect is, perhaps, not strong enough to be a major design consideration, at least at very small platform measurements for which the linear model might be assured adequate. However, it suggests that a 60 ° elbow, a compact but easily constructed design, is quite appropriate for micro-probe, where modest torsional stiffness is required.

there might be a case for using a large elbow angle for force transfer artefacts, where high torsional stiffness is desirable. The concluded remarks are stated as

- Firstly, the great benefits to the future research and industrial user.
- Secondly, the other things that will show differently in the physical (non-linearity) test in later chapter 6, 7 and 8.

The validation of the triskelion program will be performed later on in chapter 9.

Chapter 5

Triskelion polymeric artefacts: specification and design

5.1 Introduction

This chapter considers methods for the fabrication of samples of triskelion force artefacts suitable for investigating stiffness behaviour. The linear elastic models of triskelions presented in chapter 3 requires small batches of varied design for validation experiments. The use of polymers artefacts increases the commercial capability to exploit polymers in a mass production scale for micro triskelion force artefacts.

An alternative low-cost approach has been explored for the first time for fabricating the polymeric triskelion force artefacts. It may be seen that published technologies and methods are economically unattractive for this purpose. It is proposed, originally, that polymeric artefacts may offer a good solution here and also have a wider application.

While a purely linear system can be studied at any convenient scale. The anticipated non-linearities here required that test run samples at least broadly representative of sensible practical triskelion force artefacts. The triskelion force transfer artefacts will probably most usefully apply to small instruments (such as micro-indenters) and in ranges where dimensional load cells are not readily available. These typical dimensional scales should be from a few millimeters downwards and force might range from just a few sub-newtons. Following

the general principle that handling smaller samples and higher sensitives measurements is more expensive (in all the senses mentioned above), the first study has been et at the top of these ranges. An experimental scheme using a special test-rig based on previously proven concept could then be used; it is descried in the chapter 6. This leaves the question of making small numbers of different triskelion designs for the test samples.

5.2 Development of triskelion force artefacts

Given the essential need to validate the models and to explore how and what point inevitable non-linearities become significant, what are the best practical compromises for a measurement scheme taking account of cost, reliability, etc?

With the measurement scheme chosen, how might a suitable range of representative samples be produced. The secondary part of the question is whether (or to what extent) can reflect a current or potential route of applications for the triskelion force artefacts. It feels preferable, but is by no means essential. This methods has plausibly wider use in future.

5.2.1 Challenges with sample design

1. The desired test program requires a small number samples for several designs, varying in just design parameters. Published triskelion suspension for micro-probes are produced in metal or silicon.

2. Industrial groups involve either MEMS technology (smaller devices or assembly of components (lager devices).

3. Samples required here are sizes intermediate between these groups, being quite large for MEMS but rather small for convent reliable assembly.

4. MEMS approaches give good repeatability but setup costs are very high and so they do not suit current needs.

5. Assembly has high unit cost generally and will require jigs or other tooling for each variant design.

6. Plausibly, metallic samples could be machined from solid, at moderate cost using CNC machines, but the scale is a little small and thin sections will be vulnerable during producing (any subsequent assembly).

7. Hence, a new question is posed here for first times: is it realistic to use polymers to make triskelion or similar force artefacts and suspensions?

5.2.2 Brief description manufacturing techniques

Three manufacturing techniques, such as injection moulding, Stereolithography (SL) and microstereolithography (MSL), and LIGA are briefly discussed in this section.

Injection moulding

The classic plastics technologies are capable of high throughput and precise production. The injection moulding technique has high setup cost but very low unit cost. This technique is not suitable for current needs, but fully justifies the possibility of a low-cost, disposable device.

Stereolithography and microstereolithography

SL and MSL techniques are not cheap at present (wasteful of resins) but are certainly able to produce one-offs direction from computer aided development (CAD). Commercially available technology is perhaps a marginal resolution for current needs. Promises are seen for small-batch bespoke designs for furore applications.

LIGA

LIGA technique is essentially ways of making precise small mould or pressing, rather than direct fabrication route for present needs.

Hence manufacturing is not an impediment (actually an attraction) to polymer triskelion and further study of them is justified. But none of these processes readily meets the needs for the samples here and a special method is preferred.

5.2.3 Polymeric triskelion force artefacts: Pros and cons

1. The obvious concern is that polymers are rarely used for precision engineering devices. They have relatively high thermal expansion coefficients and relatively poor long term material stability, so they seem poor suited to precision structures.

2. However, triskelion force artefacts here are flexures, not structures and the case is less clear-cut.

3. Long-term stability is not critical for the present research work and might not matter so much in some applications, e.g., for low-cost "use once" checking pieces (samples).

4. The use of polymers first time open new route to manufacture.

5. The low Young's modulus leads to physically more robust more triskelion force artefacts for given stiffness; in particular, ligament thickness can be larger and more easily controlled.

6. Hence, there are sufficient positive arguments to make the part of this thesis an investigation of triskelion force artefacts.

5.3 Basic requirements for triskelion force artefact's samples for testing experiments

Two linear elastic models for triskelion force artefacts have been introduced in chapter 3, corresponding to classic design and angle-beam design. these models extend previous research work by allowing all geometries design parameters to be varied independently, so for example allowing investigation of the effects of the elbow angle on the force artefact stiffness. The practical validation of these models requires the production of triskelion force artefacts in a variety of different geometric configurations; only a small no of each design are needed, with low unit cost and rapid access to new designs being of some importance.

The test triskelion force artefacts should broadly representative of plausible practical applications, but it is convenient to make them relatively large for robustness and ease of handling during tests. Considering the type of the instruments likely to require force

calibration and for which commercial load-cells do not offer an immediate solution, the following specifications is proposed. Overall dimensions might be up to about 10 mm, force might be up to large fraction of a newton and correspond deflections up to several hundred micrometers. This is a factor of 10-100 times larger than the triskelion devices likely to be used with the NPL Low Force Balance. Working at this scale has added advantage of allowing the tests to be based on modification of well-proven technique, described in chapter 6.

All the triskelion test samples should have the same over all design scheme. Triskelion force artefacts are near-planar with a central axis of symmetry (usually regards as z-axis) normal to their nominal plane. A central hub is regarded as rigid, which is adequately ensured by making it of commercially greater depth than the flexible suspension beams. The hub might conveniently rigid arm (of the same depth as the hub) to facilitate connection to the suspension beams. The other end of the beams are connected to a deep ('rigid') outer framework that forms the reference mount for the triskelion force artefact; it can easily be shape but commonly shown as a circularly ring. this description constitute a classic design. The only essential change for an angle-beam triskelion force artefact is that the arm takes the same depth as beam rather than that of hub. For the present needs, the hub can be 2-3 mm diameter, while the suspension beams will be several millimeters long, with other dimensions set accordingly to provide overall stiffness in the z-axis of the order of 1 kN/m.

The published work on triskelion system for either micro-probe suspension or force transfer artefacts has concentrated either on quite large metallic versions assembled from individual components or on small metal or silicon triskelion devices (triskelion force artefacts or triskelion micro-probe suspension) manufactured by typical MEMS fabrication methods. none of these is obviously attractive for present needs, so a basic review of established methods, a relevant materials, for producing millimetre scale components is given.

5.4 Potential fabrication approaches for 1-10 mm triskelion force artefacts

Before proceeding further, there is need to examine briefly the range of approaches available for making triskelion force artefacts (or other suspensions in variety of materials. Routes to manufacture are important factors in the feasibility of different designs and so in the choices selected for detailed study in this work. There are three major classes for fabrication that are categorised as follows:

1. Microelectromechanical systems (MEMS) fabrication using methods devices from silicon processing technologies.
2. Stereolithography (SL) and Microstereolithography (MSL).
3. Injection moulding and Die casting .

5.4.1 MEMS fabrication: silicon micromachining

At the beginning of 1990s MEMS emerged by integrating mechanical elements, actuators, sensors, and electronics onto a single electronic chip [199]. MEMS technology has been identified as one of the most promising technologies for the 21^{ist} first century. It has great potential to revolutionise both industrial and customer products with micro-machining technology looking directly to silicon based micro-electronics [200].

MEMS technology introduces new concepts to the system design, fabrication processes, materials selection, generated functionality and production methodologies. Functional devices may be fabricated within a small compact space. MEMS fabrication is a manufacturing technology for developing complex mechanical devices and systems using batch fabrication techniques. It uses the same techniques that are used for standard microelectronic technologies, including wafer fabrication, monolithic processing and signal interconnecting packages [201]. It is dominated at present by the methods of silicon micromachining. These approaches involve very high set up costs and are suited to large production runs or very high value-add components. They have been applied to microprobe suspension but are not appropriate for the present research work.

Silicon micromachining refers to using silicon substrate to allow the fabrication of MEMS in the millimetre to micrometre range. Two technologies bulk and surface micromachining are major classes of processing. Both are essential planar (or $2\frac{1}{2}$) methods based on controlled sequence of masking and etching operations (usually called "photolithography"). In bulk micromachining, the device is built into the substrate (e.g. a single system silicon), whereas surface micromachining uses the depositing and pattering of thin films to produce potentially complex microstructures on the surface of the silicon wafer.

The LIGA process draw on the same idea from micromachining to address the needs for high aspect-ratio devices. It is developed to produce the molds for the fabrication of micromachined components that are thick and three dimensional [199]. LIGA is a German acronym for Lithographie, Galvanoformung, Abformung (lithography, galvanoforming and moulding). It was developed in the early 1980s at the Karlsruhe Research Centre (Forschungszentrum Karlsruhe), and is based on X-ray technique. Detail of LIGA process and its applications are given in [202].

LIGA uses lithography, electroplating, casting and moulding processes that are capable of producing microstructure in the range of 1 mm high. One disadvantage of the LIGA process is that structures fabricated by LIGA are not fully three dimensional (3D). Thus, to build 3D MEMS devices, another approach was developed: AMANDA (acronym for abforming, oberflachenmkromechanik und membranubertragung or surface micromachining, moulding, and diaphragm transfer. AMANDA processes are powerful for polymer MEMS fabrication [199], [203]. These methods are prohibitively expensive for producing test devices here, but are relevant in demonstrating a potential route to manufacturing very small polymeric triskelion suspensions.

5.4.2 Stereolithography (SL) and Microstereolithography (MSL)

Rapid prototyping (RP) was originally conceived as a way of checking whether the designs of complex 3D parts were fully geometrically compatible with an assembled system prior to the manufacture of moulds or other expensive and time consuming procedures. RP exists in many forms, typically called solid free-form [199]. These models are non-functional, being

made from easy-to-manipulate materials (after of flow strength and stiffness). Technologies inspired by RP are now becoming of interest for specialist small-batch production for cases where these materials are functionally adequate.

Additive manufacturing (AM) technology is a group of process for rapid production of models to provide necessary support for the adoption of simultaneous or concurrent engineering. Conventional processes are called R formative methods, e.g. casting, injection moulding, compressive moulding [204]. Thus, AM technology has reduced the cycle of new products. AM processes mostly use some form of localised energy to modify material locally, using vector-base or imaging technologies. Most stereolithography (SL) systems and their micro-versions work through an additive layers process, where each layer or conventional is cured into a photosensitive resin by light source (UV laser used to trigger a chain reaction in the monomer) in a process that is called photo-polymerisation [205].

Microstereolithography (MSL) is derived from conventional lithography and was introduced in 1993 to fabricate high-aspect ratio and complex structure [199]. MSL is also called photoforming [206], [207]. Nakajima and Takagin were the first to work on micro 3D structure using vector by vector (scanning method) in 1993 called microstereolithography (MSL) or micro-photoforming. They achieve a three dimensional structure with a resolution 0.8 μm [207]. Later on Ikuta and Hirowatari claimed that their apparatus was able to achieve up to 0.25μm in XY and 1μm in z-direction [206].

MSL is an additive process, which allows to fabricate high-aspect ratio microstructure. The MSL process μML is also compatible with silicon process and allow batch fabrication [208]. The various different MSL systems have been developed. Two basic approaches, scanning MSL [206], [207], [209], [210], [211] and projection [212], [213], [214] have been developed. In the scanning method, a well focussed laser beam, spot size ($\sim$ 1 micron) is directed on to the resin surface to initiate plolymerisation and by repeating layer preparation, a 3D microstructure is formed and the scanning method is called MSL method [199]. Scanning MSL is used to build solid micro-parts point by point and line by line fashion. Projection MSL is used to build a full layer with one exposure, thus saving a significantly

amount of time. Functional polymer parts have high flexibility and low density [206]. μML has been used for exploring the electroplating of micro parts [206], [208], [212]. Microceramic structures have also been fabricated by MSL for both structural ceramic and function ceramic [209], [210], [211], [213], [214], [215].

A large number of MSL methods have been developed, such as IH series processes (integrated harden polymer sterolithography) Mass IH process, two photon MSL, projection MSL and integrated MSL [208], [210], [212] [216]. MSL technology is very attractive for developing 3D MEMS, where it had been not possible by silicon. One of the great disadvantage of MSL is slow fabrication speed that prevents it from producing large batches economically. A method such as that of Ikuta in 1996 increased the speed of fabrication through the use of an array of optical fibers. The projection method developed by Sun et al. in 2005 also reduced the fabrication time. It forms the part by layer by layer exposure through a pattern mask instead of laser scanning. The most widely used materials for MSL are acrylate, epoxy and vinyl ether. There is no doubt that with the advancement of its technology, MSL is becoming more readily applicable, but it still has limitations in speed for fabrication of batches and that it require high cost in ultra-precision applications. Most developed MSL systems are suitable for prototyping rather for batch production.

Microsterolithography is a feasible appearance for making triskelion suspensions. It could provide small batches or one-off prototype test-pieces at acceptable, but not negligible cost. However, it is doubtful whether the currently available system has resolution needed for very small artefacts; the cost of experimental high-resolution system remain prohibitive.

5.4.3 Injection moulding and Die-casting

The third popular class used by industries is discussed in this section.

Injection moulding

The injection moulding process is one of the most common methods used for mass production of polymer plastic parts. An essential injection moulding machine melts feedstock the plastic and then injects it under pressure into the mold, where it cools down and solidifies

into final shape of required part [217]. With reusable hard metal moulds the process is extremely useful and used to manufacture a great variety of simple to three dimensional parts. Thus this technique is highly capable of processing the different type of polymers, resins, reinforced plastics and elastomers. The injection moulding technique is used for a large proportion of all plastic products that used daily in our houses [218]. John Wesley Hyatt was first to inject hot celluloid into mold, thus producing billiard balls in 1968. Later on, he and his brother patented an injection moulding machine that uses a plunger in 1972. James Henry built the fist screw injection moulding, brought a revolution in the plastic industry. All moulding machines (95%) use screws efficiently to heat, mix and plastic into mold [219], [220].

Precision injunction moulding is an advanced subclass of the conventional process with new distinct set of design, process-ability and optimisation criteria and further detail may be seen in [221]. Conventional injection moulding is not capable of producing optical parts with high accuracy. However, recent advancements have made it possible to produce optical parts with high accuracy, based on three or four combinations of photolithography, etching, electrodeposition and thermal or mechanical process for material removal [222].

Ultra-high precision, injection moulding achieves high precision and a minimisation of process variation during injection moulding. The process variation can be caused by any external variable, such as plastic material's consistency, moulding machine accuracy and thermodynamic controls of moulds. All these variables are impacted by the environmental characteristics of mould plant, and are mitigated by new technology [223].

Die casting

Die casting is a process that has been used for several decades. Metal parts are produced by a casting process in which reusable, hard moulds or dies are injected with the molten metal under a pressure. Products of many various types sizes and applications are made by die casting processes. It is able to produce highly detailed and accurate parts and is suitable for the mass production of products. The die casting process is further divided into categories [220], [223].

- Hot chamber die casting.
- Cold chamber die casting.

In hot chamber die casting, the injection system is immersed in a pool of molten metal and there is also less time exposure of melt to the plunger wall, whereas cold chamber die casting uses a ladle to transport the molten metal from a holding furnace into the injection cylinder. As the plunger moves in the inlet part of cylinder, it allows a new change of molten metal to fill the cavity. This method is used for metals of low melting points and high fluidity such as zinc and tin. The die casting process started in the mid 1980s. In the beginning lead and tin alloys were used for die casting process but after 1920s these alloys were mostly replaced by aluminium and zinc.

The great advantage of the die casting technique is that there is no special restriction on the type of alloys or metals for the die casting process. It is possible to produce variety of products with different shape and sizes. Another advantage of die casting is reducing the production time because commonly no subsequent processes are required. Nowadays aluminium is one of the most commonly used alloys for die casting process. One main reason for using aluminium die casting is that it is light weight and has dimensional stability for thin wall applications and complex shapes.

Die-casting could conceivably make metallic triskelion suspensions at a scale of millimetre upwards, but still not attractive for this propose.

5.5 The use of triskelion force artefacts

Section 5.3 has highlighted that polymers are attractive from a material processing point of view for making triskelion force artefacts such as millimetre-scale triskelions. However, polymers are not commonly used for precision applications, mainly from concern about their stability. They have large coefficients of thermal expansion and can absorb moisture to give some dimensional dependence on humidity. They have much lower stiffness than metals or ceramics, which can effect the working stability of petrological reference loops, and son. It is proposed here that these concerns may not be at all severe in many potential

applications of triskelions. For example, the suspension in a contact micro-probe needs to have quite well defined stiffness, but it will not affect practical applications if it varies a little from day to day. The suspension must be very stable if its internal strains are used directly as the gauging principle, but it much less critical in other designs. It would be desirable that a force artefact used in a major calibration laboratory maintained highly repeatable characteristic, but strictly it is sufficient that its stiffness remain unchanged only over the time to calibrate it on the force balance then move it to the target instruments. This is not so demanding. if, as is likely, the process is carried out in a laboratory with close environmental control. For general compliance checking in industrial situations, access to simple artefacts of modest provenance many will be adequate and preferred.

It is, therefore advocated here for first time that polymeric devices are very plausible both for current needed test samples and for more general applications. There is, of course, a need to demonstrate feasibility and this becomes one of threads of this work. Once it is accepted then polymeric triskelions are worthy of investigation several potential advantages become apparent:

- Injection moulding allows the possibility of making large number of al most idealized devices at very low unit cost. This opens up possibility of single-use, disposable checking pieces, or at least once where the cost of replacement after accidental damage is low. Commercially it would encourage best practice in using regular instruments verification (if not full calibration).

- Batches of various size, e.g. for suspensions, could be produced by the most economic of several methods. Over a wide range sizes the unit cost is likely to be lower than that from, say, commercial MEMS fabrication.

- Using techniques such as MSL, bespoke, one-off special devices becomes economical and would be supplied by a suitably set up service organization.

- The low Young's modulus of polymers means that for a given nominal stiffness and overall devices size, the (usually quite delicate) suspension beams will be considerably cheaper than in other classes of material. Hence, we can expect polymeric devices to be more robust.

- The overall elastic properties of polymers suggest that triskelion devices will have quite large operational ranges in comparison to overall sizes.

5.6 Low-cost production of polymer triskelion test specimens

Based on the proceeding arguments, polymers will be used for all experimental studies in this thesis. As well as the immediate convenience, this allows initial demonstrations of the performance such system can offer. However, all methods discussed for making them have disadvantages. MSL can deliver modified design with a rapid turn-around and at the significant excessive cost. However, there are doubts about the quality of part-to-part repeatability at the scale reading to be used here (at least for the systems accessible to this project). Consequently, even more basic casting method has been devised and investigated.

It is quite simple to generate a CNC (computer numerical code) program describing the shape of a typical triskelion at the scale required for the specimens. Following this, it is easy to modify the code to reflect small changes to the design for further specimens. However, although feasible, it is not attractive to use a CNC milling machine to cut the devices from, say, acrilic sheet. The unsupported beams are still thin enough to be very vulnerable to fracture during machining. At the same time, milling negative versions into flat surface of the aluminium block to create simple mould is a very reliable and fast process.

Casting resins is intended to take replicas of the surface texture for subsequent measurement have been commercially available for several decades. Clearly, they have an excellent ability to occupy and reproduce surface features with high precision and they release easily from metal surfaces. An almost instant production might therefore be obtained simply by pouring prepared resin into mould, filling it by gravity, then smoothing off of top surface (e.g., by sliding a glass microscope slide across it) and allowing it to self-cure. Such a process could not be expected to be satisfactory with complex, fully 3D objects, but seems well suited to near-planar form of triskelion flexure. A few preliminary traits with very simple moulds showed the techniques to simple execute and effective enough to test fully as a way of making the triskelion specimens. Typical moulds with elbow angle 60° and 1200° are illustrated in figures 5.1 and 5.2.

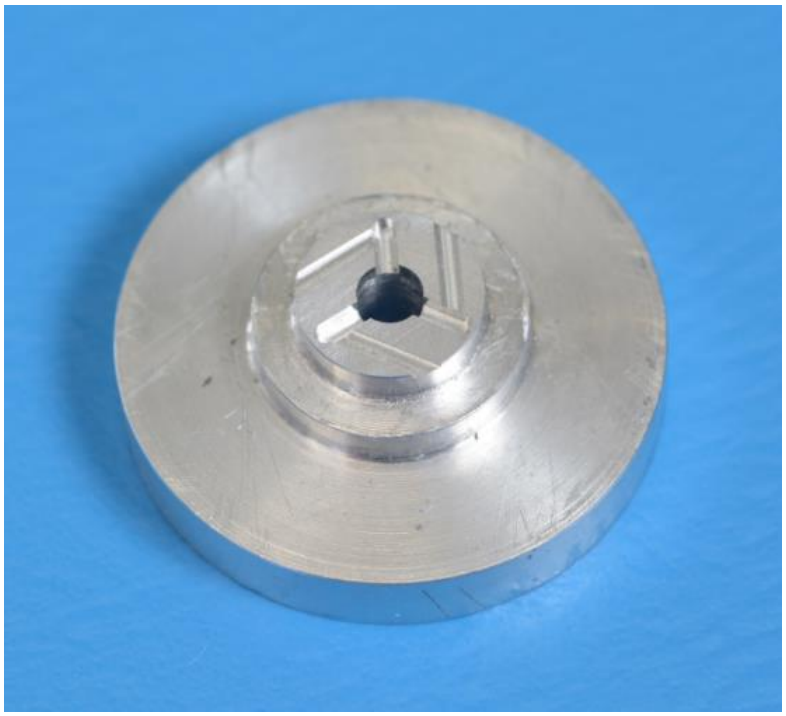

Figure 5.1: The triskelion mould with elbow angle 60 °.

Figure 5.2: The triskelion mould with elbow angle 120 °.

5.7 Triskelion force artefacts

Triskelion artefact's type, specification for their samples and fabrication, batches charaterisation and uncertainty expression for stiffness of triskelion force artefact's samples are disused in this section.

5.7.1 Type of triskelion artefacts

The two types of triskelion analytical models have been described in chapter 3, the triskelion analytical linear model and triskelion angled-beam model. The first type of artefacts that follows triskelion analytical linear model and the second type of artefacts follow triskelion angled-beam model.

Classic triskelion force artefacts

The first type of polymer artefacts have a circular hub and arm that make a rigid platform, which is thicker as compared to the beam thickness. This type of artefact is called classic triskelion artefact. The triskelion artefact has three arms disposed symmetrically, but equivalent systems with more arms are possible e.g we will consider four arms, tetraskelion artefacts in chapter 8. The arms free ends are jointed with beams that are mounted on a rigid base. The prepared samples of classic triskelion force artefacts are shown in figures 5.3, 5.4, 5.5 and 5.7.

Angle-beam triskelion force artefacts

The second type of artefacts have thicker hubs. Both arms and beams have the same thickness. Each arm and beam is considered to be one part called angled beam. Therefore, this type of polymer artefact is know as angled-beam triskelion artefact. Three angled-beams are mounted to a rigid hub symmetrically, and they are fixed to a rigid base. The prepared samples of classic triskelion force artefacts are shown in figures 5.6, 5.8 and 5.9.

5.7.2 Specification for artefact samples: classic and angle-beam triskelion

It is clear that there are good means for manufacturing in larger number very low-cost (even disposable) triskelion suspensions polymeric materials. However, injection moulding cannot really address the relatively small production runs more typical of their current

applications unless a quite high premium can be charged for each item.

Four batches of the first type of artefacts (classic triskelion) and three batches for second type (angle-beam triskelion) of artefacts are designed. The built in angles for both type of artefacts are the same, i.e. $60\,^{\circ}$, $90\,^{\circ}$ and $120\,^{\circ}$. Both types of artefact have the same dimensions for their hub, arm, beam length and width, but differ in thicknesses of these features. Each bach of artefacts is comprises of two samples. The detailed specification of each batch of artefact is given in Tables 5.1, 5.2.

Table 5.1: Specification for classic triskelion force artefacts with $60\,^{\circ}, 90\,^{\circ}$, & $120\,^{\circ}$ elbow angle.

SNo.	Parameter of TSKFA	Batch 1	Batch 2	Batch 3	Batch 4
1	$elbow's\ angle\ e_b$	$60\,^{\circ}$	$90\,^{\circ}$	$120\,^{\circ}$	$60\,^{\circ}$
2	$hub's\ radius\ r_h$	1.5 mm	1.5 mm	1.5 mm	1.5 mm
3	$hub's\ thickness\ t_h$	1.0 mm	1.0 mm	1.0 mm	1.0 mm
4	$arm's\ length\ \ell_a$	2.0 mm	2.0 mm	2.0 mm	2.0 mm
5	$arm's\ width\ w_a$	1.0 mm	1.0 mm	1.0 mm	1.0 mm
6	$arm's\ thickness\ t_a$	1.0 mm	1.0 mm	1.0 mm	1.0 mm
7	$beam's\ length\ \ell_b$	4.0 mm	4.0 mm	4.0 mm	4.0 mm
8	$beam's\ width\ w_b$	1.0 mm	1.0 mm	1.0 mm	1.0 mm
9	$beam's\ thickness\ t_b$	0.2 mm	0.2 mm	0.2 mm	0.2 mm

Fabrication of triskelion artefact's samples

For ease of handling, etc. it is convenient to run linearity and validation tests using triskelion force artefacts a little larger than that those used in a typical micro-probe. Increased size also eases the demands on sample fabrication. The effect is that the artefacts

Table 5.2: Specification for angle-beam triskelion force artefacts with $60\,^{\circ}, 90\,^{\circ}$, & $120\,^{\circ}$ elbow angle.

SNo.	Parameter of TSKFA	Batch 1	Batch 2	Batch 3
1	$elbow's\ angle\ e_b$	$60\,^{\circ}$	$90\,^{\circ}$	$120\,^{\circ}$
2	$hub's\ radius\ r_h$	1.5 mm	1.5 mm	1.5 mm
3	$hub's\ thickness\ t_h$	0.2 mm	0.2 mm	0.2 mm
4	$arm's\ length\ \ell_a$	2.0 mm	2.0 mm	2.0 mm
5	$arm's\ width\ w_a$	1.0 mm	1.0 mm	1.0 mm
6	$arm's\ thickness\ t_a$	0.1 mm	0.1 mm	0.1 mm
7	$beam's\ length\ \ell_b$	4.0 mm	4.0 mm	4.0 mm
8	$beam's\ width\ w_b$	1.0 mm	1.0 mm	1.0 mm
9	$beam's\ thickness\ t_b$	0.2 mm	0.2 mm	0.2 mm

to be used here will cover a range more typically 100 mN and 1 mN likely to be used with the low force balance for use with low force balance. This scaling does not affect the basic purpose of validation methods. Polymer resins (acrylics & epoxies) are commonly available for surface feature replication purposes and they clearly have the ability to adopt the features of triskelion artefacts of this scale at room temperature and without pressure. Thus, following some initial trials a method based on using them in open molds has been adopted.

Acrulite liquid and powder are poured into the mixing vessel or a porcelain bowl (2:1 ratio) and stirred continuously at it dissolves. The surface of the mould should be free from oil, grease and should be dry. If some intricate surfaces exist then it may help to remove the cured acrulite if the sample is sprayed with a silicone-based mould release agent. This works by filling up small cracks and pores on the surface into which the acrulite might otherwise key itself, which would make removal difficult. The mixture of acrulite is poured carefully into the mould. If any air bubbles exist that may be dragged to the surface with a small stick at this time. When the mixture has adequately covered the mould it is left to stand until it sets and the replicate is removed from the mould after 24 hours.

5.7.3 Measurements of beam parameters of triskelion force artefact's samples

The data sets for beam parameters (length ℓ and width w) of half triskelion and tetraskelion force artefact's samples were measured by a WYKO NT2000 scanning white light interferometer (profile). Some difficulty was encountered for thickness t of samples, because of force artefact's samples were not found to be totally flat. The thickness of half samples was measured by using TEZA inductive gauge by tapping between the probe tip and flat reference plate. The remaining half data sets for beam parameters (length ℓ, width w and thickness t) for samples of triskelion and tetraskelion force artefacts were measured by using digital Vernier Caliper. The data sets for beams of all samples triskelion and tetraskelion force artefacts are presented in Tables 5.3 and 5.4. The dimensions of two samples, classic triskelion sample and angle-beam triskelion sample measured by the WYKO Profiling System are show in figures 5.10 and 5.11 and remainder are given in appendix E.

Figure 5.3: The sample CS1-60 of a classic triskelion force artefact with elbow angle 60 °.

Figure 5.4: The sample CS2-604 of a classic triskelion force artefact with elbow angle 60 °.

Figure 5.5: The sample CS1-90 of a classic triskelion force artefact with elbow angle 90 °.

Figure 5.6: The sample ABS2-90 of a angle-beam triskelion force artefact with elbow angle 90 °.

Figure 5.7: The sample CS2-120 of a classic triskelion force artefact with elbow angle 120 °.

Figure 5.8: The sample ABS2-120 of a angle-beam triskelion force artefact with elbow angle 120 °.

Figure 5.9: The sample ABS1-60 of a angle-beam triskelion force artefact with elbow angle 60 °.

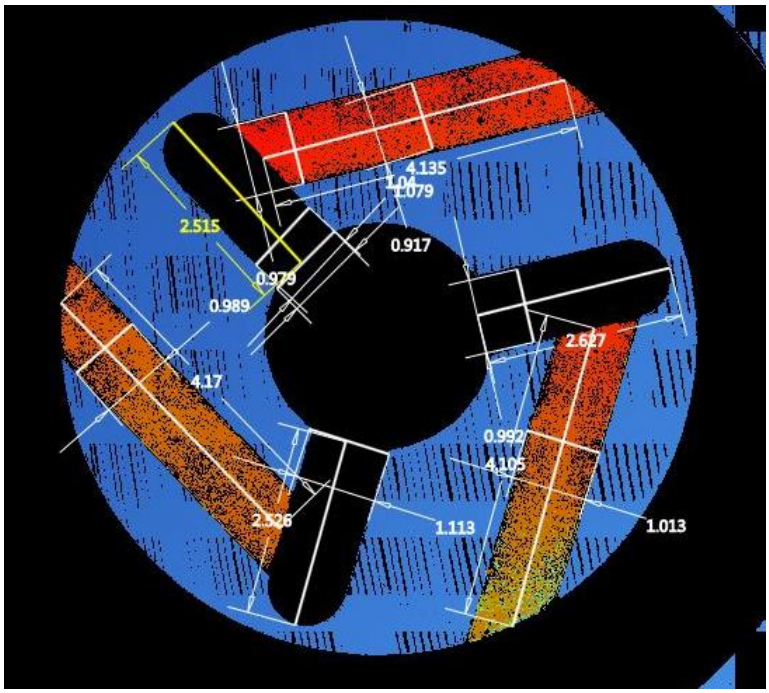

Figure 5.10: Measured dimensions of classic triskelion sample CS1-60, with elbow angle 60 °.

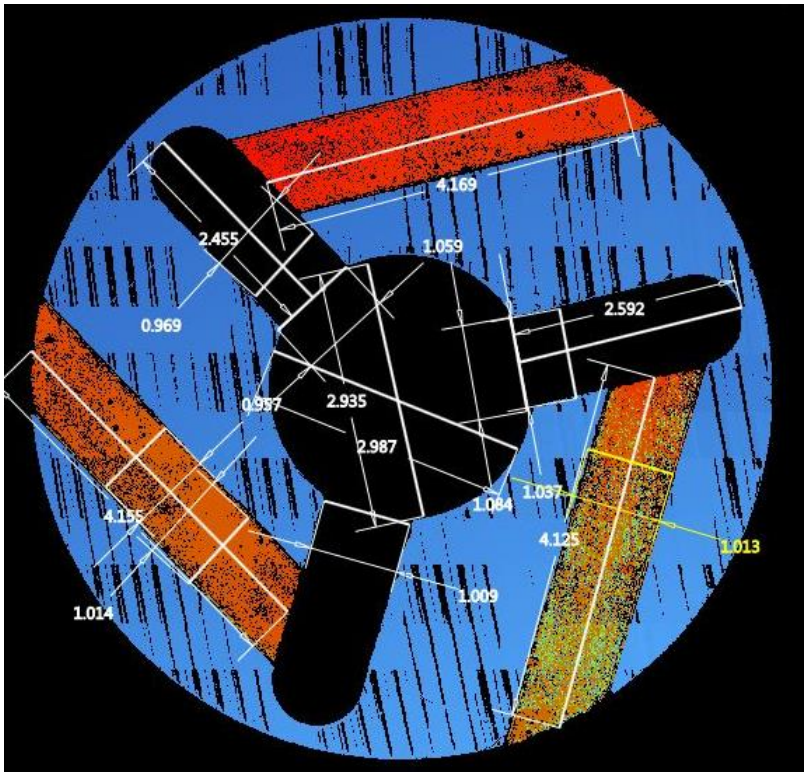

Figure 5.11: Measured dimensions of angle-beam triskelion sample CS1-60, with elbow angle 60 °.

5.7.4 Batches charaterisation

Examples of polymer artefacts produced by using the moulding technique are shown in figures 5.3, 5.4, 5.5, 5.6, 5.7, 5.8, and 5.9. The complete set of classic and angle-beam trsiskelion samples of force artefacts are shown in the appendix C. The accuracy of the dimensions using this moulding technique is clearly somewhat limited and its consistency has been investigated. Tables 5.3 and 5.4 summerise the dimensions of the first set of sample. Each of the variant angles was made from a different new mix of the resin. Batches 1 and 2 were made at significantly different times. Nevertheless, the variations in dimension are encouragingly small.

Young's modulus plays an important role in the value of artefact stiffness. We cannot exactly know the value of Young's modulus for polymer artefacts made of Acrulite (liquid and powder, 2:1 ratio mixed) and it will vary with each batch. These issues will be discussed in the next chapter.

Table 5.3: Classic triskelion samples of force artefacts

Sample ID	Beam No. 1			Beam No. 2			Beam No. 3		
	ℓ mm	w mm	t mm	ℓ mm	w mm	t mm	ℓ mm	w mm	t mm
CS1-60	4.13	1.07	0.188	4.17	0.98	0.185	4.10	1.0	0.189
CS1-90	4.40	1.11	0.190	4.40	1.05	0.187	4.49	1.0	0.185
CS1-120	4.59	1.08	0.189	4.39	1.01	0.183	4.59	1.0	0.186
CS2-60	4.17	1.02	0.189	4.15	1.04	0.186	4.12	1.03	0.190
CSS2-120	4.46	1.01	0.186	4.54	1.03	0.182	4.51	1.02	0.185
CS1-604	4.20	1.00	0.350	4.23	1.03	0.340	4.53	0.97	0.320

Table 5.4: Angle-beam triskelion samples of force artefacts

Sample ID	Beam No. 1			Beam No. 2			Beam No. 3		
	ℓ mm	w mm	t mm	ℓ mm	w mm	t mm	ℓ mm	w mm	t mm
ABS1-60	4.16	1.01	0.161	4.10	1.01	0.159	4.08	0.97	0.156
ABS1-90	4.09	1.00	0.190	4.04	1.04	0.187	4.06	1.01	0.184
ABS1-120	3.95	1.03	0.175	3.80	1.03	0.172	3.93	1.04	0.176
ABS2-60	4.12	1.03	0.155	4.17	1.17	0.152	4.18	1.14	0.153
ABS2-90	4.06	1.02	0.189	4.03	0.99	0.187	4.05	1.03	0.184
ABS2-120	3.98	1.02	0.167	3.74	0.99	0.164	3.88	1.05	0.162

5.8 Conclusion

This chapter describes the novel contribution of low-cost approach for validating of linear elastic models that were presented in chapter 3. This chapter identifies the possibility of using polymers. Through a more detailed examination of this idea, it proposes for the first time that polymeric triskelions could have applications in force artefacts and micro-probe suspensions. Hence the whole project is broadened to study this feasibility in some detail.

The particular challenge of making one or two samples of slightly varied designs at low cost and with minimum delays, this chapter investigates very simple, but novel low-cost approach. The basic sample shapes are machined into the surface of aluminium blocks, which are used as open moulds for casting pieces in a commercial surface replica resin. While clearly not a precision technique, this is shown by practical investigation to offer sufficiently consistent control of dimensions for running the tests for model validation and investigating stiffness non-linearity. This method is therefore adopted for all work reported in this thesis.

Chapter 6

Experimental analysis of stiffness: Classic triskelion force artefacts

6.1 Introduction

This chapter describes the development of a test-rig method and associate methodology to measure the stiffness of classic triskelion force artefacts. The classic triskelion force artefacts were manufactured for the validation of a linear elastic model presented in chapter 3. MEMS fabrication methods are used by industry for micro probe with elbow angle 60 ° and these were also used by Jones [148] for low force measurement, but this approach is highly expensive and time consuming. Thus, this research work adopts an alternative low-cost approach discussed in the previous chapter for fabrication of polymeric triskelion samples. Polymeric triskelion force artefacts have not been seen in any published paper except our conference paper [224]. Apart from the triskelion force artefact with elbow angle 60 °, new triskelion force artefacts with elbow angle 90 ° and 120 ° were also manufactured in the workshop at the School of Engineering, University of Warwick.

In order to investigate both axial and tilt stiffness, readings of z-axis of force and displacements of triskelion force artefacts, using the calibrated apparatus. ORIGIN software was used for plotting and analysing the graph data [225].

6.2 Development of new method to measure the stiffness

The basic requirement for testing triskelion specimens (samples of triskelion force artefacts) is to apply a know force normal to and at a controlled position in the specimen hub and measure the resulting (normal) defection at the same point. This would, of course, be equivalent to imposing a known displacement and measuring the force required to achieved it. There is here considerable similarity with the concepts of a micro-hardness testing in instrument, although the required ranges are rather different. It is very difficult at this scale to apply safely a dead-weight had and obtain an aligned displacement measurement, so 'point load' will applied via a contacting probe and force actuator.

An instrument incorporating these ideas at more relevant ranges has been in use in the Surface Engineering Laboratories at the University of Warwick some years and from the basis of the new test-rig. Originally developed by Liu [226] for studying of surface profilometry under different stylus force conditions, it is modified Talysurf 5 (Taylor Hobson). The key feature for the present research work is the incorporation of a magnet-coil force actuator closely in-line with the stylus, as shown in the schematic of figure 6.1. The profilometer traversing features are not required for the studies of triskelions, but instrument axes provide very convenient control for positioning the probe correctly on the specimen hub. The Talysurf sensor has an in-built bias spring, so there will be a small variation in the tip force as the tip moves.

A very simple preliminary experiment with a specimen placed on worktable of the Liu instrument demonstrated that the approach was feasible and reasonable easy to use. However, especially with slightly larger specimens preferred for reasons discussed in chapter 5, the operating ranges were insufficient to investigate non-linearity characteristics and a larger magnet could not be safely mounted onto the delicate sensor. Therefore, a new test-rig using the same principle and sharing some subsystem but using more robust long range sensor was designed and built. Additionally to answer excellent linearity a nulling technique was added for use in the longer-range measurement.

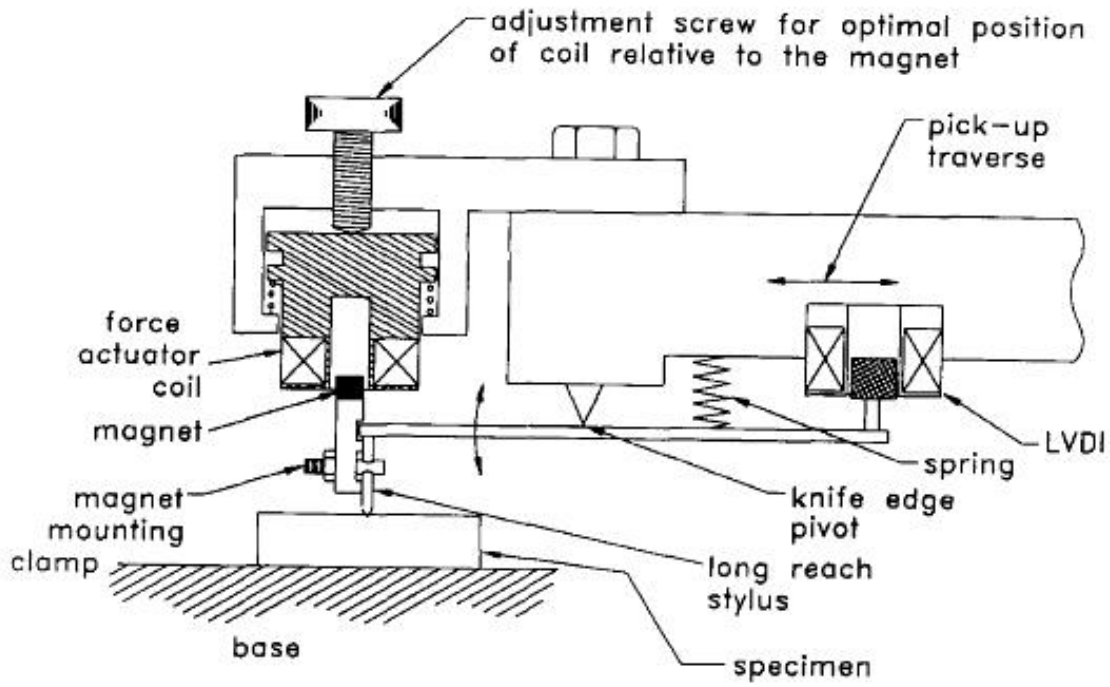

Figure 6.1: Experimental arrangement for the variable tracking force using a magnetic force transducer from [27] and [28].

6.2.1 Operational principle of test-rig method

The test-rig method has been developed, and comprises of a Talysurf 5 system, traversal unit, motorised stand, standard current source (Knick model), Heindenhain gauge, probe from roundness instrument (Talor Hobson Talyrond), digital voltmeter, xyz-adjustable table, and small hallow cylinder for mounting the sample. The important characteristic of test-rig method is that when a small known force is applied on the hub of the triskelion sample and it measure the defection. The maximum force that can be applied is 1 N, and the maximum defection is 1 mm. The scale of the device used requires sub-μm resolution.

The apparatus was set up as shown in the figure 6.2 and 6.3. The force was applied to triskelion sample vertically along z-axis and deflection occurs in the same vertical direction. An optical probe (Heindenhain) with 1 μ resolution was used to monitor the vertical motion of the table. The probe from the roundness instrument (Taylor Hobson Talyround) was a side acting inductive gauge and was mounted on a cradle, which also carried a solenoid coil. A small clamp is used to carry a magnet on the probe arm, which engages the coil to provide force actuation and a tiny ball nearly 0.2 mm probe tip (Renishaw). Thus in this

way, a deflection was measured. For fine vertical control, the whole cradle was bolted to the traversal unit of a Talysurf 5 (Taylor Hobson) profiling instrument. Further, the internal electronic setup system of the Talysurf 5 was used to drive the gauge and to provide a wide range with its own setup conditions.

The Talymin side-acting inductive gauge used on may Talyrond (Taylor Hubson) roundness measuring instruments is larger and more robust but electronically compatible with a Talysuf 5 sensor. It is well able to carry the more massive magnet needed to achieve the forces up to about 1 N without excessive heat generation in the coil. Also, it has interchangeable probe-arms, making it easy to tune the displacement range to a specific application. This suggest that a simple swapping of the probe system would suffice. However, the more robust probe bearing and bias system could lead to a significant but poorly characterised variation of force with displacement. Also, the displacement measurement must be highly linear if the test-rig is to be used to detect the onset of non-linearity in the specimen stiffness. Simple tests of the gauge with an operationally convenient size of the probe arm indicated that it would be unwise to use it outside of the central $\pm$ 200 μm of its operating range.

Most of these disadvantages could be overcome by using a quite basic null-measurement technique. The specimen is placed horizontally on the table of a stiff z-axis adjuster. As the downwards force is imposed by the probe increases, the specimen deflects downwards but the table raised to keep the Talymin gauge output signal as near as possible constant (i.e. a null condition). A long-range, highly linearity displacement sensor (while could not be physically loaded directly against the specimen) can report the change in table hight, which reflects the specimen deflection to the precision of the null. The inductive gauge can then be used at relatively high gain to get good null sensitively and with almost no reliance on its inherent linearity. Also, since the probe arm in principle is kept in the same position there is minimal effect of force variation from the bias springs.

The practical implementation of this system is shown in figures 6.2 and 6.3. The inductive gauge is mounted on a 'rigid' cradle, which also carries the solenoid coil for the

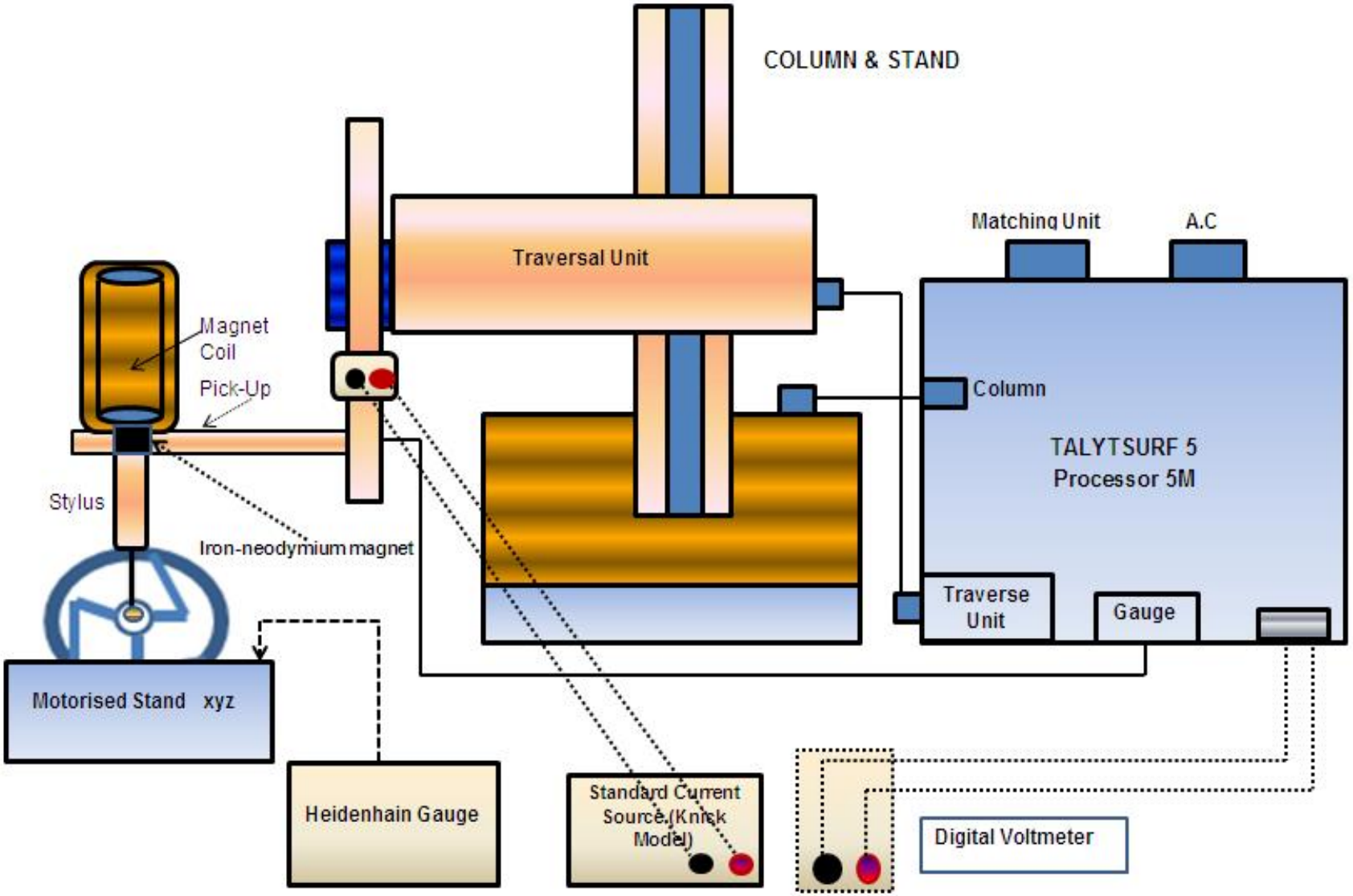

Figure 6.2: New Method: Schema of Test-rig Method to measure the stiffness of triskelion force artefacts.

Figure 6.3: New Method:Picture of Test-rig Method to measure the stiffness of triskelion force artefacts

force actuator. A small aluminium structure is clamped by a set-screw to the probe arm and has a flat top surface to which the magnet can be glued and underside thread for mounting commercially miniature probe tips. The cradle is mounted by a bracket to the Talysurf traverse unit so that it sits, in effect, parallel to the normal Talysurf probe. As well as allowing the Talysurf system (motorized column, horizontal traverse, etc.) to be used for aligning the probe. This configuration allows rapid switching between two similar instrument systems of different sensitively, as required.

The new scheme uses 0.2 mm ruby probe (Renishaw) and a nominal 50 mm probe arm. The magnetic-coil actuator ideal scale with volume so nominal design was taken by comparison with known characteristics of the small system on this original instrument. The dimensions of iron-neodymium magnet are 5 mm by 6 mm diameter and the coil dimensions are 10 $\times$ 14.7 mm, 5.9 mm internal diameter and 14.7 mm external diameter, 3776 with number of turns of 0.12 mm gauge copper wire.

The tests are essentially static and they were judged quite adequate and simplest to use mechanical control of null measurement. The force would be changed step-wise and restoring adjustment each time. Consequently, a small, stiff xyz adjuster table with fine thread manual screw was employed. The x- and y-axes are not used in the measurement but provide further aid when aligning specimen and probe. The z hight of the table was measured by a 1 μm resolution optical grating probe (Heidenhain HH60).

The inductive gauge was conducted to the Talysurf electronic unit, an output voltage proportional to displacement. The unit has variable gain, but was usually operated at 125 μm/V for tests reported here. The output was read from a simple digital voltmeter. Force is directly proportional to the coil current. The latter was set manually at each step using standard current source (Knick model). With the coil being used, this could be deliver up to $\pm 140mA$ with 1 μA resolution.

Note that from this setup, the applied force was adjusted using the weight of the probe. Thus, generally, force actuator was used to provide an upwards force applying the weight

and the current was reduced to increase the force on the triskelion samples i.e.

$$F_{spring} = W_{probe} - F_{coil} \tag{6.1}$$

6.2.2 Procedure to measure the stiffness

The following steps were performed to measure of the stiffness of triskelion polymeric sample.

- Firstly, the coil current was adjusted so that the probe, which hanging freely, gave approximately zero voltage (i.e. actuator force approximately balances probe weight). The current was recorded as i_o.

- Secondly, the probe was lowered gently on to the triskelion sample using the Talysurf z-column, until initial contact caused a voltage change. It was important to keep the initial deflection and force on the platform of the triskelion sample very low and as close to zero as possible.

- Thirdly, Haidenhain gauge monitoring the sample table was rest to zero and the value of voltage V_o from the probe gauge was recorded. After performing the third step, the loop of the experiment was started as follows:

Loop

- Firstly, the xyz-adjustable table was moved upwards by predefined step of $\triangle z$ and read from the Heidenhain digital displacement. For every measurement, the incremental step was selected to provide a reasonable but not excessive number of readings across the total desired range; usually steps were 25 μm or 50 μm. It is also obvious that as the platform of triskelion sample moves upwards, the voltage V from the inductive gauge also increases.

- Secondly, the coil current i should be continuously reduced until $V \sim V_o$.

- Since the sample platform is now closely at the same height, as it was originally, it is also closely δz lower with respect to the sample based and the force required to cause this relative defection is represented by $(i - i_o)$.

- Thirdly, the loop was started once again moving the xyz-adjustable table upwards. Hence in this manner all steps are repeated and values of current are recorded for each step. As an example a recorded reading is presented in the Table.

- Finally, The choice to assert fixed defection steps and asses the required force was judged to be less likely to lead to accidental damage to the samples then would be the equally valid alternative method of using preset steps of force.

6.2.3 Calibration of the force transducer

Characterization and calibration of the force-current relationship; for the smaller Talysurf-based, system used a dead-weight method. With the probe-arm hanging freely, small weights were suspended from the arm, as close as possible to tip, and balanced by applying current to actuator coil. The weights were short lengths of wire, cut and size and weighted as an electronic laboratory balance and bent into hook shapes that would fit around the probe arm. The steps in the process were to:

- Allow the stylus to hang freely, the gauge output voltage, V_{out} will be large.

- Ensure the pen shift on the Talysurf electronic unit is set close to zero.

- Increase the coil current slowly until the output voltage, V_{out} becomes adequately close (equal) to zero.

- Apply different wire hooks of known weight, the arm defect the downwards.

- Change the current to get input voltage, V_{out}, again approximately equal to zero and reord that current.

The current was recorded for the different wire hooks to the arm of known weight that are given in the table R.

Table 6.1 shows three trials recording the change in current needed to balance each hook, while figure 6.3 plots the means from these trials. the actuator calibration constant is $c = 118m$ μN/A.

Table 6.1: Recorded current data sets for different hooks of known weight.

S-No	*Weight mg*	*Current* i_1 *mA*	*Current* i_2 *mA*	*Current* i_3 *mA*	*Average current* i_o *mA*
1	10	136.06	136.28	136.16	136.16
2	20	136.86	137.20	136.83	133.96
3	50	139.64	139.30	139.77	139.57
4	100	143.85	143.95	143.91	143.90
5	150	147.67	147.98	148.11	147.92
6	200	152.58	152.08	152.28	152.31

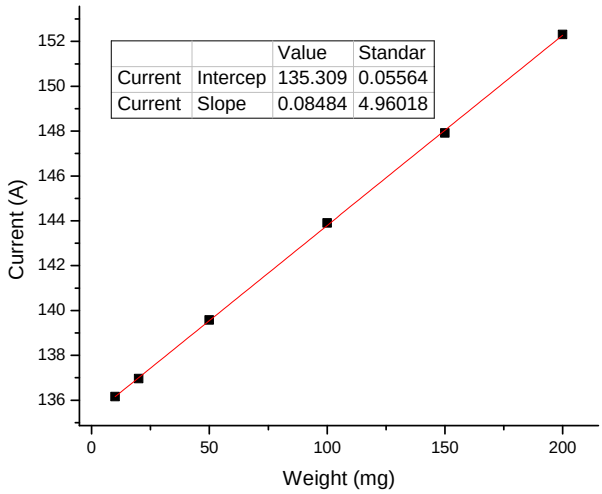

Figure 6.4: Calibration to determine the constant of the force Talysurf transducer.

6.3 Experimental test requirement

The performance and repeatability of each sample of polymer artefacts were taken into account while measuring the stiffness. Three readings were taken at the centre of hub and three at off-set points. These types of artefact will cover a range of forces from 1 to 10 mN. It is taken to be acceptable for the present test to apply the force mechanically through a small probe and to measure the deflection of that probe as representing the artefact motive. Ideal use of the artefacts places the force centrally on the hub. However, off setting the probe allows for the testing of sensitivity misalignment, and applies a resultant force/moment pair for validating twisting effects affects within the model.

6.4 Uncertainty expression for stiffness

The stiffness is the ratio of measured force F and its displacement δ between the force sensor and probing element according to

$$k = \frac{F}{\delta} \tag{6.2}$$

The force F and displacement are considered to be independent parameters for determining the standard uncertainty of stiffness. Following the general processes described in the G.U.M. system ref, uncertainties from the independent sources by quadrature addition weighted by coefficients of the partial derivative of equation (6.2). Thus, taking the positive square root. Thus, by taking the positive square root,

$$U_k = \sqrt{\left(\frac{\partial k}{\partial F}U_F\right)^2 + \left(\frac{\partial k}{\partial \delta}U_\delta\right)^2} \tag{6.3}$$

$$U_k \simeq \sqrt{\left(\frac{U_F^2}{\delta^2}\right) + U_F^2\left(\frac{F^2}{\delta^4}\right)} \tag{6.4}$$

The stiffness uncertainty U_k in equation (6.4) for test-rig method is calculated by considering the three factors, which have uncertainty in their values that are given as follows:

- Applied force on the hub of tri-skellion force artecfacts.
- Measurement of displacement δ.
- Probe correction for indentation δ_{ind}.

The force derives directly from the current in the solenoid coil controlled by the Kinck current source . Thus uncertainty of the applied force F is given as

$$U_F = (C_{coil} \cdot U_i) \tag{6.5}$$

where C_{coil} has fixed errors and second order effects and $U_i \sim 1\ \mu$A.

The nulling operation uses the inductive gauge voltage output, attempting to return it to the same value at each step. The actual calibration of this gauge causes only second-

order uncertainties under these condition. Because of noise, drift and so on, each resetting to null is in practice limited to above 10 mV. In the configuration usually used the gauge sensitivity is nominally 125 μm/V, so the uncertainty of resetting the gauge position is ± 0.7 μm. However, the actual displacement measurement occur between two such re-settings. They are taken as independent to give an overall

$$U_{null} \sim \sqrt{2}U_{induct} \sim 1\mu m \tag{6.6}$$

where U_{induct} is estimated at 2 μm. The uncertainty in the Heidenhain reading is $U_H \sim 1\mu$m. The uncertainty for probe correction is calculated from Hertz theory [227] as

$$\delta_{ind} \sim \left(\frac{9F^2}{10RE}\right)^{\frac{1}{3}} \tag{6.7}$$

Thus taking R $\sim$ 1 mm, E$\sim$ 2 GPa and F $\sim$ 1 N, we have from above equation (6.7), δ_{ind} = 0.55$\times 10^{-5}$ m and for F = 0.1N, δ_{ind} = 0.28$\times 10^{-5}$ m. If correction for the induction is applied to the displacement measured by the Heidenhain gauge, we have

$$\delta = (\delta_H - \delta_{ind}) \tag{6.8}$$

If these tests δ_H regularly rises to several hundred micrometres, so generally $\delta_{ind} \sim 0.01\ \delta$ or even smaller. Its continuation to the uncertainty is therefore second order at most. So, effectively $U_\delta \sim U_{\delta_{meas}}$ More precisely,

$$U_{\delta meas} = \left(\sqrt{U_H^2 + U_{null}^2}\right) \tag{6.9}$$

Thus taking, as before $U_H \sim 1$ μm and from equation (6.2) $U_{null} \sim 1\mu$m, equation (6.9), yields the value of $U_{\delta_{meas}}$ is 1.4 μm.

The current source delivers a quite reliable 1 μA resolution up to its maximum output of 200 mA. Uncertainty from this resolution will be negligible compared to the other effects accumulation around imperfections in the actuator system; these are conservatively estimated to give $U_F \sim$ 1mN under our operating conditions.

For mid-range operation, using $F \sim 200$ mN and $\delta \sim 200$ μm, the equation (6.4), yields the $U_k = 8.4$ N/m. So we may reasonably assume stiffness measurements are really (at the 95 % confidence level) if these are more than about 20 N/m apart.

6.5 Stiffness measurement of classic triskelion force artefacts

The design, specifications and preparation of samples for both types of triskelion artefacts, classic and angled-beam are discussed in chapter 5. Stiffness measurements for all batches of samples are measured for both type of triskelion artefacts by using the test-rig method and procedure just described. Four batches of triskelion polymeric artefacts were prepared and each batch had two samples. Each batch of triskelion polymeric artefacts differs by only the built in angle at the elbow of each sample. The sample types are differentiated as

- Batch a: Samples CS1-60 and CS2-60 with elbow angle 60 °.
- Batch b: Samples CS1-90 and CS2-90 with elbow angle 90 °.
- Batch c: Samples CS1-120 and S2-120 with elbow angle 120 °.

The beam dimensions are 4 × 1 mm in all cases and the arm length is always 1.5 mm to the centre. The thickness of the suspension beam is 0.2 mm for batches a,b and c, but for batch d, which has an elbow angle 60 °, the thickness is 0.4 mm. The experimental data sets were recorded for all batches of samples, and graphs are plotted for each set of readings. Investigating the quality of fitting various polynomial, and other functions to these non-linear curves indicated that a cubic expression regularly provided an excellent match. The coefficients of the best-fit cubic equation are presented in the form of tables D.1, D.2, D.3, D.4, D.5, and D.6 in appendix D. Six readings were recorded for each sample at the centre of a hub (figure E.1) and at off-centre points of the triskelion sample as shown in figure E.1, they are normally 1 mm from the centre.

The set of six readings for each sample can indicate the repeatability or errors. Only two graphs for each batch are shown in this chapter and the remainder are presented in the Appendix E.

Qualitative examination of the measurements revealed a quite gentle stiffening non-linear characteristic, with quite wide deflection range over while an assumption of linearity would be reasonable in practice. General investigation of curve fitting to those data sets revealed that almost all were represented by a cubic characteristic; the only exceptions were few simples with thicker beams. Consequently, a least squares cubic was computed as part of the analysis for each measurement.

All graphs were plotted as force vs displacement, so for best cubic we have

$$F_z = \beta_3 x^3 + \beta_2 x^2 + \beta_1 x + \beta_0 \tag{6.10}$$

All measurement was relative to an assumed zero deflection at zero force so having an intercept of zero, so β_0 β_0 will always will zero.

$$F_z = \beta_3 x^3 + \beta_2 x^2 + \beta_1 x \tag{6.11}$$

or

$$F_z = \left(\beta_3 x^3 + \beta_2 x^2\right) + \beta_1 x \tag{6.12}$$

where β_1 represents the small-range linear stiffness and $\left(\beta_3 x^3 + \beta_2 x^2\right)$ represents the deviation from linearity at some x.

We can define some value of displacement n_ℓ (ℓ for linear) below which the device stiffness exhibits suitably linear behaviour ; x_ℓ is the effective 'linear range' of the device. We might, for example, consider 1% deviation from linearity to be acceptable. From equation (6.12), the part of the force associated with non-linearity is

$$F_{nl}(x) = \left(\beta_3 x^3 + \beta_2 x^2\right) \tag{6.13}$$

and for linear contribution

$$F_l(x) = \beta_1(x) \tag{6.14}$$

Hence the limit of the linear range is when x_l to satisfies the quality of condition

$$F_{nl}(x_l) \leq \frac{F_l(x_l)}{100} \tag{6.15}$$

or

$$\beta_3 x_l^2 + \beta_2 x_l = \frac{\beta_1}{100} \tag{6.16}$$

The β coefficients and maximum linear range x_l obtained for equation (6.16) for each graph is given in tables D.1, D.2, D.3, D.4, D.5, and D.6 in Appendix D.

6.5.1 Batch a : Classic triskelion force artefacts with angle 60°

The six tests were executed on samples CS1-60 and CS2-60 with displacement steps of 50 μm until the limit of force actuator was reached. Three independent measurements were taken on each sample with the probe tip placed as closely as possible to the centre of hub. A further three independent measurements were taken with the probe tip placed close to the periphery of the hub, an offset from the centre of approximately 1 mm. The general pattern and the magnitudes of tests were similar, more closely so on one specimen that between them. Both figure 6.5 and 6.6 show plots of force verses displacement from two individual measurements on sample CS1-60 as a topical example; a complete set of results is plotted in appendix E. Figure 6.5 shows a case of central loading and figure 6.6 and also shows one of offset loading. Note that in both cases the measurements consider total displacement along the line of action of applied force.

The graphs show a slight upward curvature indicative of both a stiffening characteristic and substantial range over which linear behaviour (i.e. constant stiffness) is a reasonable working assumption. The coefficients of linear fit for all tests are given in tables D.1 and D.2 in the appendix D. It is noted in all tables, the tests 1, 2, and 3 for central loading, whereas 4, 5, 6 and 7 are for offset loading. The mean central stiffness is 1459.53 N/m and 1096.47 N/m for sample CS1-60 and CS2-60 respectively. The corresponding mean offset position stiffness is 1274.41 N/m and 1032.25 N/m. Consistently very high R^2 values confirm that

measurements closely follow a cubic pattern. The effective linear region is never less than 550 μm on CS1-60 or CS2-60, (table 6.2).

6.5.2 Batch b : Classic triskelion force artefacts with angle 90°

The six tests were executed on samples CS1-90 and CS2-90 with displacement steps of 50 μm until the limit of force actuator was reached. Three independent measurements were taken on each sample with the probe tip placed as closely as possible to the centre of hub. A further three independent measurements were taken with the probe tip placed close to the periphery of the hub, an offset from the centre of approximately 1 mm. The general pattern and the magnitudes of tests were similar, more closely so on one specimen that between them. Both figure 6.7 and 6.8 show plots of force verses displacement from two individual measurements on sample CS1-90 as topical example; a complete set of results are plotted that are given in appendix E. Figure 6.7 shows a case of central loading and figure 6.8 and also shows one of offset loading. Note that in both cases the measurements consider total displacement along the line of action of applied force.

The graphs show a slight upward curvature indicative of both a stiffening characteristic and substantial range over which linear behaviour (i.e. constant stiffness) is a reasonable working assumption. The coefficients of linear fit for all tests are given in tables D.3 and D.4 in the appendix D. It is noted in all tables, the tests 1, 2, and 3 for central loading, whereas 4, 5, 6 and 7 are for offset loading. The mean central stiffness is 955.29 N/m and 918.18 N/m for sample CS1-60 and CS2-60 respectively. The corresponding mean offset position stiffness is 814.95 N/m and 772.98 N/m. Consistently very high R^2 values confirm that measurements closely follow a cubic pattern. The effective linear region is less than 400 μm on CS1-90 or CS2-90 (table 6.2).

6.5.3 Batch c : Classic triskelion force artefacts with angle 120°

The six tests were executed on samples CS1-120 and CS2-120 with displacement steps of 50 μm until the limit of force actuator was reached. Three independent measurements were taken on each sample with the probe tip placed as closely as possible to the centre of hub. A further three independent measurements were taken with the probe tip

placed close to the periphery of the hub, an offset from the centre of approximately 1 mm. The general pattern and the magnitudes of tests were similar, more closely so on one specimen that between them. Both figure 6.9 and 6.10 show plots of force verses displacement from two individual measurements on sample CS1-120 as topical example; a complete set of results are plotted that are given in appendix E. Figure 6.9 shows a case of central loading and figure 6.10 and also shows one of offset loading. Note that in both cases the measurements consider total displacement along the line of action of applied force.

The graphs show a slight upward curvature indicative of both a stiffening characteristic and substantial range over which linear behaviour (i.e. constant stiffness) is a reasonable working assumption. The coefficients of linear fit for all tests are given in tables D.5 and D.6 in the appendix D. It is noted in all tables, the tests 1, 2, and 3 for central loading, whereas 4, 5, 6 and 7 are for offset loading. The mean central stiffness is 1179.07 N/m and 1070.01 N/m for sample CS1-60 and CS2-60 respectively. The corresponding mean offset position stiffness is 1075.65 N/m and 938 N/m. Consistently very high R^2 values confirm that measurements closely follow a cubic pattern. The effective linear region is less than 250 μm on CS1-120 or CS2-120 (table 6.2).

6.5.4 Batch d : Classic triskelion force artefacts ($t = 4$ mm)with angle 60°

The six tests were executed on samples CS1-604 and CS2-604 with displacement of step 25 μm until the limit of force actuator was reached. Three independent measurements were taken on each sample with the probe tip placed as closely as possible to the centre of hub. A further three independent measurements were taken with the probe tip placed close to the periphery of the hub, an offset from the centre of approximately 1 mm. The general pattern and the magnitudes of tests were similar, more closely so on one specimen that between them. Both figure 6.9 and 6.10 show plots of force verses displacement from two individual measurements on sample CS1-604 as topical example; a complete set of results are plotted that are given in appendix E. Figure 6.9 shows a case of central loading and figure 6.10 and also shows one of offset loading. Note that in both cases the measurements consider total displacement along the line of action of applied force.

The graphs indicated similar trends with acceptable repeatability. The stiffness were notably

higher than in the previous tests on the classic triskelion samples and the test-rig could only supply sufficient force for deflection around 0.25 mm. This was slightly unacceptable, and this was insufficient to enter a distinct non-linear region and so simple fits were used to estimate the stiffness. The coefficients of linear fit for all tests are given in tables D.7 and D.8 in the appendix D. It is noted in all tables that the tests 1, 2, and 3 for central loading, whereas 4, 5, 6 and 7 are for offset loading. The mean central stiffness is 5288.22 N/m and 5205.72 N/m for sample CS1-604 and CS2-604 respectively. The corresponding mean offset position stiffness is 5022.36 N/m and 4980.85 N/m. Consistently very high R^2 values confirm that measurements closely follow a linear pattern. The effective linear region is never less than 200 μm on CS1-604 or CS2-604 (table 6.2).

6.6 Discussion for stiffness behaviour of classic triskelion force artefacts

The mean linear stiffness values of classic triskelion samples is summarised in table 6.2, taking the data from tables D.1, D.2, D.3, D.4, D.5, and D.6 given in appendix D. Table 6.2 also include estimations of the useful linear-range, based on the 1 % non-linearity criterion discussed in section 6.5. Samples CS1-60 & CS1-60 from batch *a* with elbow angle 60 ° have higher value cental stiffness compared to the batches *b* and *c*. The variation in average stiffness between two samples of each batch tends to be greater than the variation in measurement on one sample, but remains small enough for patterns of behaviour to show clearly. The variation in batch *b* triskelion samples CS1-90 & CS2-90 is 1.5%, which is small compared to those of batches *a* and *c* (33.1% & 10.18%). This variation is almost certainty due to the dimensional uncertainties arising from production process. The variation in stiffness between samples of each batch could possibly be significantly reduced if these were fabricated by using a MSL technique. All measurements show expected stiffening spring characteristic but it is quite gentle up to the order of 1 mm deflection. Taken across all samples, the 1 % linear range is nearer less than — μm. A slightly surprising feature is that , despite the net curvature being consistent, the signs of the higher order coefficients of the best cubic fit (β_3 and β_2) are not always constant. There is no pattern to this inconsistency that might suggest a fundamental physical cause and might well be computational effect

Table 6.2: Measured stiffness of classic triskelion force artefacts from tables D.1, D.2, D.3, D.4, D.5, D.6, D.7 and D.8.

Sample ID	*Linear range*	*R-Squared*	*Average stiffness at*	
	μm		centre of hub N/m	off-centre point N/m
CS1-60	550	0.999	1459.53	1274.41
CS2-60	550	0.999	1096.47	1032.25
CS1-90	400	0.999	0955.29	0814.95
CS2-90	400	0.999	0918.18	0772.98
CS1-120	250	0.999	1179.07	1075.65
CS1-120	250	0.999	1070.01	0938.00
CS1-604	200	0.999	5288.22	5022.36
CS1-604	200	0.999	5205.72	4980.85

from fitting to slightly noisy data over a range that deviates only slightly from linearity. The R^2 fitting coefficient is always better than 0.999, and so there are no concerns that real measurements are being poorly represented. Combining these observations with relatively high inconsistency on suspension beam thickness in the samples, it would be unwise too place to much weight on batch b (90 ° elbow angle) having significantly lower stiffness than the other designs. However, it is fully valid to compare in detail variations in behaviour based on different tests on the same sample.

In every sample the off-centre stiffness is less than the central stiffness. This is fully expected; the offset force generates a moment that, from the torsional stiffness of the platform, superposes a tilt adding extra deflection to the central motion. In basic expression, if we represent the z-stiffness and torsional stiffness as k and λ, then for a offset distance q, we have

$$z_{oc} = \frac{F}{k_c} + q\frac{M}{\lambda} \tag{6.17}$$

$$M = qF \tag{6.18}$$

The in-line offset z-stiffness is there expressible using equation (6.18) in equation (6.17).

$$z_{oc} = \left(\frac{1}{k_c} + \frac{q^2}{\lambda}\right) F = \left(\frac{1}{k_{oc}}\right) F \tag{6.19}$$

Showing that it is always smaller than k_c. The equation allows an estimate for the torsional stiffness λ to be made, assuming that central measurement directly yields a good estimate for k_c. table 6.2 lists the estimated torsional stiffness for all six samples.

6.7 Conclusion

This chapter has described a development of a novel test-rig method to measure the stiffness of triskelion or similar planar flexures that might be used as force artefacts. The main objective of this research was to test the classic triskelion samples for validation of the linear elastic model that has been presented in the chapter 3 and to characterize non-linearity of these samples are investigated that has great importance for the industrial application. These samples were manufactured at the University of Warwick by using a novel low-cost technique. Two samples of each three designs were nominally identical except for having elbow angles of 60 °, 90 ° and 120 ° were measured on the new test-rig.

A stiffening spring non-linearity was detected for all these classic triskelion samples. It closely follows a best cubic fit. The linear range dominates for a wide range that is sufficient for the practical purpose of industrial application. The validation of the classic triskelion model against the samples will be discussed in chapter 9.

Although the non-linearity is always small in these test, it may be concluded that triskelion samples CS1-60 & CS2-60 with the elbow angle 60 ° are slightly more linear than the other designs. These samples with elbow angle 60 ° have good small displacement linear behaviour over a under region of 550 μm.

The next chapter follows the new family of angle-beam triskelion force artefacts that are introduced first time.

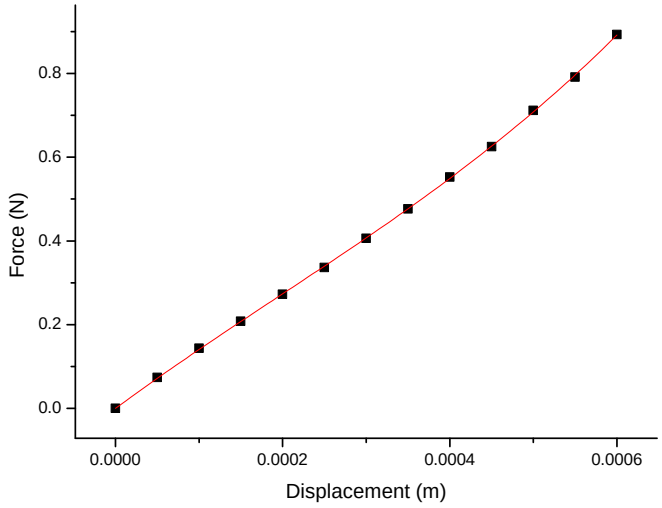

Figure 6.5: Stiffness measured at the centre of hub for classic triskelion sample CS1-60 S.No. 1, D.1

.

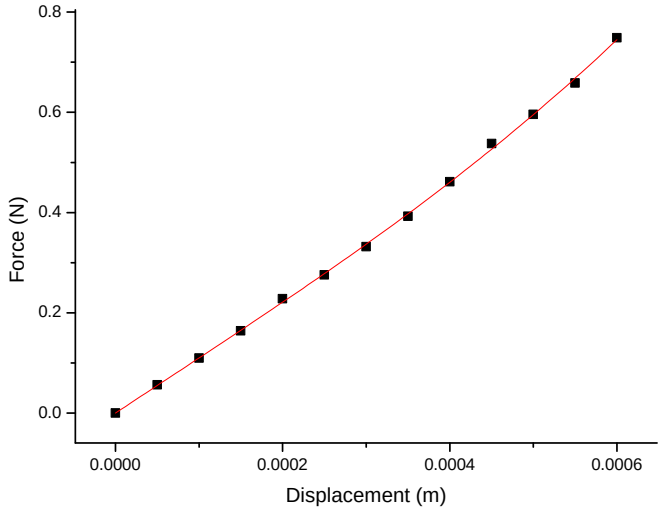

Figure 6.6: Stiffness measured at off-centre point for classic triskelion sample CS1-60 S.No. 4, D.1

.

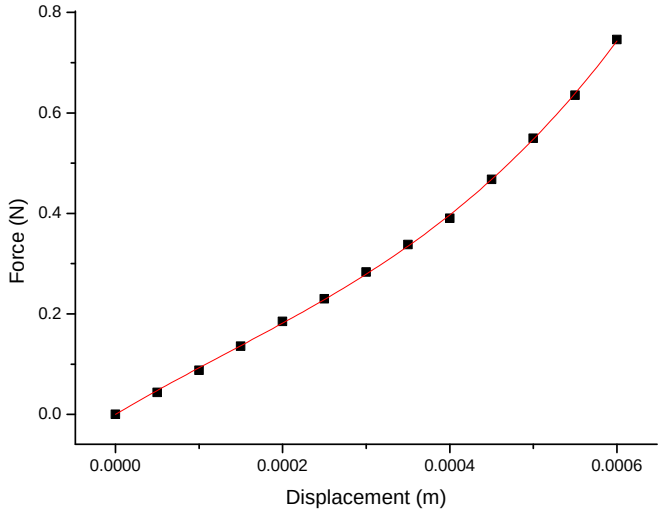

Figure 6.7: Stiffness measured at the centre of hub for classic triskelion sample CS1-90 S.No. 2, D.3

.

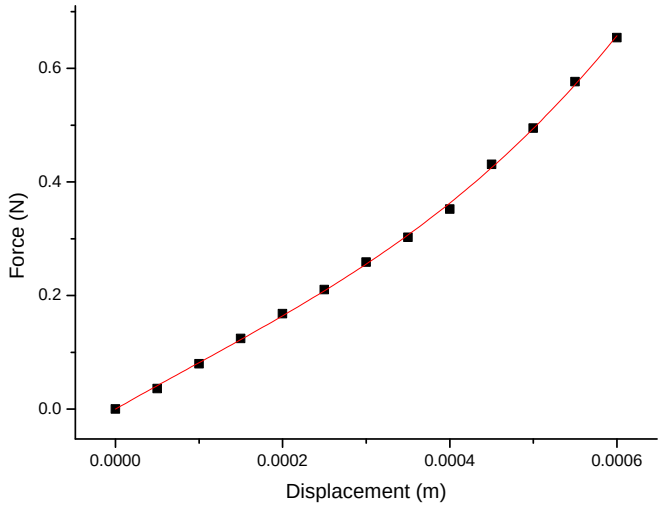

Figure 6.8: Stiffness measured at off-centre point for classic triskelion sample CS1-90 S.No. 4, D.3

.

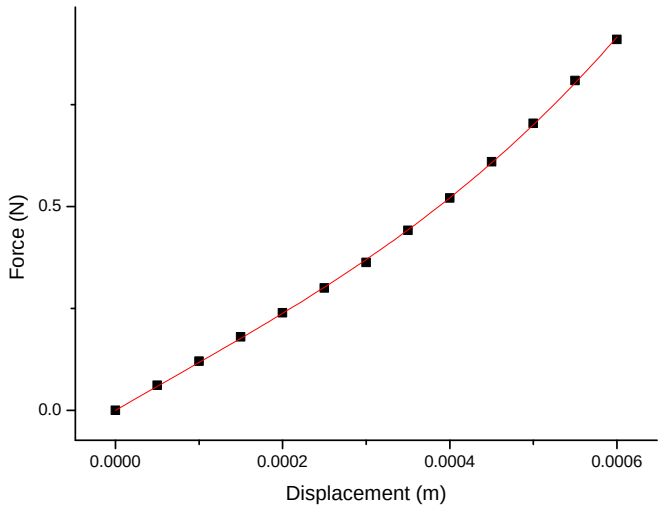

Figure 6.9: Stiffness measured at the centre of hub for classic triskelion sample CS1-120 S.No. 3, D.5

.

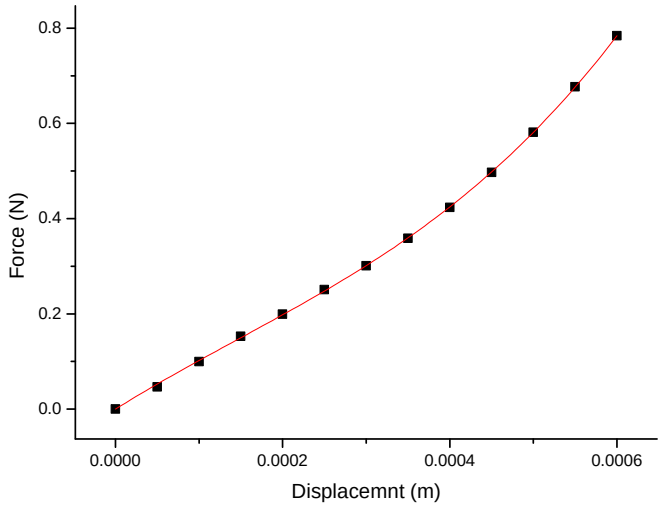

Figure 6.10: Stiffness measured at off-centre point of hub for classic triskelion sample CS1-120 S.No. 4, D.5

.

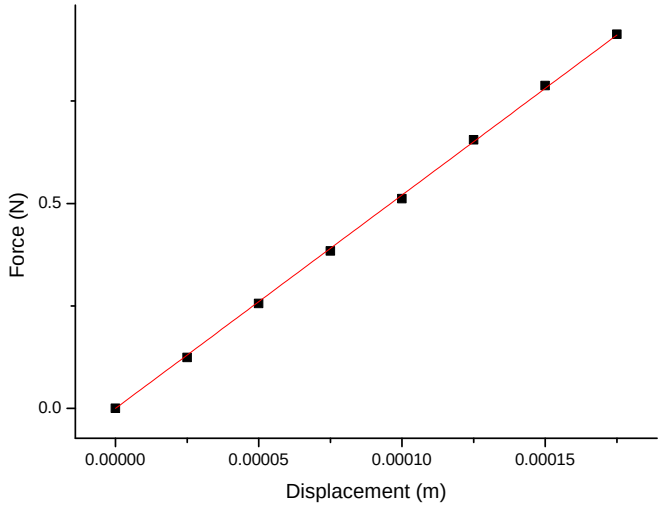

Figure 6.11: Stiffness measured at the centre of hub for classic triskelion sample CS1-120 S.No. 1, D.7

.

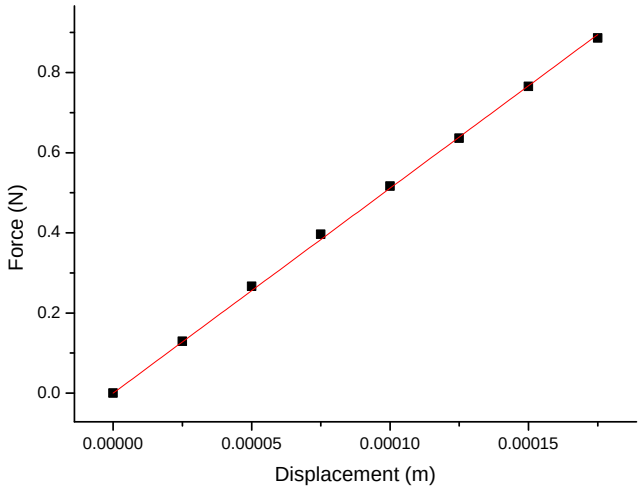

Figure 6.12: Stiffness measured at off-centre point of hub for classic triskelion sample CS1-120 S.No. 4, D.7

.

Chapter 7

Experimental analysis of stiffness: Angle-beam triskelion force artefacts

7.1 Introduction

This chapter describes the measurement of angle-beam triskelion planar suspension, as might be used in force artefacts. Their specification, design and fabrication using a low-cost technique was discussed in chapter 4. The angle-beam triskelion force artefacts were manufactured in order to validate an angle-beam model presented in chapter 3 and measurements were also intended to cost more light on the potential for using polymeric device in practical applications. These types of polymeric angle-beam triskelion force artefacts were made in the school of engineering workshop at the University of Warwick. The non-linearity and general behaviour of angle-beam triskelion force artefacts will be investigated in this chapter.

The test-rig and method designed in chapter 6 was used to record three readings of the force-deflection characteristic for each sample of angle-beam triskelion force artefact. All recorded data for each sample were plotted by using the ORIGIN software [225].

7.2 Angle-beam triskelionforce artefacts

The design of angle-beam triskelion suspensions are the same as class triskelion one except that the arms and suspension beams of the angle-beam force artefacts are of uniform thickness than that of the hub.

7.2.1 Motivation for angle-beam triskelion force artefacts

As discussed in more detail in chapter 6, the classic triskelion design has quite a high degree of over-constraints, and is equivalent kinematic representation. This would be expected to correlate with relatively high stiffness and stiffening spring characteristic. For applications such as small force transfer artefacts, there is distinct interest in achieving low stiffness in physical compact devices and obtaining a large working range of practical linearity. The angle-beam triskelion designs reduce the number of equivalent kinematic constraints by allowing bending and torsion in the (now thinner) arm projecting from the hub in the main suspension beams. They might therefore offer an attractive, improved solution for some applications. However, the reduced level of constraint might also seriously effect their mechanical stability and so further investigation is needed. A linear model was developed in chapter 3, which requires general physical validation. Tests here, notably involving various elbow angles, address this issue and more generally examine the practicality of polymeric angle-beam triskelion suspensions

7.2.2 Stiffness measurement of angle-beam triskelion force artefacts

The design, specifications and preparation of samples for the angled-beam triskelion force artefacts are discussed in chapter 5. Stiffness measurements for all batches of angle-beam triskelion samples are measured by using the test-rig, a new method and procedure described in chapter 6. Three batches of triskelion polymeric artefacts were prepared and each batch had two samples. Each batch of triskelion polymeric artefacts differs by only the built in angle at the elbow of each sample. The sample types are differentiated as

- Batch e: Samples ABS1-60 and ABS2-60 with elbow angle 60 °.
- Batch f: Samples ABS1-90 and ABS2-90 with elbow angle 90 °.
- Batch g: Samples ABS1-120 and ABS2-120 with elbow angle 120 °.

The beam dimensions are 4 × 1 mm in all cases and the arm length is always 1.5 mm to the centre. The thickness of the suspension beam and arm is 0.1 mm for batches e, f and g. The experimental data sets were recorded for all batches of samples, and graphs were plotted for each set of readings. The experimental data sets have been recorded for all batches of samples and graphs are plotted for each set of reading. For best fit equation, the coefficients are presented in form of tables F.1, F.2, F.3, F.4, F.5, and F.6 in Appendix F. Six readings were recorded for each sample at the centre of a hub (see one figure 7.1 for and at off-centre points of the angle-beam triskelion sample as shown in figure 7.2, they are normally 1 mm from the centre.

The set of six readings for each sample can indicate the repeatability or errors. Only two graphs for each batch are shown in this chapter and the remainder are presented in the Appendix G. A very good cubic best fit curve can be seen for all graphs.

Qualitative examination of the measurements revealed a less gentle stiffening non-linear characteristic as compared to classic triskelion samples, with quite wide deflection range over while an assumption of linearity would be reasonable in practice. A general investigation of curve fitting to those data sets revealed that almost all were represented by a cubic characteristic; the only exceptions were few simples with thicker beams. Consequently, a least squares cubic was computed as part of analysis for each measurement.

7.2.3 Batch a :Angle-beam triskelion force artefacts with angle 60°

The six tests were executed on samples ABS1-60 and ABS2-60 with displacement of step 50 μm until the limit of force actuator was reached. Three independent measurements were taken on each sample with probe tip placed as closely as possible to the centre of hub. A further three independent measurements were taken with the probe tip placed close to the periphery of the hub, an offset from the centre of approximately 1 mm. The general pattern and the magnitudes of tests were similar, more closely on one specimen that between them. Both figure 7.1 and 7.2 show plots of force verses displacement from two individual measurements on sample CS1-60 as topical example; a

complete set of results are plotted that are given in appendix G. Figure 7.1 shows a case of central loading and figure 7.2 and also shows one of offset loading. Note that in both cases, the measurements consider total displacement along the line of action of applied force.

The graphs show a slight upward curvature indicative of both a stiffening characteristic and substantial range over which linear behaviour (i.e. constant stiffness) is a reasonable working assumption. The coefficients of linear fit for all tests are given in tables F.1 and F.2 in the appendix F. It is noted in all tables, the tests 1, 2, and 3 for central loading, whereas 4, 5, 6 and 7 are for offset loading. The mean central stiffness is 536.97 N/m and 478.97 N/m for sample ABS1-60 and ABS2-60 respectively. The corresponding mean offset position stiffness is 503.38 N/m and 443.90 N/m. Consistently very high R^2 values confirm that measurements closely follow a cubic pattern. The effective linear region is never less than on 600 μm on CS1-60 or CS2-60 7.1.

7.2.4 Batch b :Angle-beam triskelion force artefacts with angle 90°

The six tests were executed on samples ABS1-90 and ABS2-90 with displacement of step 50 μm until the limit of force actuator was reached. Three independent measurements were taken on each sample with probe tip placed as closely as possible to the centre of hub. A further three independent measurements were taken with the probe tip placed close to the periphery of the hub, an offset from the centre of approximately 1 mm. The general pattern and the magnitudes of tests were similar, more closely so on one specimen that between them. Both figure 7.3 and 7.4 show plots of force verses displacement from two individual measurements on sample ABS1-90 as topical example; a complete set of results are plotted that are given in appendix G. Figure 7.3 shows a case of central loading and figure 7.4 and also shows one of offset loading. Note that in both cases the measurements consider total displacement along the line of action of applied force.

The graphs show a slight upward curvature indicative of both a stiffening characteristic and substantial range over which linear behaviour (i.e. constant stiffness) is a reasonable working assumption. The coefficients of linear fit for all tests are given in tables F.3 and F.4 in the appendix F. It is noted in all tables that the tests 1, 2, and 3 are central loading,

whereas 4, 5, 6 and 7 are for offset loading. The mean central stiffness is 873.62 N/m and 1213.50 N/m for sample ABS1-60 and ABS2-60 respectively. The corresponding mean offset position stiffness is 838.05 N/m and 1009.03 N/m. Consistently very high R^2 values confirm that measurements closely follow a cubic pattern. The effective linear region is never less than 500 μm on ABS1-90 or ABS2-90 7.1.

7.2.5 Batch c :Angle-beam triskelion force artefacts with angle 120°

The six tests were executed on samples ABS1-120 and ABS2-120 with displacement of step 50 μm until the limit of force actuator was reached. Three independent measurements were taken on each sample with probe tip placed as closely as possible to the centre of hub. A further three independent measurements were taken with the probe tip placed close to the periphery of the hub, an offset from the centre of approximately 1 mm. The general pattern and the magnitudes of tests were similar, more closely on one specimen that between them. Both figure 7.5 and 7.6 show plots of force verses displacement from two individual measurements on sample ABS1-120 as topical example; a complete set of results are plotted that are given in appendix G. figure 7.5 shows a case of central loading and figure 7.6 and also shows one of offset loading. Note that in both cases the measurements consider total displacement along the line of action of applied force.

The graphs show a slight upward curvature indicative of both a stiffening characteristic and substantial range over which linear behaviour (i.e. constant stiffness) is a reasonable working assumption. The coefficients of linear fit for all tests are given in tables F.5 and F.6 in the appendix F. It is noted in all tables, the tests 1, 2, and 3 are central loading, whereas 4, 5, 6 and 7 are for offset loading. The mean central stiffness is 734.61 N/m and 602.99 N/m for sample ABS1-120 and ABS2-120 respectively. The corresponding mean offset position stiffness is 613.85 N/m and 579.82 N/m. Consistently very high R^2 values confirm that measurements closely follow a cubic pattern. The effective linear region is never less than 300 μm on ABS1-120 or ABS2-120 7.1.

7.3 Discussion and stiffness analysis of angle-beam triskelion force artefacts

The mean linear stiffness values of classic triskelion samples is summarised in table (7.1 using the tables F.1, F.2, F.3, F.4, F.5, and F.6 given in appendix F. Table 7.1 also include estimations of the useful linear-range, based on the 1 % non-linearity criterion discussed in section 6.5. The 1 % linear range reduces notably with increasing the elbow angle. With one just exception (sample ABS1-90), the angle beam triskelion samples are less stiff than equivalent classic design. For the sizes trend in these experiments, the difference are not all great, perhaps just by enough to be potentially useful. For samples ABS1-60 and ABS1-60, the linear seems to be better than for classic designs, suggestive of a lower degree of over-constraints as predicted. The effective stiffness is consistently lower for all angle-beam triskelion samples, but the differences are often small indicating relatively high platform torsional stiffness compared to its axial stiffness. The variation in stiffness of batch e angle-beam samples ABS1-90 & ABS2-90 are seen higher as compared to the triskelion samples of batches d and f. The variation in stiffness between triskelion samples of each batch could be reduced if these triskelion samples are fabricated by using the MSL technique.

Table 7.1: Measured stiffness of angle-beam triskelion force artefacts from tables F.1, F.2, F.3, F.4, F.5, and F.6.

Sample ID	Linear range	R-Squared	Average stiffness at	
	μm		centre of hub N/m	off-centre point N/m
ABS1-60	600	0.999	536.95	503.38
ABS2-60	600	0.999	478.57	443.90
ABS1-90	500	0.999	873.02	838.05
ABS2-90	500	0.999	1213.50	1009.30
ABS1-120	300	0.999	734.61	613.85
ABS1-120	300	0.999	602.99	579.92

7.4 Conclusion

The novel contribution of polymeric angle-beam triskelion force artefacts that was first time introduced by using the low-cost techniques at the University of Warwick for the validation of analytical angle-beam model presented in the chapter 3. The experimental results of these batches d, e and f of angle-beam triskelion force artefacts show that the

angle-beam triskelion samples of all batches are more sensitive when compared to classic triskelion force artefacts.

It has been concluded from the results summarised in the table for all samples of angle-beam triskelion force artefacts that angle-beam triskelion samples ABS1-6- and ABS2-60 with elbow angle 60 ° have a wider range than the other samples of batches e and f. The angle-beam samples of batches d and e are seen less stiffer than samples of batches e. These angle-beam samples with elbow angle 60 °, 90 ° and 120 ° have linear behaviour in a small displacement under region of 600, 500 & 300 μm as compared to the batches *a*, *b*, and *c*. The stiffness variation has been seen between two samples in each batch. The variation in stiffness of batch e angle-beam samples ABS1-90 & ABS2-90 is seen as higher compared to the batches d and f of angle-beam samples of triskelion force artefacts. This variation is due to the dimensional uncertainties of triskelion samples of each batch.

As with the classic triskelion force artefacts, the non-linearity of angle-beam triskelion force artefacts also follows the best cubic fit. The angle-beam triskelion samples also be used for industrial instruments that require micro force calibration when commercial load-cell fail. The linear range dominated for the batches d and e with elbow angle 60 ° and 90 ° have a wider range for a purpose of industrial application of micro force measurement.

The validation of angle-beam triskelion force artefacts will be discussed later in chapter 9. The next chapter will describe the new family of triskelion force artefacts called tetraskelion force artefacts that were initially fabricated.

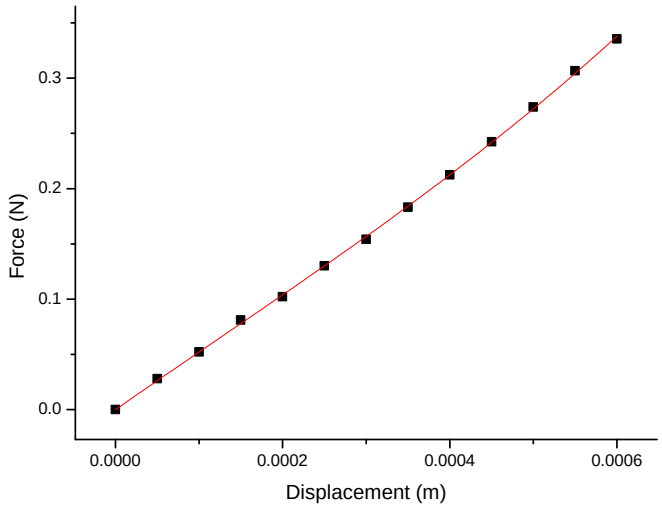

Figure 7.1: Stiffness measured at the centre of hub for angle-beam triskelion samples ABS1-60 S.No. 1, Table F.1

.

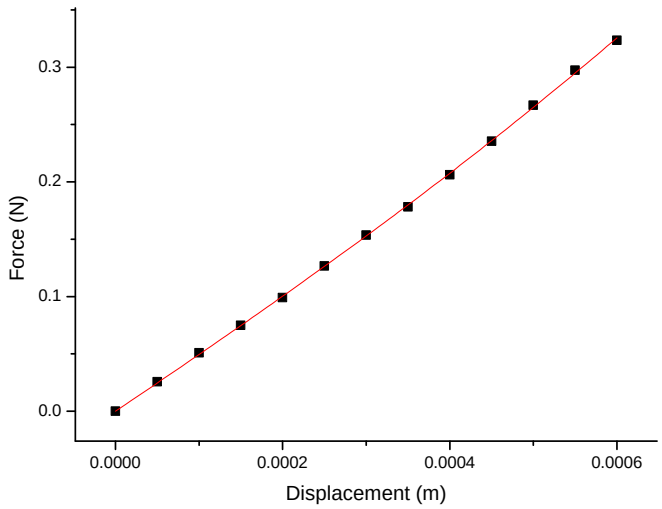

Figure 7.2: Stiffness measured at off-centre point for angle-beam triskelion samples ABS1-60 S.No. 4, Table F.1

.

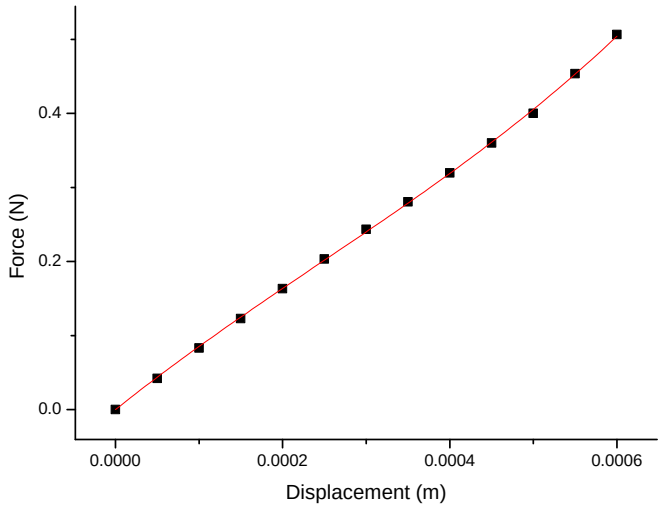

Figure 7.3: Stiffness measured at the centre of hub for angle-beam triskelion samples ABS2-90 S.No. 1, Table F.3

.

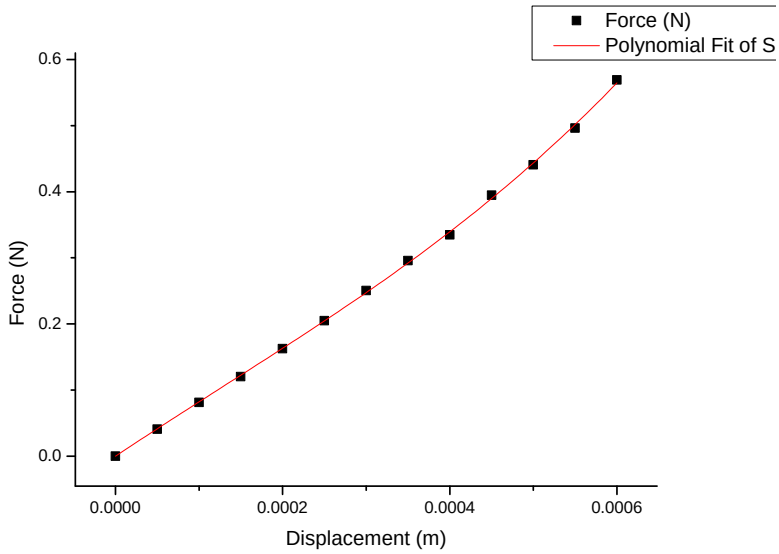

Figure 7.4: Stiffness measured at off-centre point for angle-beam triskelion samples ABS1-90 S.No. 4, Table F.3

.

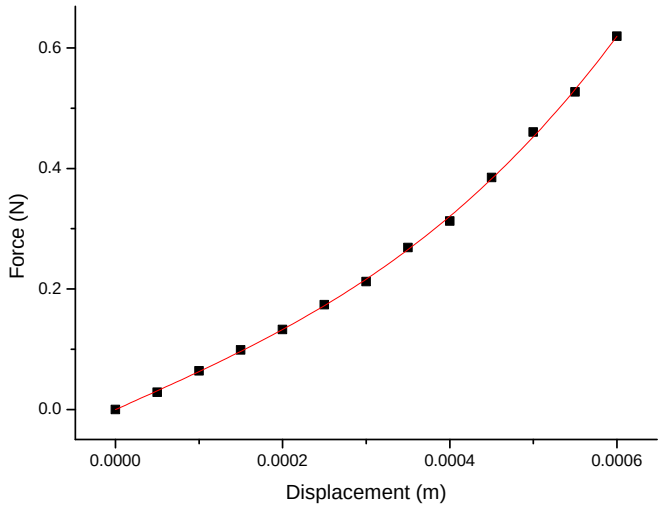

Figure 7.5: Stiffness measured at the centre of hub for angle-beam triskelion samples ABS1-120 S.No. 1, Table F.5

.

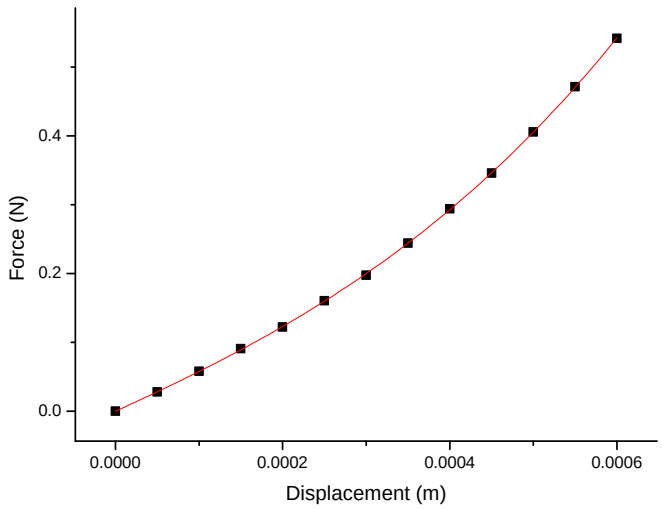

Figure 7.6: Stiffness measured at off-centre point for angle-beam triskelion samples ABS1-120 S.No. 4, Table F.5

.

Chapter 8

Tetraskelion force artefacts: specification, design, experimental analysis of stiffness and numerical investigations

8.1 Introduction

This chapter describes the measurement of stiffness of tetraskelion force artefacts. Their design is an extension of triskelion force artefacts with an extra leg. Polymeric samples of tetraskelion force artefacts were fabricated using the low-cost technique in chapter 5. Both classic and angle-beam samples of tetraskelion force artefacts are introduced and polymeric test samples were made in the School of Engineering workshop, at the University of Warwick.

The new implementation of linear elastic models discussed in chapter 3 provide great flexibility to vary parameters around the basic concept triskelion-like planar flexures. The triskelion in several minor variants are easily accommodated by it and so have a short-range linear behaviour of such devices is also investigated in simulation and with compared to the expected results.

8.2 Motivation for tetraskelion force artefacts

As was explored in earlier chapters, the triskelion suspension behaves essentially as an over constrained, three degree of freedom device. Ideally applications, such as force transfer artefacts could have a simple freedom, an ideal that is theoretically denied to planar flexures. This raises the question whether increasing the degree of over constraint might in a purely practical sense moves us closer to this ideal. The expected disadvantages would be one of greater stiffness and more serve non-linearity. However, the evidence gathered here shows polymeric triskelion more than adequate 'linear' ranged. These observations therefore motivate a brief experimental study of a few tetraskelion designs, based on the method used earlier.

8.3 Types and design tetraskelion force artefacts

Two types of tetraskelion called (in keeping with previous nomenclature) the classic and angle-beam tetraskelion force artefacts were fabricated for the general study and the practical validation of linear elastic models is presented in chapters 6, 7 and 8. The tetraskelion shares many features with the triskelion with also having important differences, most notably four-fold symmetry about the z-axis. Figures 8.1 & 8.2 and 8.3 & 8.4 show basic geometries of classical tetrakelion suspension and further model simplification. Two layouts are of immediate interest here: the arms can be centrally disposed such that all four of their centre-lines intersect at the centre of the hub; alternatively the centre lines of opposite pair of arm could be parallel but offset to pass equally to either side of the hub centre. Clearly, providing it is sufficiently rigid, the shape of the hub is unimportant but circular or square shapes are natural choices. Both of these layouts allow two types of devices. The first type, the classic polymeric tetraskelion suspension has a hub and projecting arms that make a rigid platform, which is thicker as compared to the beam thickness. The second type, the angle-beam tetraskelion suspension but has thicker hubs and but both arms and beams have the same smaller thickness. Each arm and beam is considered to be one part called an angled-beam. The four arms in each type are disposed symmetrically. The arms connected to the hub and to the beams that are mounted on an outer rigid base structure,

as shown in figure 8.1 and 8.3. All these joints are notionally built-in and fully constrained types, although clearly having some compliances in practice.

8.3.1 Specification, fabrication and dimensions measurement for classic & angle-beam tetraskelion samples

Samples were designed for both classic and angle-beam tetraskelions in each case with centre symmetric (CS) and diagonal symmetric (DS). All used 90 ° elbow angles, which are most readily compatible with four fold symmetry. In all cases, dimensions were made same as for some of the triskelion samples already studied. The detailed dimensional specifications are given in Table 8.1 . The fabrication of polymeric triskelion samples were discussed in

Table 8.1: Specification for classic tetraskelion, CS & DS and angle-beam tetraskelion, CS & DS force artefacts with 90 °, elbow angle.

Parameters	Classic, CS & DS	Angle-beam, CS & DS
$hub's\ radius\ r_h$	1.5 mm	1.5 mm
$hub's\ thickness\ t_h$	1.0 mm	1.0 mm
$arm's\ length\ \ell_a$	2.0 mm	2.0 mm
$arm's\ width\ w_a$	1.0 mm	1.0 mm
$arm's\ thickness\ t_a$	2.0 mm	2.0 mm
$beam's\ length\ \ell_b$	4.0 mm	4.0 mm
$beam's\ width\ w_b$	1.0 mm	1.0 mm
$beam's\ thickness\ t_b$	0.2 mm	0.2 mm

chapter 5 and same procedure was used for tetraskelion samples. The basic casting method has also been devised and investigated for tetraskelion force artefacts. The data sets for beams parameters of all tetraskelion force artefacts are presented in tables 8.2 and 8.3. The dimensions of two samples, classic tetraskelion samples and angle-beam triskelion samples measured by the WYKO NT2000 Profiling System are show in figures 8.5 and 8.6 and the remainder are given in appendix E.

8.4 Stiffness measurement for classic tetraskelion and angle-beam samples

The same test-rig configuration and procedure used to evaluate the triskelion samples and discussed in chapter 6 was used to measure the stiffness of all tetraskelion samples. Four moulds were made corresponding to classic and angle-beam variations for centre symmetric

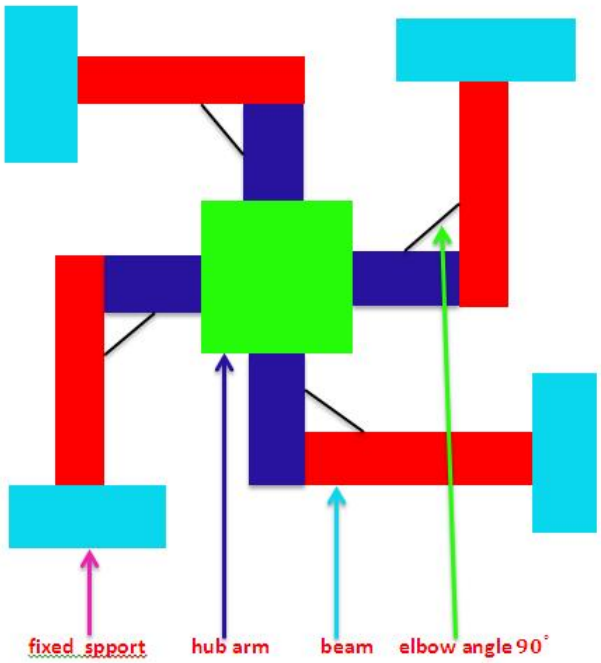

Figure 8.1: The classic tetraskelion suspension with centre symmetric (CS) and a layout with elbow angle 90 °

.

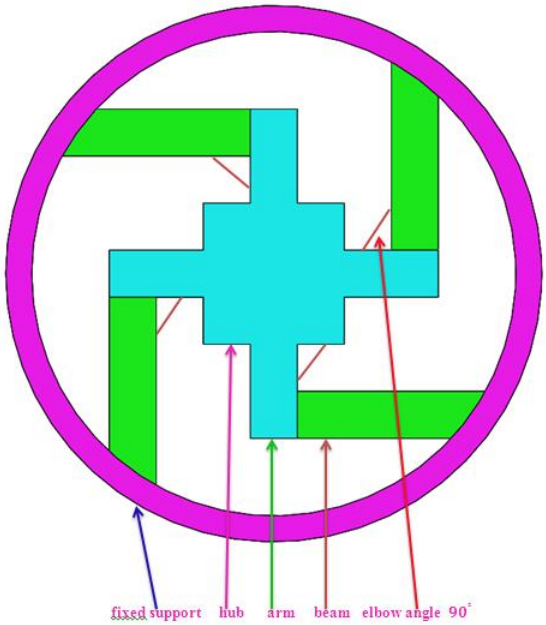

Figure 8.2: The classical tetraskelion suspension with centre symmetric and further model simplification with elbow angle 90 °

.

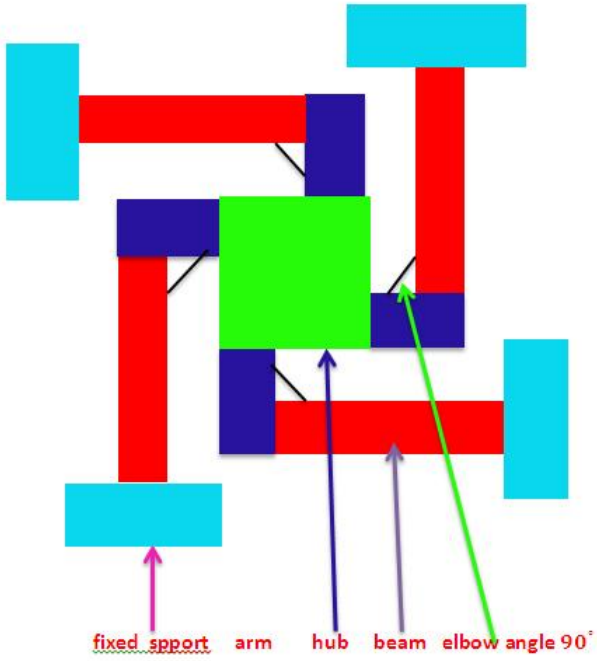

Figure 8.3: The classic tetraskelion suspension with diagonal symmetric (DS) and a layout with elbow angle 90 °

.

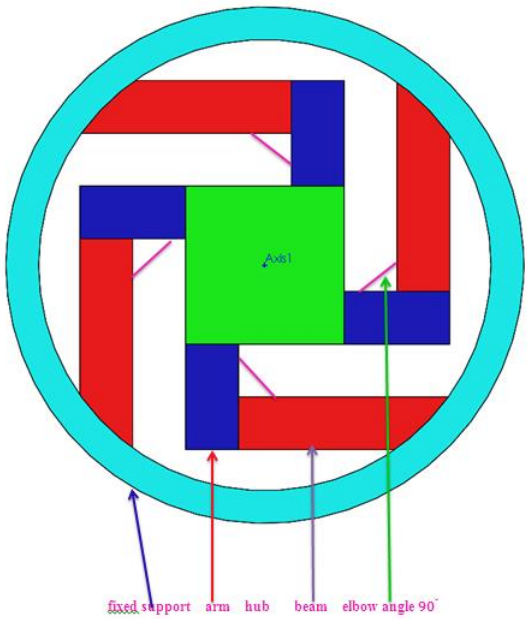

Figure 8.4: The classical tetraskelion suspension with diagonal symmetric (DS) and further model simplification with elbow angle 90 °

.

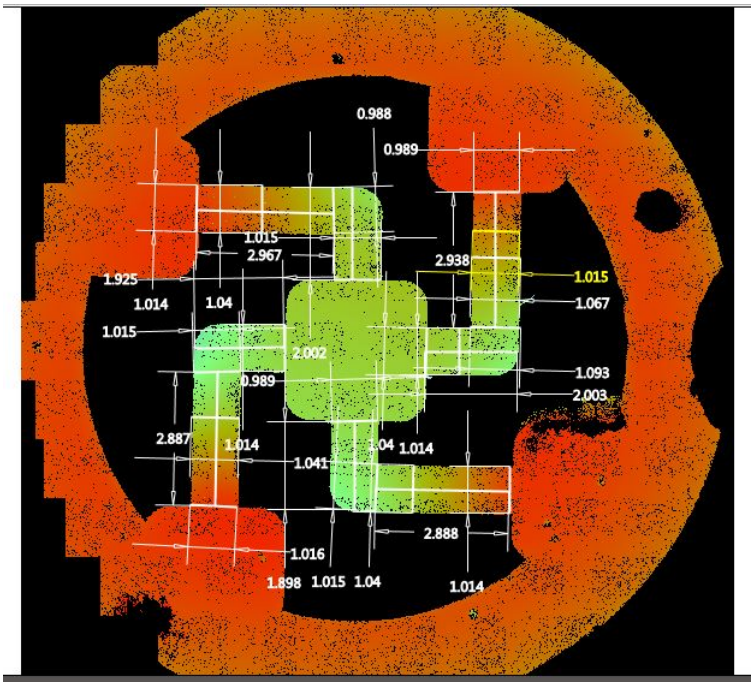

Figure 8.5: Measured dimensions of classic triskelion sample CS1-CS-90, with elbow angle 90 °.

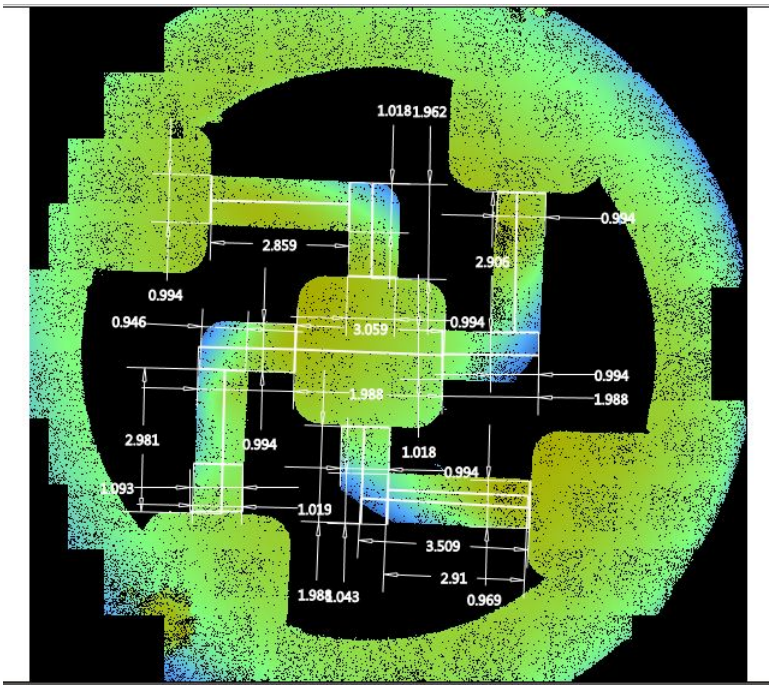

Figure 8.6: Measured dimensions of angle-beam triskelion sample ABS1-CS-90, with elbow angle 60 °.

Table 8.2: Classic tetraskelion samples of force artefacts

Sample ID	Beam No. 1			Beam No.2			Beam No.3			Beam No. 4		
	ℓ mm	w mm	t mm	ℓ mm	w mm	t mm	ℓ mm	w mm	t mm	ℓ mm	w mm	t mm
CTTS1-CS	2.93	1.01	182	2.96	1.01	180	2.88	1.01	179	2.88	1.01	184
CTTS1-CD	2.89	1.09	189	3.02	1.03	186	2.89	1.01	190	2.98	1.03	187
CTTS2-CS	2.97	1.00	185	2.99	1.02	183	2.95	1.00	180	2.94	1.02	188
CTTS2-CD	2.94	1.01	190	2.92	1.00	188	2.96	1.02	184	2.90	1.00	186

Table 8.3: Angle-beam tetraskelion samples of force artefacts

Sample ID	Beam No. 1			Beam No. 2			Beam No. 3			Beam No. 4		
	ℓ mm	w mm	t mm	ℓ mm	w mm	t mm	ℓ mm	w mm	t mm	ℓ mm	w mm	t mm
CTTS1-CS-90	2.90	0.99	138	2.85	0.99	134	2.98	1.09	136	3.01	0.96	140
CTTS1-DS-90	2.84	1.01	156	2.96	1.09	152	2.84	1.05	154	2.94	1.08	153

(CS) and diagonal symmetric (DS) types. The four fold symmetry for classic and angle-beam tetraskelions is shown in figure 8.7. The hub is square shape and each side of square has length h mm. For CS case $s = 0$ mm (the perpendicular distance from centre of the hub) and $s = (\frac{h_r}{2} - \frac{w_a}{2})$ mm. Two samples for each (batches i & j) were made for the classic designs, but only one each of the angle-beam designs (but still referred to as k & ℓ, for consistency. All samples had elbow angles 90 °. To summarise, the identification of the tetraskelion sample is:

- Batch i: Classic samples CS1-CS-90 and CS2-CS-90 with elbow angle 90 °.
- Batch j: Angle-beam samples CS1-DS-90 and CS2-DS-90 with elbow angle 90 °.
- Batch l: Angle-beam samples ABS1-CS-90 and ABS2-DS-90 with elbow angle 90 °.

The experimental data sets were recorded for all sample of batches i, j, k, & l and graphs were plotted for each set of readings. For each sample seven readings were recorded at the centre of the hub and at off-centre points at the edge of the hub of tetraskelion. For each batch the set of seven readings plotted clearly indicate repeatability or errors. Two graphs for each batch are shown in this chapter and the remainder are graphs are given in the appendix I. The coefficients of linear fit for all tests are given in tables H.1, H.2, H.3, H.4, H.5, and H.6 in appendix H.

8.4.1 Batch i : Classic tetraskelion force artefacts, centre symmetric with elbow angle 90 °

The seven tests on samples CS1-CS-90 and CS2-CS-90 were executed with displacement of step 25 μm until the limit of force actuator was reached. On each sample three independent measurements were taken with the probe tip placed as closely as possible to the centre of hub. A further four independent measurements were taken with the probe tip placed close to the periphery of the hub, an offset from the centre of approximately 1 mm. The general pattern and the magnitudes of tests were similar and more closely so on one specimen than between them. Figures 8.8 and 8.9 show plots of force against displacement form two individual measurements that were executed on sample CS1-CS-90 & CS2-CS-90 as topical example; a complete set of results are plotted that are presented in appendix I. Figure 8.8 shows a case of central loading and figure 8.9 and also shows one of offset loading. Note

that in both cases the measurement is of the total displacement along the line of action of applied force.

The graphs show a straight line that follows a linear fit or best fit of polynomial of order 1. The graphs curve indicated similar trends with acceptable repeatability. the stiffness was notably higher than in previous tests on triskelion samples and test-rig could only supply sufficient force for defection around 0.2 mm. Slightly unexpectedly, this was insufficient to enter in a distinct non-linear region and so simple linear fits were used to estimate the stiffness. The coefficients of linear fit for CS1-CS-90 and CS2-CS-90 are given in tables H.1 and H.2 in appendix H. Note that in all tables, the tests 1, 2, and 3 are for central loading, whereas 4, 5, 6 and 7 are for offset loading. The mean central stiffness is 2781.40 N/m and 2867.80N/m for sample CS1-CS-90 and CS2-CS-90 respectively. The corresponding mean offset position stiffness is 2741.20 N/m and 2569.60 N/m. The R-squared value is closer to 1, showing that the straight line can predict well the value of next step linear spring behaviour.

8.4.2 Batch j : Classic tetraskelion force artefacts, diagonal symmetric with angle 90°

The seven tests were executed on samples CS1-DS-90 and CS2-DS-90 with displacement of step 25 μm until the limit of force actuator was reached. Three independent measurements were taken on each sample with the probe tip placed as closely as possible to the centre of hub. A further four independent measurements were taken with the probe tip placed close to the periphery of the hub, an offset from the centre of approximately 1 mm. The general pattern and the magnitudes of tests were similar, more closely so on one specimen that between them. Both figure 8.10 and 8.11 show plots of force verses displacement form two individual measurements that were executed on sample CS1-DS-90 & CS2-DS-90 as topical example; a complete set of results are plotted that are given in appendix I. Figure 8.10 shows a case of central loading and figure 8.11 and also shows one of offset loading. Note that in both cases the measurements consider total displacement along the line of action of applied force.

The graphs in figures figure 8.10 and 8.11 show a straight line that follows a linear fit or best fit of polynomial of order 1. The graphs curve indicated similar trends with acceptable repeatability. The stiffness was notably higher than in previous tests on triskelion samples and test-rig could only supply sufficient force for defection around 0.2 mm. Slightly unexpectedly, this was insufficient to enter a distinct non-linear region and so simple linear fits were used to estimate the stiffness. The coefficients of linear fit for samples CS1-DS-90 and CS2-DS-90 are given in tablesH.3 and H.4 in appendix H. It is noted in all tables, the tests 1, 2, and 3 for central loading, whereas 4, 5, 6 and 7 are for offset loading. The mean central stiffness is 4617.30 N/m and 4322.80 N/m for sample CS1-CS-90 and CS2-CS-90 respectively. The corresponding mean offset position stiffness is 4521.60 N/m and 4304.70 N/m. The value of R-squared is closer to 1, showing that the straight line can predict well the linear spring behaviour.

8.4.3 Batch k & ℓ : Angle-beam tetraskelion force artefacts, centre & diagonal symmetric with angle 90°

Similar to batches i and j, seven tests on samples ABS1-CS-90 and ABS2-DS-90 were executed with displacement of step 25 μm until the limit of force actuator was reached. For both samples three independent measurements were taken with the probe tip placed as closely as possible to the centre of hub. A further three independent measurements were taken with the probe tip placed close to the periphery of the hub, an offset from the centre of approximately 1 mm. The general pattern and the magnitudes of tests were similar, more closely on one specimen that between them. Figure 8.12 and 8.13 show plots of force against displacement form two individual measurements that were executed on sample ABS1-CS-90 & ABS2-CS-90 as topical example; a complete set of results are plotted that are presented in appendix I. Figure 8.12 shows a case of central loading and figure 8.13 also shows one of offset loading. Note that in both cases the measurements consider total displacement along the line of action of applied force.

The graphs in figures 8.12 and 8.13 also show a straight line that follows a linear fit or best fit of polynomial of order 1. The stiffness was notably higher than in previous tests on triskelion samples and test-rig could only supply sufficient force for defection around 0.2

mm. Slightly unexpectedly, this was insufficient to enter in a distinct non-linear region and so simple linear fits were used to estimate the stiffness. The coefficients of linear fit for ABS1-CS-90 and ABS2-DS-90 are given in tables H.5 and H.6 in appendix H. Note that in all tables, the tests 1,2, and 3 for central loading, whereas 4, 5, 6 and 7 are for offset loading. The mean central stiffness is 1211.88 N/m and 1746.64 N/m for sample CS1-CS-90 and CS2-CS-90 respectively. The corresponding mean offset position stiffness is 1129.65 N/m and 1660.82 N/m. The R-squared value is closer to 1, and this shows that the straight line can predict the value of next step using the linear equation of line which consequently results in having linear behaviour.

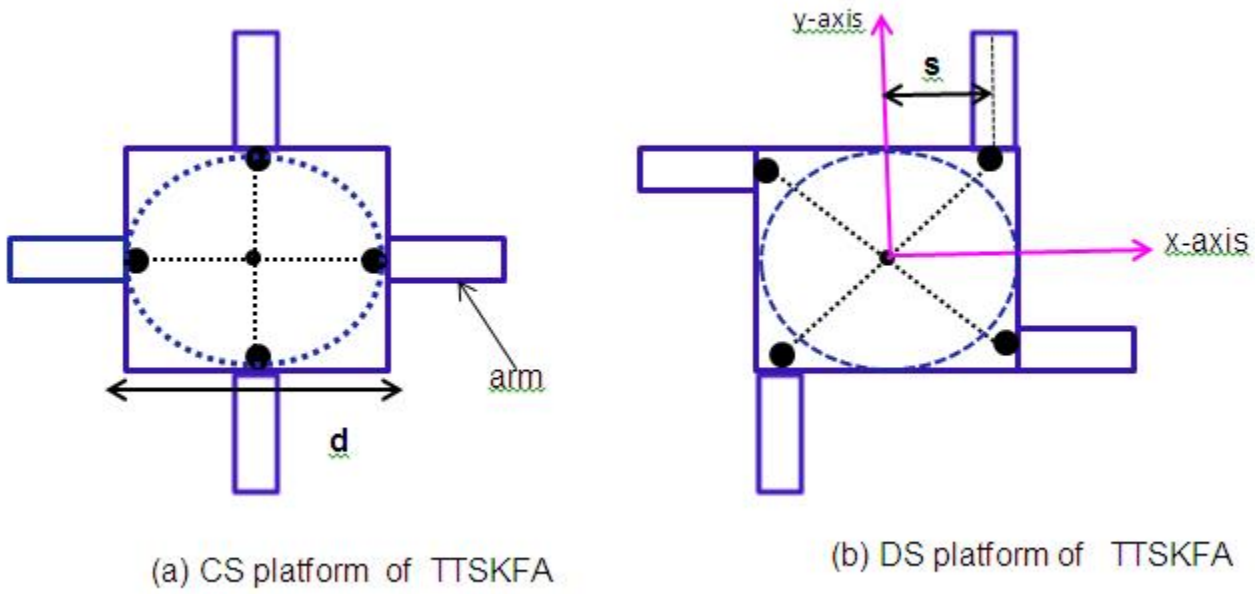

Figure 8.7: Symmetry of the platform for tetraskelion (CS & DS), d is length of square type hub $\simeq$ diameter of the hub, s is perpendicular distance from the platform centre to the arm-cental-line. $s = 0$ for CS case and $s = \frac{d}{3}$ for DS case.

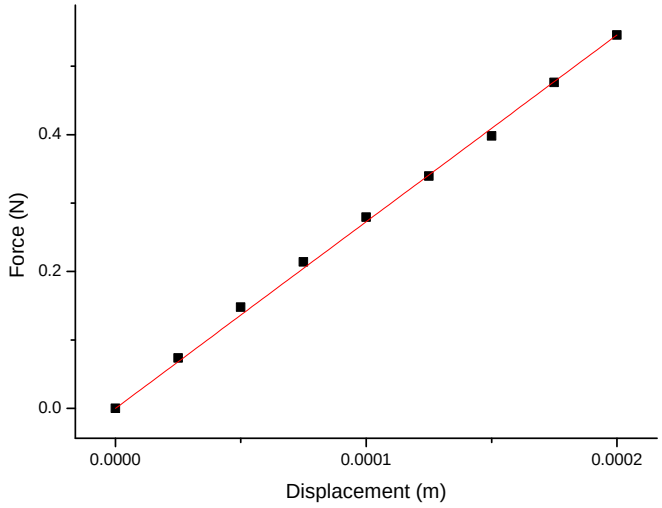

Figure 8.8: Stiffness measured at the centre for classic tetraskelion samples CS1-CS-90.No. 1, Table H.1.

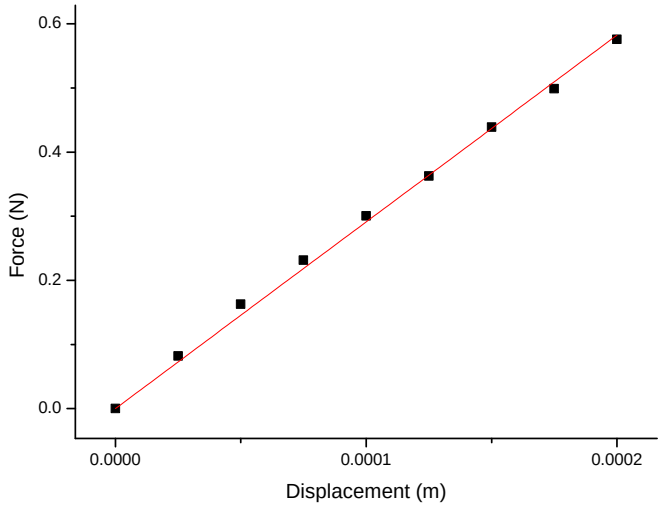

Figure 8.9: Stiffness measured at off-point for classic tetraskelion samples CS1-CS-90.No. 4, Table H.1.

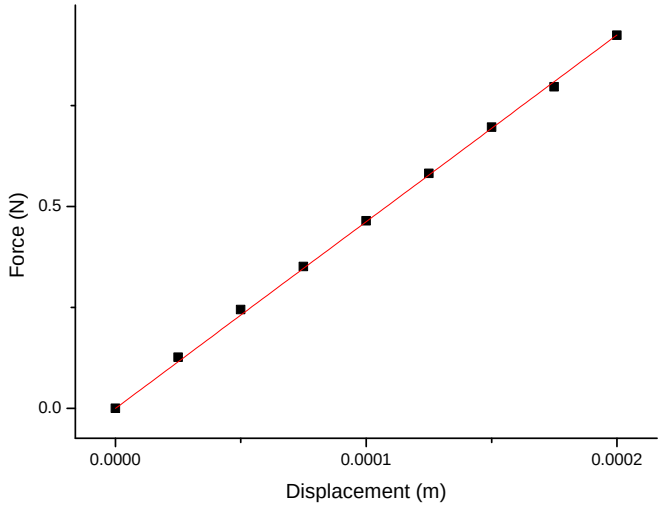

Figure 8.10: Stiffness measured at the centre of hub for classic tetraskelion samples CS1-DS-90 S.No. 3, Table H.3.

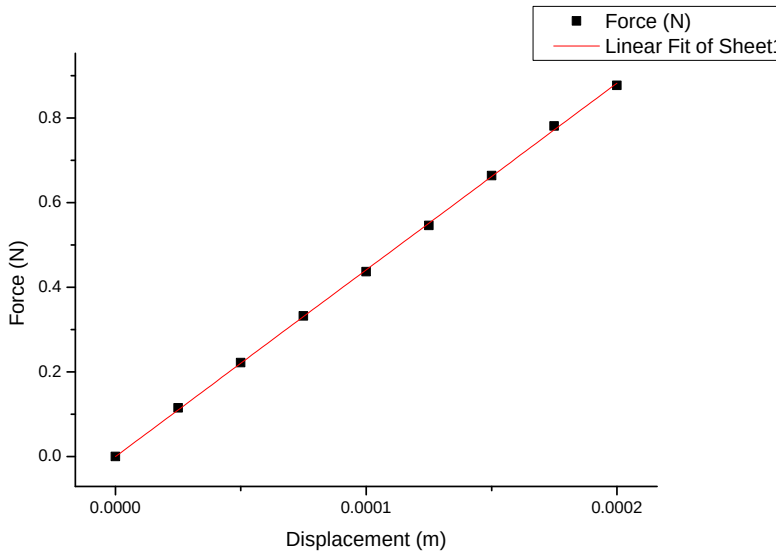

Figure 8.11: Stiffness measured at off-point for classic tetraskelion samples CS2-DS-90 S.No. 4, Table H.4.

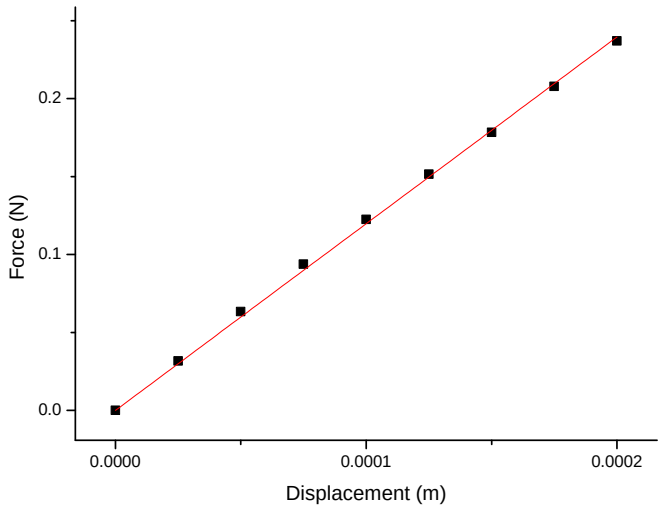

Figure 8.12: Stiffness measured at the centre of hub for classic triskelion samples CS1-CS-90 S.No. 3, Table H.5.

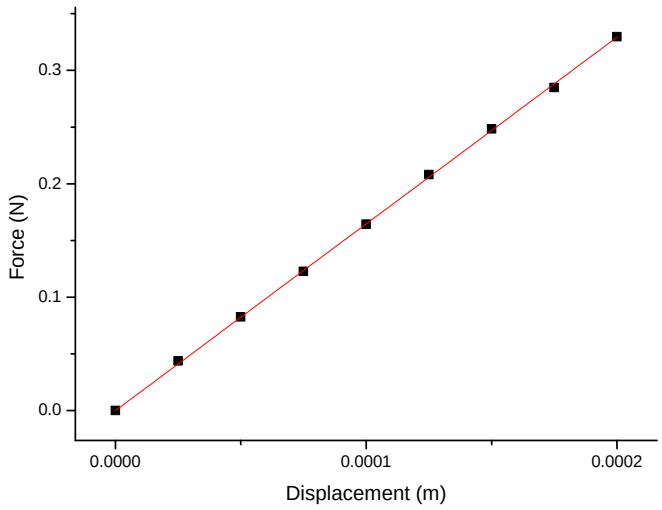

Figure 8.13: Stiffness measured at off-centre point of hub for classic tetraskelion samples CS1-DS-90 S.No. 6, Table H.6

8.5 Stiffness behaviour of tetraskelion force artefacts

The mean linear stiffness values of tetraskelion samples are summarised in table 8.4 taking that data from tables H.1, H.2, H.3, H.4, H.5, and H.6 given in appendix H. Both classic diagonal symmetric samples CS1-DS-90 & CS2-DS-90 have very high value stiffness compared to batches from i and k of tetraskelion force artefacts. There is some variation in average stiffness seen between two samples of each batch but much less between the batches. The classic diagonal symmetric sample CS1-DS-90 has higher stiffness (66% at hub centre and 76% at off-centre points on hub) relative to the classic centre symmetric sample CS1-CS-90. The angle-beam sample ABS1-DS-90 also has a higher value of stiffness as compared to the classic centre symmetric sample ABS1-CS-90, which is (44% & 47% at centre and off-centre points). This variation is due to the dimensional uncertainties of the tetraskelion samples of each batch. Some of the variation is due to dimensional uncertainties, but systematic difference are clear. The lower stiffness on the angle-beam sample compared to an otherwise similar classic design is fully expected because the former contains more flexing elements in series. The difference between otherwise similar diagonal and centre symmetric version is more interesting. It relates to on superficial consideration, it might be assumed that the position of the arms would not be critical in cases where there is purely z-axis translation of the hub, but this is not so. If the long axes of the arms do not pass through the hub centre, then a central force will impose a moment on those axes. For a symmetrical devices a pair of arms will experience equal and opposite moments, maintaining zero net moment on the hub. However, these moments individually affect different sections of the whole suspension, with the $90\,^{\circ}$ elbow angles investigated here an effective torsional term on the arm will become a moment the main bending direction of the suspension beams. It can, therefore, considerably increase the total work that must be done to defect the hub; that is, z-axis stiffness increases. For the scale of devices studied here this effect is highly significant; perhaps to a surprising level. Experimentally, there is approaching a $2:1$ increase for an arm offset of only 1 mm. The distance from the hub centre to the joint with the first flexing element is some what greater in diagonal symmetric devices compared to otherwise similar centre symmetric one. Thus, a small increase in the platform tilt stiffness also occurs as a sperate, additive effect.

The variation in stiffness between samples of each batch could be significantly reduced if these samples are fabricated by using an MSL technique.

Table 8.4: Measured stiffness of classic and angle-beam tetraskelion force artefacts from Tables H.1, H.2, H.3, H.4, H.5, and H.6.

Sample ID	*Linear range*	*R-Squared*	*Average stiffness at*	
	μm		centre of hub N/m	off-centre point N/m
CS1-CS-90	200	0.999	2781.40	2741.20
CS2-CS-90	200	0.999	2867.80	2569.60
CS1-DS-90	200	0.999	4617.30	4521.60
CS1-DS-90	200	0.999	4322.80	4304.70
ABS1-CS-90	200	0.999	1211.88	1129.65
ABS1-DS-90	200	0.999	1746.64	1660.82

8.6 Tetraskelion software program

An analytical linear model for tetraskelion suspensions has been derived in chapter 3. The modelled tetraskelion polymeric system have four arms and four beams as shown in figures 8.2 & 8.4. The design variables of tetraskelion program (platform, suspension beams and material constant parameters) are same to the triskelion software program already discussed in the chapter 4. All the basic equations used in the of enhanced linear model designed in chapter are valid for linear model for the tetraskelion. A new program has been developed to compute, forces, moments, stress, stiffness for tetraskelion polymeric artefacts. The linear model for the tetraskelion is flexible, allowing for changes over its subscript $i = 4$ for the dimensional parameters for arms a_i, beams b_i, orientation angles (α_i & β_i), forces $P_i = (F_i, M_i)^T$ with $F_i = (F_x, F_y, F_z)^T$ and $M_i = (M_x, M_y, M_z)^T$. It provides a valid linear model for tetraskelion suspensions or tetraskelion micro-probes.

The dependency diagram for the tetraskelion program is shown in figure 8.14. The design of the tetraskelion program is similar to the triskelion program that is given in appendix B. The codes for the tetraskelion program are also given in appendix E. The new tetraskelion program works in the same fashion as discussed for the software program for triskelion in chapter 3. The input specification of triskelion software program is given in tables 8.5 and 8.6. The new computed results from the tetraskelion program are discussed in the next section.

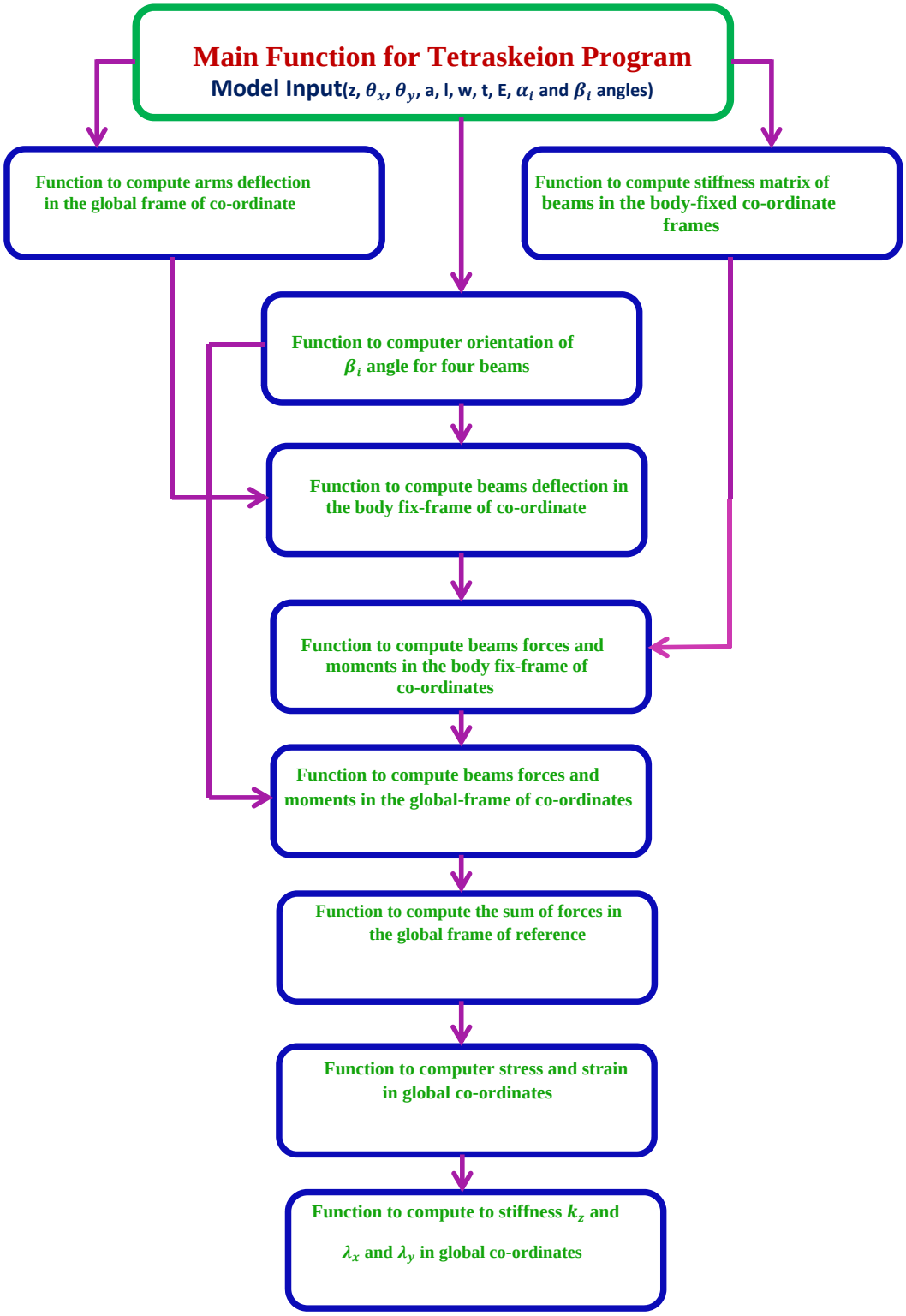

Figure 8.14: Dependency Diagram for Tetraskelion Program

Table 8.5: α_i and β_i for tetraskelion model

Tetraskelion force artefact ID	α_1	α_2	α_3	α_4	β_1	β_2	β_3	β_4
TTSFA-CS-90	0	$(\frac{\pi}{2})$	(π)	$3(\frac{\pi}{2})$	$-(\frac{\pi}{2})$	0	$(\frac{\pi}{2})$	(π)
TTSFA-CS-135	0	$(\frac{\pi}{2})$	(π)	$3(\frac{\pi}{2})$	$-3(\frac{\pi}{4})$	$-(\frac{\pi}{4})$	$(\frac{\pi}{4})$	$3(\frac{\pi}{4})$
TTSFA-CS-180	0	$(\frac{\pi}{2})$	(π)	$3(\frac{\pi}{2})$	$-(\pi)$	$-(\frac{\pi}{2})$	0	$(\frac{\pi}{2})$
TTSFA-DS-90	$-(\frac{\pi}{4})$	$(\frac{\pi}{4})$	$3(\frac{\pi}{4})$	$-3(\frac{\pi}{4})$	$-3(\frac{\pi}{4})$	$-(\frac{\pi}{4})$	$(\frac{\pi}{4})$	$-5(\frac{\pi}{4})$
TTSFA-DS-135	$-(\frac{\pi}{4}$	$(\frac{\pi}{4})$	$3(\frac{\pi}{4})$	$-3(\frac{\pi}{4})$	$-(\pi)$	$-(\frac{\pi}{2})$	0	$-3(\frac{\pi}{2})$
TTSFA-DS-180	$-(\frac{\pi}{4})$	$(\frac{\pi}{4})$	$3(\frac{\pi}{4})$	$-3(\frac{\pi}{4})$	$-5(\frac{\pi}{4})$	$-3(\frac{\pi}{4})$	$-(\frac{\pi}{4})$	$-7(\frac{\pi}{2})$

Table 8.6: Input parameters specification for TSFAs with $60\,^\circ, 90\,^\circ, 120\,^\circ, 150\,^\circ$ & $180\,^\circ$.

S.No.	Parameter	Values & Unit
1	z	5×10^{-6}m
2	θ_x	1×10^{-3}rad
3	θ_y	1×10^{-3}rad
4	$a = (h_r + a_\ell)$	$(1.5 + 0.002)$m
5	ℓ	0.004m
6	w	0.001m
7	t	0.0002m
8	E_s	2.5×10^9pascal
9	α_1 , α_3 , & α_3	table(8.5)
10	β_1 , β_3 , & β_3	table(8.5)

8.7 Numerical experiments for tetraskelion force artefacts

Numerical experiments were carried out for centre symmetric and diagonal symmetric tetraskelion force artefacts TTSFA-CS-90, TTSFA-DS-90, TTSFA-CS-135, TTSFA-DS-135, TTSFA-CS-180, & TTSFA-DS-180 with elbow angles $90\,^\circ$, $135\,^\circ$ and $180\,^\circ$ as shown in figure 8.15 to 8.20 by using the procedure just discussed. Some of the tests cover changes in parameters where the effects in linear model can be strongly intuited from the basic beam theory, where the other such a variations in elbow angles are new. The whole set therefore acts simultaneously to check the software implementation and to provide new data for designers.

8.7.1 Numerical experiments phase 4: Investigation of arm length a_ℓ

The numerical experiments for triskelion force artefacts are already discussed in the chapter 4. The same strategy has been adopted for these experiments. The numerical experiments for all tetraskelion force artefacts were performed with displacement only of z=5×10^{-6} μm using the input specification given in tables 8.5 and tables 8.6.

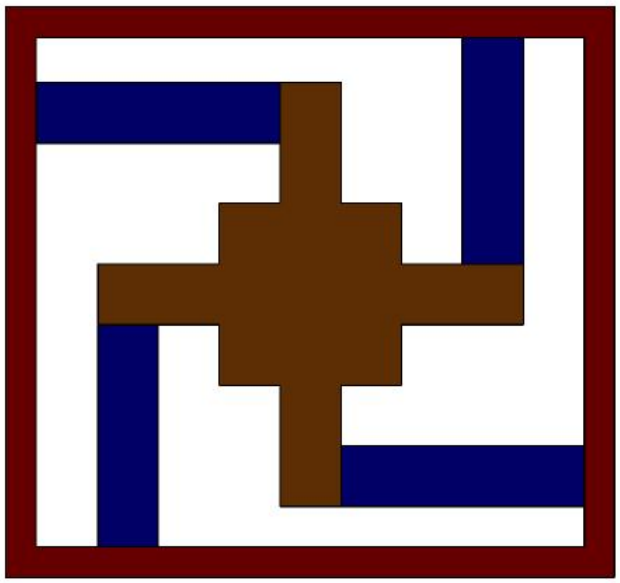

Figure 8.15: The simplified model for tetraskelion force artefacts, centre symmetric (TTSFA-CS-90) with elbow angle 90 °.

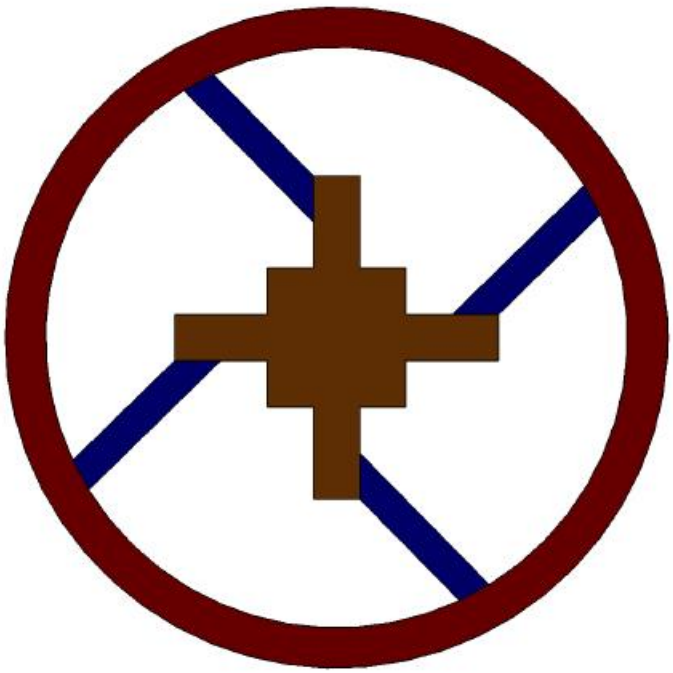

Figure 8.16: The simplified model for tetraskelion force artefacts, centre symmetric (TTSFA-CS-135) with elbow angle 135 °.

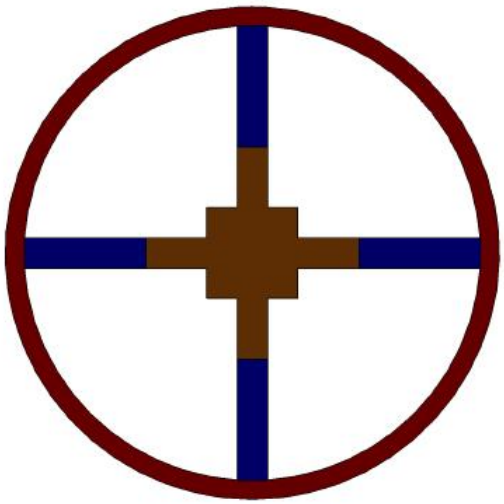

Figure 8.17: The simplified model for tetraskelion force artefacts, centre symmetric (TTSFA-CS-180) with elbow angle 180 °.

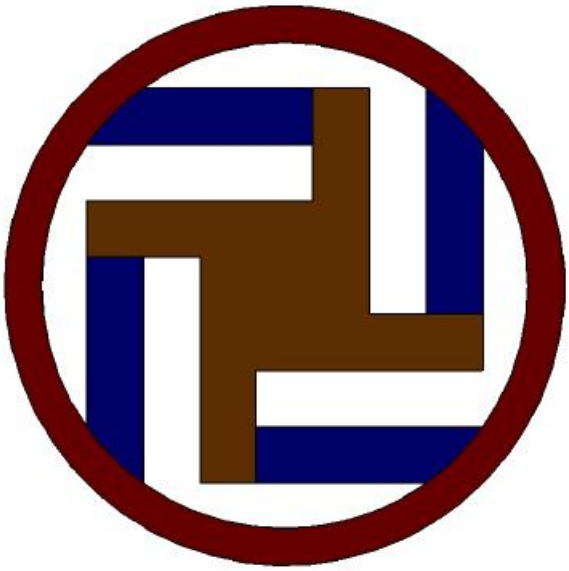

Figure 8.18: The simplified model for tetraskelion force artefacts, diagonal symmetric (TTSFA-DS-90) with elbow angle 90 °.

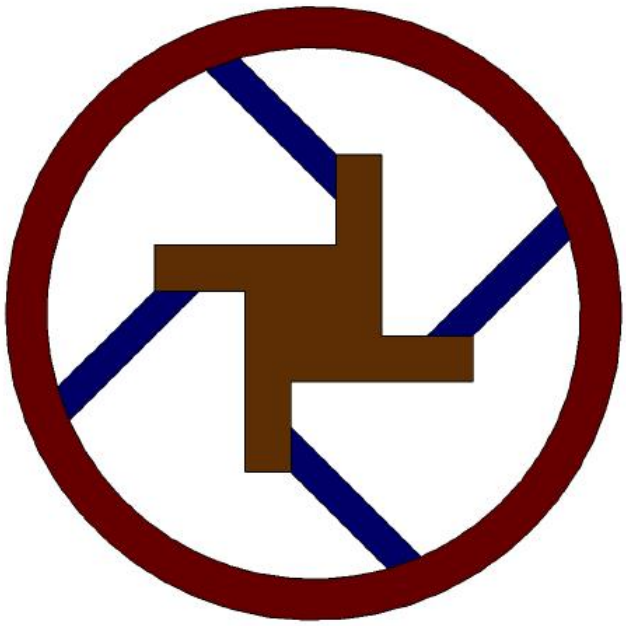

Figure 8.19: The simplified model for tetraskelion force artefacts, diagonal symmetric (TTSFA-DS-135) with elbow angle 135 °.

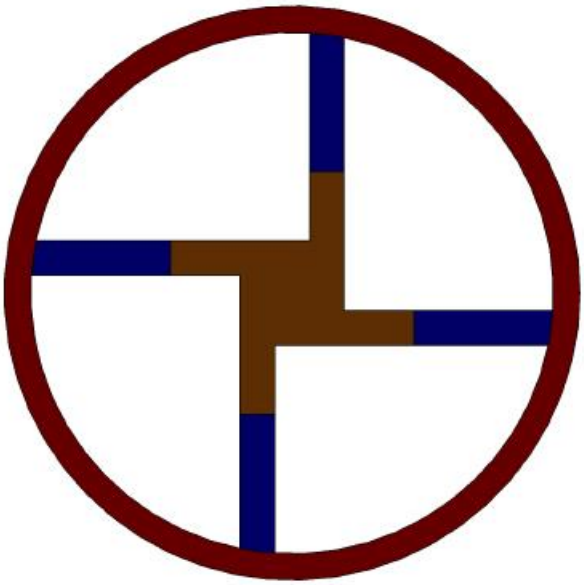

Figure 8.20: The simplified model for tetraskelion force artefacts, diagonal symmetric (TTSFA-DS-180) with elbow angle 180 °.

Relationship between a_ℓ and k_z

The computed value of stiffness at each elbow angle are shown in figure 8.21. It is evident from the figure 8.21 that all tetraskelion force artefacts have same value of stiffness i.e. k_z is independent of the arm length. This result was expected from general experience because the arm length interacts with the platform tilt, but not interaction.

Relationship between a_ℓ and λ_x

The values of torsional stiffness λ_x computed by the tetraskelion software program are shown in figure 8.22. It is evident from the figure that λ_x depends upon the arm length and elbow angle of the tetraskelion artefacts. At all arm lengths, the tetraskelion force artefacts with elbow angle 90° has a lower value of torsional stiffness λ_x and it rises steadily with increasing elbow angle. Figure 8.22 clearly shows that by increasing the length of arm, the value of λ_x also increases for tetraskelion force artefacts. The tetraskelion force artefacts TTSFA-CS-90 and TTSFA-DS-90 with elbow angle 90° have a lower value of torsional stiffness λ_x.

8.7.2 Numerical experiments phase 5: Investigation of stiffness k_z and beam parameters (ℓ, w, & t)

Similar to the numerical experiments that have been discussed in chapter 4 (section 4.6), further numerical experiments are carried out for tetraskelion force artefacts TTSFA-CS-90, TTSFA-DS-90, TTSFA-CS-135, TTSFA-DS-135, TTSFA-CS-180, & TTSFA-DS-180 for the translational motion of the platform only using the same strategy to investigate the relationship between k_z and beam parameters(ℓ, w, t).

Relationship between ℓ and k_z

The computed value of stiffness k_z as beam length is changed for all tetraskelion force artefacts are shown in figure 8.23. It is evident from figure 8.23 that all tetraskelion force artefacts have the same value of stiffness k_z. As we increase the length of the beam, the stiffness k_z also decreases and thus closely follows the inverse cubic law of individual suspension subject of the z-displacement only. The stiffness k_z is independent of the elbow angle of the tetraskelion force artefacts if the beam parameters are unchanged. This was

expected by the linear elastic model that pure translation of the platform does net impose twist. The actual stiffness value for the beam length of 4mm and 8mm are 1250.00 N/m and 156.25 N/m (for E = 2.5 GPa), with a ratio 8 that is expected by the cubic law.

Relationship between w and k_z

The computed values of stiffness k_z as beam width changes of all tetraskelion force artefacts, as shown in figure 8.24. Their stiffness is independent of the elbow angle, as expected. It is evident from the figure 8.24 that the value of the stiffness k_z is increased by increasing the beam width, closely linearly as expected of an individual beam under simple defection. The actual stiffness values for the beam width of 1mm and 2mm are 1250.00 N/m and 2500.00 N/m (for E = 2.5 GPa), with a ratio 2 that is expected.

Relationship between t and k_z

The computed values of stiffness k_z as beam thickness is varied for all tetraskelion force artefacts are shown in figure 8.25. It is evident that the value of the stiffness k_z for all tetraskelion force artefacts also increases by increasing the beam thickness. The actual stiffness value for the beam thickness of 0.2 mm and 0.4 mm are 1250.00 N/m and 156.25 N/m (for E = 2.5 GPa), with a ratio 8 that is expected by the cubic law.

8.7.3 Numerical experiments phase 6: Investigation of torsional stiffness λ_x and beam parameters (ℓ, w, & t)

Similar to the experiments in phase 3 of chapter 4, further numerical experiments to investigate the relationship between the beam parameters (ℓ, w, & t) and the torsional stiffness λ_x are carried out for tetraskelion force artefacts TTSFA-CS-90, TTSFA-DS-90, TTSFA-CS-135, TTSFA-DS-135, TTSFA-CS-180, & TTSFA-DS-180 with elbow angles 90 °, 135 ° and 180 ° for pure rotation motion x-axis of the platform.

Relationship between ℓ and λ_x

The computed values of torsional stiffness λ_x as beam length varies for all tetraskelion force artefacts are shown in figure 8.26. It is evident from the figure 8.26 that for any length the tetraskelion force artefact, centre symmetric with elbow angle 90 ° has the lower

value of torsional stiffness λ_x and as we increase the elbow angle, the value of torsional stiffness also increases steadily but not linear. If we increase the beam length, the value of torsional stiffness λ_x decreases. As the platform tilts, the suspension beams are subject to a combination of end-force, end-moments (bending) and end moments (axial torsion); the exact combination will differ with parameters such as elbow angle and for the individual beams according to the orientation compared to the tilt direction. All of these effect will be expected to reduce the over all stiffness as the length is increased; for a simple the relationship is inverse linear for torsion, inverse square for other moments and inverse cubic for the direct force. Linear and cubic laws therefore limit the range of actual behaviour. For the geometries studied the net effect is quite close to an inverse square law. Thus, the relationship with length approaches the inverse square law expected for both torsion and bending modes of a individual suspension beam. The actual stiffness value for the beam length of 0.4 mm and 0.8 mm are 0.0070.00 N/rad and 0.00256 N/rad (for E = 2.5 GPa), with a ratio 2.7.

Relationship between w and λ_x

The computed torsional stiffness λ_x for all tetraskelion force artefacts are shown in figure 8.27. These results show the torsional stiffness λ_x again varies slightly with the elbow angle; it is consistently lowest for the tetraskelion force artefacts with the elbow angle 90 °. The proportional change with the elbow angle is the same for all widths. The torsional stiffness λ_x for all tetraskelion force artefacts increases linearly with increasing the beam width as expected for both torsion and bending modes of a suspension beam. The actual stiffness value for the beam width of 0.1mm and 0.2mm are 0.01417 N/rad and 0.0070.00 N/rad (for E = 2.5 GPa), with a ratio 2 that is expected.

Relationship between t and λ_x

The computed torsional stiffness λ_x increases as beam thickness varies for all tetraskelion force artefacts is shown in figure 8.28. The torsional stiffness increases λ_x rapidly by increasing the thickness of the beam and also increases slightly with the elbow angle of the tetraskelion force artefacts. The relationship with thickness approaches the cubic law expected for both torsion and bending modes of an individual suspension beam. The ac-

tual stiffness value for the beam thickness of 0.2 mm and 0.4 mm are 0.0070 N/rad and 8.85×10^{-4} N/rad, with a ratio 7.8 that is close to 8 expected by cubic law.

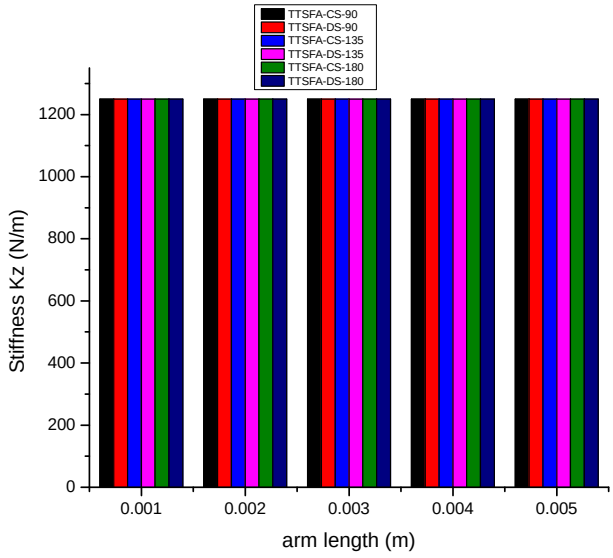

Figure 8.21: Graph for variable arm's length verses computed results for stiffness k_z of tetraskelion force artefacts TTSFA-CS-90, TTSFA-DS-90, TTSFA-CS-135, TTSFA-DS-135, TTSFA-CS-180, & TTSFA-DS-180 with elbow angles 90 °, 135 ° and 180 °

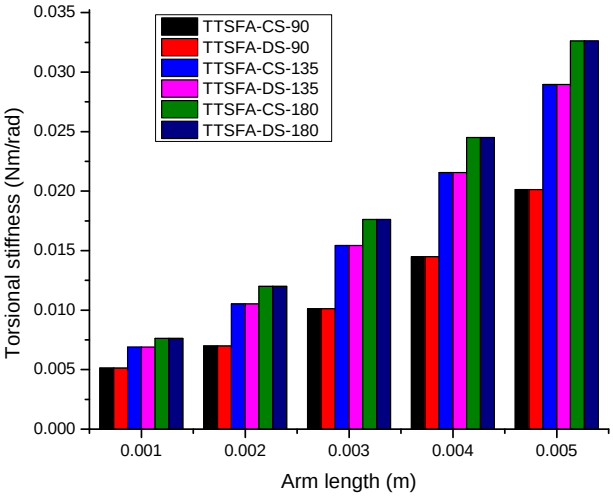

Figure 8.22: Graph for variable arm's length verses computed results for torsional stiffness λ_x of tetraskelion force artefacts TTSFA-CS-90, TTSFA-DS-90, TTSFA-CS-135, TTSFA-DS-135, TTSFA-CS-180, & TTSFA-DS-180 with elbow angles 90 °, 135 ° and 180 °.

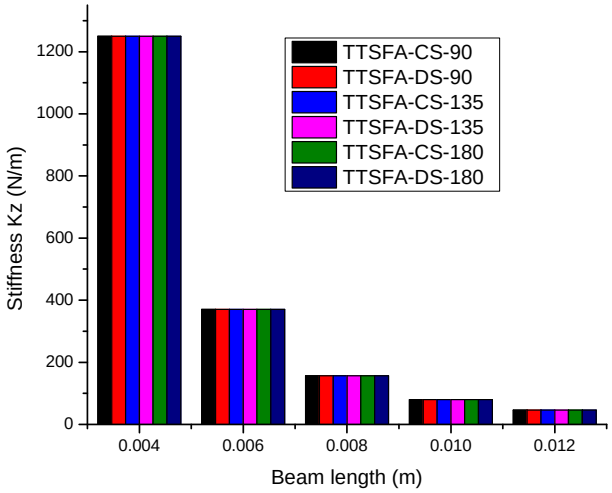

Figure 8.23: Graph for beam's length verses computed results for stiffness k_z of tetraskelion force artefacts TTSFA-CS-90, TTSFA-DS-90, TTSFA-CS-135, TTSFA-DS-135, TTSFA-CS-180, & TTSFA-DS-180 with elbow angles 90 °, 135 ° and 180 °

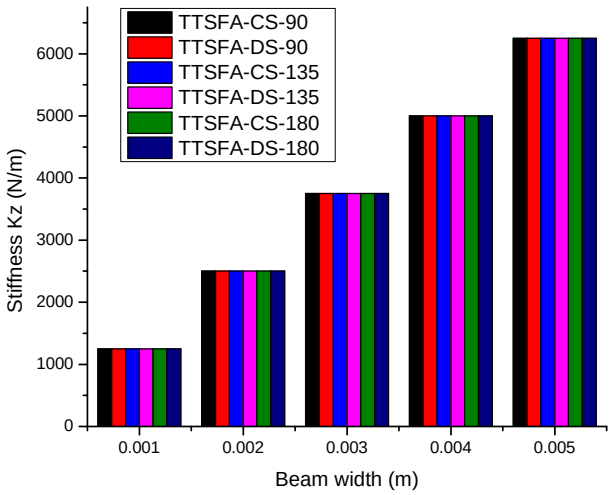

Figure 8.24: Graph for variable beam's length verses computed results for stiffness k_z of tetraskelion force artefacts TTSFA-CS-90, TTSFA-DS-90, TTSFA-CS-135, TTSFA-DS-135, TTSFA-CS-180, & TTSFA-DS-180 with elbow angles 90 °, 135 ° and 180 °.

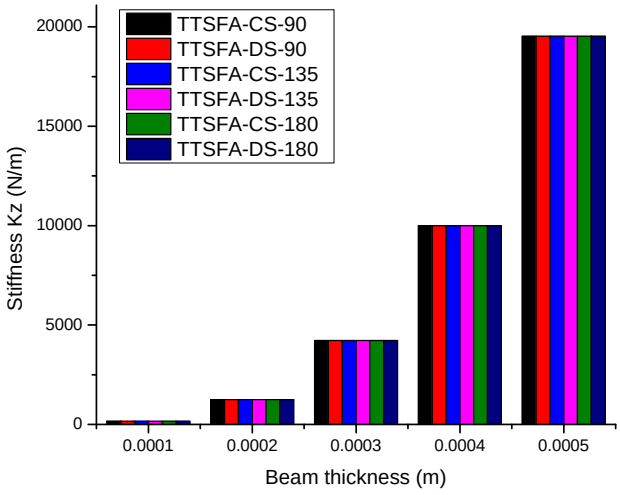

Figure 8.25: Graph for beam's thickness verses computed results for stiffness k_z of tetraskelion force artefacts TTSFA-CS-90, TTSFA-DS-90, TTSFA-CS-135, TTSFA-DS-135, TTSFA-CS-180, & TTSFA-DS-180 with elbow angles 90 °, 135 ° and 180 °

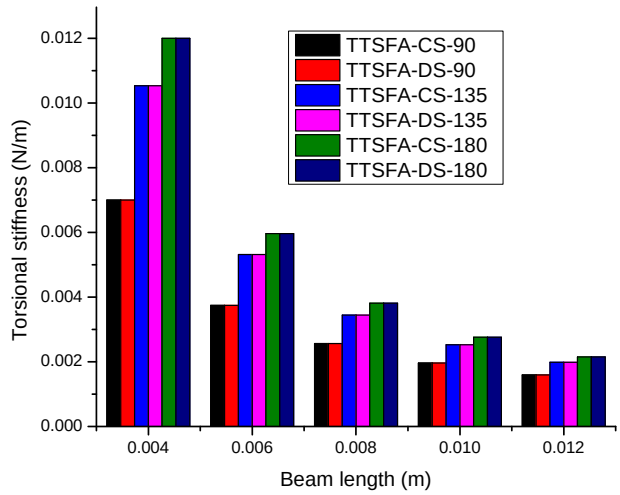

Figure 8.26: Graph for variable beam's length verses computed results for torsional stiffness λ_x of tetraskelion force artefacts TTSFA-CS-90, TTSFA-DS-90, TTSFA-CS-135, TTSFA-DS-135, TTSFA-CS-180, & TTSFA-DS-180 with elbow angles 90 °, 135 ° and 180 °.

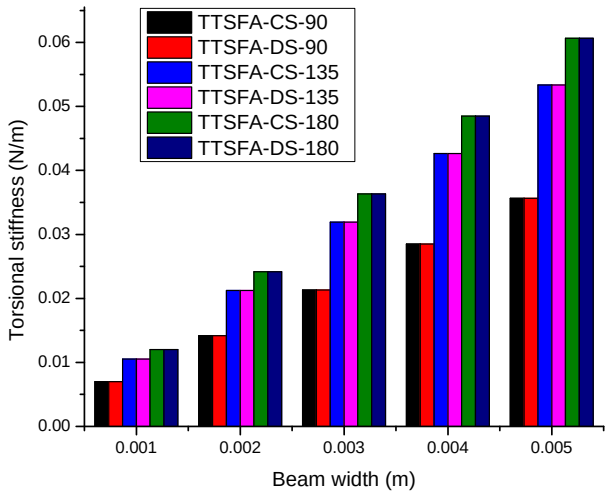

Figure 8.27: Graph for beam's width verses computed results for torsional stiffness λ_x of tetraskelion force artefacts TTSFA-CS-90, TTSFA-DS-90, TTSFA-CS-135, TTSFA-DS-135, TTSFA-CS-180, & TTSFA-DS-180 with elbow angles 90 °, 135 ° and 180 °

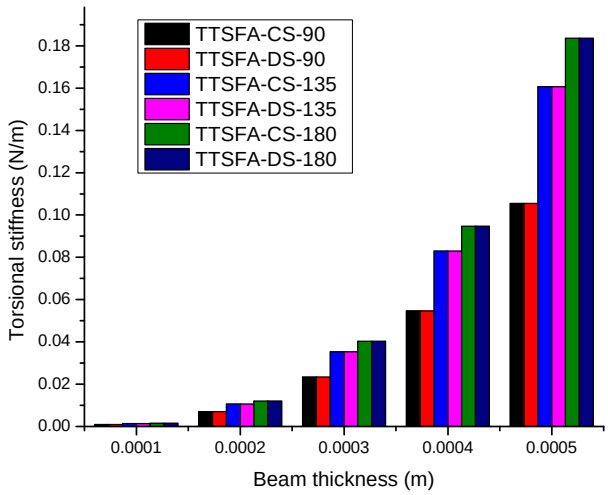

Figure 8.28: Graph for variable beam's thickness verses computed results for torsional stiffness λ_x of tetraskelion force artefacts TTSFA-CS-90, TTSFA-DS-90, TTSFA-CS-135, TTSFA-DS-135, TTSFA-CS-180, & TTSFA-DS-180 with elbow angles 90 °, 135 ° and 180 °.

8.8 Discussion of computed results

The computed values of stiffness k_z and λ_x for input specifications given in table for tetraskelion force artefacts TTSFA-CS-90, TTSFA-DS-90, TTSFA-CS-135, TTSFA-DS-135, TTSFA-CS-180, & TTSFA-DS-180 with elbow angles of $90\,^\circ$, $135\,^\circ$ and $180\,^\circ$ have been critically analysed and may be summarised as follows:

1. As is expected by the linear elastic model, when we increase the arm length of the platform or change in the elbow angle of any tetraskelion force artefacts with the same input specifications. The value of k_z is found to be 1250 N/m. This true for all cases (see figure 8.21).

2. Beam bending stiffness indicates that when we increase the ℓ of the suspension beam, the stiffness decreases with $(\ell + \triangle\ell)^3$, where $\triangle\ell$ is the increment in the beam length. Moreover, a z-translating platform effectively places only force-displacements related loads on the ends of the idealised suspension beams, so the stiffness k_z is independent of the elbow angle. Both these features are confirmed in figure 8.21.

3. The computed axial bending stiffness k_z increases linearly with suspension beam width, and independent of the elbow angle of all tetraskelion force artefacts as shown in figure 8.24. This is expected physically from the behaviour individual beams in a simple bending.

4. The computed axial stiffness k_z indicates that when we increase the beam thickness t, the stiffness increases by a factor $(t + \triangle t)^3$, where $\triangle t$ is the increment in the beam thickness as shown in the figure 8.25. It is clear that axial stiffness is independent of the elbow angle of all tetraskelion force artefacts. These results are consistent with the physical behaviour in which bending nodes are present in the suspension beams; the linear elastic model discounts possible cross-coupling of nodes.

5. The computed torsional stiffness λ_x for all tetraskelion force artefacts are shown in the figure 8.22, 8.26, 8.27 and 8.28. These results show that the torsional stiffness λ_x is dependent of both arm length and elbow angles of the tetraskelion force artefacts. Figure 8.22 clearly indicates the torsional stiffness increases gently with increases in the platform arm length on the elbow angle and also increases a little with elbow

angle at all length tested. The value is more sensitive to the elbow angle at larger arm lengths. The increase in the arm length follows closely a square law.

8.9 Conclusion

The significantly enhanced functionality of new implementation of the enhanced linear elastic model for triskelion planar suspensions has been demonstrated successfully by setting up a model for four-fold symmetric tetraskelion. The model has generally been validated by comparison of its prediction for pattern of behaviour to those of physical samples. The experimental results summarised in table 8.4 for all samples of tetraskelion force artefacts show that angle-beam tetraskelion samples (ABS1-CS-90 and ABS1-DS-90 with elbow angle 90 °) that follow the classic (rigid arm) design. All samples have linear behaviour for small displacements up to at least 200 μm region (table 8.4). The linear range of tetraskelion force artefacts could be increased by using an actuator of bigger size. These devices were tested on the system designed for lower-stiffness triskelion samples and it would not reliably drive them into a clear non-linear region. General physical arguments imply that the more over-constrained tetraskelion would have proper linearity than comparable sizes of triskelion. Clearly, though, a useful 'linear' region is available in practice.

For suspension elements of the same physical size, adding a fourth arm would be expected to increase device stiffness, and this is confirmed. Angle-beam triskelion are, as expected, less stiff than otherwise similar classic tetraskelions (i.e. that having rigid arms). For the scale of devices studied, the angle-beam triskelions typically have stiffness quite similar to those of classic triskelions. It has been shown that the stiffness of a device of given size can be substantially increased by offsetting the axes of the arms relative to the centre of hub.

The numerical experiments have been performed for classic tetraskelion force artefacts (CS and DS) having platform arm length 1 mm and 5 mm; suspension beam length between 4 mm and 12 mm, width between 1 mm and 5 mm and thickness between 0.1 and 0.5 mm and elbow angles, 90 °, 135 ° and 180 °. These type of results have not been

seen in any public domain documents. The tetraskelion software program predict the same stiffness values CS and DS force artefacts (TTSFA-CS-90, TTSFA-DS-90, TTSFA-CS-135, TTSFA-DS-135, TTSFA-CS-180, & TTSFA-DS-180 with elbow angles 90 °, 135 ° and 180 °) with the same choices of beam dimensions. The physical experiments have shown a pretty big difference in stiffness values for CS and DS force artefacts that are given in table 8.4. If the model is implemented properly, this suggests the more heavily over-constrained tetraskelions is not satisfactorily modelled by these methods.

The computed axial stiffness of the platform k_z in these numerical experiment is independent of the elbow angle and arms length. The linear elastic model imposes restrictions (relating to idealised connections for transmission of forces between the elements) that allow only z-translation of the platform only couple to the bending modes of the suspension beams of tetraskelion models (in the own xz planes). The linear elastic model works as expected on the other dimensional parameters, consistent with linear elastic theory for the individual beams. These results will be compared to the linear and non-linear behaviour of a range of physical polymeric tetraskelion force artefacts in the next chapter.

The numerical experiments only studied axially-symmetric designs. It is confirmed by the new tetraskelion program that all direction of the platform tilt provide the same torsional stiffness λ_x. Looking consistently across all the designs, there is a tendency for torsional stiffness λ_x to increase slightly with the elbow angle. This effect is probably not strong enough to be a major design consideration, at least for the very small moments for which the linear elastic model might be assumed adequate. However, it suggests that centre symmetric or diagonal symmetric tetraskelion force artefacts might allow a compact design useful for micro probes, where modest torsional stiffness is required. There might also be other cases for using a large elbow angle for force transfer artefacts, where highest torsional stiffness is desirable.

Chapter 9

Best Choices of triskelion and tetraskelion force artefacts for industrial applications

9.1 Introduction

This chapter describes the validation of triskelion and tetraskelion samples by using the two software programs (triskelion and tetraskelion software simulations). Both Triskelion and tetraskelion software programs are based on enhanced linear elastic models for the variant design of triskelion force artefacts. The enhanced linear elastic model has the ability to set independently all potential design parameters such as the elbow angles of triskelion force artefacts (which appear not to be have been studied perviously).

Linearity is extracted from the whole range of experiments on the classic and angle beams triskelion and tetraskelion force artefact samples. The performance and linear ranges were investigated for both triskelion and tetraskelion force artefact samples, both to determine valid ranges for the models and to established convenient ranges for practical artefacts.

Moreover, the numerical experiments are extended to explore the effects of the elbow angles for the best designs of micro probe suspension and force artefacts for industrial applications.

9.2 Measurements of beam parameters of triskelion and tetraskelion force artefact's samples

The characterization of all the physical samples was discussed in detail in chapter 5. The simple manufacturing method used could lead to relatively large sample-to-sample and batch-to-batch variations in beam parameters that are important when comparing model results. The length (ℓ) and width (w) of the beam were measured with good precision and repeatability by either microscope (using a WYKO NT2000 Profiling System) or digital Vernier Calipers. Measurement of thickness (t) has higher uncertainty because the dimension is smaller and the beams are, in practice, neither uniform nor flat. Again, different methods were used on different samples. The particular significance here is that beam stiffness depends on the cube of thickness and so this measurement uncertainty reflects strongly into how closely it is reasonable to expect model to compare to physical tests; the dependency on width and inversely on length cubed will likely have smaller significance. The measured values are reported in tables 5.3, 5.4, 8.2 and 8.3 and the relevant ones repeated within the Tables 9.1 to 9.4 of this chapter.

The other critical parameter is Young's modulus, which is poorly defined for the hand-mixed resins used in this work. It was impractical to measure it on the thin beams of the actual samples. However, device stiffness is in principle proportional to Young's modulus. This allows it, subject to maintaining physically sensible values, to be used rather like an empirical scaling factor in the models.The general literature suggests that it is likely to be in the region of 2 GPa to 3 GPa for tests on bulk material (polymer) of this type. A preliminary study of the model prediction indicated that taking E $\approx$ 2.9 GPa tended to give a better match to the test results than did lower values. Unless otherwise stated, it is used in all the comparisons discussed in this work.

9.3 Validation of classic and angle-beam triskelion force artefacts with elbow angle $60\,^\circ$

The classic triskelion micro probe suspension design with elbow angle $60\,^\circ$ is very popular in industries. For example, IBS and NPL have a used classic triskelion micro probe

suspension design with 60 ° elbow angle. Jones [148] has also adapted a classic triskelion micro probe suspension design with 60 ° for force aretfacts. The first example for linear model prediction is considered for classic triskelion force artefact's sample CTS2-60 with elbow angle 60 ° having nominal beam parameters (ℓ = 0.00412 m , w = 0.00103 m and t = 0.000190 m table 5.3 & or repeated table 9.1) and Young's modulus = 2.9×10^9 Pa (The exact value of Young's modulus for triskelion and tetraskelion polymeric samples is not know, but for polymer the Young's modulus value lies between 2-3$\times^9$ Pascals.

The triskelion software program predicts the stiffness k_{z_p} as 918 N/m for sample CTS2-60 of force artefact with elbow angle 60 °. The experimental value of stiffness $k_{z_{exp}}$ for sample CTS2-60 was measured by the bestspoke test-rig method presented in chapter 6 in table 6.2 is 1100 N/m at the centre of hub and 1032 N/m at off-centre point of the hub. Thus the ratio $k_{z_{exp}}/k_{z_p}$ for both experimental values at centre of hub & off-centre point and validated value is found 1.19 and 1.12 respectively. The validated value is closer to experimental values at the centre of hub and off-centre point, indicating errors 178 and 113 N/m respectively.

The second example for linear model prediction considered here is for the sample ABTS1 of angle-beam triskelion force artefact have beam parameter (ℓ = 0.00410 m, w = 0.00101 m and t = 0.000159 m table 5.4 or repeated table 9.2). The triskelion software program predicts the stiffness k_{z_p} equal 512.48 N/m for sample ABTS1-60 of force artefact with elbow angle 60 °. The experimental value of stiffness $k_{z_{exp}}$ for sample ABTS2-60 was measured and presented in chapter 7 in table 7.1 is 536 N/m at the centre of hub and 503 N/m at off-centre point of the hub. Thus the ratio $k_{z_{exp}}/k_{z_p}$ of experimental values at centre of hub & off-centre point and validated value is found 1.04 and 0.98 respectively. The validated value is closer to experimental values at the centre of hub and off-centre point, indicating errors 24.47 and -9.1 N/m respectively. The validation experiment predicts the stiffness value that was closer to the experimental values at their centre of the hub and the off-centre point of the hub of sample ABTS1-60 with elbow angle 60 °.

The third example for linear model prediction considered here also relates to the sample of classic triskelion force artefact CSTS1-604 with elbow angle 60 ° that have beam parameters (ℓ = 0.00420 m, w = 0.001 m and t = 0.000350 m table 5.3 or repeated table 9.1). The thickness of sample CSTS1-60 was doubled as compared to sample CTS1-60 and CTS2-60. The triskelion software program predicts the stiffness k_{z_p} equal 5034 N/m for sample CSTS1-604 of the force artefact. The experimental value of stiffness $k_{z_{exp}}$ for sample ABTS2-60 was measured 5288 N/m at the centre of the hub and 5022.37 N/m at off-centre point presented in chapter 6 in table 6.2. The ratio $k_{z_{exp}}/k_{z_p}$ of experimental values at centre of hub & off-centre point and validated value is found 1.05 and -0.99 respectively. The validated value is closer to experimental values at centre of hub and off-centre point indicating errors 253.52 and -0.0025 N/m respectively.

9.4 Effects of elbow angle on classic and angle-beam triskelion force artefacts

The results of various physical and computational experiments on classic and angle-beam triskelion force artefact designs having elbow angle of 60 °, 90 ° and 120 ° are presented and discussed in chapters 6 & 7 and 4 & 8. The main values are also summarized within in tables 9.5, 9.6, 9.7 and 9.8. The predicted and measured values of stiffness are at similar numerical levels and show some patterns of variation with geometrical patterns. In a few cases the divergence between predicted and actual stiffness is usually large, but there is no evidence that it is fundamentally associated with a particular design.

Taking account of inevitable uncertainties, the novelty and validity of an enhanced linear elastic model is confirmed from the validation experiments of classic and angle-beam sample of triskelion force artefacts. The validation results also confirm the validity of the triskelion software program. The triskelion software program discussed in chapter 4 is considered a powerful tool for predicting the stiffness of classic and angle-beam samples of triskelion force artefacts.

9.5 Performance and linear ranges for triskelion for artefacts

The performance of classic and angle-beam samples of triskelion force artefacts are shown in figures 9.1, 9.2, 9.3 and 9.4 for their linear region. The angle-beam samples of force artefacts are more sensitive as compared to classic samples of triskelion force artefacts. The performance of classic samples of force artefacts are shown in figures 9.1 and 9.2. It is important that force transfer artefacts present a clearly force-displacement curve (i.e. constant stiffness) over a useful working range of displacement. This was explored in section 6.5. The 'linear' range was defined as coefficient β_1 in cubic equation 6.10. The actual characteristics of a selection of classic and angle-beam triskelion force artefacts are summarized within their linear ranges in figure 9.1 to 9.4. The classic samples with elbow angle 60 ° have a higher range of 500 μm as compared with having elbow angle 90 ° and 120 °, which have a working linear region of 400 μm and 250 μm respectively.

The angle-beam samples have working linear region a little higher than those of the otherwise similar classic designs: 600 μm, 400 μm and 300 μm for elbow angles 60 °, 90 ° and 120 ° respectively. The performance of angle-beam force artefacts is show in figures 9.3 and 9.4.

9.6 Effects of elbow angle on classic and angle-beam tetraskelion force artefacts

The experimental and predicted results of classic and angle-beam tetraskelion samples of force artefacts are presented in tables 9.9, 9.10 9.11 and 9.12. It was expected that the addition of an extra leg in triskelion suspension will also increase the stiffness of the device. Both predicted and experimental results confirmed that tetraskelion samples of force artefacts have higher values of stiffness as compared to triskelion samples of either type of force artefacts. Angle-beam samples of tetraskelion force artefacts have a lower value of stiffness that is closer to that of triskelion samples of force artefacts. The validated values of stiffness are closer to the experimental values of stiffness. The ratio $k_{z_{exp}}/k_{z_p}$ experimental values at centre of hub & off-centre point and predicted values for tetraskelion and angle beam samples of force artefacts CTTS1-CS-90, CTTS2-CS-90 °, CTTS1-CD-90, CTTS2-CD-90,

ABTTS2-90-CS & ABTTS1-CD-90 with elbow angles 90 ° are given in Tables 9.9, 9.10, 9.11 and 9.12. The experimental values of stiffness at off-centre points of the hub are also seen to be closer to the predicted value of stiffness. The predicted results presented in tables 9.6 and 9.8 confirm the novelty and stability of enhanced linear elastic model. The accuracy of the tetraskelion software program is confirmed by the predicted values of stiffness for those novel designs, within the valid range of linear elastic model. Thus, the enhanced linear model may also be used to predict the stiffness of any "n" legs suspension design for micro probe or force artefacts by the relatively trivial adaptation of the current software program.

9.7 Performance and linear ranges for tetraskelion for artefacts

The working performances of classic and angle-beam samples of force artefacts are seen as being similar to classic and angle-beam triskelion samples of force artefacts. The linear range for classic and angle-beam tetraskelion force artefacts samples are around 200μm. The classic and angle-beam tetraskelion samples of force artefacts have more strongly stiffening spring characteristics as compared to classic and angle-beam triskelion samples of force artefacts.

9.8 Enhanced numerical experiments for triskelion and tetraskelion force artefacts

The numerical results have been presented for triskelion and tetraskelion force artefacts in chapter 4 and 8. These results have motivated the author to explore the best triskelion and tetraskelion designs for the micro probe suspension and force artefacts. The enhanced numerical experiments for triskelion and tetraskelion force artefacts are investigated in this section. The approach and methodology are the same as used previously, as does the style of presentation. Triskelion design are briefly, considered in the subsection 1.9.1 in figures 9.5 to 9.12. Then, tetraskelion designs are reviewed in subsection 1.9.2 and figures 9.13 to 9.20.

9.8.1 Enhanced numerical experiments for triskelion artefacts with elbow angle 60°, 45°, 30°, and 15°

1. It is evident from figure 9.5 that stiffness k_z is independent of the arm length a_ℓ and of elbow angle.

2. Figure 9.6 shows that the value of torsional λ_x stiffness steadily increases by increasing the elbow angle of the force artefacts. It increases with arm length a_ℓ as expected.

3. Figures 9.7, 9.8 and 9.9 confirm that stiffness k_z is independent of the elbow angle. The relationship of k_z to the beam length ℓ, width w and thickness t are as expected, respectively inverse cubic, linear and cubic.

4. Figure 9.10 shows that increasing the elbow angle, the increase of torsional stiffness λ_x steadily but not linearly. Increasing the beam length decreases torsional stiffness λ_x. The relationship with length approaches the inverse square law expected for both the torsion and bending of an individual suspension beam. Figure 9.11 confirms that the torsional stiffness λ_x for all triskelion force artefacts increases linearly with increasing the beam width as expected for both torsion and bending of suspension beam. Figure 9.12 shows that relationship with thickness approaches the cubic law expected for both torsion and bending of an individual suspension beam.

9.8.2 Enhanced numerical experiments for tetraskelion artefacts with elbow angle 60°,45°, 30°,and 15°

1. The relation between arm a_ℓ and stiffness k_z for all triskelion force artefacts with elbow angles 60°,45°, 30°,and 15° is same i.e 1250.00 N/m. It is evident from the figure 9.13 that stiffness k_z is independent of the arm length a.

2. The relationship between arm length a_ℓ and axial torsional stiffness λ_x for all triskelion force artefacts is shown in figure 9.14. It is evident from the figure that the value of torsional λ_x stiffness steadily increases by increasing the elbow angle of the force artefacts. The force artefacts with elbow angle 15° have a low value of λ_x.

3. The relationship beam length ℓ & stiffness k_z, beam width w & stiffness k_z, and beam thickness t & stiffness k_z in figures 9.15, 9.16 and 9.17 clearly indicate that stiffness

k_z is independent of the elbow angle for all force artefacts with elbow angles 60 °,45 °, 30 ° and 15 °.

4. The actual stiffness in figure 9.15 for the beam length of 4 mm and 8 mm are 1250.00 N/m and 156 N/m (for E= 2.5×10^9) with the ratio 8 that is expected by cubic law.

5. The actual stiffness in figure 9.16 for the beam width of 2 mm and 1 mm are 2500.00 N/m and 1250 N/m (for E= 2.5×10^9) with the ratio 2 that is expected .

6. The actual stiffness in figure 9.15 for the beam thickness of 0.8 mm and 0.4 mm are 10000.00 N/m and 1250 N/m (for E= 2.5×10^9) with the ratio 8 that is expected by cubic law.

7. Figure 9.18 clearly shows as we increase the elbow angle, the value of torsional stiffness λ_x also increases steadily but not linear. If we increase the beam length, the value of torsional stiffness λ_x decreases. The relationship with length approaches the inverse square law expected for both torsion and bending of an individual suspension beam. The actual stiffness values for the beam length of 0.8 mm and 0.4 mm are 22.5 N/m and 95.0 N/m, with a ratio 0.236.

8. Figure 9.18 clearly shows the torsional stiffness λ_x for all tetraskelion force artefacts increases linearly with increasing the beam width as expected for both torsion and bending of suspension beam. The actual stiffness value for the beam width of 0.2 mm and 0.1 mm are 192.00 N/m and 95.00 N/m, with a ratio 2 expected.

9. Figure 9.18 clearly shows, the torsional stiffness increases λ_x rapidly by increasing the thickness of the beam and also increases slightly with the elbow angle of the tetraskelion force artefacts. The relationship with thickness approaches the cubic law expected for both torsion and bending of an individual suspension beam. The relationship with thickness approaches the cubic law expected for both torsion and bending of an individual suspension beam. The actual stiffness value for the beam thickness of 0.4 mm and 0.2 mm are 747.00 N/m and 95.00 N/m, with a ratio 7.86 that is close to the 8 expected by cubic law.

9.9 Major Applications of triskelion and tetraskelion force artefacts

This thesis has presented a systematic study, by means of computational and physical testing, of the effects of varying the elbow angle in both classical and angle-beam devices. It has also similarly explored tetraskelion designs. The following, general trends may become important future application:

1. All current (2014) commercial IBS and NPL triskelion suspension designs have an elbow angle of 60 °. The recent work presented in this thesis indicates that classic triskelion suspension designs with elbow angles 15 °, 30 °, 45 ° could be considered to be the best designs for some probe system because they have lower torsional stiffness λ_x as compared to triskelion with elbow angle 60 °. A more robust low-stiffness device might be achieved using smaller elbow angles. The triskelion suspension design with elbow angle 15 ° shown in figure 9.24 may encounter technical problems in its fabrication. Two other classic triskelion and angle-beam suspension designs shown in figure 9.23 and 9.22 with elbow angles 30 ° & 45 °. These triskelion suspension designs with elbow angles 30 ° & 45 ° are confirmed by the numerical experiments, and might become improved designs for some micro probe suspensions. These designs might be popular in the future for industrial applications, where they will have lower sensitivity to slight misalignment of the applied test force.

2. The other applications of triskelion suspension designs are for force transfer artefacts, which require a more stiff characteristic. Therefore, classic triskelion suspension designs with bigger elbow angles 180 °, 150 °, 120 °, and 90 ° (discussed in chapter 4) should be considered. They have a higher value of torsion stiffness λ_x as compared to classic and angle-beam triskelion suspension designs with elbow angles of 60 ° or less (45 ° 30 °, ,15 °). The classic and angle beam triskelion designs with higher relative value of torsional stiffness λ_x have great potential for industrial applications of triskelion force artefacts.

3. Current commercial triskelion designs exploit the classic architecture. However, both numerical physical experiments here indicate that angle-beam design can be very effective. They present lower stiffness than the classic designs of the same overall size

while using thicker, potentially more robust flexure beams. They behave similarly to classic design in term of elbow angle. Despite having relatively low levels of quasi-kinematic constraint, they do not exhibit instabilities at the scales tested.

4. Tetraskelion designs have been shown to be effective and potential alternative to triskelions. They offer a different torsional range relative to linear stiffness that might justify addition complexity in some force artefact applications.

5. Although originally introduced in this work as an experimental convenience, polymeric triskelions have proved to be very effective. They offer a combination of stiffness and robustness not available in the other materials and open up the possibility of low-cast mass production. On the evidence in this thesis, they have considerable practical promise and are clearly worthy of further extensive investigations.

9.10 Best triskelion and tetraskelion suspensions designs

A complete picture of axial stiffness k_x and torsional stiffness λ_x for triskelion and tetraskelion force artefacts force artefacts with elbow angles 15 °, 30 °, 45 °, 60 °, 90 °, 120 °, 150 ° and 180 ° have been shown in figure 9.14 and 9.16. This figure 9.14 clearly shows that all triskelion force artefacts have the same value of axial stiffness 938 N/m. Researchers and industrial experts could not decide about the best triskelion suspension design for microprobe on the basis of axial stiffness. The curve of torsional stiffness values clearly shows the triskelion force artefacts with elbow angles 15 °, 30 °, 45 ° have low values of torsional stiffness as compared to triskelion force artefacts with elbow angle 60 °. The triskelion suspension for the micro probe is very papular in industries. Researchers and industrial experts (NPL and IBS) have continued to use triskelion suspension design since 2000. The extensive study of numerical experiments have confirmed that triskelion suspensions are designed with elbow angles 15 °, 30 ° and 45 ° can generate better results for the triskelion micro probe .

Similarly in figure 9.16, the force artefacts with elbow angles 15 °, 30 °, 45 °, 60 °, 90 °, 120 °, 150 ° and 180 ° have also have same values of axial stiffness k_z 1250 N/m. Not all of these force artefacts were able to give indication about the best design tetraskelion

suspension designs for micro probe and transfer force artefacts. The tetraskelion force artefacts with elbow angles 15 °, 30 ° and 45 ° also have low value of stiffness compared to tetraskelion force artefacts with elbow angle 60 °. Numerical experiments confirm tetraskelion suspension design for transfer force artefacts with beam parameters (ℓ = 4.5 mm, w= 1.1 mm, t= 0.2 mm), Young's modulus = 2.5 $\times 10^9$ Pascal for pure z-displacement = 5×10^{-6}m, & $\theta_x = 1\times10^{-3}$ rad for tetraskelion force artefacts have values axial stiffness k_z 965 & torsional stiffness λ_x = 4150 Nm/rad, k_z 965 & torsional stiffness λ_x = 3114 Nm/rad and k_z 965 & torsional stiffness λ_x = 2462 Nm/rad for elbow angle 45 °, 30 ° and 15 ° as compared to triskelion design with elbow angle 60 ° and beam parameters (ℓ = 4 mm, w= 1.1 mm, t= 0.2 mm), Young's modulus = 2.5 $\times 10^9$ Pascal for pure z-displacement = 5×10^{-6}m, & $\theta_x = 1\times10^{-3}$ rad have k_z 1031 N/m & torsional stiffness λ_x= 5270 Nm/rad. The tetraskelion suspension design with elbow angles 15 °, 30 ° and 45 ° may also generate better results if they are used for a micro probe as compared to triskelion suspension with elbow angle 60 °, which has higher torsion stiffness. However, tetraskelion suspensions designs with elbow angles 90 °, 120 °, 150 ° and 180 ° are considered best designs for force artefacts for industrial applications.

The arm length a, was made double 4 mm in figures 9.14 and 9.15, as it was 2 mm in figures 9.14 and 9.15, while the beam parameters were kept same in these figures. The general pattern of behaviour in figures 9.14 to 9.15 is monotonic. The consistency in the shape of the curves between different styles is remarkable.

9.11 Conclusion

Comparisons of the results of the physical tests on triskelion and tetraskelion force artefacts have confirmed the validity of the enhanced linear elastic models of design tools. Triskelion and tetraskelion software programs are based on newly enhanced linear elastic models that are powerful tools for predicting the short-range stiffness k_z and axial torsional stiffness λ_x for classic triskelion, angle-beam triskelion, and tetraskelion micro probe suspensions and force transfer artefacts. Moreover it is confirmed that, although the real devices of these types have stiffening spring characteristics, an assumption of (adequately) linear behaviour

holds over a very usefully larger range of displacement.

Further numerical investigations have confirmed that trends observed and reported in earlier chapter continue: very similar patterns of torsional stiffness increasing non-linearity with elbow angle were seen for all designs studied. The classic and angle-beam suspensions for micro probe with elbow angles 30 ° or 45 ° might provide an alternative choice for triskelion micro probe suspension designs that offer better performance for some industrial and research purposes.

This work also indicates that triskelion and tetraskelion suspension designs with larger elbow angles such as 120 °, 150 ° or even 180 ° might be considered to be the best designs for some types of the force artefacts. Of particular interest in this regard is the potential to increase torsional stiffness for a given z-stiffness within relatively compact designs.

While it is no surprise to confirm that angle-beam designs offer lower stiffness than otherwise similar classic designs, the research work indicates that they remain mechanically stable and predictable. They can, therefore, offer the promise of a more robust, compact device with low stiffness, which might be advantageous to some industrial applications.

The comparison studies have shown that making triskelion and tetraskelion suspensions from polymer leads to devices that are predictable and repeatable. This potentially opens up a whole new range of cost-sensitive applications.

Further numerical investigations have confirmed that trends observed and reported in earlier chapters continue: a very similar patterns of torsional stiffness increasing non-linearity with elbow angle were seen in all designs studied.

Finally, enhanced numerical experiments of triskelions indicate that classic triskelion suspension designs with elbow angles 30 °, 45 ° could be considered to be the best designs for some probing. The new family of triskelion ‘tetraskelion, designs may also have great potential for industrial applications of force artefacts.

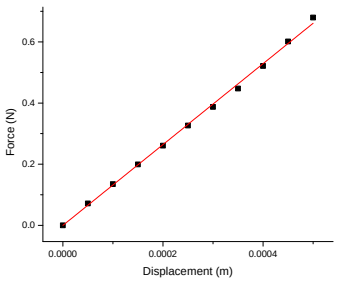

(*a*) CS1-60 table D.1, S.No.3

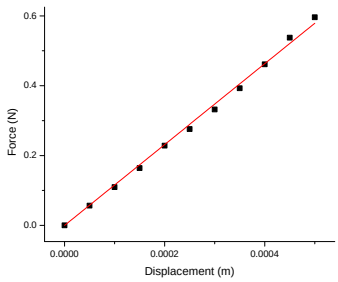

(*b*) CS1-60 table D.1, S.No.4

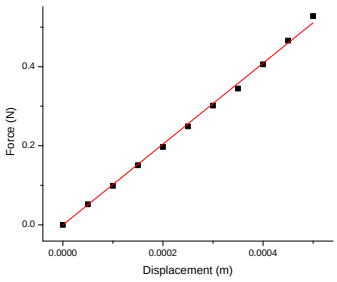

(*c*) CS2-60 table D.2, S.No.1

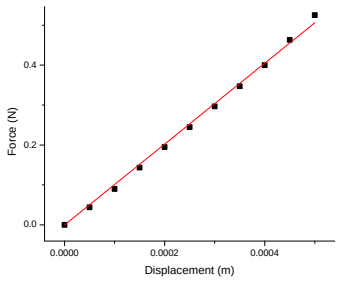

(*d*) CS2-60 table D.2, S.No.4

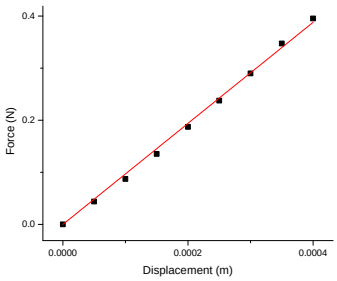

(*e*) CS1-90 table D.3, S.No.1

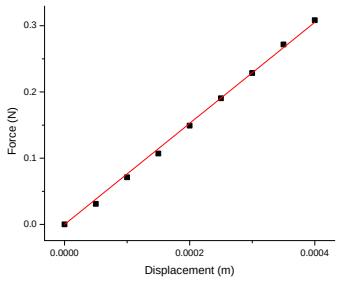

(*f*) CS1-90 table D.3, S.No.6

Figure 9.1: Classic triskelion force artefacts ((a), (b), (c), & (d) with elbow angle 60 ° and (e) & (f) with elbow angle 90 °) indicate their performances in the linear region

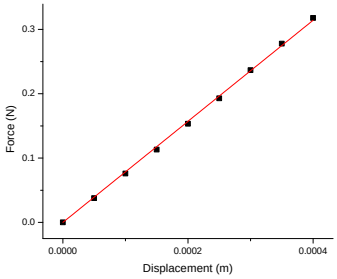

(*g*) CS2-90 table D.4, S.No.3

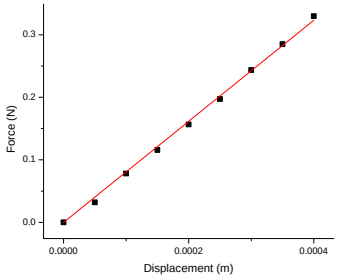

(*h*) CS2-90 table D.4, S.No.6

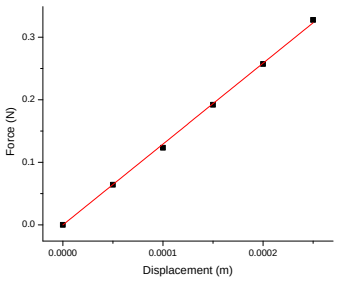

(*i*) CS1-120 table D.5, S.No.1

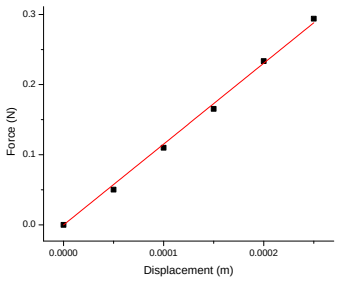

(*j*) CS2-120 table D.5, S.No.4

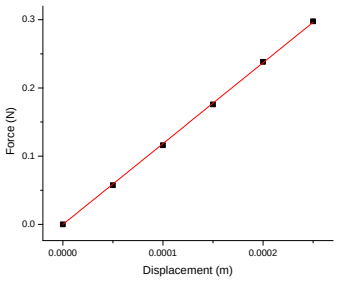

(*k*) CS2-120 table D.6, S.No.2

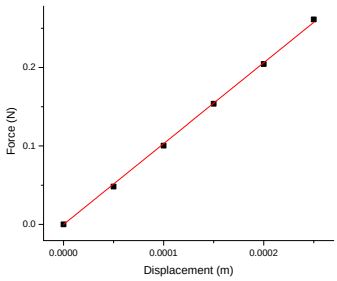

(*l*) CS2-120 table D.6, S.No.5

Figure 9.2: Classic triskelion force artefacts ((g) & (h)with elbow angle 90 ° and (i), (j), (k) & (l) with elbow angle 120 °) indicate their performances in the linear region

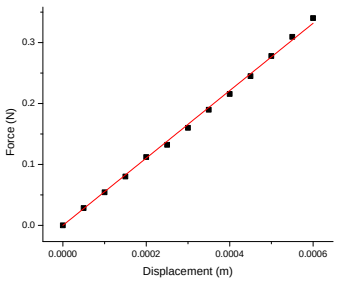

(*a*) ABS1-60 table F.1, S.No.1

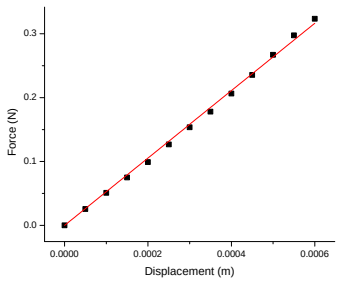

(*b*) ABS1-60 table F.1, S.No.4

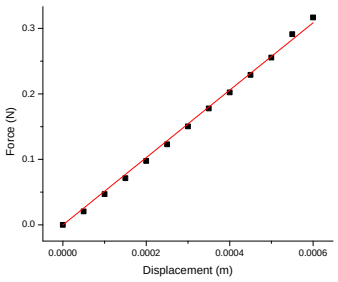

(*c*) ABS2-60 table F.2, S.No.2

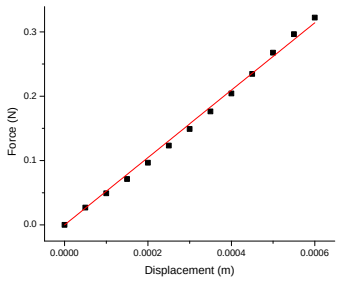

(*d*) ABS2-60 table F.2, S.No.4

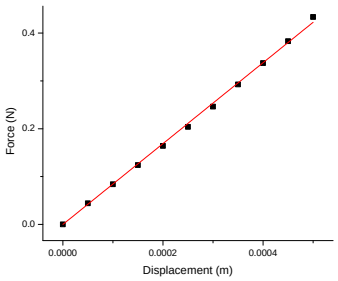

(*e*) ABS1-90 table F.3, S.No.2

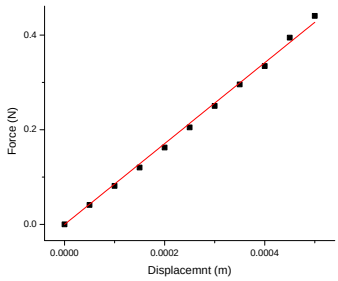

(*f*) ABS1-90 table F.3, S.No.4

Figure 9.3: Angle-beam triskelion force artefacts ((a), (b), (c), & (d) with elbow angle 60 ° and (e) & (f) with elbow angle 90 °) indicate their performances in the linear region

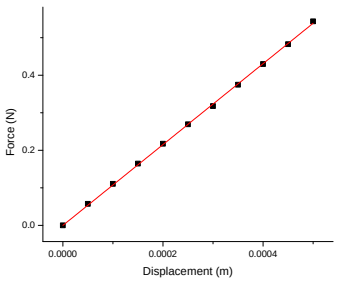

(*g*) ABS2-90 table F.4, S.No.1

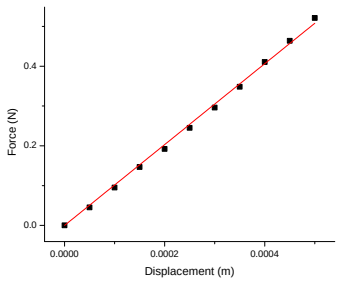

(*h*) ABS2-90 table F.3, S.No.4

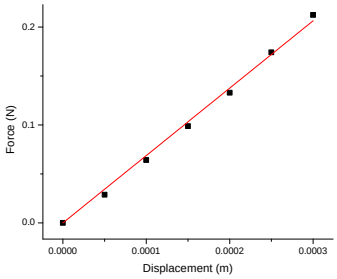

(*i*) ABS1-120 table F.5, S.No.1

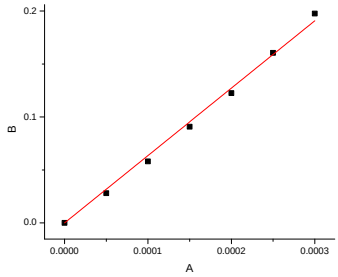

(*j*) ABS1-120 table F.5, S.No.4

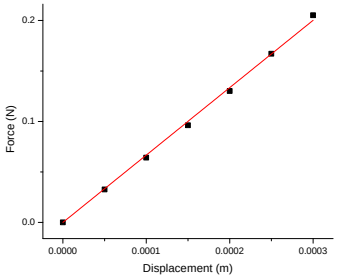

(*k*) ABS2-120 table F.6, S.No.2

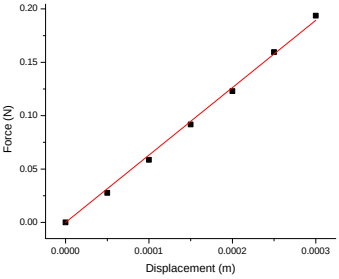

(*l*) ABS2-120 table F.6, S.No.5

Figure 9.4: Angle-beam force artefacts ((g) & (h)with elbow angle 90 ° and (i), (j), (k) & (l) with elbow angle 120 °) indicate their performances in the linear region

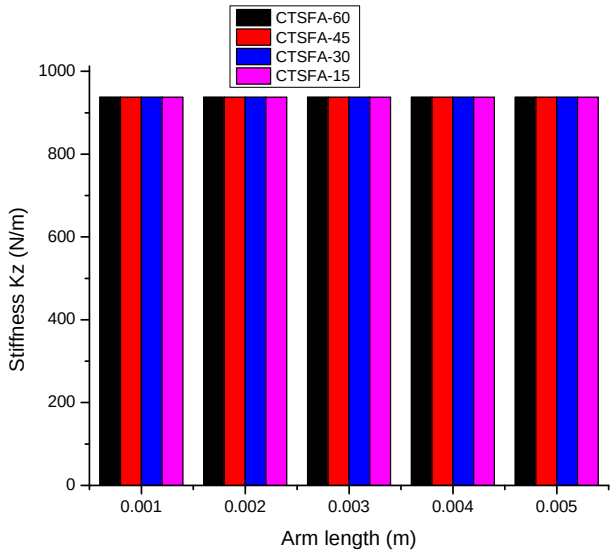

Figure 9.5: Graph for arm length versus computed results for axial stiffness k_z of triskelion force artefacts CTSFA-60, CTSFA-45, CTSFA-30, & CTSFA-15 with elbow angles 60 °, 45 °, 30 °, and 15 °

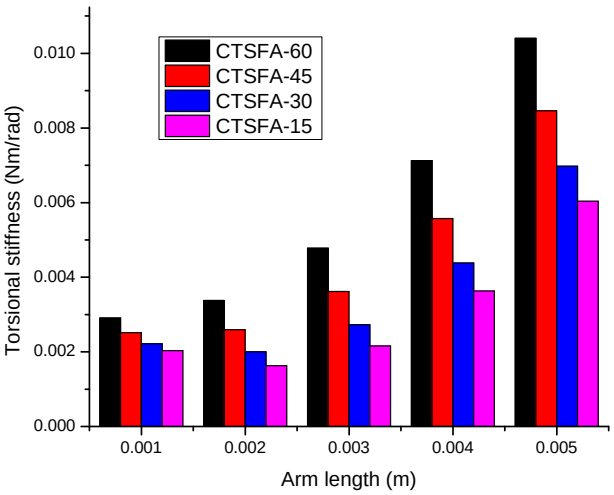

Figure 9.6: Graph for arm length versus computed results for torsional stiffness k_x of triskelion force artefacts CTSFA-60, CTSFA-45, CTSFA-30, & CTSFA-15 with elbow angles 60 °, 45 °, 30 °, and 15 °.

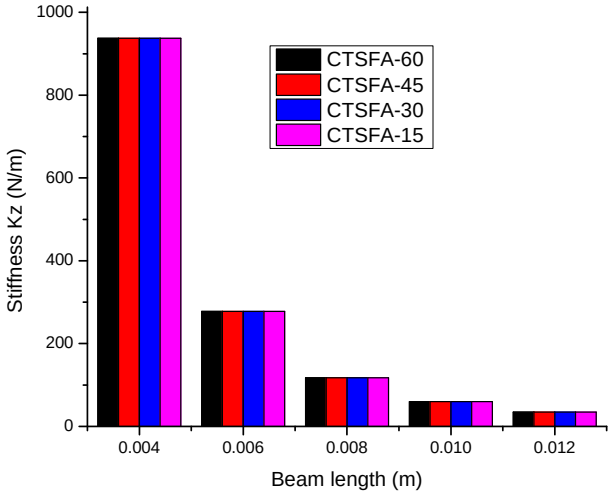

Figure 9.7: Graph for beam length versus computed results for axial stiffness k_z of triskelion force artefacts CTSFA-60, CTSFA-45, CTSFA-30, & CTSFA-15 with elbow angles 60 °, 45 °, 30 °, and 15 °

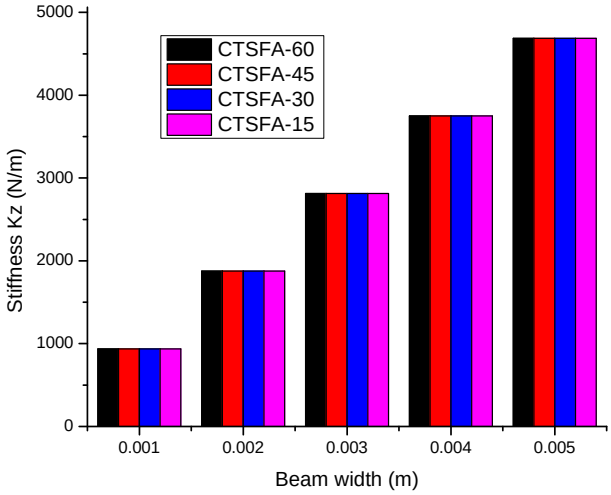

Figure 9.8: Graph for variable beam length versus computed results for axial stiffness k_z of triskelion force artefacts CTSFA-60, CTSFA-45, CTSFA-30, & CTSFA-15 with elbow angles 60 °, 45 °, 30 °, and 15 °.

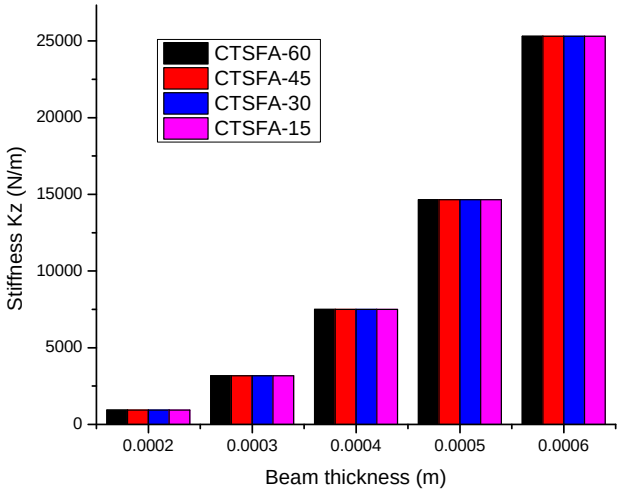

Figure 9.9: Graph for beam thickness verses computed results for axial stiffness k_z of triskelion force artefacts CTSFA-60, CTSFA-45, CTSFA-30, & CTSFA-15 with elbow angles 60 °, 45 °, 30 °, and 15 °

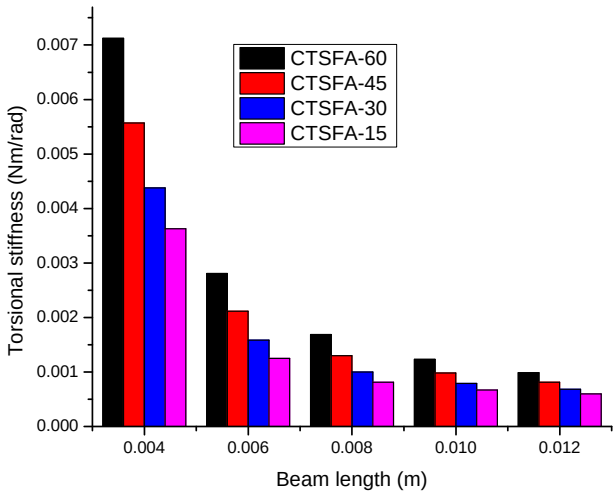

Figure 9.10: Graph for variable beam length versus computed results for torsional stiffness λ_x of triskelion force artefacts CTSFA-60, CTSFA-45, CTSFA-30, & CTSFA-15 with elbow angles 60 °, 45 °, 30 °, and 15 °.

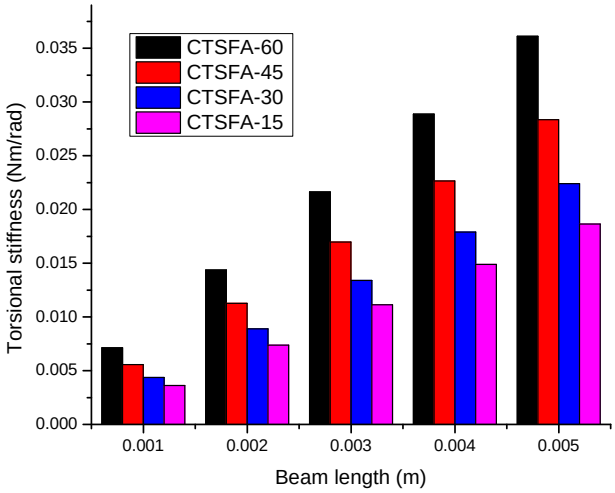

Figure 9.11: Graph for beam width versus computed results for torsional stiffness λ_x of triskelion force artefacts CTSFA-60, CTSFA-45, CTSFA-30, & CTSFA-15 with elbow angles 60 °, 45 °, 30 °, and 15 °.

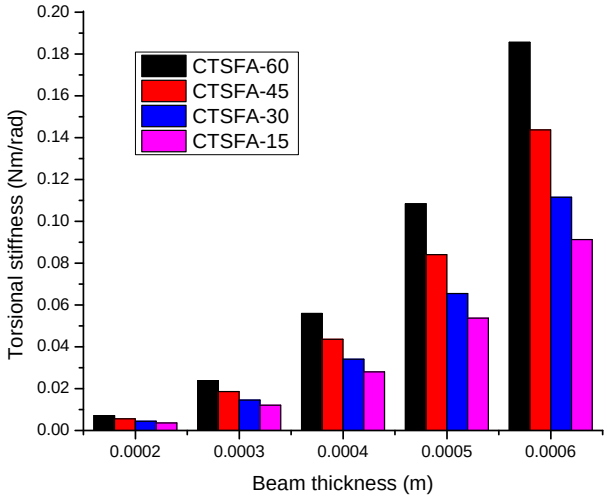

Figure 9.12: Graph for variable beam thickness versus computed results for torsional stiffness λ_x of triskelion force artefacts CTSFA-60, CTSFA-45, CTSFA-30, & CTSFA-15 with elbow angles 60 °, 45 °, 30 °, and 15 °.

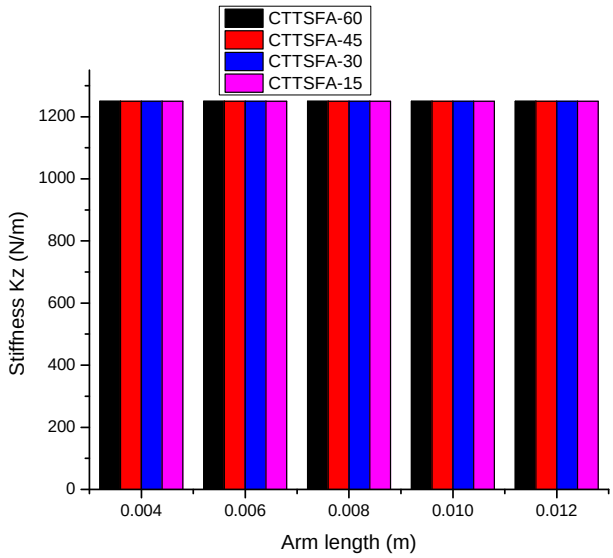

Figure 9.13: Graph for variable arm length verses computed results for axial stiffness k_z of tetraskelion force artefacts CTTSFA-60, CTTSFA-45, CTTSFA-30, & CTTSFA-15 with elbow angles 60 °, 45 °, 30 °, and 15 °

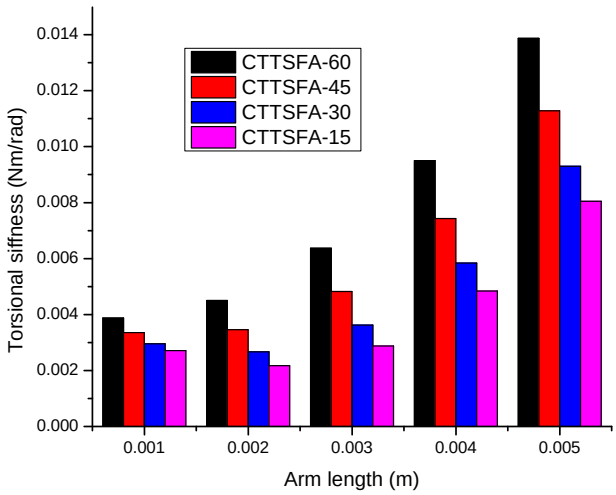

Figure 9.14: Graph for variable arm length versus computed results for torsional stiffness k_x of tetraskelion force artefacts CTTSFA-60, CTTSFA-45, CTTSFA-30, & CTTSFA-15 with elbow angles 60 °, 45 °, 30 °, and 15 °.

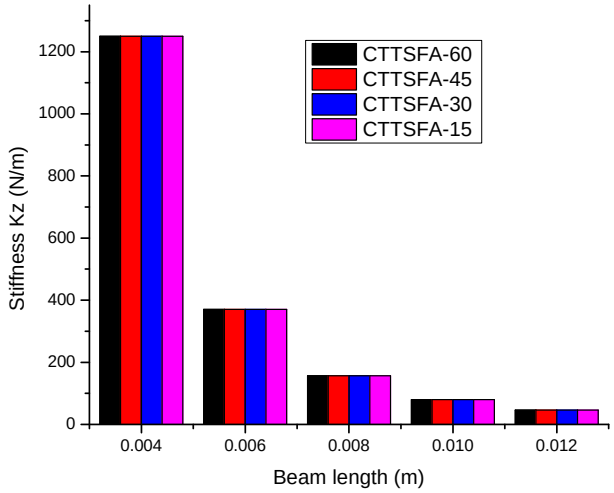

Figure 9.15: Graph for beam length versus computed results for axial stiffness k_z of tetraskelion force artefacts CTTSFA-60, CTTSFA-45, CTTSFA-30, & CTTSFA-15 with elbow angles 60 °, 45 °, 30 °, and 15 °

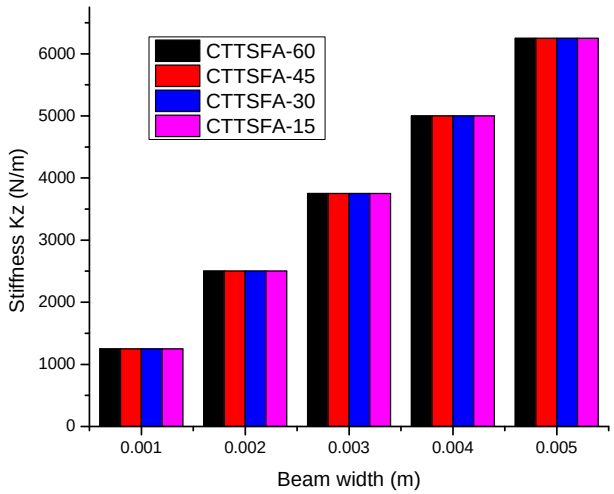

Figure 9.16: Graph for variable beam length versus computed results for axial stiffness k_z of tetraskelion force artefacts CTTSFA-60, CTTSFA-45, CTTSFA-30, & CTTSFA-15 with elbow angles 60 °, 45 °, 30 °, and 15 °.

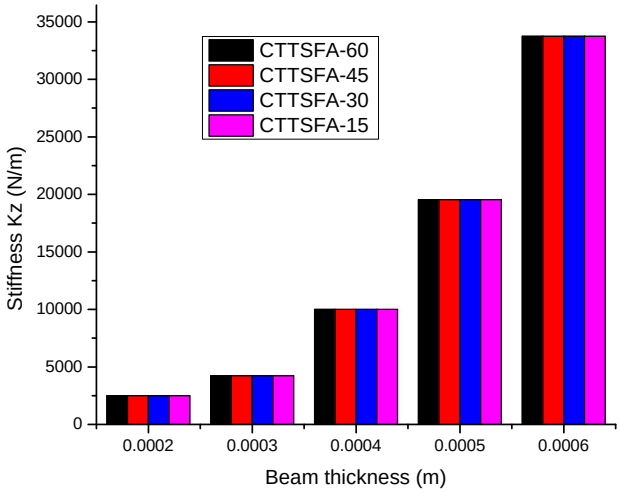

Figure 9.17: Graph for beam thickness versus computed results for stiffness axial k_z of tetraskelion force artefacts CTTSFA-60, CTTSFA-45, CTTSFA-30, & CTTSFA-15 with elbow angles 60 °, 45 °, 30 °, and 15 °

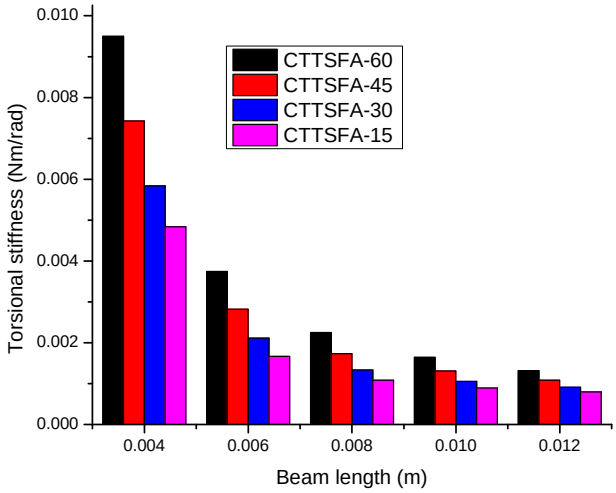

Figure 9.18: Graph for variable beam length versus computed results for torsional stiffness λ_x of tetraskelion force artefacts CTTSFA-60, CTTSFA-45, CTTSFA-30, & CTTSFA-15 with elbow angles 60 °, 45 °, 30 °, and 15 °.

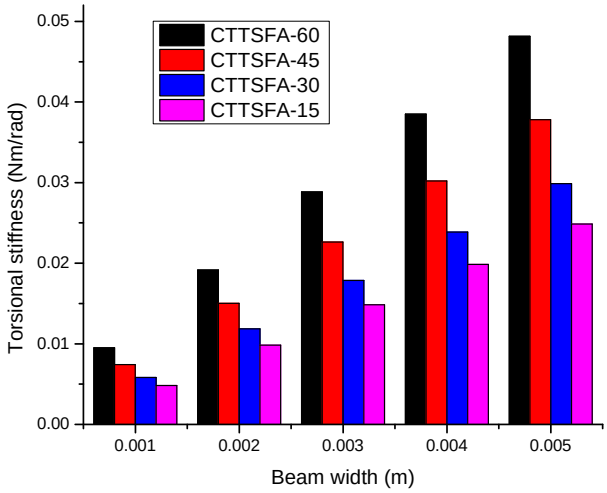

Figure 9.19: Graph for beam width verses computed results for torsional stiffness λ_x of tetraskelion force artefacts CTTSFA-60, CTTSFA-45, CTTSFA-30, & CTTSFA-15 with elbow angles 60 °, 45 °, 30 °, and 15 °.

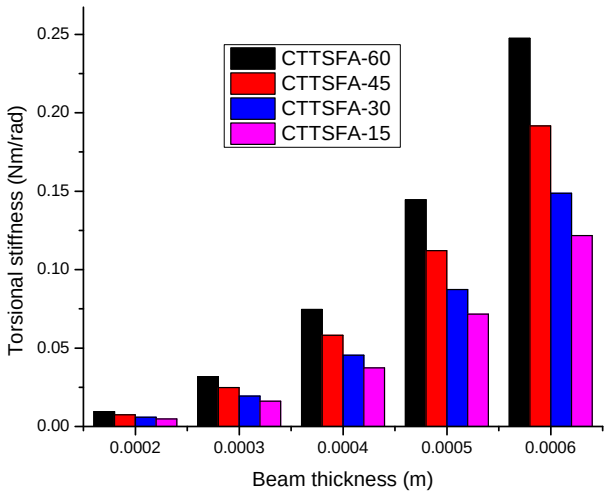

Figure 9.20: Graph for variable beam thickness verses computed results for torsional stiffness λ_x of tetraskelion force artefacts CTTSFA-60, CTTSFA-45, CTTSFA-30, & CTTSFA-15 with elbow angles 60 °, 45 °, 30 °, and 15 °.

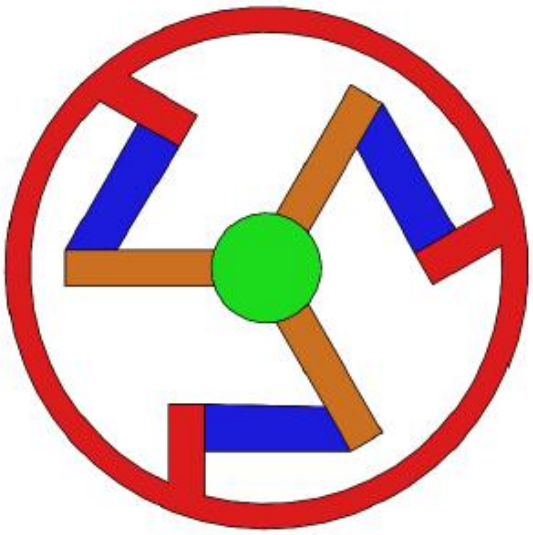

Figure 9.21: The simplified model for triskelion force artefacts with elbow angle 60 °.

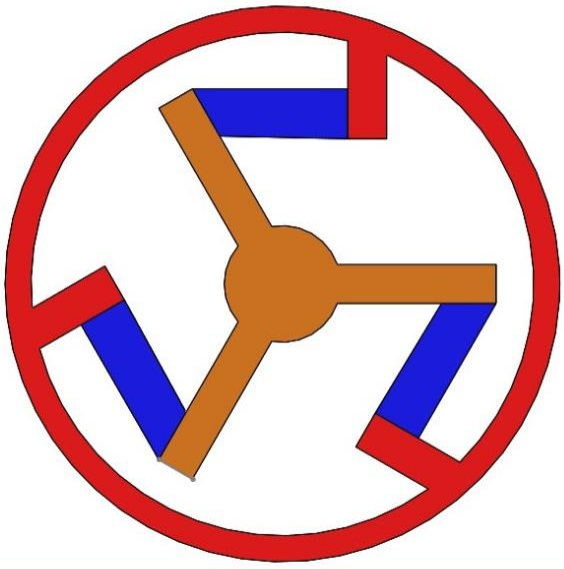

Figure 9.22: The simplified model for triskelion force artefacts with elbow angle 45 °.

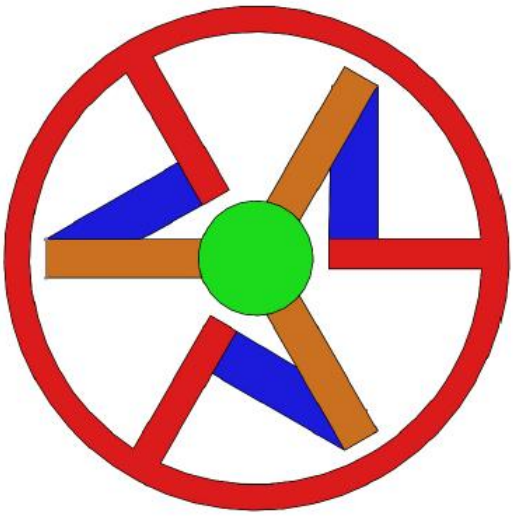

Figure 9.23: The simplified model for triskelion force artefacts with elbow angle 60 °.

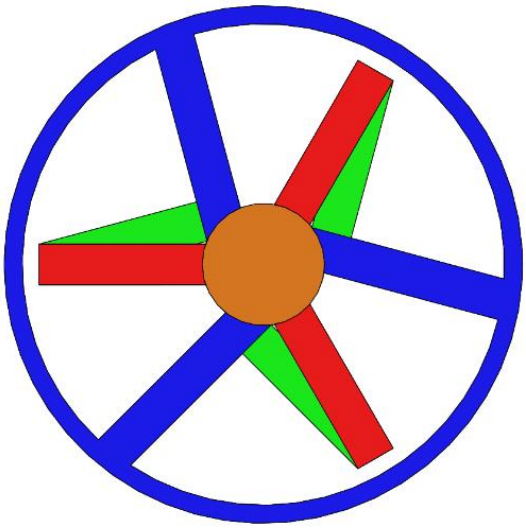

Figure 9.24: The simplified model for triskelion force artefacts with elbow angle 45 °.

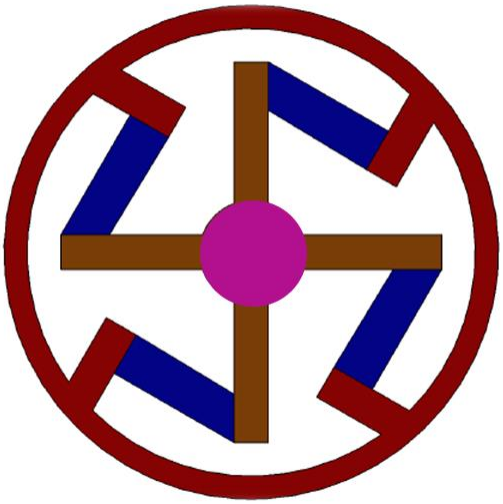

Figure 9.25: The simplified model for tetraskelion force artefacts with elbow angle 60 °.

Figure 9.26: The simplified model for tetrakelion force artefacts with elbow angle 45 °.

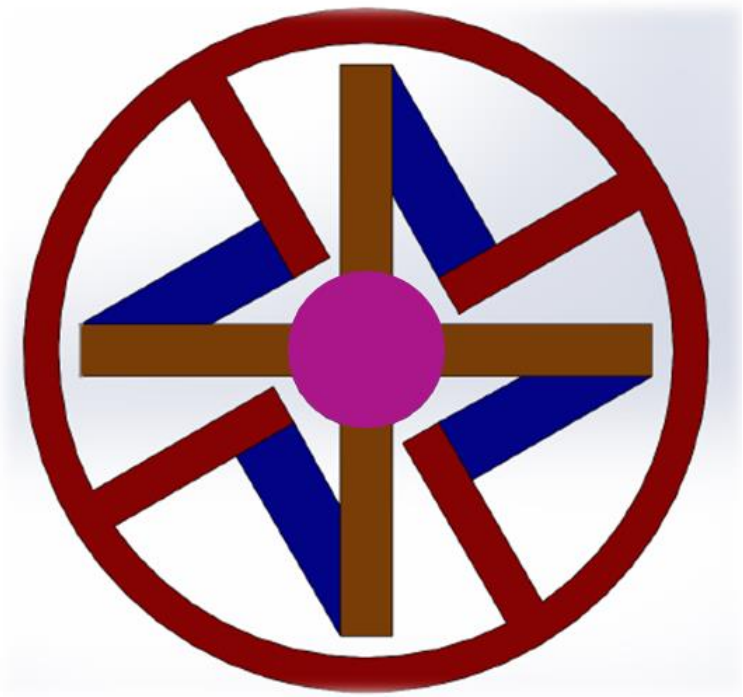

Figure 9.27: The simplified model for tetraskelion force artefacts with elbow angle 60 °.

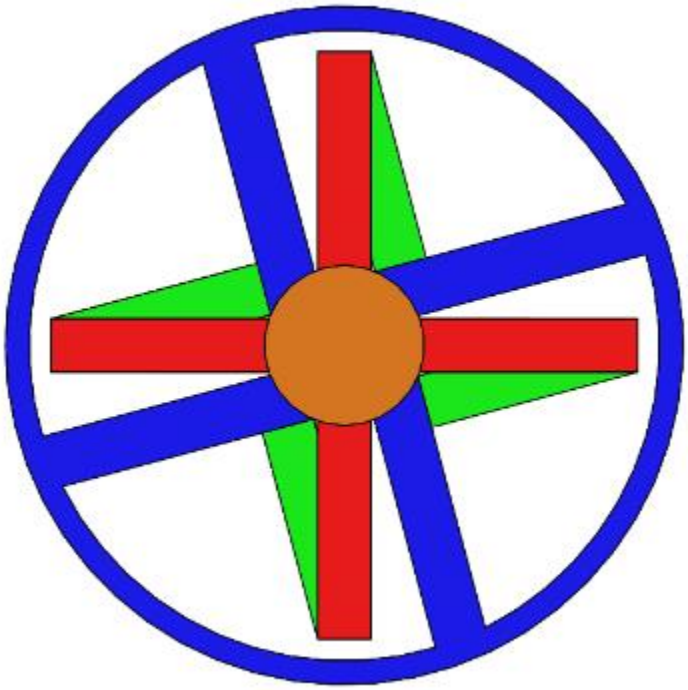

Figure 9.28: The simplified model for tetraskelion force artefacts with elbow angle 45 °.

Table 9.1: Classic triskelion samples of force artefacts

Sample ID	Beam No. 1			Beam No. 2			Beam No. 3		
No.	ℓ mm	w mm	t mm	ℓ mm	w mm	t mm	ℓ mm	w mm	t mm
CTS1-60	4.13	1.07	0.188	4.17	0.98	0.185	4.10	1.0	0.189
CTS1-90	4.40	1.11	0.190	4.40	1.05	0.187	4.49	1.0	0.185
CTS1-120	4.59	1.08	0.189	4.39	1.01	0.183	4.59	1.0	0.186
CTS2-60	4.17	1.02	0.189	4.15	1.04	0.186	4.12	1.03	0.190
CTS2-90	4.29	1.00	0.187	4.30	1.01	0.185	4.28	1.02	0.184
CTS2-120	4.46	1.01	0.186	4.54	1.03	0.182	4.51	1.02	0.185
CTS1-604	4.20	1.00	0.350	4.23	1.03	0.340	4.53	0.97	0.320

Table 9.2: Angle-beam triskelion samples of force artefacts

Sample ID	Beam No. 1			Beam No. 2			Beam No. 3		
No.	ℓ mm	w mm	t mm	ℓ mm	w mm	t mm	ℓ mm	w mm	t mm
ABTS1-60	4.16	1.01	0.161	4.10	1.01	0.159	4.08	0.97	0.156
ABTS1-90	4.09	1.00	0.190	4.04	1.04	0.187	4.06	1.01	0.184
ABTS1-120	3.95	1.03	0.175	3.80	1.03	0.172	3.93	1.04	0.176
ABTS2-60	4.12	1.03	0.155	4.17	1.17	0.152	4.18	1.14	0.153
ABTS2-90	4.06	1.02	0.189	4.03	0.99	0.187	4.05	1.03	0.184
ABTS2-120	3.98	1.02	0.167	3.74	0.99	0.164	3.88	1.05	0.162

Table 9.3: Classic tetraskelion samples of force artefacts

Sample ID	Beam No. 1			Beam No.2			BeamNo.3			Beam No. 4		
No.	ℓ mm	w mm	t mm	ℓ mm	w mm	t mm	ℓ mm	w mm	t mm	ℓ mm	w mm	t mm
CTTS1-CS	2.93	1.01	182	2.96	1.01	180	2.88	1.01	179	2.88	1.01	184
CTTS1-CD	2.89	1.09	189	3.02	1.03	186	2.89	1.01	190	2.98	1.03	187
CTTS2-CS	2.97	1.00	185	2.99	1.02	183	2.95	1.00	180	2.94	1.02	188
CTTS2-CD	2.94	1.01	190	2.92	1.00	188	2.96	1.02	184	2.90	1.00	186

Table 9.4: Angle-beam tetraskelion samples of force artefacts

Samples ID	Beam No. 1			Beam No. 2			Beam No. 3			Beam No. 4		
No.	ℓ mm	w mm	t mm	ℓ mm	w mm	t mm	ℓ mm	w mm	t mm	ℓ mm	w mm	t mm
CTTS1-CS-90	2.90	0.99	138	2.85	0.99	134	2.98	1.09	136	3.01	0.96	140
CTTS1-DS-90	2.84	1.01	156	2.96	1.09	152	2.84	1.05	154	2.94	1.08	153

Table 9.5: Comparative analysis of stiffness k_{z_p} N/m predicted by triskelion software program and experimental values $k_{z_{exp}}$ N/m at the centre of the hub; ℓ, w & t are beam parameters of classic triskelion force artefacts.

Sample ID	ℓ m	w m	t m	Predicted stiffness k_{z_p} N/m	Experimental stiffness $k_{z_{exp}}$ N/m	$k_{z_{exp}}/k_{z_p}$
CTS1-60	0.00410	0.001	0.000189	0853.45	1459.33	1.70
CTS1-90	0.00413	0.0014	0.000188	0777.58	0955.29	1.22
CTS1-120	0.00459	0.00108	0.000189	0655.98	1070.01	1.63
CTS2-60	0.00412	0.00103	0.000190	0834.32	1096.47	1.31
CTS2-90	0.00429	0.001	0.000187	0720.56	918.18	1.27
CTS2-120	0.00451	0.00102	0.000186	0622.48	1070.01	1.71
CTS1-604	0.00420	0.001	0.000350	5034	5280	0.95

Table 9.6: Comparative analysis of stiffness k_{z_p} N/m predicted by triskelion software program and experimental values of stiffness $k_{z_{exp}}$ N/m at off-centre point of hub (M_x term consider the hub regions only); ℓ, w & t are beam parameters of classic triskelion force artefacts.

Sample ID	ℓ mm	w mm	t μm	Predicted stiffness k_{z_p} N/m	Experimental stiffness $k_{z_{exp}}$ N/m	$k_{z_{exp}}/k_{z_p}$
CTS1-60	0.00410	0.001	0.000189	853.45	1274.41	1.49
CTS1-90	0.00413	0.0014	0.000188	777.58	0814.95	1.04
CTS1-120	0.00459	0.00108	0.000189	655.98	1075.65	1.63
CTS2-60	0.00412	0.00103	0.000190	834.32	1032.25	1.23
CTS2-90	0.00429	0.001	0.000187	720.56	0772.98	1.07
CTS2-120	0.00451	0.00102	0.000186	622.48	1075.65	1.72
CTS1-604	0.00420	0.001	0.000350	5034.00	5022.00	1.00

Table 9.7: Comparative analysis of stiffness k_{z_p} N/m predicted by triskelion software program and experimental values of stiffness $k_{z_{exp}}$ N/m at of the hub; ℓ, w & t are beam parameters of angle-beam triskelion force artefacts.

Sample ID	ℓ mm	w mm	t μm	Predicted stiffness k_{z_p} N/m	Experimental stiffness $k_{z_{exp}}$ N/m	$k_{z_{exp}}/k_{z_p}$
ABTS1-60	0.00416	0.00101	0.000163	528.60	0536.95	1.01
ABTS1-90	0.00409	0.001	0.000190	872.19	0873.02	1.00
ABTS1-120	0.00395	0.00103	0.000175	799.25	1213.50	1.51
ABTS2-60	0.00412	0.00103	0.000155	477.16	0478.57	1.00
ABTS2-90	0.00406	0.00102	0.000189	895.21	1213.50	1.35
ABTS2-120	0.00398	0.00102	0.000167	655.57	0602.99	0.91

Table 9.8: Comparative analysis of stiffness k_{z_p} N/m predicted by triskelion software program and experimental values stiffness $k_{z_{exp}}$ N/m at off-centre point (M_x term consider the hub regions only); ℓ, w & t are beam parameters of angle-beam triskelion force artefacts.

Sample ID	ℓ mm	w mm	t μm	Predicted stiffness k_{z_p} N/m	Experimental stiffness $k_{z_{exp}}$ N/m	$k_{z_{exp}}/k_{z_p}$
ABTS1-60	0.00416	0.00101	0.000163	528.31	0503.38	0.95
ABTS1-90	0.00409	0.001	0.000190	872.19	0838.05	0.96
ABTS1-120	0.00395	0.00103	0.000175	799.25	0613.85	0.85
ABTS2-60	0.00412	0.00103	0.000155	477.16	0443.90	0.93
ABTS2-90	0.00406	0.00102	0.000189	895.21	1009.30	1.12
ABTS2-120	0.00398	0.00102	0.000167	655.57	0779.92	1.18

Table 9.9: Comparative analysis of stiffness k_{z_p} N/m predicted by triskelion software program and experimental values of stiffness $k_{z_{exp}}$ N/m at the centre of hub; ℓ, w & t are beam parameters of classic tetraskelion force artefacts.

Sample ID	ℓ m	w m	t m	Predicted stiffness k_{z_p} N/m	Experimental stiffness $k_{z_{exp}}$ N/m	$k_{z_{exp}}/k_{z_p}$
CTTS1-CS	0.00293	0.00101	0.000179	2671.40	2781.40	1.04
CTTS1-DS	0.00289	0.00109	0.000189	3536.50	4617.30	1.30
CTTS2-CS	0.00297	0.001	0.000185	2803.50	2867.80	1.02
CTTS2-DS	0.00294	0.00101	0.000190	3162.30	4322.80	1.36

Table 9.10: Comparative analysis of stiffness k_{z_v} N/m predicted by triskelion software program and experimental values $k_{z_{exp}}$ N/m at off-centre point of the hub (M_x term consider the hub regions only); ℓ, w & t are beam parameters of classic tetraskelion force artefacts.

Sample ID	ℓ m	w m	t m	Predicted stiffness k_{z_p} N/m	Experimental $k_{z_{exp}}$ N/m	$k_{z_{exp}}/k_{z_p}$
CTTS1-CS	0.00293	0.00101	0.000179	2671.40	2741.20	1.02
CTTS1-DS	0.00289	0.00109	0.000189	3536.50	4521.60	1.27
CTTS2-CS	0.00297	0.001	0.000185	2803.50	2569.60	0.91
CTTS2-DS	0.00294	0.00101	0.000190	3162.30	4304.70	1.36

Table 9.11: Comparative analysis of stiffness k_{z_p} N/m predicted by triskelion software program and experimental values of stiffness $k_{z_{exp}}$ N/m at the centre of the hub; ℓ, w & t are beam parameters of angle-beam tetraskelion force artefacts.

Sample ID	ℓ mm	w mm	t μm	Predicted stiffness k_{z_p} N/m	Experimental stiffness $k_{z-c_{exp}}$ N/m	$k_{z_{exp}}/k_{z_p}$
ABTTS1-CS	0.00298	0.00109	0.000136	1201.09	1211.88	1.00
ABTTS1-DS	0.00296	0.00109	0.000152	1712.10	1746.64	1.02

Table 9.12: Comparative analysis of stiffness k_{z_p} N/m predicted by triskelion software program and experimental values of stiffness $k_{z-_{exp}}$ N/m at off-centre point of the hub (M_x term consider the hub regions only); ℓ, w & t are beam parameters of angle-beam tetraskelion force artefacts.

Sample ID	ℓ mm	w mm	t μm	Predicted stiffness k_{z_p} N/m	Experimental stiffness $k_{z_{exp}}$ N/m	$k_{z_{exp}}/k_{z_p}$
ABTTS1-CS	0.00298	0.00109	0.000138	1255.70	1129.65	0.89
ABTS2-DS	0.00296	0.00109	0.000152	1712.10	1660.82	0.97

Table 9.13: Performance of classic and angle-beam triskelion samples of force artefacts.

Sample ID	Linear region m	Sample No.	Linear region m
CTS1	500	ABTS1-60	600
CTS2	500	ABTS2-60	600
CTS1	400	ABTS1-60	500
CTS2	400	ABTS2-60	500
CTS1	250	ABTS1-120	300
CTS2	250	ABTS2-120	300

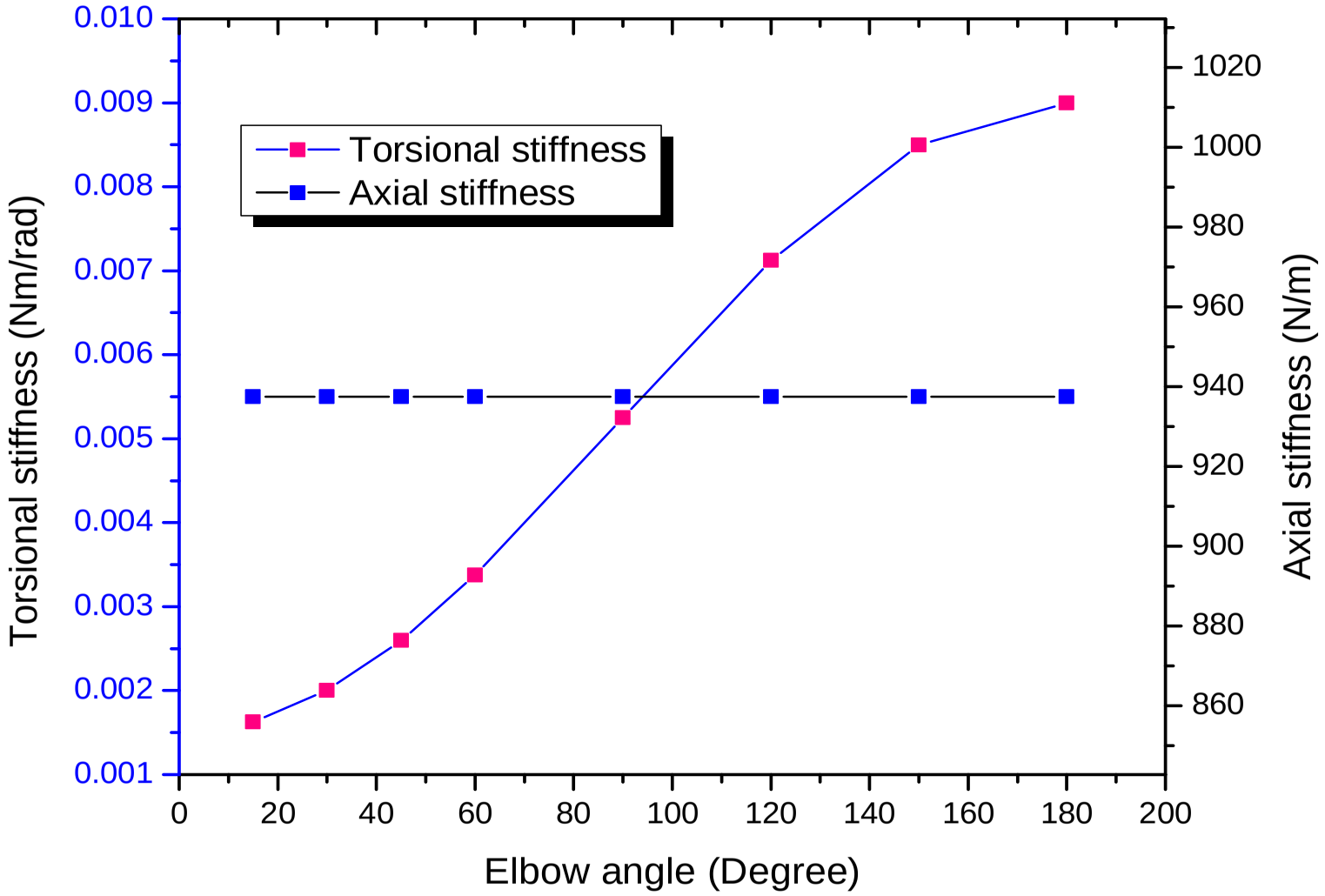

Table 9.14: The complete picture of predicted axial and torsional stiffness by the enhanced linear elastic model for triskelion force artefacts with elbow angle 15 °, 30 °, 45 °, 60 °, 90 °, 120 °, 150 ° and 180 °,.

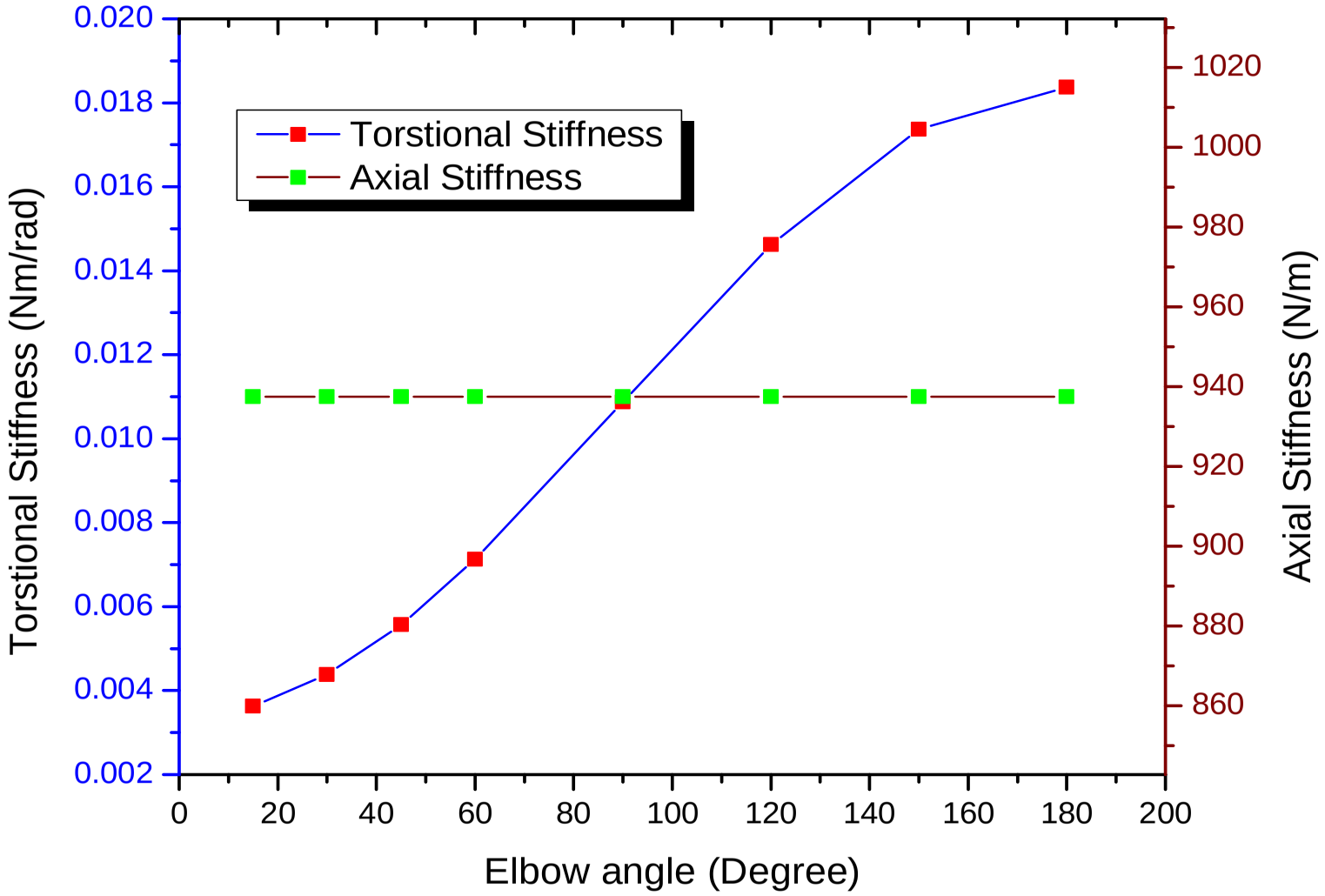

Table 9.15: The complete picture of predicted axial and torsional stiffness by the enhanced linear elastic model for triskelion force artefacts with elbow angle 15 °, 30 °, 45 °, 60 °, 90 °, 120 °, 150 ° and 180 °,.

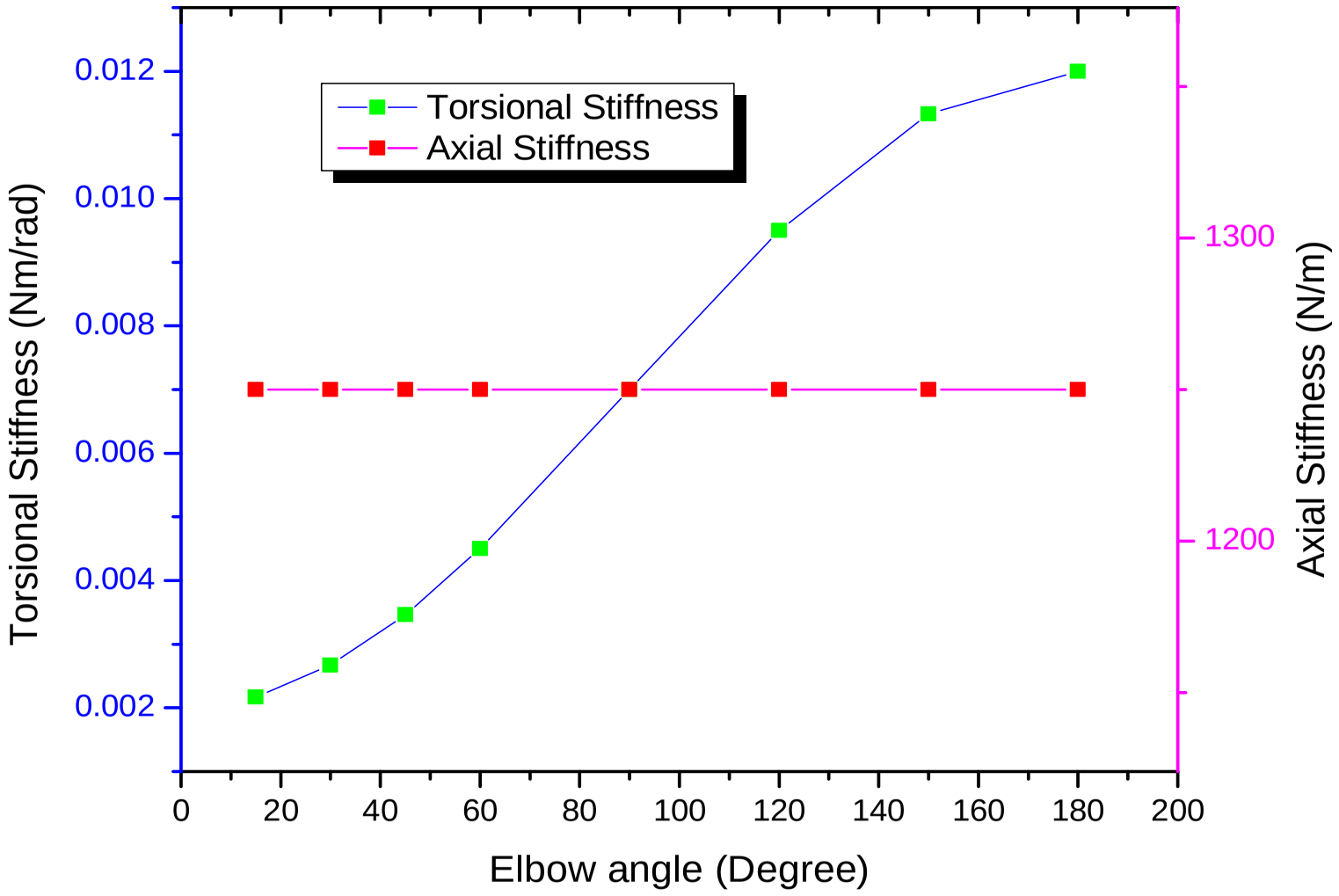

Table 9.16: The complete picture of predicted axial and torsional stiffness by the enhanced linear elastic model for triskelion force artefacts with elbow angle 15 °, 30 °, 45 °, 60 °, 90 °, 120 °, 150 ° and 180 °,.

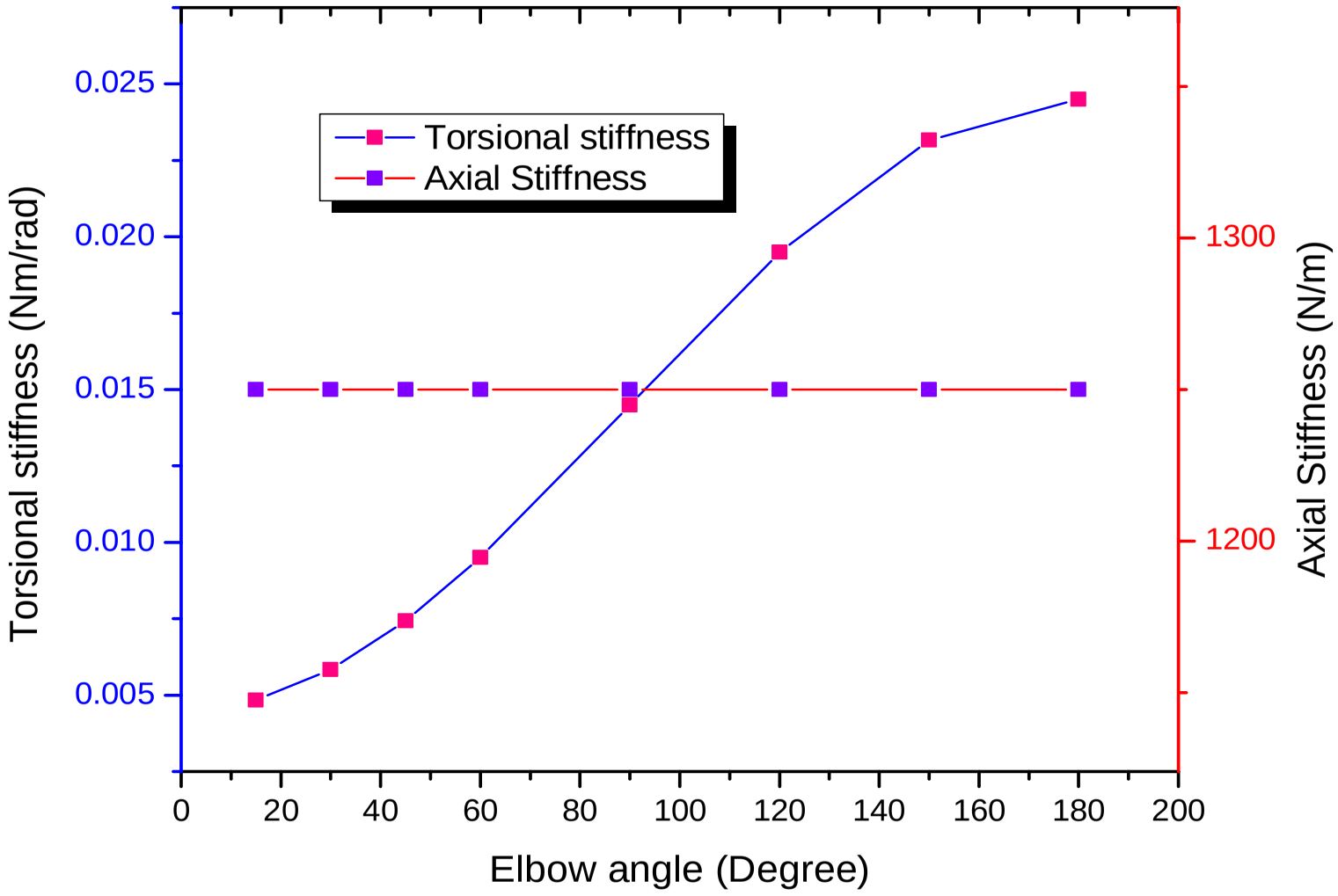

Table 9.17: The complete picture of predicted axial and torsional stiffness by the enhanced linear elastic model for triskelion force artefacts with elbow angle 15 °, 30 °, 45 °, 60 °, 90 °, 120 °, 150 ° and 180 °,.

Chapter 10

Conclusion

Low force and formal metrology measurement has been a demanding research area since around the year 2000 and has great importance in biophysics, biotechnology and other areas of research in the sciences. This thesis presents novel contributions for traceability of low force for industrial applications. The aims, objectives and specifications for this program of research work were set out in chapter 1. These aims and objectives were successfully achieved. The contributions of the research work performed that highlights to improved understanding, design and application of the triskelion-like planar flexures some time used as micro-probe suspension and potentially as source of physical artefacts for traceable low force calibration in industrial applications. The scope of thesis is summarised in figure 10.1.

This thesis contains six key areas of novel contributions for low force traceability that have great importance in metrology and nanotechnology. The first area describes extensive review confirmed/revealed that all published research work on triskelion style devices (triskelion force artefacts or triskelion micro-probe suspension) concentrated for no clearly explained reasons on a very narrow range of possible design variants. The major thrust of this is to examine whether other designs have pointed benefits further applications.

The second area is based on an extended version of the published linear elastic model of triskelion suspension that has been devised and implemented, giving user control over of geometric parameters. In particular the model systematically handle arbitrary number of

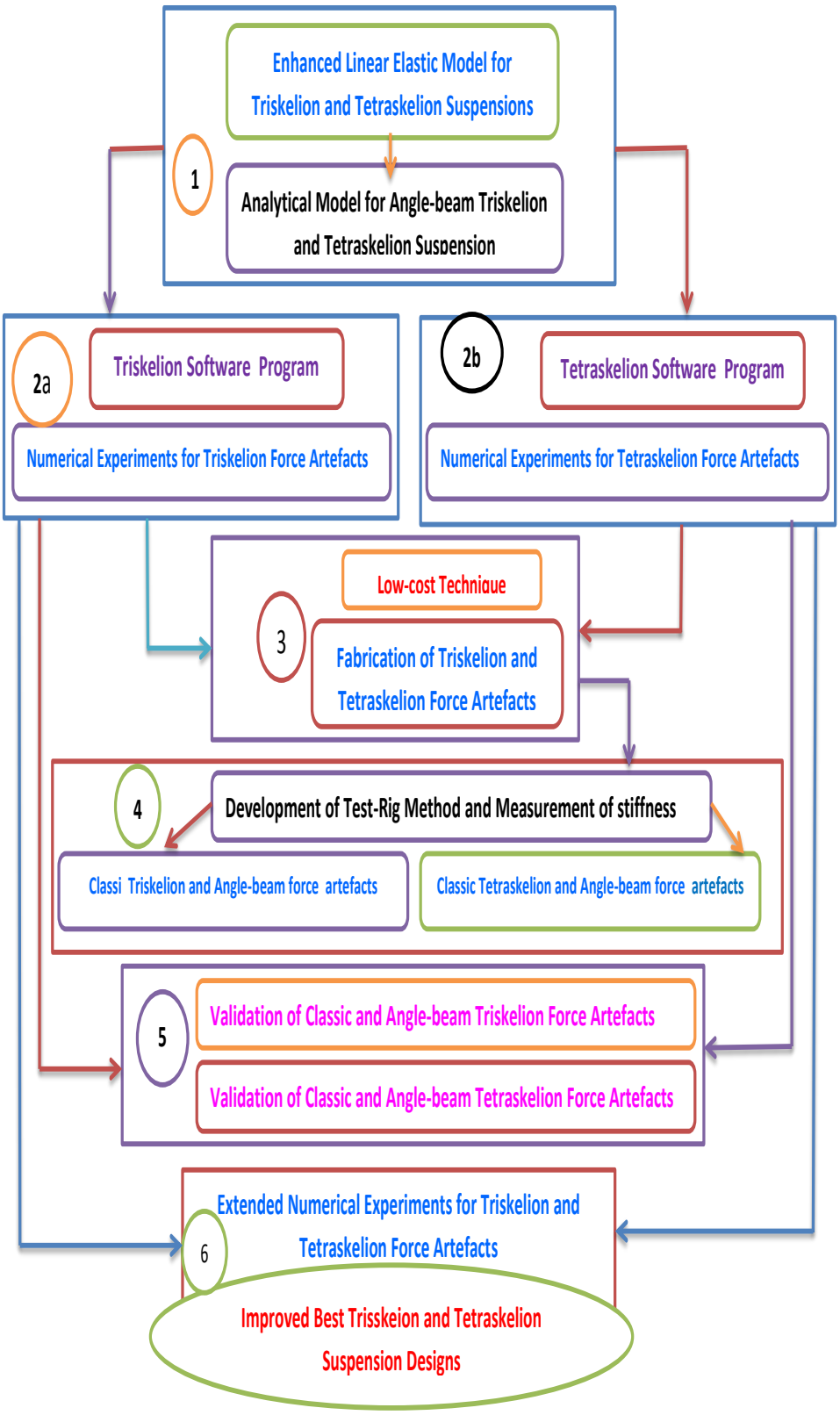

Figure 10.1: The scope of the research work performed in this thesis.

suspension limbs and arbitrary 'elbow angle' in those limbs.

The third area covers a spacial test-rig method that has been developed for physically evaluating devices under loads in the 1 mN to 1N region and deflection up to around 1 mm. Tests with it have verified the reasonableness of new models for describing small defection behaviour of triskelion and tetraskelion devices. Further tests have established that the expected stiffening spring characteristic of these devices is present and tends to follow closely a cubic force-displacement relationship. It is shown that these devices have an effectively linear range quite adequate for many applications as micro-probe suspensions or force transfer artefacts.

The fourth area focuses on the results that clearly confirm the novelty and stability of enhanced linear elastic model and capability to predict the stiffness for variant designs of triskelion and tetraskelion suspensions or distribution of "n" suspension beams around the centre of platform (hub) with elbow angle from 15 ° to 180 °. Polymeric devices have been made using a very simple technique, readily made more consistent for low-cost production. They performed even better than expected, leading to further exploration being one of the main recommendation for this research work. They offer the designer new options in terms of combination of overall size, robustness and stiffness.

The fifth area discuses physical and computational experiments that controlling the elbow angle provides alternative means for adjusting the overall values and ratio between linear and angular stiffness in these type of devices. Torsional stiffness increases monotonically but non-linearity with angle. Controls of this stiffness ratio is (to different targets) important for both micro-probe suspension and force artefacts.

The sixth area describes the classic triskelion suspension, and uses a relatively rigid inner arm section for its limbs. Physical and computational experiments confirm the intuition that alternative "angle-beam" design offer lower stiffness and so offer further options. Moreover it is shown that the reducing levels of elastic (quasi-kinematic) constraints do

not lead to low mechanical stability.

Finally, compact triskelion devices can offer different linear and torsional stiffness to triskelion in ranges that might be advantageous for some force transfer artefact applications.

10.1 Recommendation for the future production of triskelion and tetraskelion devices

The experiments performed in this thesis suggest that small polymeric devices perform very well, even with very simple methods used. This opens up new, attractive options for low-stiffness, robust suspensions and further study is strongly recommended.

For industrial applications, the injection molding technique is also recommended for the mass production of triskelion and tetraskelion suspension designs for micro probe and force artefacts.

Furthermore, the following suggestion is also recommended for the future research work.

- The casting technique has inevitably a limited dimensional precision but can still produce quite reasonable consistency that has been seen from device to device. The promising results indicate its good prospects for low force technology. The accuracy in the practical stiffness of force artefacts may also be achieved by using stereolithography technique.

Bibliography

[1] What is Traceability? `http://www.nist.gov/pml/mercury_traceability.cfm` (accessed: 23 July 2014).

[2] Low force measurement:Low Force balance. `http://www.npl.co.uk/science-technology/dimensional/research/low-force-measurement`(accessed: 26 August 2014).

[3] Cumpson P.J. Hedley J. and Clifford C.A. Microelectromechanical device for lateral force calibration in the atomic force microscope: Lateral electrical nanobalance . *Journal of Vacuum Science & Technology B Microelectronics and Nanometer Structures (Vol. 23, Issue 5)*, pages 1071–1023, 2005.

[4] Pratt J.R. Kramar J. Newell D. and Smith D.T. Review of SI traceable force metrology for instrumented indentation and atomic force microscopy. *Measurement Science and Technology 16 2129*, page 21292137, 2005.

[5] Niehe S. New experiences with a force measuring facility from the range from 1 mN to 5 N. `http://www.imeko.org/publications/tc3-2005/IMEKO-TC3-2005-024u.pdf`(accessed: 25 August 2014), 2005.

[6] Kumme R. A new calibration facility for dynamic forces up to 10 kN. In *Proceedings, XVII IMEKO World Congress, June 22 27, Dubrovnik, Croatia*, 2003.

[7] Nesterov V. Facility and methods for the measurementof micro and nano forces in the range below 10^{-5}N with a resolution of 10^{-12}N (development concept) . *Meas. Sci. Technol. 18*, page 360366, 2007.

[8] Slanina O. *"Aufbau einer Kraft"-Normalmesseinrichtung im Nennlastbereich von 0.1 bis 200 mN*: Diploma Thesis, Braunschweig, 2010.

[9] Choi J.H. Choi D.J. and Kim S.H. The modelling and design of a mechanism for micro-force measurement.

[10] Kim M.S. Choi J.H. Kim J.H. and Park Y.K. SI-traceable determination of constants of varius atomic force microscope cantilvers with a small uncertainty of 1%. *Meas. Sci. Techni. 18*, pages 3351–3358, 2007.

[11] Choi J.K. Kim M.S. and Park Y.K. Quantum-based mechanical force realization in pico-newton range. `arxiv.org/pdf/cond-mat/0606022`(accessed: 5 August 2013), 2006.

[12] Schwartz R. and Michael Borys M. The proposed new SI: consequences for mass metrology. *ACTA IMEKO Vol.3, No. 2,*, pages 3–8, June 2014.

[13] Hocken J.R. and Pereira P.H. *Coordinate measuring machines and systems, second edition.* CRC Press., 2011.

[14] Pril W.O. *Development of high precision mechanical probe for coordinate measuring machines.* PhD thesis, Geboren te Eindenhoven, 2002.

[15] Dorozhovets N. Manske E. Balzer F.G., Hausotte T. and Jager G. Tactile 3D micro-probe system with exchangeable styli. *Meas. Sci. Technol. 22*, page 5, 2011.

[16] Phataralaoha A. Tibrewala T. and Buttgenbach S. Analysis of full and cross-shaped boss membranes with piezoresistors in transversal strain configuration. *J. Micromech. Microeng*, 2008.

[17] Donker R. Widdershoven I. and Spaan H. Isara 400:enabling ultra-precision coordinate metrology for large parts . In *Proc. 10th Euspen Int. Conf. vol 1*, pages 204–208, 2010.

[18] Bos E. Delbressine F. and Dietzel A. Characterization of measurement effects in an MST based nano probe. In *e Proc. 5th Euspen Int. Conf*, pages 349–352, 2005.

[19] Stalder A. and Durig U. Nanoguitar Oscillating string as force sensor. *Rev. Sci. Instrum. 66 (6), 3576-3579*, pages 3576–3579, 1995.

[20] Shibamoto M. Mitsuya Y. Fukuzawa F., Ando T. and Zhang H. Monolithically fabricated double-ended tuning-fork-based force sensor. *J. Appl. Phys. 99 094901*, 2006.

[21] Li A. Vedula S.R.K. Lim C.T. Zhou E.H. and Fu H.X. Experimental techniques for single cell and single molecule biomechanics. *Materials Science and Engineering C 26*, page 12781288, 2006.

[22] Oberhauser A.F. Marszalek P.E.Vazquez C.M. and Julio M. Fernandez J.M. Single protein misfolding events captured by atomic force microscopy. `http://www.nature.com/nsmb/journal/v6/n11/abs/nsb1199_1025.html`(accessed: 13 August 2014), 1999.

[23] Rief M. Gautel M. Oesterhelt F. Fernandez F.J. and Hermann E.G. Reversible unfolding of individual titin immunoglobulin domains by AFM. *Science, New Series, Vol. 276, No. 5315*, pages 1109–1112, May 1997.

[24] Viani M.B. Schaffer T.E. Chand A. Matthias Rief M. Gaub H.E. and Hansma P.K. Small cantilevers for force spectroscopy of single molecules. *Journal of Applied Physics, Vol. 86, No. 4*, 1999.

[25] Gates R.S. and Pratt J.R. Prototype cantilevers for SI-traceable nanonewton force calibration. *Meas. Sci. Technol. 17*, page 28522860, 2006.

[26] Clifford C.A. Cumpson P.J. and Hedley J. Quantitative analytical atomic force microscopy: a cantilever reference device for easy and accurate AFM spring-constant calibration. *Meas. Sci. Technol. 15*, page 13371346, 2004.

[27] Chetwynd D. G. Liu X. and Smith S. T. Signal Fidelity and tracking forces in stylus profilometry.

[28] Liu X. *Fidelity study in surface measurements in nano metrology.* PhD thesis, University of Warwick, 1994.

[29] Pratt J.R. The small force metrology laboratory at the National Institute of Standards and Technology. http://www.imeko.org/publications/wc-2006/PWC-2006-RT-TC3-002u.ppt(accessed: 3 August 2013), 2006.

[30] Illemann J. Future force standard machines from newton to piconewton at PTB. http://www.imeko.org/publications/wc-2006/PWC-2006-RT-TC3-003u.ppt(accessed: 29 March 2014), 2006.

[31] Kim M.S. The status of academic and industrial force metrology below 1 N and the corresponding strategy at the Korea Research Institute of Standards and Science. <http://www.imeko.org/publications/wc-2006/PWC-2006-RT-TC3-001u.ppt>(accessed: 29 March 2014), 2006.

[32] Muller D.J. and Y.F. Dufrene Y.F. Atomic force microscopy as a multifunctional molecular toolbox in nanobiotechnology. *Nature Nanotechnology 3 (5)*, page 261269, 2008.

[33] G. Bao G. Zhu C. and N. Wang N. Cell mechanics: mechanical response, cell adhesion, and molecular deformation. *nnual Review of Biomedical Engineering 2*, page 189226, 2000.

[34] Mehta A.D. Rief M. Spudich J.A. Smith D.A. and Simmons R.M. Single molecule biomechanics with optical methods.

[35] Quate C.F. Binnig, G. and C. Gerber. Atomic force microscope. *Phys. Rev., 56(9)*, page 930933, 1986.

[36] N. Jalili and K. Laxminarayana. A review of atomic force microscopy imaging systems: application to molecular metrology and biological sciences. *Mechatronics, 14(8)*, page 907945, 2004.

[37] Leite F.L. Mattoso L.H.C. Oliveira Jr O.N. and Herrmann Jr P.S.P. The atomic force spectroscopy as a tool to investigate surface forces: basic principles and applications. http://www.formatex.org/microscopy3/pdf/pp747-757.pdf(accessed: 29 August 2014), 2007.

[38] Oliver W.C. and Pharr G.M. An improved technique for determining hardness and elstic modulus using load and displacement sensing identation experiments. *J. Metter. Res. 76*, pages 1564–1583, 1992.

[39] Willemsen O.H. Snel1 M.S.E. Cambi A. Greve J. Grooth B.G.D. and Figdor C.G. Biomolecular interactions measured by atomic force microscopy. *Biophys. J. 79*, page 32673281, 2000.

[40] Mohideen U. and Roy A. Precision measurement of the Casimir force from 0.1 to 0.9μ. *Physical Review Letters 81(21)*, pages 4549–4552, 1998.

[41] A Raman A. Melcher J. and Tung R. Cantilever dynamics in atomic force microscopy. *Nano Today, Vol. 3*, page 2027, NUMBER 1-2 2008.

[42] Zafari H. Amanati S. Damircheli A.M. Korayem, M. and N Ebrahimi. Analysis and control of micro-cantilever in dynamic mode AFM. *Nonlinear Dynamics, 20*, page 197220, 1999.

[43] Y Zhang X Liu, K Kim and Y Sun. Nanonewton force sensing and control in microrobotic cell manipulation. *The International Journal of Robotics Research*, page 10651076, 2009.

[44] Prater C.B. P.G. Maivald P.G. Kjoller K.J. and Heaton M.G. Probing nano-scale forces with the atomic force microscope. `http://web.mit.edu/cortiz/www/3.052/3.052CourseReader/11_VeecoNanoscaleforces.pdf`(accessed: 7th October 2014).

[45] Leach R. K. *Fundamental princple of engineering nanmetrology.* 1^{st} Edition William Andrew, USA, 2010.

[46] Seugling R.M. and Pratt J.R. Traceable force metrology for micronewton level calibration. *Proceedings of the annual meeting- american society for precision engineering*, pages 430–433, 2004.

[47] Pratt J.R. Karamar J.A. Newell D.B. and Smith D.T. Review of SI traceabilty force instrumated indentation and atomic force microsope. *Meas. Sci. 16*, pages 2129–2137, 2005.

[48] Leach R.K. Traceble nanonewton force measurement at National Physical Laboratory, UK. In *Proceeding of* 6^{th} *internation conference-Baden Bei Wien*, 2006.

[49] Blunt L. Haycocks J. Harris P. Jackson K. Oldfield S. Leach R., Chetwynd D. and Reilly S. Recent advances in traceable nanoscale dimension and force metrology in the UK. *Meas. Sci. Technol. 17*, pages 467–476, 2006.

[50] Leach R.K. Claverley J. Giusca C. Jones C.W. Nimishakavi L. and Sun W. Advances in engineering nanometrology at the National Physical Laboratory. *Meas. Sci. Technol. 23 (2012)*, page 9, 2012.

[51] Choi J.H. Kim M.S. Park Y.K. and Choi M.S. Parallel error analysis and compansation for micro-force measurement. *Meas. Sci. Technol. 15*, pages 237–247, 2004.

[52] Choi J.H. Kim M.S. Park Y.K. and Choi M.S. KRISS approach to pico-newton standard force realisation. *Proc. XIX IMEKO World.*, 2009.

[53] Carbone L. Cavalleri A. Ciani G. Dolesi R. Hueller M. Tombolato S. Vitale S. and Weber W.J. Torsion pendulum facility for direct force measurements of LISA GRS related disturbances. `http://arxiv.org/abs/gr-qc/0611036`(accessed: 5 August 2013), 2006.

[54] Chen S.J. and Pan S.S. Nanonewton force generation and detection on a sensitive torsion pendulum. *Instrumentation and Measurement 58*, pages 897–901, 2009.

[55] Chen S.J. and Pan S.S. Introduction to research activities on traceable force measurements below 10μN in center for measurement standards. `http://www.imeko.org/publications/tc3-2010/IMEKO-TC3-2010-WS-004.pdf`(accessed: 5 August 2013), 2010.

[56] Chen S.J. and Pan S.S. A force measurement system based on an electrostatic sensing and actuating technique for calibrating force in a micronewton range with a resolution of nanonewton scale . *Meas. Sci. Technol. 22, No. 4*, page 045104 (8pp), 2011.

[57] Claverley J.D. and Leach R.K. A vibrating micro-scale CMM probe for measuring high aspect ratio structures. *Microsystem Technologies 16, 8-9*, pages 1507–1512, 2010.

[58] Gaub H.E. Helenius J., Heisenberg C.-P. and Muller D.J. Single-cell force spectroscopy. *Journal of Cell Science 121,*, pages 1785–1791, 2008.

[59] Kim M.S. Choi J.H. and Park Y.K. Quantum-based mechanical force realization in the piconewton range. *Appl. Phys. Lett 90 073117*, 2007.

[60] Park Y.K. Kim Y.W. Choi J.H., Kim M.S. and Kang D.I. Kriss approach to piconewton standard force realization. *XIX IMEKO World congress fundamental and applied metrology, September 6-11, 2009, Lisbon, Portugal*, pages 406–409, 2009.

[61] Traceability. `http://l-a-b.com/information/traceability/`(accessed: 23 July 2014).

[62] Role of measurement and calibration in the manufacture of products for the global market. `http://www.unido.org/fileadmin/user_media/Publications/Pub_free/Role_of_measurement_and_calibration.pdf`.

[63] BIPM IEC IFCC ISO IUPAC IUPAP and OIML. *Guide to the Expression of Uncertainty in Measurement (Geneva, Switzerland: International Organisation for Standardisation) ISBN 92-67-10188-9*. 2010.

[64] BIPM IEC IFCC ILAC ISO IUPAC IUPAP and OIML. *Evaluation of measurement data - Guide to the expression of uncertainty in measurement (GUM 1995 with minor corrections. Joint Committee for Guides in Metrology, JCGM 100)*. 2008.

[65] BIPM IEC IFCC ILAC ISO IUPAC IUPAP and OIML. *Evaluation of measurement data-Supplement 2 to the "Guide to the expression of uncertainty in measurement"-Extension to any number of output quantities Propagation of Distributions Using a Monte Carlo Method (Joint Committee for Guides in Metrology, JCGM 102*. 2010.

[66] Young H. D. and Freedman R. A. *University physics with modern physics*. 13th Edition Addison-Wesley, 2010.

[67] Stefanescu D.M. *Handbook of Force Transducers*. springer, 2011.

[68] Hasan E.H. A review of concept of force measurements between past and today. *Sensors and Transducers Journal, Vol. 129, Issue 6*, pages 1–15, 2011.

[69] Jones C.W. Kramar J.A. Davidson S. Leach R.K. and Pratt J.R. Comparison of NIST SI force scale to NPL SI mass scale. *Meas. Sci. Technol. 17*, pages 2852–2860, 2008.

[70] Jones C.W. Low force metrology at the National Physical Laboratory, UK. `http://www.imeko.org/publications/tc3-2010/IMEKO-TC3-2010-WS-002.pdf` (accessed: 3 August 2013), 2010.

[71] Choi J.H. Measurement, back-action and future standard in ultra-small force metrology,. `http://www.imeko.org/publications/tc3-2010/IMEKO-TC3-2010-WS-005.pdf`(accessed: 3 August 2013), 2010.

[72] Kim M.S. Current status and perspective on low force metrology in Korea. `http://www.imeko.org/publications/tc3-2010/IMEKO-TC3-2010-WS-003.pdf`(accessed: 3 August 2013), 2010.

[73] Menelao F. Micro and Nanoforce metrology at PTB. `http://www.imeko.org/publications/tc3-2010/IMEKO-TC3-2010-WS-001.pdf`(accessed: 3 August 2013), 2010.

[74] Pan S.S. The activities of micro force measurement below 10 mN in Center for Measurement Standards. http://www.imeko.org/publications/tc3-2010/IMEKO-TC3-2010-WS-004.pdf(accessed: 3 August 2013), 2010.

[75] Kim M.S.and Pratt J.R. SI traceability: Current status and future trends for forces below 10 microNewtons. *Measurement 43*, page 169182, 2010.

[76] ICS. Standards catalogue. http://www.iso.org/iso/home/search.htm?qt=ISO+376&sort=rel&type=simple&published=on(accessed: 3 August 2013), 2011.

[77] Kim M.S. Pratt J.R. Brand U. and Jones C.W. Report on the first international comparison of small force facilities: a pilot study at the micronewton level . *Metrologia 49*, page 7081, 2012.

[78] Rosielle N. Henselmam R. and Cacace L. Low-force measurement facility design report review report. Technical report, Eindenhoven university of technolgy, pricision mechanics department, optical instrumentation division, TNO TPD.

[79] Newell D. Kramar J. Pratt J. Smith D. T. and Williams E. The nist microforce realization and measurement project. *IEEE Transactions on Instrumentation and Measurement*, pages 508–511, 2003.

[80] Pratt J. R. Smith D.T. Newell D. Kramar J.A. and Whitenton E. Progress toward Systeme International d'Unites traceable force metrology for nanomechanics . *Journal of Materials Research 19*, pages 366–379, 2004.

[81] Physikalisch-Technische Bundesanstalt (PTB). Mass and derived quantities(accessed: 4 august 2014). https://www.ptb.de/cms/.../2008/Mass_and_Derived_Quantities.pdf, 2008.

[82] Niehe S. A new force measuring facility for the range of 10 mN to 10N. In *in: Proceedings of 17th IMEKO World Congress, Dubrovnik*, page 2003.

[83] Kim M.S. Choi J.K. and Park Y.K. Accurate determination of spring constant of atomic force microscope cantilever and comparison with other methods. http://www.imeko.org/publications/wc-2006/PWC-2006-TC3-019u.pdf(accessed: 5 August 2013), 2006.

[84] Henselmans R. Rosielle N. Cacace L. Kappelhof P. Klinkhamer F. and Spierdijk H. Low force measurement facility: mechanical design report (Technical University of Eindhoven) . page 2004.

[85] Leach R.K. Oldfield S. Awan S. Blackburn J. and Williams J. Design of a bidirectional electrostatic actuator for realising nanonewton to micronewton forces. *NPL Report DEPC-EM001*, 2004.

[86] Jackson K. Leach R., Haycocks J. and Lewis A. Advances in traceable nanometrology at the National Physical Laboratory. *Nanotechnology 12.*, pages R1–R6 www.iop.org/Journals/na PII: S0957–4484(01)16633–X, 2000.

[87] Lewis S.L. and Havard D.C. History of Kilogram 18 and Other Important UK Reference Mass Standards . *NPL Report MOT1*, 1996.

[88] Luna J.P. Edwards C.H. and Gonzalez J.A. Development status of the ESA micro-Newton thrust balance . In *32nd International Electric Propulsion Conference, September 11 15*, 2011.

[89] Jones C.W. Low force metrology at the national physical. www.imeko.org/publications/tc3-2010/IMEKO-TC3-2010-WS-002.pdf(accessed: 4 August 2013), 2010.

[90] Harley J. and Kenny T.W. A high-stiffness axial resonant probe for atomic force microscopy . *Journal of Microelectromechanical Systems 10*, pages 434–441, 2001.

[91] Cumpson P.J. and Hedley J. Accurate force measurement in the atomic force microscope: a microfabricated array of reference springs for easy cantilever calibration. *Nanotechnology 14*, pages 918–924, 2003.

[92] Matei G.A. Thoreson E.J. Pratt J.R. Newell D.B. and Burnham N.A. Precision and accuracy of thermal calibration of atomic force microscopy cantilevers. *Rev. Sci. Instr. 77, 083703*, 2006.

[93] Pratt J. Newell D. Kramar J. and Seugling R. Realizing and disseminating the SI micronewton with the next generation NIST electrostatic force balance . In *Proc. ASPE 2004 Annual Meeting (Orlando, FL)*, 2004.

[94] Pratt J.R. and Kramar J.A. SI realisation of small forces using an electrostatic force balance . In *Proceedings of the 18th IMEKO World Congress, (Rio de Janeiro, Brazil)*, pages 17 – 22, 17-22-2006.

[95] Keine-Besten T Brand U Hoffmann W, Loheide S and Schlachetzki. A 2000 method of characterizing micro mechanical beams and its calibration for the application in micro force measurement systems . *Proceedings of the Micro Tee, Hannover, Germany, 25th - 27th September*, 2000.

[96] Illemann J. The achievable uncertainty for balance-based force standard machines in the range from micronewton to newton . *in:Proceeding of the Joint International Conference IMEKO TC3/TC16/TC22, Merida, Mexico*, 2007.

[97] Illemann J and Kumme R. Research for a national force standard machine in the range from micro Newton to Newton relying on force compensation. In *in: Proceedings of 18th IMEKO World Congress, Rio de Janeiro*, 2006.

[98] Behrens I. L. Doering L. and Peiner E. Piezoresistive cantilever as portable micro force calibration standard . *Journal of Micromechanics and Microengineering 13 (4)*, page S171S177, 2003.

[99] Illmann J. The achiveable uncertainty for balance-based force standard machines in the range from micronewton to newton. In *IMEKO* 20^{th} *TC3*, 2007.

[100] V Nesterov. Micro- and Nanoforce Metrology at PTB-IMEKO. www.imeko.org/publications/tc3-2010/IMEKO-TC3-2010-WS-001.pdf(accessed: 5 August 2013), 2012.

[101] Schlegel C. Slanina Haucke G. and Kumme R. Construction of a standard force machine for the range of 100 N 200 mN. http://www.imeko.org/publications/tc3-2010/IMEKO-TC3-2010-NP-009.pdf(accessed: 5 August 2013), 2010.

[102] Choi J.H. Kim M.S. Park Y.K. Kim Y.W. and Kang D.I. Kriss approach to piconewton standard force realization . www.imeko2009.it.pt/Papers/FP_458.pdf.

[103] Choi J.K. Kim M.S. Park Y.K. and Choi M.S. Quantum-based mechanical force realization in piconewton range. *Appl. Phys. Lett. Vol. 90, Issue 7, http://dx.doi.org/10.1063/1.2476385.*

[104] Chen S.J. and Pan S.S. Nanonewton force generation and detection based on a sensitive torsion pendulum. *IEEE Transactions on Instrumentation and Measurement*, pages 897–901, 2009.

[105] Stock M. The watt balance: determination of the Planck constant and redefinition of the kilogram. *Phil. Trans. R. Soc. A 2011*, pages 369, doi: 10.1098/rsta.2011.0184, September 2011.

[106] Fujii Y. Method of generating and measuring static small force using down-slope component of gravity. *Review of Scientific Instruments 78 (6) 066104*, 2007.

[107] Jones C.W. Kramar J.A. Davidson S. Leach R. K. and Pratt J. R. Comparison of NIST SI force scale to NPL SI mass scale . *Proc. ASPE, Oregon, USA*, 2008.

[108] Kim M.S. Choi J.H. Park Y.K. and Kim J.H. Atomic force microscope cantilever calibration device for quantified force metrology at micro- or nano-scale regime: the nano force calibrator (NFC). *Metrologia 43*, pages 389–395, 2006.

[109] Stock M. Watt balance experiments for the determination of the Planck constant and the redefinition of the kilogram. *Metrologia. 50*, pages R1–R16, 2013.

[110] On the possible future revision of the SI. `http://www.bipm.org/en/si/new_si/`(accessed: 11 August 2014).

[111] . `http://www.bipm.org/en/si/new_si/what.html.`(accessed: 9 August 2014).

[112] Shisong L. Bing H. Zhengkun L. and Jiang L. Precisely measuring the Planck constant by electromechanical balances. *Measurement 45*, pages 1–12, 2012.

[113] CCM Recommendation G. Considerations on a new definition of the kilogram. `http://www.bipm.org/utils/common/pdf/CCM12.pdf`(accessed: 9 August 2014), 2010.

[114] Mohr P.J. Taylor B.N. and Newell D.B. CODATA recommended values of the fundamental physical constants: 2010. *Rev. Mod. Phys. 84*, pages 1527–605, 2012.

[115] Baumann H. et al. Realization of the anticipated definition of the kilogram . In *Proc. Conf. on Precision Electromagnetic Measurements (CPEM) (Washington DC, 16 July)Conference Digest, 340*, pages Conference Digest, 340, 2012.

[116] Baumann H. Eichenberger A. Cosandier1 F. Jeckelmann1 B. Clavel R. Reber D. and Tommasini D. Design of the new METAS watt balance experiment Mark II. *Metrologia 50*, page 235242, 2013.

[117] Baumann H. Eichenberger A. Jeckelmann B. Tommasini D. Cosandier F. Clavel R. Beguin Ch. and Reber D. The new watt balance experiment. In *at METAS 20th IMEKO World Congress (Busan, Republic of Korea, September, 10-14*, 2012.

[118] Bos E.J.C. *Tactile 3D probing system for measuring MEMS with nanometer uncertainty.* PhD thesis, Geboren te Eindenhoven, 2008.

[119] Bos E.J.C. Widdershoven I. and Haitjema H. Calibration and redesign of a nano probe based on MST technology. In *Proceedings of the 4th EUSPEN international conferecne: May 31-June 2, Glasgow, UK*, 2004.

[120] Lewis A.J. Peggs G.N. and S. Oldfield. Design for a compact high-accuracy CMM. *Annals of CIRP, 48/1*, pages 417–20, 1999.

[121] Claverley J.D. and Leach R.K. Development of a three-dimensional vibrating tactile probe for miniature CMMs. *Precision Engineering, 37, 2*, pages 491–499, 2013.

[122] Triskelion ultra-precision touch probe. `http://www.ibspe.com/category/triskelion-touch-probe.htm`(accessed: 12 August 2014), 2014.

[123] Isara 400 ultra precision coordinate measuring machine. `http://www.ibspe.com/category/isara-400-3d-cmm.htm`(accessed: 12 August 2014), 2014.

[124] Issra 400: Ultra precision coordinate measuring machine. `http://www.ibspe.com/category/isara-400-3d-cmm.htm`(accessed: 12 August 2014).

[125] Modelling the interaction forces between an ideal measurement surface and the stylus tip of a novel vibrating micro-scale cmm probe.

[126] Van Seggelen J.K. *A 3D coordinate measuring machine with low moving mass for measuring small products in array with nanometre uncertainty.* PhD thesis, Eindhoven University of Technology, 2007.

[127] Vermeulen M.M.P.A. *High-precision 3d-coordinate measuring machine: Design and prototype-development.* PhD thesis, Eindhoven University of Technology, 1999.

[128] W.P. Van Vliet. *Development of a fast mechanical probe for coordinate measuring machines.* PhD thesis, Technische Universiteit Eindhoven, 1998.

[129] H. Haitjema and W. O. Pril. Development of a silicon-based nanoprobe system for 3-d measurements. *Annals of CIRP, 50/1*, pages 365–368, 2001.

[130] J.K. Schellekens P.H.J. Pril W.O. Haitjema H. Van Seggelen and E. Pruik. Metrology for MEMS; MEMS for Metrology. In *Proc. of Memstand Int. Conf., p. 2.*, pages 18–228, 2003.

[131] Pril W.O. Struik K.G. and Schellekens P.H.J. Development of a 2D probing system with nanometre resolution,. In *Proc. of the 16th ASPE*, page 438442, 1997.

[132] Van Vliet W. P. and Schellekens P.H.J. Accuracy limitations of fast mechanical probing. *Annals of CIRP, 45/1*, page 483 487, 1996.

[133] Meli F. Bieri M. Thalmann R. Fracheboud M. Breguet J.-M. Clavel R. and Bottinelli S. Novel 3D analogue probe with a small sphere and low measurement force. In *Proceedings ASPE Summer Topical Meeting on CoordinateMeasuring Machines, and in German*, pages 69–73, 2003.

[134] Meli F. Fracheboud M. Bottinelli S. Bieri M. Thalmann R. Breguet J.M. and Clavel R. High precision, low force 3D touch probe for measurements on small objects. In *euspen Int.Topical Conference, Aachen, Germany*, 2003.

[135] Test & Measuring Instruments-Coordinate Measuring Instruments. `http://news.thomasnet.com/news/test-measuring-instruments/coordinate-measuring-instruments/100`(accessed: 23 August 2014).

[136] Coordinate Measuring Machines-Mitutoyo UK Ltd. `https://www.mitutoyo.co.uk/media/pdf/Catalogue/cmm.pdf`(accessed: 23 August 2014).

[137] Coordinate Measuring Machines: Bulletin No. 1598R. http://www.mitutoyo.com/pdf/1598R.pdf(accessed: 23 August 2014).

[138] Carmignato S. and De Chiffre L. A new method for thread calibration on coordinate measuring machines. *Annals of CIRP, 52/1*, pages 447–450, 2003.

[139] Pornnoppadol P. Cao S. Schmidt M. Wilke R. Buetifisch S. Nesterov V. and U. Brand. Three-dimensional microprobe with reduced probing forces. In *Proc. 3rd euspen Int. Conf., Eindhoven, The Netherlands*, pages 737–740, 2002.

[140] Kleine-Besten T. Loheide S. Brand U. Buetifisch S. and S. Buettgenbach. Development and characterisation of new probesfor dimensional metrology on microsystem components. In *Proc. 1st euspen Int. Conf., 2, Bremen, Germany*, pages 387–390 as it is in 10/2003, 999.

[141] Brand U. Cao S. Hoffmann W. Kleine-Besten T. Pornnoppadol P. and S. Buettgenbach. A Micro-probing system for dimensional metrology on microsystem components. In *Proc. of 2nd euspen int. Conference, Torino, Italy*, pages 266–269, 2001.

[142] U. Kleine-Besten T. Brand and H. Schwenke. Development of a special CMM for dimensional metrology on microsystem components, in:. In *Proc. ASPE Conf., Scottsdale, Arizona,22th-27th Oct.*, pages 542–546, 2000.

[143] Coordinate measuring machines: Probe systems. http://www.mitutoyo.co.uk/coordinate-measuring-machines/probes(accessed: 29 August 2014).

[144] Mark T.I. New mitutoyo cmm surftest probe system eliminates work: Changeover to second measurement device. http://www.mitutoyo.com/press_releases/new-mitutoyo-cmm-surftest-probe-system-eliminates-workpiece-changeover-to-second-m#sthash.6MatEqAS.dpuf(accessed: 29 August 2014).

[145] Technologies: Touch probes for machine tools. http://www.marposs.com/technology.php/eng/touch_probes_machine_tools(accessed: 29 August 2014).

[146] Touch probes for machine tools. http://www.heidenhain.com/en_US/products-and-applications/touch-probes/(accessed: 29 August 2014).

[147] Renishaw plc: CMM probes, software and retrofits. http://www.renishaw.com/en/cmm-probes-software-and-retrofits--6329(accessed: 29 August 2014).

[148] Jones C.W. *Development and characterisation of traceable force measurement for nano technology*. PhD thesis, University of Warwick, 2012.

[149] Delbressine F. Bos E. and Dietzel A. Characterization of measurement effects in an MST based nano probe. *probe Proc. 5th Euspen Int. Conf.*, pages 349–52, 2005.

[150] Sawla A. and Peters M. Intercomparison of Force Transducer Calibration. 1987.

[151] Leach R. Chetwynd D. Blunt L. Haycocks J. Harris P. Jackson K. Oldfield S. and Reilly S. Recent advances in traceable nanoscale dimension and force metrology in the UK. *Meas. Sci. Technol. 17*, page 467476, 2006.

[152] Madec T. Mann G and Meury P.A. Micro-mass standards to calibrate the sensitivity of mass comparators. *Metrologia 44 (5)*, page 266274., 2007.

[153] Ono A. Soto K. and Tomikawa Y. Monolithically fabricated double-ended tuning-fork-based force sensor. *Jpn. J. Appl. Phys. 42*, pages 5115–3119, 2003.

[154] Casimir H.B.G. Proceedings of the Koninklijke Nederlandse akademie van wetenschappen 51. page 793, 1948.

[155] Genet C. Lambrecht A. and Reynaud A. Temperature dependence of the Casimir effect between metallic mirrors. *Physical Review A 62, 012110*, 2000.

[156] Lamoreaux S.K. Demonstration of the Casimir force in the 0.6 to 6μm range, Physical Review Letters. *Physical Review Letters 78(1)*, pages 5–8, 1997.

[157] Sparnaay M.J. Measurement of attractive forces between flat plates . *Physica 24*, page 751764, 1958.

[158] Yan D. Castillo-Garza R., Chang C.C. and Mohideen U. Customized silicon cantilevers for Casimir force experiments using focused ion beam milling. *Journal of Physics: Conference Series 161 012005*, 2009.

[159] Torricelli G. Carter E.L. Ward M.C.L. Anthony C.J., Bowen J. and Binns C. AFM characterisation of silicon-on-insulator push-in plates for Casimir force measurements. *Micro& Nano Letters, Vol 3*, pages 7–11, 2008.

[160] Maradudin A.A. and Mazur P. Effects of roughness on the van der Waals force between macroscopic bodies. *Physical Review B 22 (4)*, pages 1677–1686, 1980.

[161] Lpez D. Decca S.R. Fischbach E. and Krause D.E. MEMS-Based force sensor: Design and applications. *Bell Labs Technical Journal 10(3)*, page 6180, 2005.

[162] Reid M.T.H. McCauley A.P. Kravchenko I.I. Lu T. Bao Y. Johnson S.G. Zou1 J. Marcet1 Z. Rodriguez A.W. and Chan H.B. Casimir forces on a silicon micromechanical chip. *Nature communications, 4:1845 DOI: 10.1038/ncomms2842*, May 2013.

[163] Fateev E.G. Quantum motor and future. `http://arxiv.org/abs/1301.4678`(accessed: 15 August 2014), 2013.

[164] Choi J.H. Kim M.S. Park Y.K. and Choi M.S. Parallel error analysis and compansation for micro-force measurement. *Appl. Phys. Lett. 90 (7), 073117*, pages 237–247, 16 Feb 2007 2007.

[165] Maxwell's equations and electromagnetic waves. `ocw.mit.edu/courses/physics/../MIT8_02SC_notes26to30.pdf`(accessed: 13 August 2014).

[166] Ashkin A. and Dziedzic M.J. Stability of optical levitation by radiation pressure. *Appl. Phys. Lett. 24, 586 (doi: 10.1063/1.1655064)*, 1974.

[167] Metzger C.H. and Karrai K. Cavity cooling of a microlever, Nature Vol. 432. `http://www.nature.com/nature/journal/v432/n7020/abs/nature03118.html`(accessed: 13 August 2014), 2004.

[168] Chen S.J. and Pan S.S. Nanonewton force generation and detection based on a sensitive torsion pendulum. `http://arxiv.org/pdf/0806.3300.pdf`(accessed: 13 August 2013), 2008.

[169] Liang Y.A. Peattie A.M. Hansen W.R. Sponberg S. Kenny T.W. Fearing R. Israelachvili J.N. Autumn K., Sitti M. and Full R. Evidence for van der Waals adhesion in gecko setae PNAS 99 12252 . *PNAS 99 12252*, 2002.

[170] Argento C. and French R.H. Parametric tip model and force-distance relation for Hamaker constant determination from atomic force microscopy. *J. Appl. Phys 80*, page 60816090, 1996.

[171] Carrion-Vazquez M. Oberhauser A., Hansma P. and Fernandez J.M. Stepwise unfolding of titin under force-clamp atomic force microscopy. *PNAS 98(2), 468-472*, pages 468–472.

[172] Erickson H. Oberhauser A., Marszalek P. and Fernandez J.H. The molecular elasticity of the extra cellular matrix protein tensacin. *Nature 393*, pages 181–185, 1998.

[173] Dumont C. Emilsson T. and Gruebele M. Reaching the protein folding speed limit with large, sub-microsecond pressure jumps. *Nature Methods 6*, pages 515–519, 2006.

[174] Kellermayer M.S.Z. Simth S.B. Granzier H.L. and Bustamante C. Folding-unfolding transition in a single titin molecule charaterised with laser twiseers. *Science, Vol. 276*, pages 1112–1116, 1997.

[175] Gao M. Lu H. and Schulten K. Simulated refolding of stretched titin immunoglobulin domains. *Biophysical journal 81*, pages 2268–77, 2001.

[176] Marszalek P.E. Oberhauser A.F. Pang Y.P. and Fernandez J.M. Polysaccharide elasticity governed by chair-boat transitions of the glucopyranose ring. *Nature 396*, pages 661–664, 1998.

[177] Ruff P. Meyer E. Lee D.W. Vettiger P. Gysin U., Rast S. and Gerber C. Temperature dependence of the force sensitivity of silicon cantilevers . *Phys. Rev. B 69 045403*, 2004.

[178] Clifford C.A. and Seah M.P. The determination of atomic force microscope cantilever spring constants via dimensional methods for nanomechanical analysis. *Nanotechnology 18*, page 16661680, 2005.

[179] Burnham N.A. Chen X. Hodges C.S. Matei G.A. Thoreson E.J. Roberts C.J. Davies M.C. and Tendler S.J.B. Comparison of calibration methods for atomic-force microscopy cantilevers. *Nanotechnology 14*, page 16, 2003.

[180] Hutter J.L. and Bechhoefer J. Calibration of atomic-force microscope tips. *Rev. Sci. Instrum. 64*, page 18681873, 1993.

[181] Tortonese M. Barrett R.C. and Quate C.F. Atomic resolution with an atomic force mciroscope using piezoresistive detection. *Appl. phys. Lett. 62*, pages 834–836, 1993.

[182] Dushkin C. Direct measurement of nanonewton capillary forces. *Journal of Col/oid and Interface Science 181*, pages 657–660, 1996.

[183] Degertekin F.L. Hadimioglu B. Sulchek T. and Quate C.F. Actuation and characterization of atomic force microscope cantilevers in fluids by acoustic radiation pressure. *Applied Physics Letters Vol. 78, No. 11*, pages 1628–1630, 2001.

[184] Smith S. T. *Flexure: elements of elastic mechanisms.* CRC Press, 2000.

[185] Olhoff N. Eschenauer H. and Schnell W. *Applied structral mechanics.* Springer-verlag Berlin Heidelberg GmbH, 1997.

[186] Smith S. T. and Chetwynd D. G. *Fundamental of ultraprecision mechanical design.* Taylor and Farancis Books Ltd., 2000.

[187] Gindy N. Sun Y., Fowkes C.R. and Leach R.K. Variation risk analysis: MEMS fabrication tolerance for a micro CMM probe. *The international journal of advanced manufacturing technology, Volume 63*, pages 1113–1120, 2010.

[188] Georgi A. Claverley J.D. and Leach R.K. Modelling the interaction forces between an ideal measurement surface and the stylus tip of a novel vibrating micro-scale CMM probe. *Precision Assembly Technologies and Systems*, pages 131–138, 2010.

[189] Tang Y.K. C Bailey Claverley J. Leach R. Rajaguru P., Stoyanov S. and Topham D. Numerical modelling methodology for design of miniaturised integrated products-an application to 3D CMM micro-probe development. In *Thermal, Mechanical & Multi-Physics Simulation, and Experiments in Microelectronics and Microsystems (EuroSimE), 2010 11th International Conference*, pages 1–8. IEEE, 2010.

[190] CW Young C.W. and Budyans R.C. *Roark's formulas for stress and strain*. McGraw-Hill, 2002.

[191] A piezoelectric translation device capable of moving up to 70 microns with very high linearity and essentially perfect repeatability. `http://www.nanopositioning.com/products/digital-piezo-translators`(accessed: September 2013).

[192] Haitjema H. Rosielle N. Kotte G. and Steijaert H. A universal parallel-moving displacement generator for nano-metrology. *Meas. Sci. Technol. 9 doi:10.1088/0957-0233/9/7/016*, 1998.

[193] Queensgate Instruments. Digital piezo translators equipped with capacitive sensors closed with a closed loop range of up to 120m. `www.nanopositioning.com/sites/nanopositioning.../QUE29-DPT-D.pdf?` (accessed: 15 September 2013).

[194] General Microtecnology & Photonics. Digital Piezo Translator (DPT) Series. `file:///C:/Users/hurkayani/Downloads/GMP_DPT_Datasheet.pdf`(accessed: 23 October 2014).

[195] Queensgate Instruments. DPT-C AX101 / AX301 Host unit operating manual. `164.54.212.3/control_systems_manuals/queensgate_manual.pdf`(accessed: 23 August 2014).

[196] Fischer-Cripps A.C. *Introduction to contact mechanics*. Springer, 2007.

[197] Panich N. and Yong N.S. Improved method to determine the hardness and elastic moduli using nano-identation. *KMITL Sci. J. Vol. 5 No. 2*, 2005.

[198] Gaylord C.N. Gaylord E.H. and Stallmeyer J.E. *Structural engineering handbook*. McGraw-Hill., 1997.

[199] Vijay K.V. Xiaoning J. and Vasundara V.V. *Microstereolithography and other fabrication techniques for 3D MEMS*. John Wiley & Sons, LTD, 2001.

[200] PRIME Faraday Partnership. *An Introduction to MEMS*. Loughborough University, 2002.

[201] Gardner J.W. Varadan V.K. and Awadelkarim O.O. *Microsensors MEMS and smart Devices*. John Wiley & Sons, Chichester, 2005.

[202] Malek C.K. and Saile V. Applications of LIGA technology to precision manufacturiung of high-aspect-ratio micro-components and systems. *Microelcetronics Journal. 35*, pages 131–143, 2004.

[203] Schomburg W.K. et al. AMANDA-low-cost production of microfluidic devices. *Sensors and Acuators, A 70*, pages 153–158, 1998.

[204] Bartolo P. J. *Stereolithography: Materials, processes and applications* . Springer, 2011.

[205] Nguyen K.T. and West J.L. Photopolymerizable hydrogels for tissue engineering applications. *Biomaterials, vol. 23, no. 22*, pages 4307–14, Nov. 2002.

[206] Ikuta K. and Hirowatari K. Real three-dimensional microfabrication using stereolithography and metal moulding. *Proc. IEEE MEMS*, pages 42–47, 1993.

[207] Takagi T. and Nakajima N. Photoforming applied to fine machining. *Proceedings IEEE Micro Electro Mechanical Systems*, pages 173–178, 1993.

[208] Ikuta K. Ogata T. Tsubio M. and Kojima S. Development of mass productive microstereolithography (Mass-IH process). pages 301–305, 1996.

[209] Zhang X. Jiang X. N. and Sun C. Mirosterolithography of polymeric and ceramic microstructures. *Sensors and Actuators, A77 (2)*, pages 149–156, 1999.

[210] Maruo S. and Kawata S. Two-photon absorbed near infrared photopolymerisation for three-dimensional microfabrication," J.Microelectromech. *J.Microelectromech. Syst.,,7*, pages 411–415, 1998.

[211] Zissi S. et al. Sterolithography and microtechnologies. *Microsystem Technologies, 2-2,*, pages 97–102, 1996.

[212] Bertsch A. et al. Mirosterolithography using a liquid crystal display as dynamic mask-genrator. *Microsystem Technologies*, pages 42–47, 1997.

[213] Nakamoto T. and Yamaguchi K. Consideration on the producing of high aspect ratio micro parts using uv sensitive photopolymer. In *Proc. of seven international symposium on micromachine and human science*, pages 53–58, 1996.

[214] Monneret S. Loubere V. and Corbel S. Mirosterolithography using a dynamic mask genrator and nanocoherent visible light source. In *Proc. SPIE, 3680*, pages 553–561, 1999.

[215] Jiang X.N. Sun C. and Zhang X. Mirosterolithography of 3D complex ceramic microstures and PZT thick film on Si substrate. *ASME MEMS 1*, pages 67–73, 1999.

[216] Sun C. Fang N. Wu D. M. and Zhang X. Projection micro-stereolithography using digital micro-mirror dynamic mask. *Sensors and Actuators A: Physical, vol. 121, no. 1*, pages 113–120, May 2005.

[217] Dominick V.R. Donald V.R. and Marlene G.R. *Injection Molding Handbook*. Springer, 2000.

[218] Plastic injection moulding specialists UK. `http://www.stephensinjectionmoulding.co.uk`(accessed: 20 May 2014).

[219] D&M Plastics Inc. The History of Plastic Moulding. `http://www.plasticmoulding.ca/default.htm`(accessed: 20th May 2014).

[220] Design and manufacturing of plastic injection mould. `http://www.bgk.uni-obuda.hu/ggyt/targyak/seged/bagim1ennb/imw.pdf`(accessed: 20 May 2014).

[221] Greener J. and Wimberger-Fried R. *Precision injection molding: Process, materials, and applications*. Hanser Publications, 2006.

[222] Mayer R. Precision injection molding-how to make polymer optics for high volumeand high precision applications. *Optik & Photonik, No.4*, pages 46–51, December 2007.

[223] MPR Plastics Inc. Ultra-Precision Injection Molding. `http://www.mprplastics.com/page/speciality-applications/precision-injection-molding`(accessed: 18 May 2014).

[224] Chetwynd D.G. H.Ur rashid Davletzhanova Z. and Kogoshi Y. Elastic behaviour of millimetre-scale polymeric tri-skellion-like flexure. In *Proceeding of* 13^{th} *euspen international conference-Berlin*, pages 553–561, 2013.

[225] OriginLab. ORIGIN:Graphing & analysis. `http://www.originlab.com/`(accessed: 15 March 2014).

[226] Liu X. *Fidelity study in surface measurements in nanometrology*. PhD thesis, University of Warwick, 1994.

[227] Greenwood I. A. Mainsah E. and Chetwynd D. G. *Metrology and properties of engineering surfaces*. Springer, 2001.

Appendix A

Basic stiffness, compliance matrices and triskelion arm

A.1 Basic stiffness and compliance matrices

For simpler illustration of the derivation of the stiffness matrices from the elemental equations, a reduced version involving only x and z axis is used.

Elemental equations for a cantilever:

$$\delta_z = \frac{L^3}{3EI} F_z \tag{A.1}$$

$$\delta_z = -\frac{L^2}{2EI} M_y \tag{A.2}$$

$$\theta_y = -\frac{L^2}{2EI} F_z \tag{A.3}$$

$$\theta_z = -\frac{L}{EI} M_y \tag{A.4}$$

and

$$\delta_x = \frac{L}{AE} F_x \tag{A.5}$$

$$\theta_x \sim \frac{L}{KG} M_x \tag{A.6}$$

with

$$I = \frac{w}{t^3} \tag{A.7}$$

$$A = \frac{w}{t} \tag{A.8}$$

and

$$K = \frac{w}{t^3} \tag{A.9}$$

(For thin section). Ignoring the y-axis (to save space !) in compliance form we have

$$\boldsymbol{\Delta} = [K]\,\boldsymbol{F} \tag{A.10}$$

or

$$\begin{pmatrix} \delta_x \\ \delta_z \\ \theta_x \\ \theta_y \end{pmatrix} = \frac{L}{wt} \begin{bmatrix} \frac{1}{E} & 0 & 0 & 0 \\ 0 & \frac{4L^2}{Et^2} & 0 & -\frac{6L}{Et^2} \\ 0 & 0 & \frac{3}{Gt^2} & 0 \\ 0 & -\frac{6L}{Et^2} & 0 & \frac{12}{Et^2} \end{bmatrix} \begin{pmatrix} F_x \\ F_z \\ M_x \\ M_y \end{pmatrix} \tag{A.11}$$

Rather than fully inverting $[C]$, solve the elemental equations directly, assessing linear superposition.

$$\frac{EI}{L^2}\delta_z = \frac{L}{3}F_z - \frac{1}{2}M_y \tag{A.12}$$

$$\frac{EI}{L}\theta_y = -\frac{L}{2}F_z + M_y \tag{A.13}$$

$\Longrightarrow$

$$\frac{EI}{L}\left(\frac{\delta_z}{L} + \frac{\theta_2}{2}\right) = \left(\frac{L}{3} - \frac{L}{4}\right)F_z \tag{A.14}$$

and

$$F_z = \frac{12EI}{L^2}\left(\frac{\delta_z}{L} + \frac{\theta_y}{2}\right) \tag{A.15}$$

$\Longrightarrow$

$$\frac{EI}{L}\left(\frac{3\delta_z}{L} + \frac{2\theta_2}{2}\right) = \left(-\frac{3}{2} + 2\right)M_y \tag{A.16}$$

and

$$M_y = \frac{2EI}{L}\left(\frac{3\delta_z}{L} + 2\theta_y\right) \tag{A.17}$$

Hence the 'compared' stiffness matrix is

$$\boldsymbol{F} = [K]\,\boldsymbol{\Delta} \tag{A.18}$$

or

$$\begin{pmatrix} F_x \\ F_z \\ M_x \\ M_y \end{pmatrix} = \frac{wt}{L} \begin{bmatrix} \mathrm{E} & 0 & 0 & 0 \\ 0 & \frac{Et^2}{L^2} & 0 & -\frac{Et^2}{2L} \\ 0 & 0 & \frac{Gt^2}{3} & 0 \\ 0 & -\frac{Et^2}{2L} & 0 & \frac{Et^2}{3} \end{bmatrix} \begin{pmatrix} \delta_x \\ \delta_z \\ \theta_x \\ \theta_y \end{pmatrix} \tag{A.19}$$

A.2 Triskelion arm: beam length ratio and stiffness

Consider one leg from a triskelion with a 90 ° elbow angle, that being a single, simple case to model. The rigid arm length is a and beam has dimension $(\ell \times w \times t)$.
Platform tilt will be better constrained by longer arms, accordingly to the intuition that as a increases the z-deflection of the beam increases for a given tilt and the moment induced by the reaction force that deflection also increases.

Assume, a pure tilt θ directly towards the beam. The beam experience a an end displacement $a\theta$ but no end rotation on the θ_y beam axis (in the first approximation). However, it does experience a rotation in its θ_x. Extracting from the stiffness equations given by [14] and equation (3.24)

$$\begin{pmatrix} F_z \\ M_x \\ M_y \end{pmatrix} = \frac{Ewt}{\ell} \begin{bmatrix} \frac{t^2}{\ell^2} & 0 & \frac{t^2}{2\ell} \\ 0 & \frac{t^2}{3} & 0 \\ -\frac{t^2}{2\ell} & 0 & \frac{t^3}{3} \end{bmatrix} \begin{pmatrix} \delta_z \\ \theta_x \\ \theta_y \end{pmatrix} \tag{A.20}$$

Then substituting $\theta_x = \theta, \theta_y = 0, \delta z = a\theta$, we have

$$\frac{M_{total}}{\theta} = \left(\frac{aF_z + M_x}{\theta}\right) = \frac{Ewt}{\ell}\left(\frac{a^2t^2}{\ell^2} + \frac{3t^2}{2}\right) = \frac{Ewt^3}{\ell}\left(\frac{1}{8} + \frac{a^2}{\ell^2}\right) \tag{A.21}$$

The direct torsion is less important, when $a > \ell/2$, but starts to dominate as a approaches $\ell/4$. Only as a approaches ℓ is length does there become a significant effect from the lever arm. Other second-order displacements will tend to add further stiffening, but this simple guideline remains of retains illustrative.

Appendix B

Computation schema and codes for triskelion program,

B.1 Computation schema for triskelion Program

A. Input a forced displacement of the platform (6-vector), function (dpl.m)

- Force δ_x, δ_y, θ_x to zero.
- Model uses linear beam theory and small-angle approximations for moments effects. therefore, restrict input to $\delta_z < t$ (beam thickness); $\delta\theta_x,\ \delta\theta_y\ < 0.01\ rad.$

B. Compute overall displacement at the extremities of the platform, function (dbp.m)

- Length to anchor points on a platform resolved to give lever lengths for additional z-deflections ($\delta\theta_x\ a\ sin\alpha$, $\delta\theta_x\ a\ cos\alpha$).
- Rotation simply resolved as their unit vectors $(cos\alpha, sin\alpha, 0)^T$
- For global frame, rotations preserved, so encode operation in (6×6) matrix that modifies only z-term of the 6-vector.

C. Input dimensions and elastic constants for the suspension beams (assume all equal), function (csa.m)

- Set,local body, fixed frames with x-axes along the individual beams and $z-$axes . Calculate (6×6) stiffness matrix in the body frame, for the end case.
- Note in this frame a θ_y rotation gives a $z-$deflection.

D. Use given arm orientations (α) to establish to establish orientations (β) in the global fram for the x-axes of the beams, by hand as 'input'.

E. Transform the global frame (or anchor point) displacements to the body frame of the relevant suspension beam, function (ctm.m)

- Translations and rotations transform independent in this case which always involves only rotation about the (common) $z-$axes.

- Remember, global $\longrightarrow$ local is the form:

$$\begin{pmatrix} \cos(\alpha_i) & \sin(\alpha_i) & 0 \\ -\sin(\alpha_i) & \cos(\alpha_i) & 0 \\ 0 & 0 & 1 \end{pmatrix} \tag{B.1}$$

F. Compute, in the body frames, the forces and moments needed to cause the end displacements of the suspension beams, function (psb.m)

- $\mathbf{F} = [K]\mathbf{x}$, 6-vectors.
- By Definition, these represent the reaction forces at the end of the hub arms (Newton's third law), but are expressed in different frames.

G. Transform the individual force vectors (6) into the global frame using the relevant value for β, function (gtbc.m)

- Local $\longrightarrow$ global, so transpose of the transformation used at E.
- Strictly, force on platform is -ve of that on beam.

H. Now in global frame (but also in body frames since z-rotation!) Sum F_z at each arm to establish the z-stiffness, functions (plstif.m + cfmg.m)

- Force 'imposed' on platform is is -ve of forces at the hub anchor points (i.e., same signs as those on beams).
- $K_z = \Sigma(F_z/\delta_z)$, where δ_z originally is imposed.

J. For each, in turn, of the global $x-$ and $y-$axes, take moment about the platform centre for all the arms reactions and sum to give the imposed moments needed. Hence compute the tilt stiffness about each axis, function (plstif.m + cfmg.m)

- 'Imposed' forces and moments are -ve of those at hub anchor points.
- Serval terms are involved.

$$\lambda_x = \frac{M_{x_i}}{\delta_x} \tag{B.2}$$

and

$$\lambda_y = \frac{M_{y_i}}{\delta_y} \tag{B.3}$$

- $-\Sigma(F_{z_i} a\ cos\alpha_i)$ about $y-$axis.
- $\Sigma(F_{z_i} a\ sin\alpha_i)$ about $x-$axis.

Then

$$\lambda_x = \frac{M_{x_i}}{\delta_x} \tag{B.4}$$

and

$$\lambda_y = \frac{M_{y_i}}{\delta_y} \tag{B.5}$$

B.2 Triskelion program: MATLAB codes

```
% Aim: Function to generate single column matrix from six input vector.

%Pre-Condition:The total inputs are six but three of them
%(dx=dy=dthetaz =0)are set zero locally and remaining three vlaueses
%(dz,dthetax, dthetay) user has to enter for executing the function.

%Post-Condtion: Six values are displayed dx,dy,dz, dthetay,
%dthetax, and detheta z.

function Dp= dpl(dz,dthetax,dthetay)
dpl = [ 0; 0; dz; dthetax; dthetay; 0;];
Dp = dpl;

% Aim: Function to compute  at Arm and Defection of the Platform.

%Pre-Condition:
% 7 input values are required for executing this function. Three of them
% are locally set equal to zero and remaining 4 values,  user has to enter
% for execution the function.

%Post-Condtion:Execution of this function generates defection of three
%beams (matric 6x1) in Plat-Coordinates

function Ds= dbp(dz, dthetax, dthetay,a, alpha1, alpha2, alpha3)

disp = dpl(dz, dthetax, dthetay);

angl = [alpha1, alpha2, alpha3];

%angl = [ -pi/6, pi/2, -5*pi/6];

doa=zeros(6,6,length(angl));

  for i = 1:length(angl)
       doa(:,:,i) = [ 1,  0,   0,   0,   0,    0;
                      0,  1,   0,   0,   0,    0;
                      0,  0,   1,   (a*sin(angl(i))), - (a*cos(angl(i))),0;
                      0,  0,   0,   1,   0,    0;
                      0,  0,   0,   0,   1,    0;
                      0,  0,   0,   0,   0,    1; ];
  end
             dbp1 = doa(:,:,1)*disp;
             dbp2 = doa(:,:,2)*disp;
             dbp3 = doa(:,:,3)*disp;



dbp = [dbp1, dbp2, dbp3];
```

```
Ds = dbp;

% Aim:Function to generate stiffness matrix  from requirement specification
% for suspension beams.

%Pre-Condition: 4 input values are required for this function. i.e. length l
%width w,thickness t and E for three beams.

%Post-Condition: Execution of this function generates a matrix (6x6) for
%each beam.

function C=csa(l,w,t,E)

%G = double(50e+9);
G = double(1e+9);
%E = double(120e+9);


k = ((G*(t^2)/E)*(1/3 - (((0.21*t)/w)*(1 - (t^4)/(12*w^4)))));

csa = [1, 0, 0, 0,0,0;  0,(w/l)^2,0,0,0, (-(w^2)/(2*l));
                   0, 0, (t/l)^2, 0,   ((t^2)/(2*l)), 0;
      0,0,0,k,0, 0; 0, 0, ((t^2)/(2*l)), 0, ((t^2)/3),0;
                    0, (-(w^2)/(2*l)),0,0,0, ((w^2)/3)];
C= ((E*t*w)/l)*csa;

%Aim: Function to Compute, Transformation to the Plate form Coordinates.

%Pre-Condition: 3 input values of angles(beta1, beta2,beta3) are required for
%function ctm.

%Post-Condition: Execution of this function generates three matrices (6x1)
%for end defections of three beams.
function tm = ctm(beta1, beta2,beta3)

ang2 = [ beta1, beta2, beta3];

tpc=zeros(6,6,length(ang2));

  for j = 1:length(ang2)
       tpc(:,:,j) =  [ cos(ang2(j)), sin(ang2(j)), 0,    0,       0,     0;
            - sin(ang2(j)), cos(ang2(j)), 0,            0,       0,     0;
                        0,           0,   1,            0,       0,     0;
                        0,           0,   0, cos(ang2(j)),sin(ang2(j)), 0;
                        0,           0,   0,-sin(ang2(j)),cos(ang2(j)), 0;
                        0,           0,   0,           0,          0,  1;];
  end
          ctm1 =   tpc(:,:,1);
          ctm2 =   tpc(:,:,2);
          ctm3 =   tpc(:,:,3);
```

```
ctmp= [ctm1,ctm2, ctm3];
tm = ctmp;

% Aim: Function to compute  at Arm and Defection of the Platform.

%Pre-Condition:
% 7 input values are required for executing this function. Three of them
% are locally set equal to zero and remaining 4 values,  user has to enter
% for execution the function.

%Post-Condtion:Execution of this function generates defection of three
%beams (matric 6x1) in Plat-Coordinates

function Ds= dbp(dz, dthetax, dthetay,a, alpha1, alpha2, alpha3)

disp = dpl(dz, dthetax, dthetay);

angl = [alpha1, alpha2, alpha3];

%angl = [ -pi/6, pi/2, -5*pi/6];

doa=zeros(6,6,length(angl));

  for i = 1:length(angl)
       doa(:,:,i) = [ 1,  0,   0,   0,   0,    0;
                      0,  1,   0,   0,   0,    0;
                      0,  0,   1,   (a*sin(angl(i))), - (a*cos(angl(i))),0;
                      0,  0,   0,   1,   0,    0;
                      0,  0,   0,   0,   1,    0;
                      0,  0,   0,   0,   0,    1; ];
  end
    dbp1 = doa(:,:,1)*disp;
    dbp2 = doa(:,:,2)*disp;
    dbp3 = doa(:,:,3)*disp;

dbp = [dbp1, dbp2, dbp3];
Ds = dbp;
% Aim: Function to compute Computation for Force(F_x,F_y,F_z) and
%Moment M_x,M_y and M_x.

%Pre-Condition: 14 input values dz, dthetax, dthetay,a,l,w, and t required
%by the user and two functions, csa & dsb  are called.

%Post-Condtion: Execution of this function genrates the values of force and
%moment for three beams in form of three matrices (6x1)

function p =psb(dz, dthetax, dthetay, a,l,w, t, E, alpha1, alpha2, alpha3,
                                                    beta1, beta2, beta3)
```

```
sm = csa(l,w,t,E);
q = dsb(dz, dthetax, dthetay, a, alpha1, alpha2, alpha3,
                                    beta1, beta2, beta3);
psb1 = sm*q(:,1);
psb2 = sm*q(:,2);
psb3 = sm*q(:,3);
p = [psb1, psb2, psb3];

%Aim: Function to Compute, Force back to Global Coordinates.

%Pre-Condition: 14 input values are required, the function dbp is also
%called.

%Post-Condtion: Execution of this function generates three matrices (6x1)
%for end defections of three beams.

function cbg = tgbc(dz, dthetax, dthetay,a,l,w,t, E, alpha1, alpha2, alpha3,
                                                        beta1, beta2, beta3)
lbf = psb(dz, dthetax, dthetay, a, l,w, t, E, alpha1, alpha2, alpha3,
                                                beta1, beta2, beta3);

tgc = ctm(beta1, beta2, beta3);


gdsb1 = (tgc(:, 1:6)' )*lbf(:,1);
gdsb2 = (tgc(:, 7:12)')*lbf(:,2);
gdsb3 = (tgc(:,13:18)')*lbf(:,3);
 sfgc = (gdsb1 + gdsb2 +  gdsb3);
 sumtgc = [gdsb1,gdsb2,gdsb3,sfgc];
cbg= sumtgc;

%Aim: Function to Compute, Force back to Global Coordinates.

%Pre-Condition: 14 input values are required, the function dbp is also
%called.

%Post-Condition: Execution of this function generates three matrices (6x1)
%for end defections of three beams.

function sfm = cfmg(dz, dthetax, dthetay,a,l,w,t, E, alpha1, alpha2, alpha3,
                                                        beta1, beta2, beta3)
radius = a;
alpha11 = alpha1;
alpha22 = alpha2;
alpha33 = alpha3;
csfm = tgbc(dz, dthetax, dthetay,a,l,w,t, E, alpha1, alpha2, alpha3,
                                                beta1, beta2, beta3);
fb1= csfm(:,1);
fb2= csfm(:,2);
fb3= csfm(:,3);
```

```
sigfzs = ((-fb1(3)) + (-fb2(3))+ (-fb3(3)));
sigmxs = ((-fb1(4)) + (-fb2(4))+ (-fb3(4)) + ((-fb1(3)*radius)*sin(alpha11)) +
          ((-fb2(3)*radius)*sin(alpha22))  + ((-fb3(3)*radius)*sin(alpha33)));
sigmys = ((-fb1(5)) + (-fb2(5))+ (-fb3(5)) - ((-fb1(3)*radius)*cos(alpha11)) -
          ((-fb2(3)*radius)*cos(alpha22))  - ((-fb3(3)*radius)*cos(alpha33)));

fms = [sigfzs, sigmxs, sigmys];

sfm= fms;

% Aim: Function to computate,  Stress and Strain.

%Pre-Condition: To execute this function, 14 input values, dz, dthetax,
%dthetay,a,l, and w. Function psb is also called here.

%Post-Condtion: Execution of this function genrates matrix (2x3). The first
%line indicates values of stress and second for strain of three beams.

function S=sigma(dz, dthetax, dthetay, a, l, w, t, E, alpha1, alpha2, alpha3,
                                                        beta1, beta2, beta3)

pg = tgbc(dz, dthetax, dthetay, a, l, w, t, E, alpha1, alpha2, alpha3,
                                                  beta1, beta2, beta3);

sigma1 = (6*((((pg(3)*l) -  pg(5)))/(w*(t^2))));
sigma2 = (6*((((pg(9)*l) -  pg(11)))/(w*(t^2))));
sigma3 = (6*((((pg(15)*l) - pg(17)))/(w*(t^2))));

sigma = [sigma1, sigma2, sigma3;  sigma1/E, sigma2/E, sigma3/E; ];
S = sigma;
%Aim: function to compute values of stiffness.

%Pre-Condition: 14 input valuesdz,dthetax,dthetay,a,l,w, and t are reqired
%to execute this function and two function psb and sigma are called here.

%Post-Condition: Execution of this function generates matrix (3x8)i.e.
% (the value of Spring constant K, F_z, Stress/F_z, Strains/F_z,  and
%Lamda_x = M_x/delta_x, Lamda_y = M_y/delta_y, Strain/M_x and Strain/M_y).

function pls = plstiff(dz, dthetax, dthetay, a, l, w, t, E,
               alpha1, alpha2, alpha3, beta1, beta2, beta3)

psg = tgbc(dz, dthetax, dthetay, a, l, w, t, E,
   alpha1, alpha2, alpha3,beta1, beta2, beta3);

ssg= sigma(dz, dthetax, dthetay, a, l, w, t, E,
   alpha1, alpha2, alpha3,beta1, beta2, beta3);

 K1 = 3*psg(3)/dz;
 K2 = 3*psg(9)/dz;
```

```
 K3 = 3*psg(15)/dz;
 LM1 = psg(4)/dthetax;
 LM2 = psg(5)/dthetay;
 LM3 = psg(10)/dthetax;
 LM4 = psg(11)/dthetay;
 LM5 = psg(16)/dthetax;
 LM6 = psg(17)/dthetay;


 K11 = [K1, psg(3),  LM1, LM2];
 K12 = [K2, psg(9),  LM3, LM4];
 K13 = [K3, psg(15), LM5, LM6];


 plstiff = [K11;K12;K13;];
 pls = plstiff;

% Main function to compute Analytical Model of Tri-Skellion Micro Probe
% all results.

%Pre-Condition: 14 input valuesdz,dthetax,dthetay,a,l,w,t, E,  are required
%alpha1, alpha2, alpha3, beta1, beta2, and  beta3 are reqired to execute this
%function.

%Post-Condtion: Execution of main function generates the computed results
%for Analytical Model of Tri-Skellion Probe thus saving time to execute
%each function one by one.

function mpl(dz,dthetax,dthetay,a,l,w,t, E, alpha1, alpha2, alpha3, beta1,
                                                                  beta2, beta3)

 disp('Input vectors are generated (6x1 matix) as follows:')
 disp('================================================')
 disp('dx,dy,dz,dthetax,dthetay,dthetaz')
 disp(' ')
 disp(dpl(dz,dthetax,dthetay));
 disp(' ')
 disp('Computation for Deflection of arms at the Platform,6x3 matrix
                                                    for three arms :')
 disp('============================================================
                                                     ============== ')
 disp('===========arm1==========arm2==========arm3')
 disp(' ')
 disp(dbp(dz,dthetax,dthetay,a, alpha1, alpha2, alpha3 ));
 disp(' ')
 disp('Computation for Deflection of three beams in Platform-Coordinates,
                                            6x3 matrix for each beam :')
 disp('============================================================
                                                                ===== ')
 disp(' ')
```

```
disp(ctm(beta1, beta2, beta3));
disp('Computation for Deflection of three beams in Platform-Coordinates,
                                        6x3 matrix for three beams :')
disp('=============================================================')
disp('==========beam1=======beam2======beam3 ')
disp(dsb(dz,dthetax,dthetay,a, alpha1, alpha2, alpha3,beta1, beta2, beta3));
disp(' ')
disp('Stiffness matrix 6x6 generated from requirement specifications:')
disp('Lenth l, width w, thickness t and Young's modulous E:')
disp('============================================================')
disp(' ')
disp(csa(l,w,t, E));
disp(' ')
disp('Computation for Force(F_x,F_y,F_z) and Moment M_x,M_y and M_x are')
disp('done in form of 6x3 Coulum Matrix:')
disp('============================================================= ')
disp('==========beam1=======beam2======beam3 ')
disp(' ')
disp(psb(dz, dthetax, dthetay, a,l,w, t, E, alpha1, alpha2, alpha3,beta1,
                                                    beta2, beta3));
disp(' ')
disp('Computation for Force(F_x,F_y,F_z), Moment M_x,M_y and M_z (6x1)
                                              matrix for each beam')
disp(' and fouth col, their sum in globel-coordinates')
disp('==========beam1=======beam2======beam3=====Sum-of-Force-For-3-beams')
disp(' ')
disp(tgbc(dz, dthetax, dthetay, a,l,w, t, E, alpha1, alpha2, alpha3,beta1,
                                                     beta2, beta3));
disp(' ')
disp('Computation for sum of Force(F_x,F_y,F_z), Moment M_x,M_y and M_z
                                               in globel-coordinates')
disp('============================================================')
disp(' ')
disp(cfmg(dz, dthetax, dthetay,a,l,w,t, E, alpha1, alpha2, alpha3,beta1,
                                                    beta2, beta3))
disp(' ')
disp('Computation for Stress and Strain, 2x3 matrix for three beams:')
disp('First Row indicates Stress for three beams:')
disp('Second Row indicates Strain for three beams:')
disp('============================================================ ')
disp(sigma(dz, dthetax, dthetay,a,l,w,t,E, alpha1, alpha2, alpha3,beta1,
                                                   beta2, beta3));
disp(' ')
disp('Spring constant K, F_z, Lamda_x = M_x/delta_x,Lamda_y = M_y/delta_y:')
disp('============================================================)
disp(' ')
disp(plstiff(dz,dthetax,dthetay,a, l, w, t, E, alpha1, alpha2, alpha3,beta1,
                                                     beta2, beta3));
disp('============================================================')
disp('==================All computation done.')=========================')
```

```
end
```

Appendix C

Polymeric triskelion samples

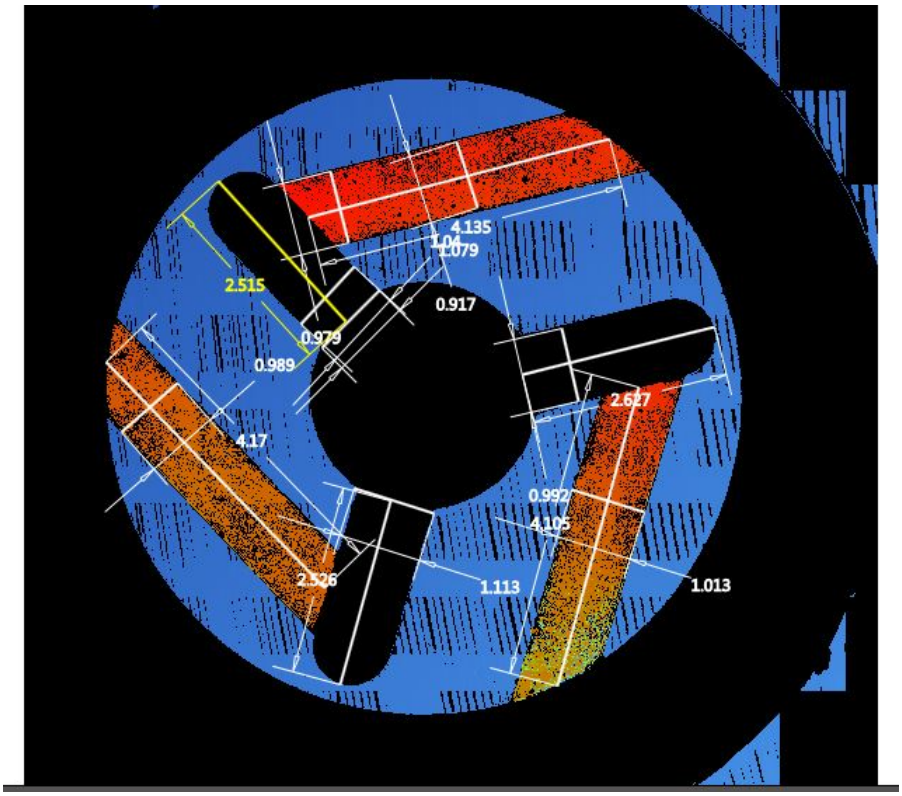

Figure C.1: Measured dimensions of classic triskelion sample CS1-60, with elbow angle 60 °.

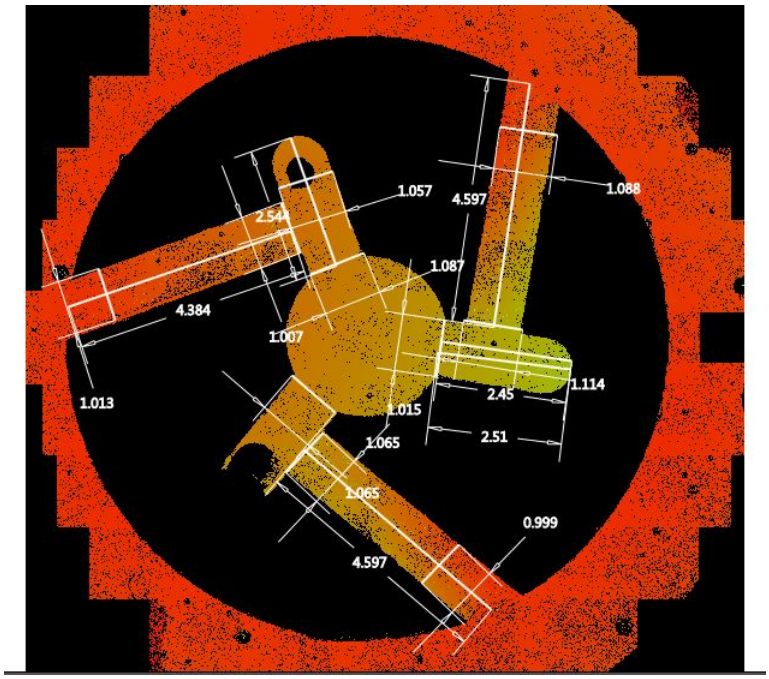

Figure C.2: Measured dimensions of angle-beam triskelion sample CS1-90, with elbow angle 60 °.

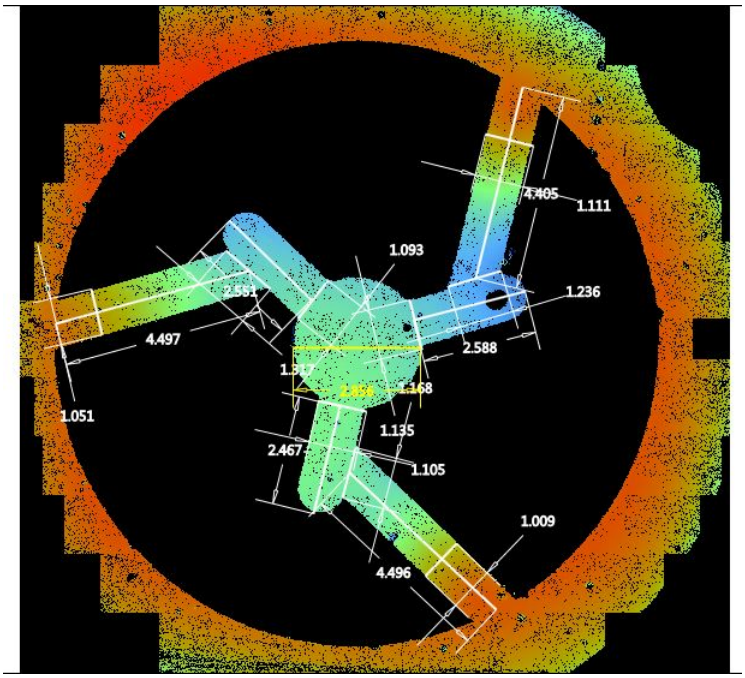

Figure C.3: Measured dimensions of classic triskelion sample CS1-120, with elbow angle 90 °.

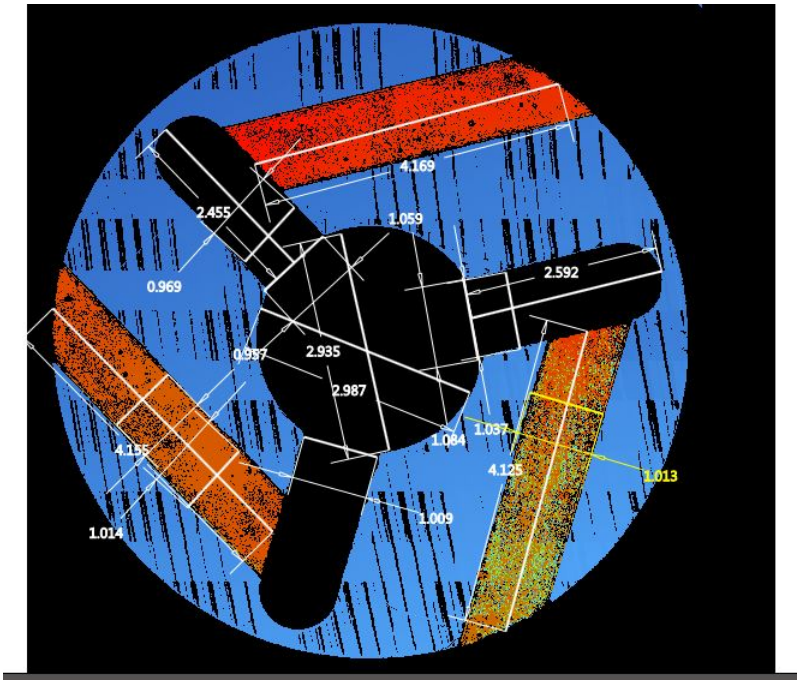

Figure C.4: Measured dimensions of angle-beam triskelion sample AS1-60, with elbow angle 60 °.

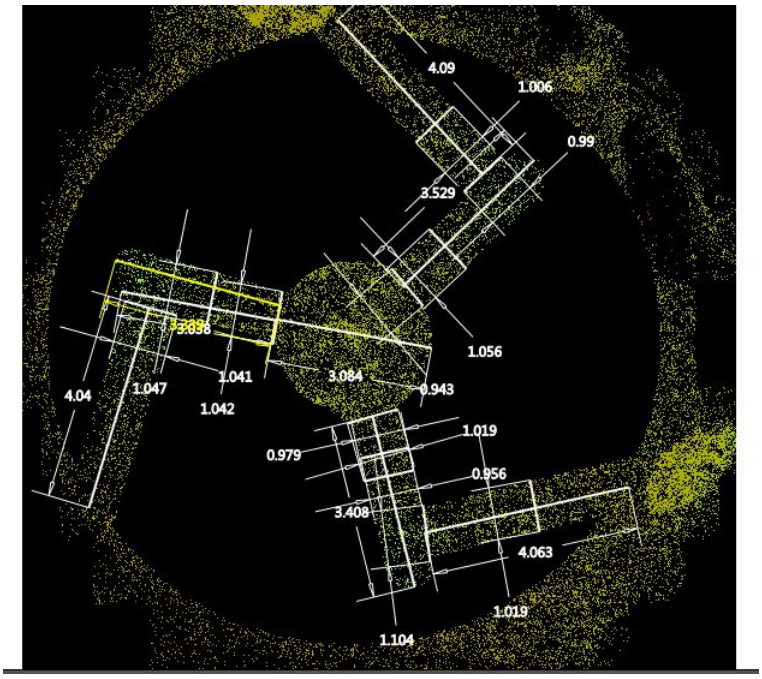

Figure C.5: Measured dimensions of angle-beam triskelion sample AS1-90, with elbow angle 90 °.

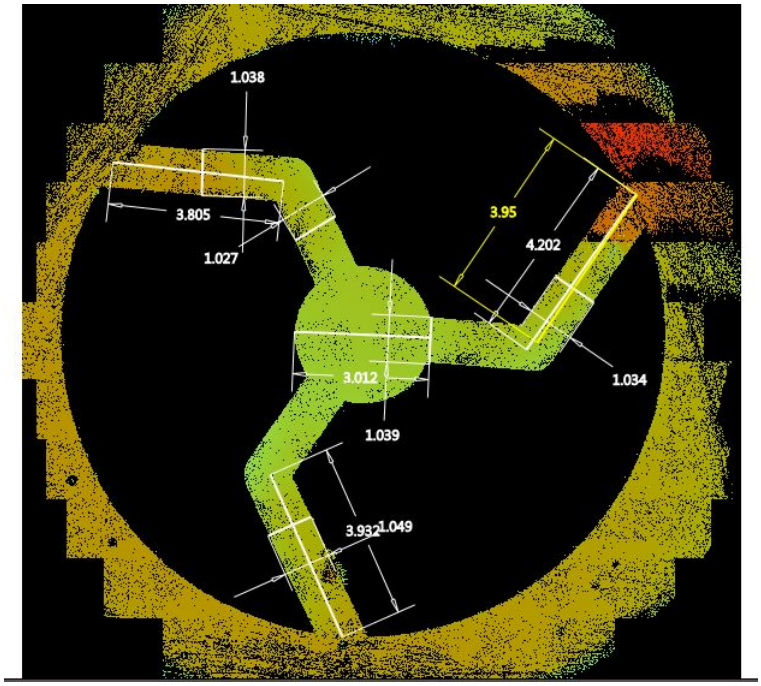

Figure C.6: Measured dimensions of angle-beam triskelion sample CS1-120, with elbow angle 60 °.

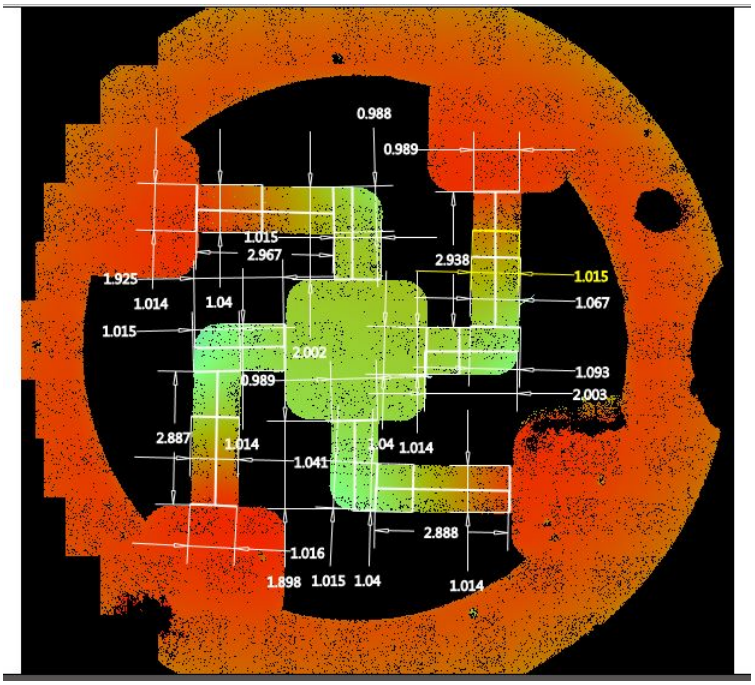

Figure C.7: Measured dimensions of classic tetraskelion sample CS1-CS, with elbow angle 60 °.

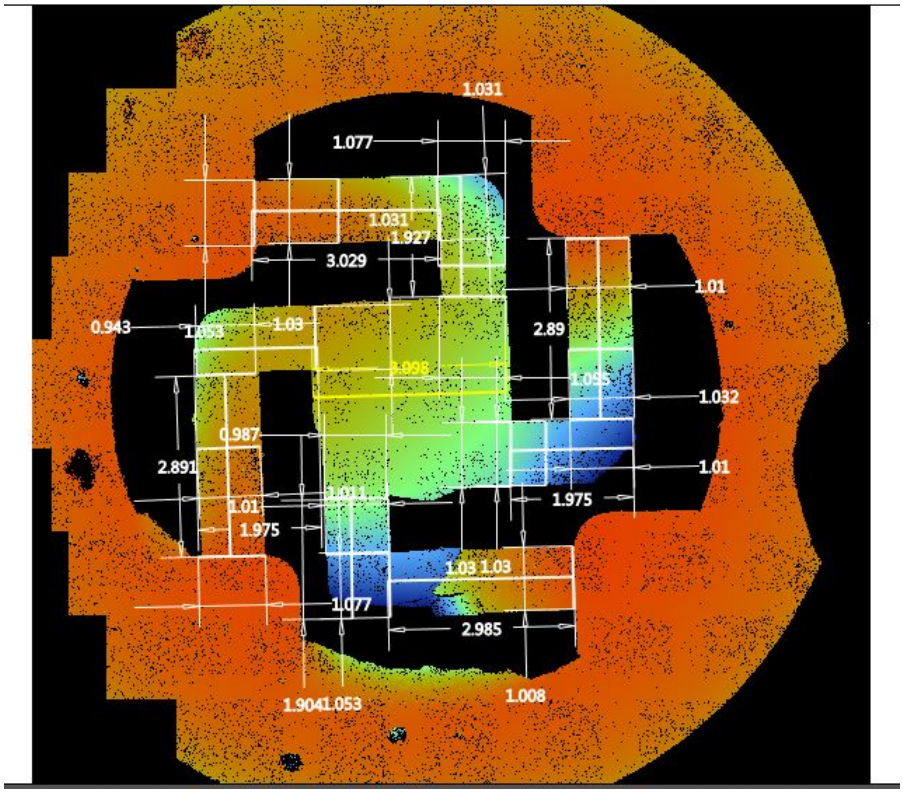

Figure C.8: Measured dimensions of classic tetraskelion sample CS1-DS, with elbow angle 60 °.

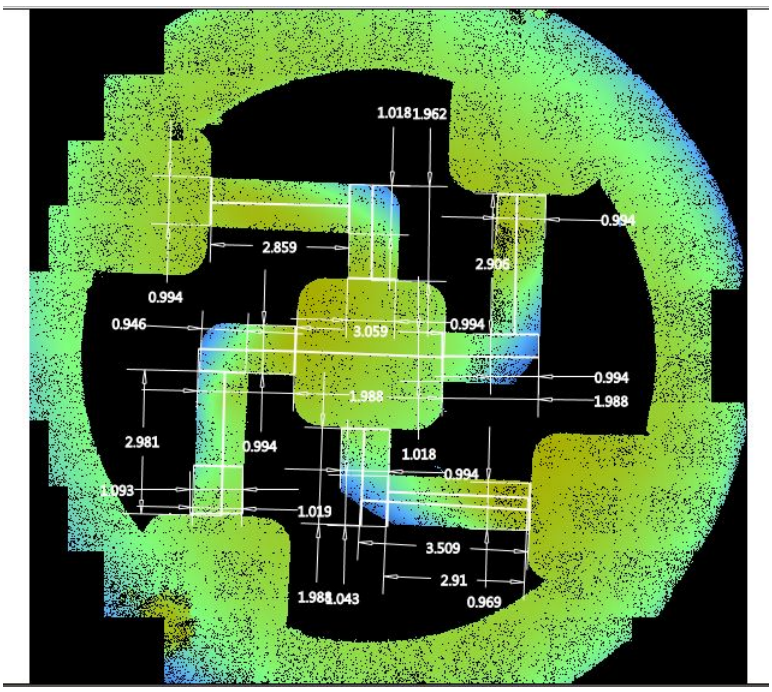

Figure C.9: Measured dimensions of angle-beam tetraskelion sample AS1-CS, with elbow angle 60 °.

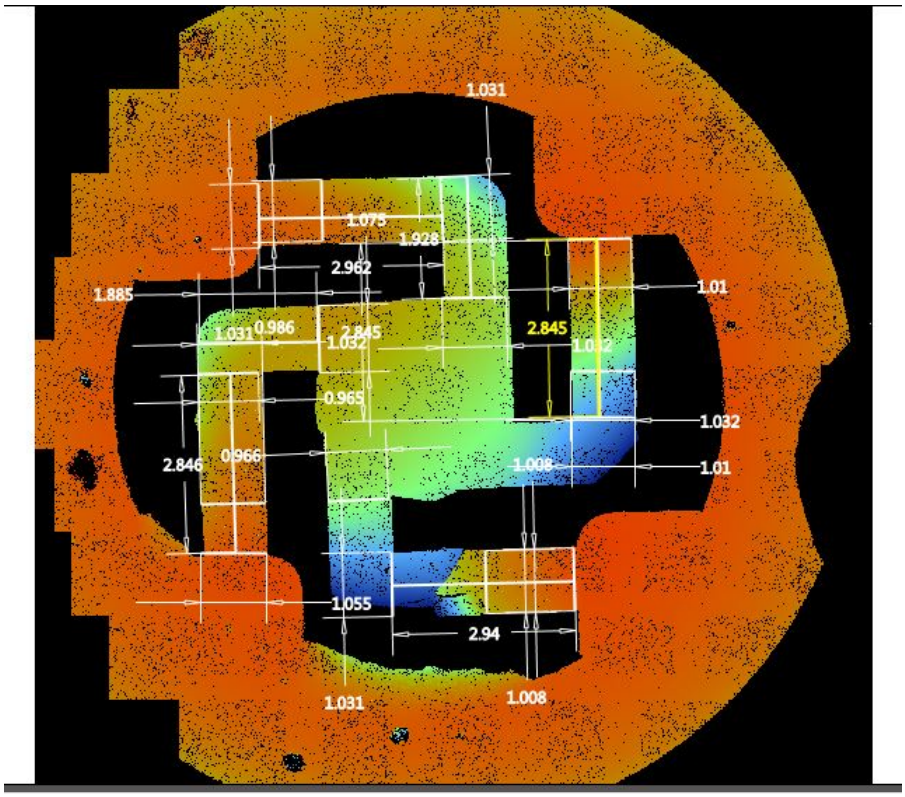

Figure C.10: Measured dimensions of angle-beam tetraskelion sample AS1-DS, with elbow angle 60 °.

Appendix D

Tables of cubic coefficients for classic triskelion force arefacts

Table D.1: Coefficients analysis of plotted graph for classic triskelion artefact CSS1-60.

S-No	$\beta_3\ Nm^{-3}$	$\beta_2\ Nm^{-2}$	$\beta_1 = k_{eff}\ Nm^{-1}$	β_0	R^2	*Max range X % mm*
1	1.35448E9	0788107.13814	1471.62903	0	0.99997	0.04
2	1.51784E9	-839990.80165	1481.76886	0	0.99998	0.05
3	1.43866E9	-874902.60683	1425.22237	0	0.99991	0.05
4	5.58730E8	-107722.01384	1104.93757	0	0.99981	0.04
5	1.47482E9	-852585.30149	1369.78832	0	0.99988	0.04
6	1.94447E9	-1.30196E6	1269.21068	0	0.99982	0.01

Table D.2: Coefficients analysis of plotted graph for classic triskelion artefact CS2-60.

S-No	$\beta_3\ Nm^{-3}$	$\beta_2\ Nm^{-2}$	$\beta_1 = k_{eff}\ Nm^{-1}$	β_0	R^2	*Max range X % mm*
1	1.17658E9	-591575.21724	1061.88474	0	0.99995	0.2
2	1.15926E9	-677255.42382	1139.06782	0	0.99987	0.01
3	9.12878E8	-439133.99808	1088.47597	0	0.99987	0.03
4	1.88852E8	0134609.99378	0925.78812	0	0.99989	0.04
5	8.17594E8	-318502.93103	1057.5112	0	0.99981	0.04
6	1.0865E9	-617060.37359	1085.95582	0	0.99983	0.04

Table D.3: Coefficients analysis of plotted graph for classic triskelion artefact CS1-90.

S-No	$\beta_3\ Nm^{-3}$	$\beta_2\ Nm^{-2}$	$\beta_1 = k_{eff}\ Nm^{-1}$	β_0	R^2	*Max range X % mm*
1	1.73968E9	-607538.27305	975.29105	0	0.99984	0.04
2	2.01654E9	-787620.98279	985.26632	0	0.99990	0.04
3	1.75348E9	-632511.79010	905.34080	0	0.99979	0.04
4	1.19407E9	-360500.02827	764.72478	0	0.99989	0.04
5	1.29126E9	-347196.10955	839.28305	0	0.99978	0.04
6	1.48308E9	-549307.44727	780.71572	0	0.99967	0.04

Table D.4: Coefficients analysis of plotted graph for classic triskelion artefact CS2-90.

S-No	$\beta_3\ Nm^{-3}$	$\beta_2\ Nm^{-2}$	$\beta_1 = k_{eff}\ Nm^{-1}$	β_0	R^2	*Max range X % mm*
1	2.18852E9	-1.13553E6	960.39724	0	0.99974	0.03
2	1.75861E9	-642827.36132	873.84325	0	0.99973	0.04
3	2.49021E9	-1.28234E6	920.31372	0	0.99967	0.01
4	1.15237E9	-595500.95188	721.41393	0	0.99957	0.04
5	1.20558E9	-516782.38742	690.93404	0	0.99981	0.01
6	1.63606E9	-670532.1848	844.39697	0	0.99982	0.04

Table D.5: Coefficients analysis of plotted graph for classic triskelion artefact CS1-120.

S-No	$\beta_3\ Nm^{-3}$	$\beta_2\ Nm^{-2}$	$\beta_1 = k_{eff}\ Nm^{-1}$	β_0	R^2	*Max range X % mm*
1	-8.42539E7	0776162.10205	1143.08049	0	0.99995	0.05
2	-4.27739E8	0917848.34034	1206.65390	0	0.99995	0.06
3	01.37127E9	-257212.07095	1187.50225	0	0.99993	0.04
4	01.98901E9	-123028.06627	1078.40566	0	0.99983	0.08
5	01.80936E9	-603476.37268	1011.95306	0	0.99991	0.04
6	2.17258E9	-945811.77313	1092.29599	0	0.99996	0.01

Table D.6: Coefficients analysis of plotted graph for classic triskelion artefact CS2-120.

S-No	$\beta_3\ Nm^{-3}$	$\beta_2\ Nm^{-2}$	$\beta_1 = k_{eff}\ Nm^{-1}$	β_0	R^2	*Max range X % mm*
1	-4.3214E8	01.07782E6	1089.80105	0	0.99988	0.04
2	01.14783E9	-237157.86101	1168.63413	0	0.99987	0.05
3	06.65204E8	0689343.71289	0951.60670	0	0.99982	0.05
4	04.35861E8	0893845.02290	0939.88109	0	0.99984	0.05
5	08.82127E8	0470048.44212	0912.91692	0	0.99982	0.09
6	9.84955E8	576723.502910	0904.64066	0	0.99984	0.05

Table D.7: Coefficients analysis of plotted graph for classic triskelion polymer artefact CS1-604.

S-No	$\beta_1 = k_{eff}\ Nm^{-1}$	β_0	R^2
1	5205.73714	0	0.99990
2	5354.08000	0	0.99969
3	5304.84571	0	0.99977
4	4829.76000	0	0.99977
5	5113.09714	0	0.99980
6	5124.25143	0	0.99995

Table D.8: Coefficients analysis of plotted graph for classic triskelion polymer artefact CS2-604.

S-No	$\beta_1 = k_{eff}\ Nm^{-1}$	β_0	R^2
1	5152.41143	0	0.9999
2	5388.64000	0	0.9994
3	5076.13714	0	0.9998
4	4990.05714	0	0.99995
5	4936.20571	0	0.99976
6	5016.29714	0	0.99962

Appendix E

Graphs, for classic triskelion samples

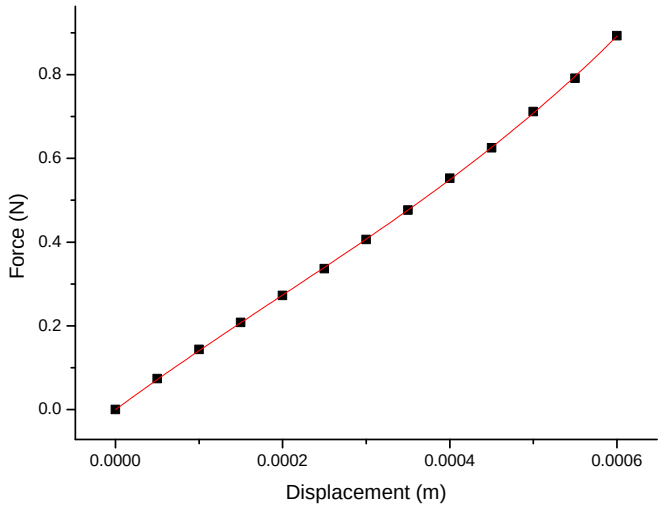

Figure E.1: Stiffness measured at the centre of hub for classic triskelion sample CS1-60 S.No. 1, Table D.1

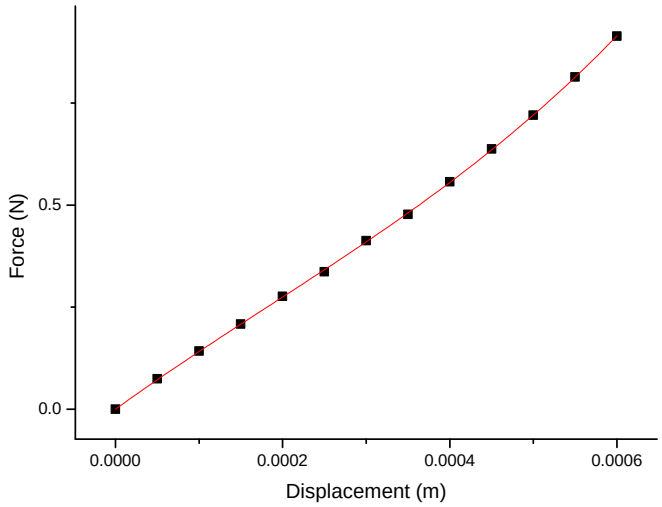

Figure E.2: Stiffness measured at the centre of hub for classic triskelion sample CS1-60 S.No. 2, Table D.1

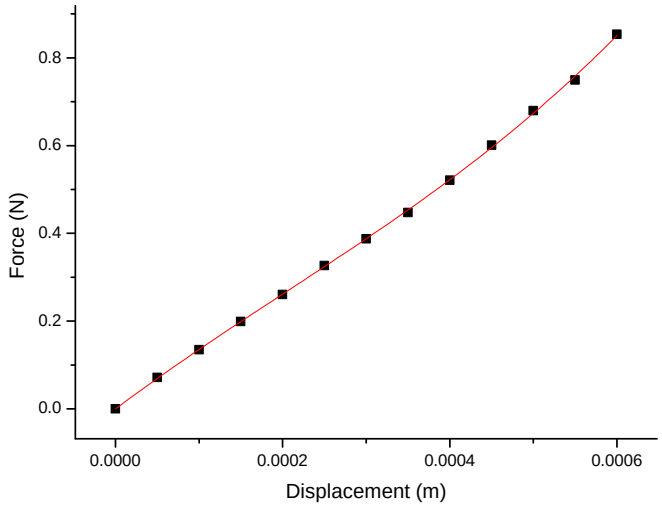

Figure E.3: Stiffness measured at the centre of hub for classic triskelion sample CS1-60 S.No. 3, Table D.1

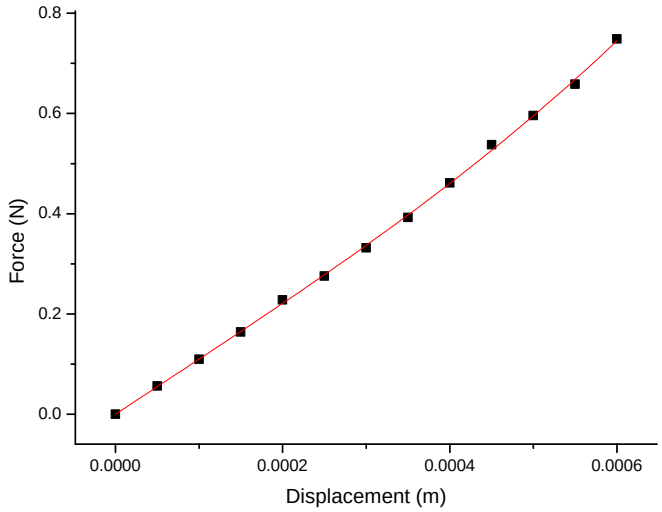

Figure E.4: Stiffness measured at the centre of hub for classic triskelion sample CS1-60 S.No. 4, Table D.1

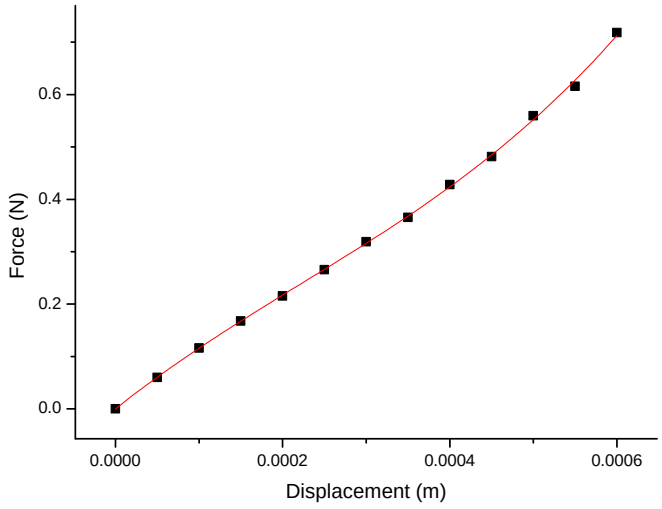

Figure E.5: Stiffness measured at the centre of hub for classic triskelion sample CS1-60 S.No. 5, Table D.1

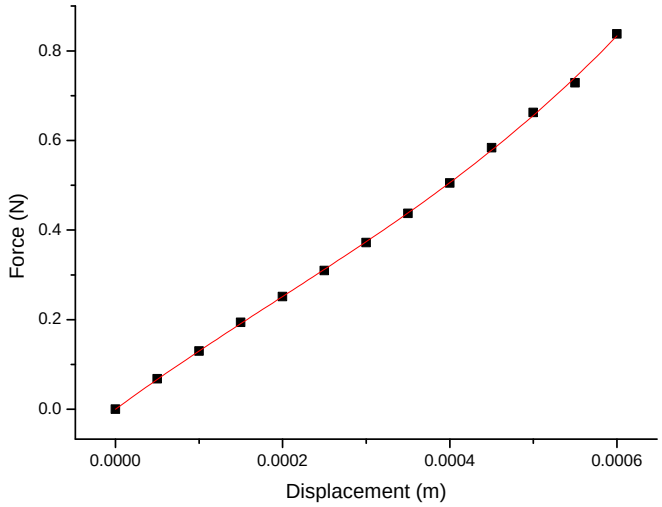

Figure E.6: Stiffness measured at the centre of hub for classic triskelion sample CS1-60 S.No. 6, Table D.1

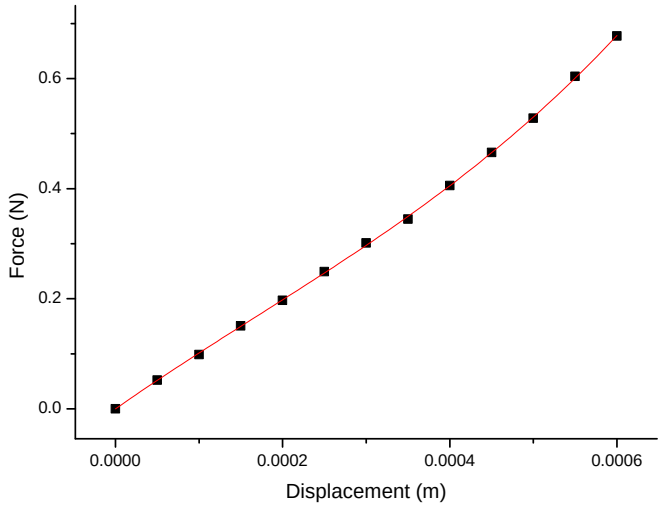

Figure E.7: Stiffness measured at the centre of hub for classic triskelion sample CS2-60 S.No. 1, Table D.2

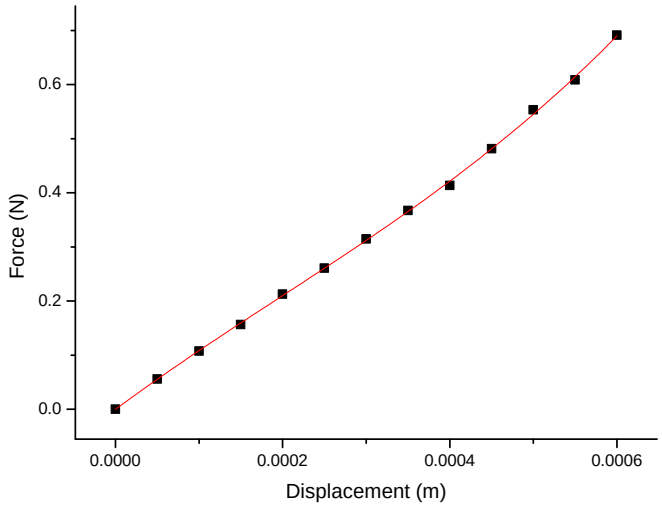

Figure E.8: Stiffness measured at the centre of hub for classic triskelion sample CS2-60 S.No. 2, Table D.2

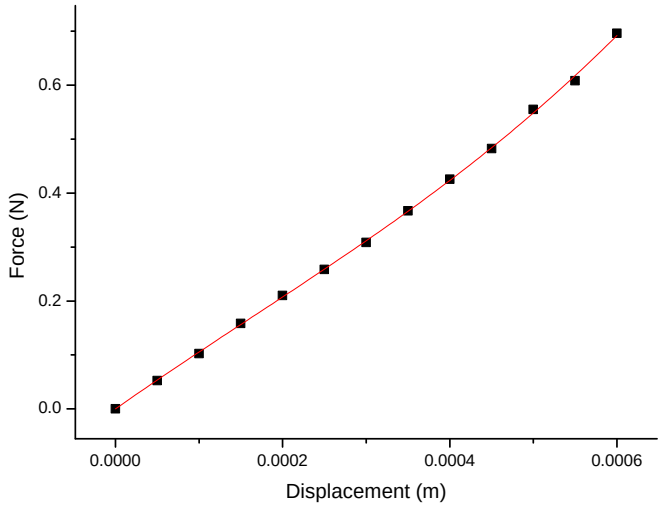

Figure E.9: Stiffness measured at the centre of hub for classic triskelion sample CS2-60 S.No. 3, Table D.2

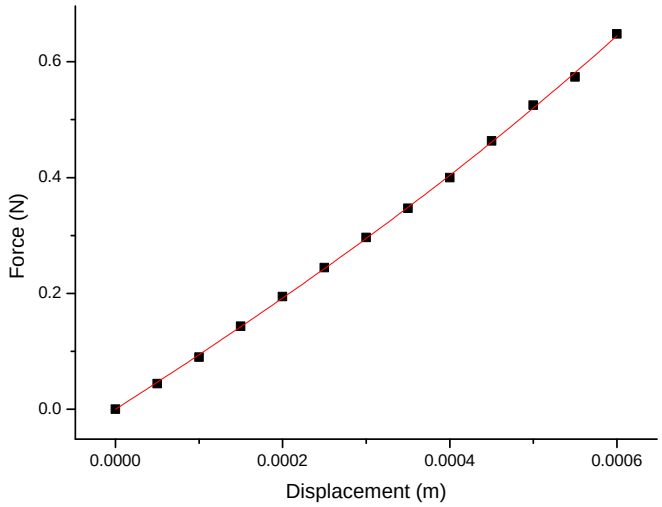

Figure E.10: Stiffness measured at the centre of hub for classic triskelion sample CS2-60 S.No. 4, Table D.2

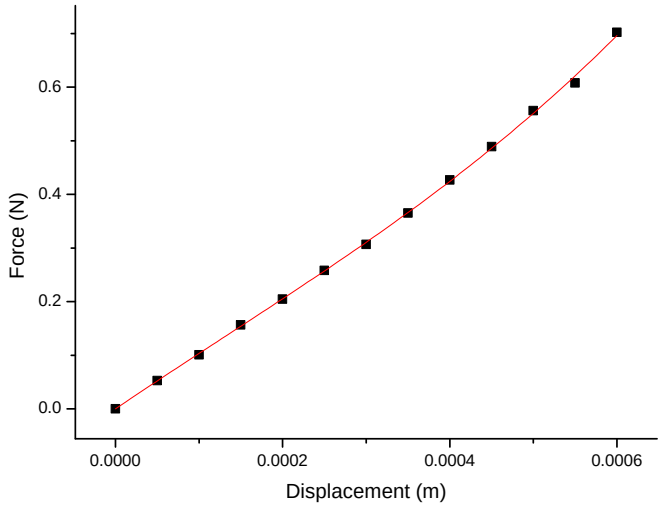

Figure E.11: Stiffness measured at the centre of hub for classic triskelion sample CS2-60 S.No. 5, Table D.1

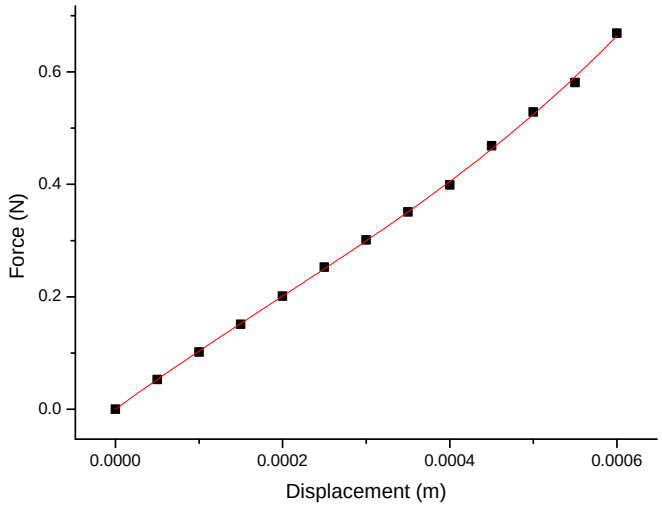

Figure E.12: Stiffness measured at the centre of hub for classic triskelion sample CS2-60 S.No. 6, Table D.2

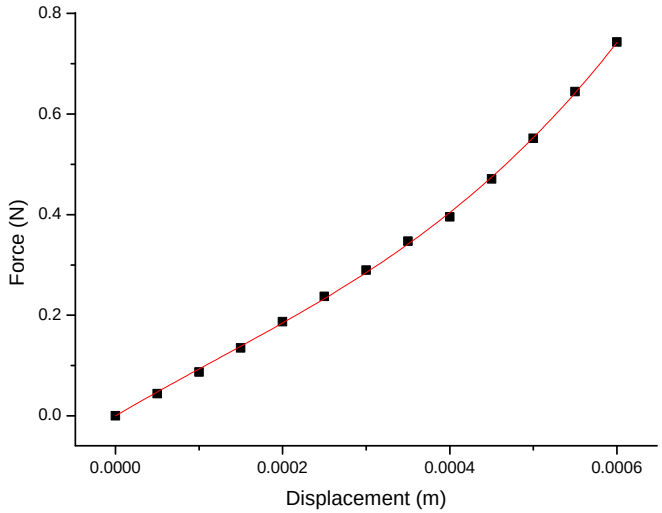

Figure E.13: Stiffness measured at the centre of hub for classic triskelion sample CS1-90 S.No. 1, AppendixAppendix D.3

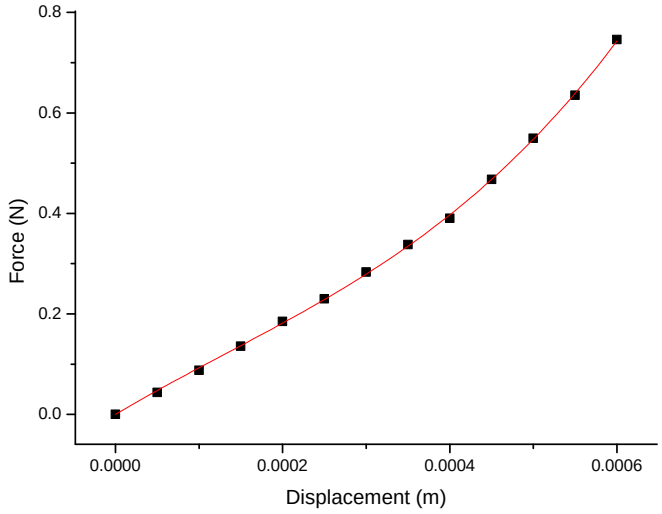

Figure E.14: Stiffness measured at the centre of hub for classic triskelion sample CS1-90 S.No. 2, Table D.3

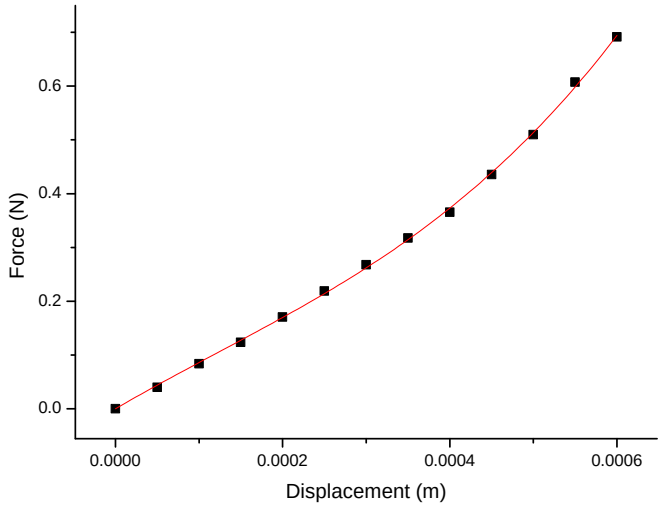

Figure E.15: Stiffness measured at the centre of hub for classic triskelion sample CS1-90 S.No. 3, Table D.3

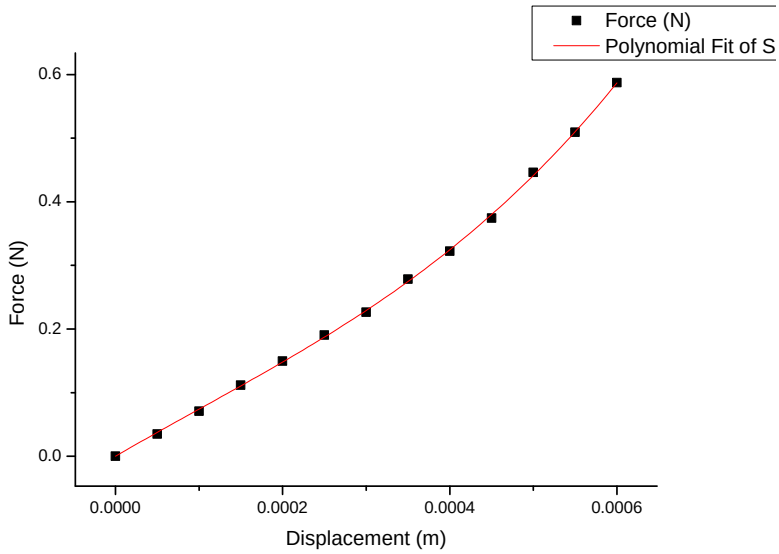

Figure E.16: Stiffness measured at the centre of hub for classic triskelion sample CS1-90 S.No. 4, Table D.3

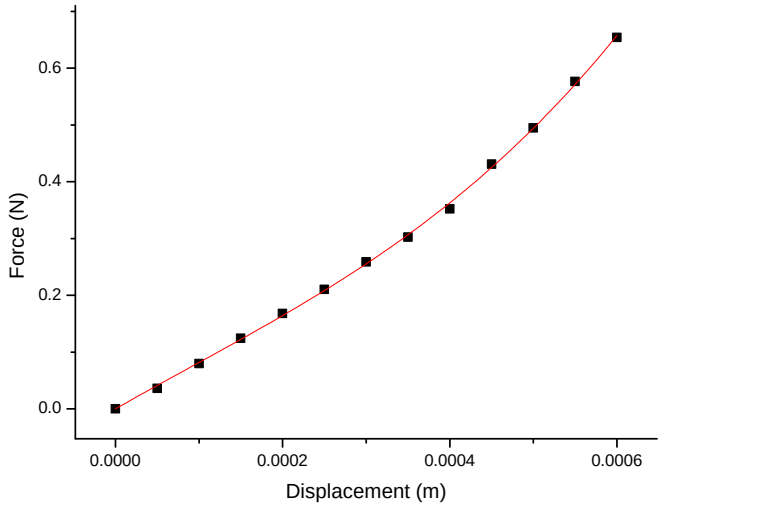

Figure E.17: Stiffness measured at the centre of hub for classic triskelion sample CS1-90 S.No. 5, Table D.3

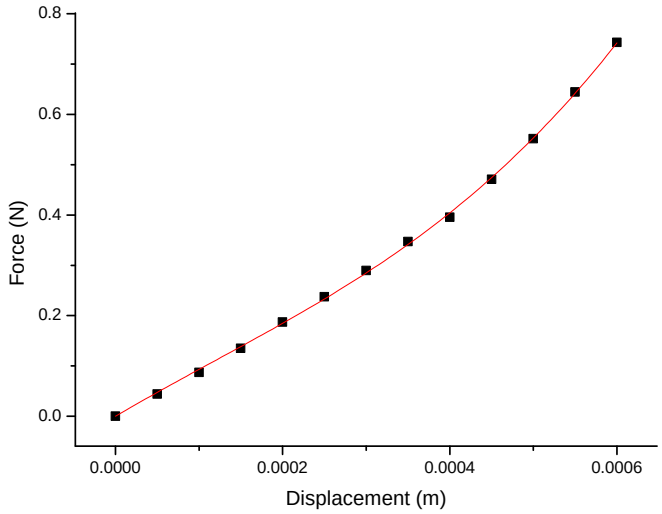

Figure E.18: Stiffness measured at the centre of hub for classic triskelion sample CS1-90 S.No. 6, Table D.3

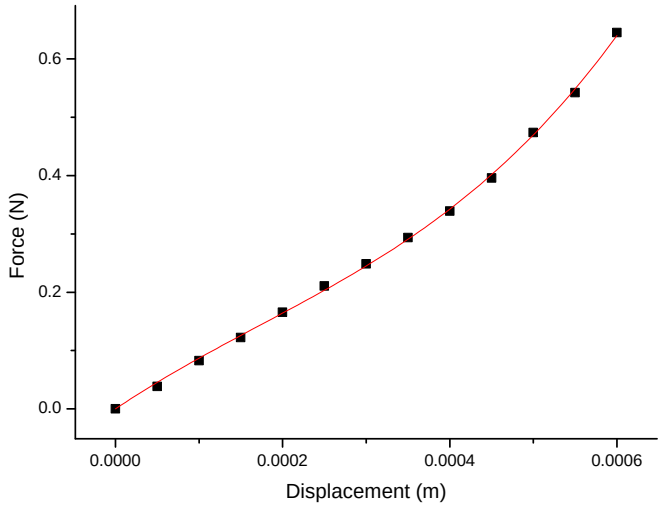

Figure E.19: Stiffness measured at the centre of hub for classic triskelion sample CS2-90 S.No. 1, Table D.4

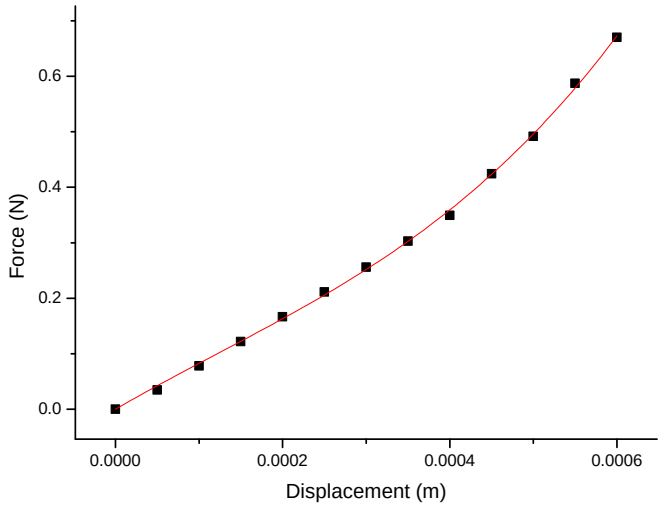

Figure E.20: Stiffness measured at the centre of hub for classic triskelion sample CS2-90 S.No. 2, Table D.4

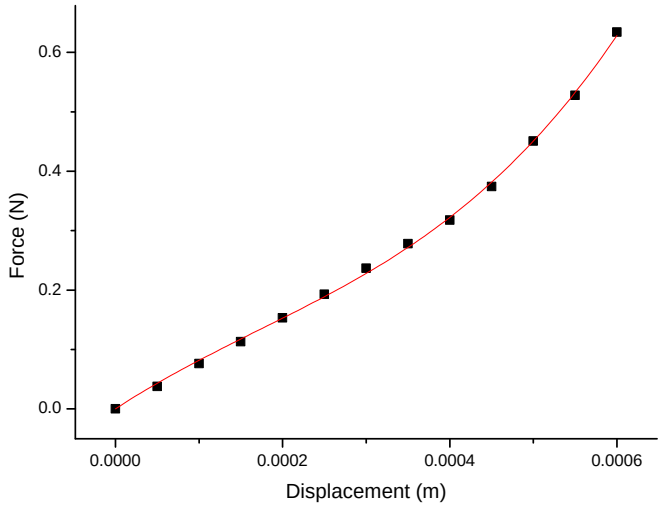

Figure E.21: Stiffness measured at the centre of hub for classic triskelion sample CS2-90 S.No. 3, Table D.4

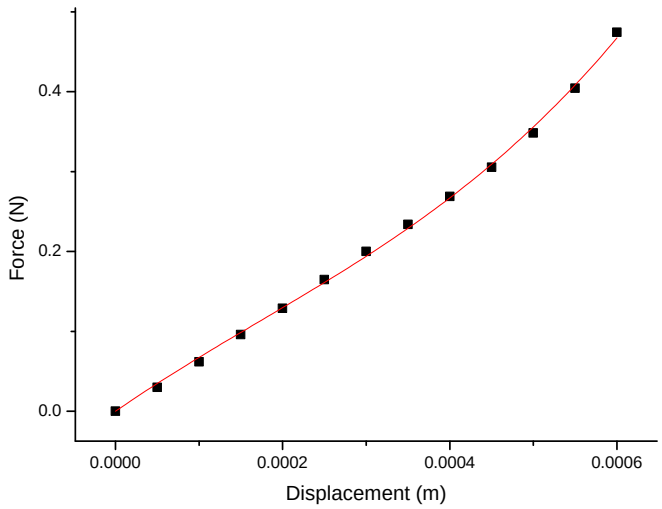

Figure E.22: Stiffness measured at the centre of hub for classic triskelion sample CS2-90 S.No. 4, Table D.4

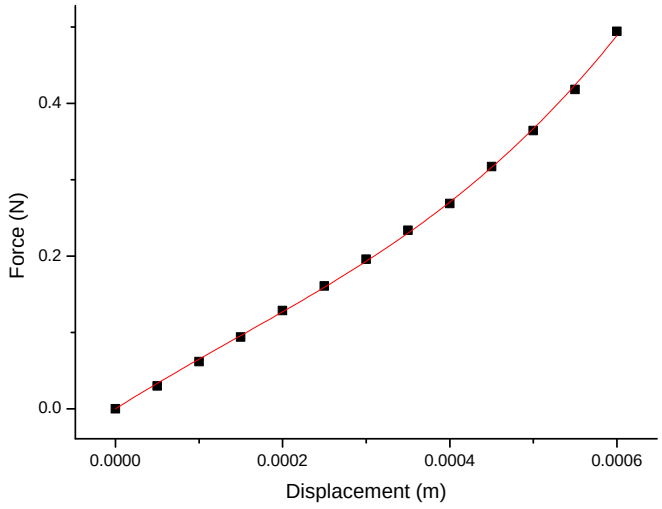

Figure E.23: Stiffness measured at the centre of hub for classic triskelion sample CS2-90 S.No. 5, D.4

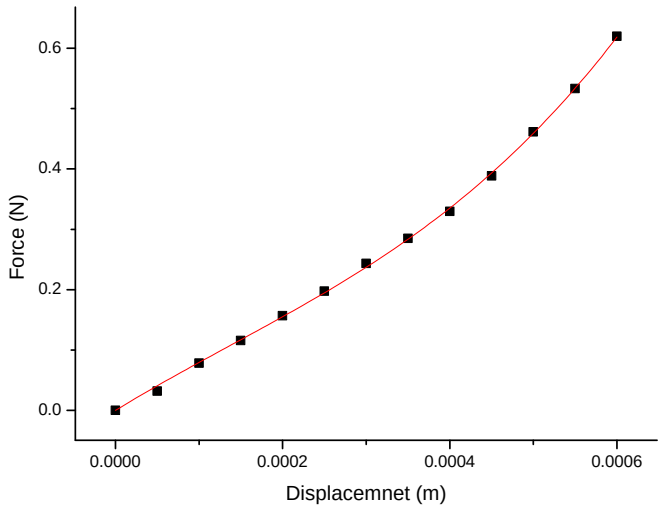

Figure E.24: Stiffness measured at the centre of hub for classic triskelion sample CS2-90 S.No. 6, Table D.4

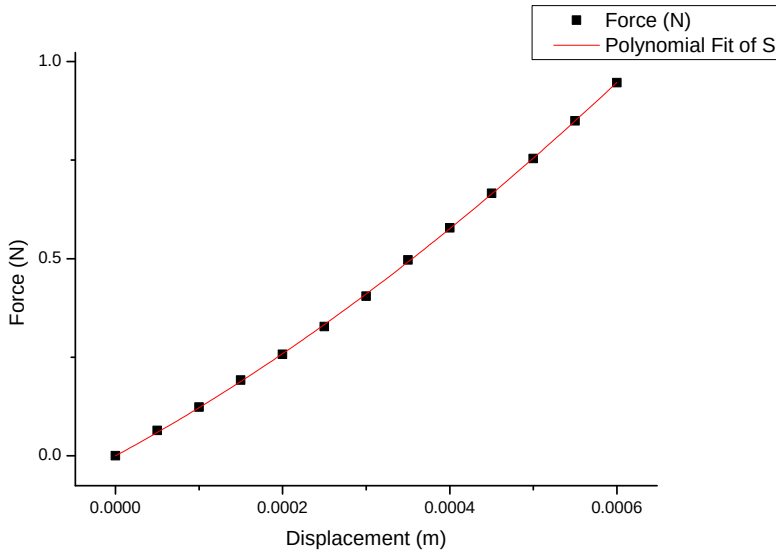

Figure E.25: Stiffness measured at the centre of hub for classic triskelion sample CS1-120 S.No. 1, Table D.5

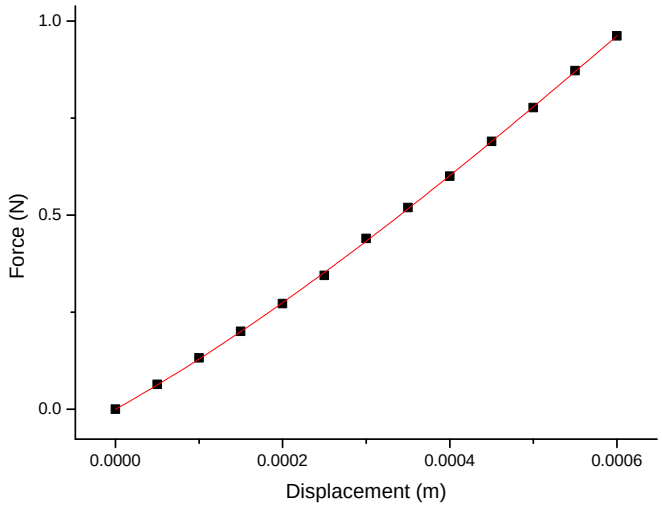

Figure E.26: Stiffness measured at the centre of hub for classic triskelion sample CS1-120 S.No. 2, Table D.5

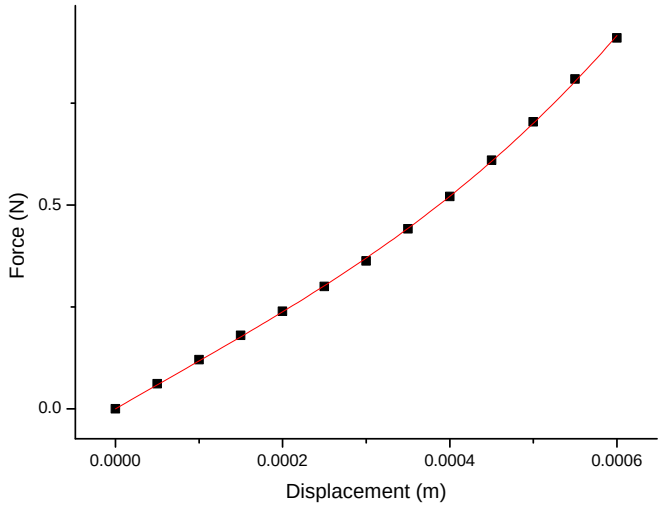

Figure E.27: Stiffness measured at the centre of hub for classic triskelion sample CS1-120 S.No. 3, Table D.5

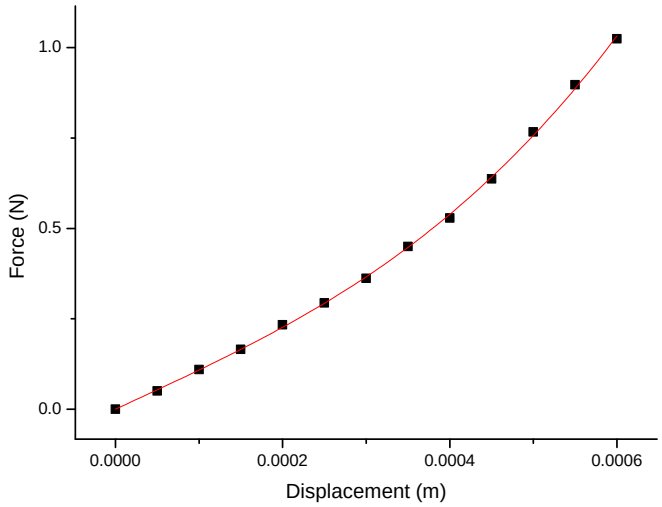

Figure E.28: Stiffness measured at the centre of hub for classic triskelion sample CS1-120 S.No. 4, Table D.5

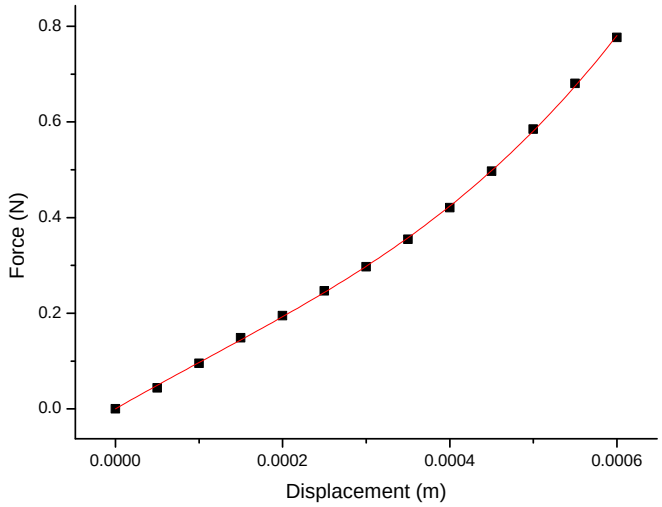

Figure E.29: Stiffness measured at the centre of hub for classic triskelion sample CS1-120 S.No. 5, Table D.5

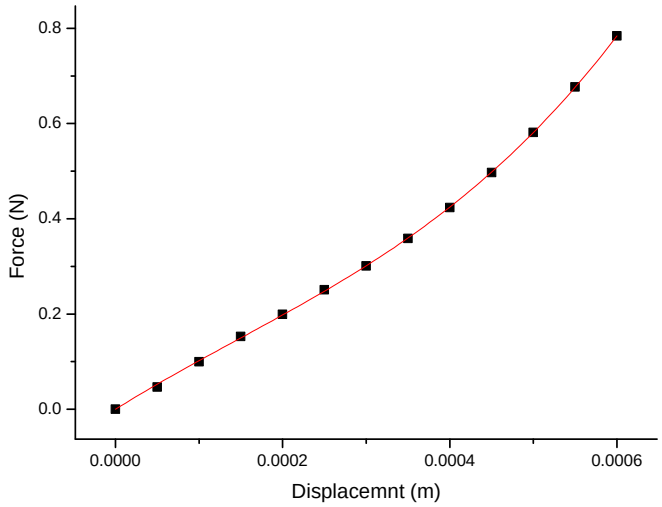

Figure E.30: Stiffness measured at the centre of hub for classic triskelion sample CS2-120 S.No. 6, Table D.5

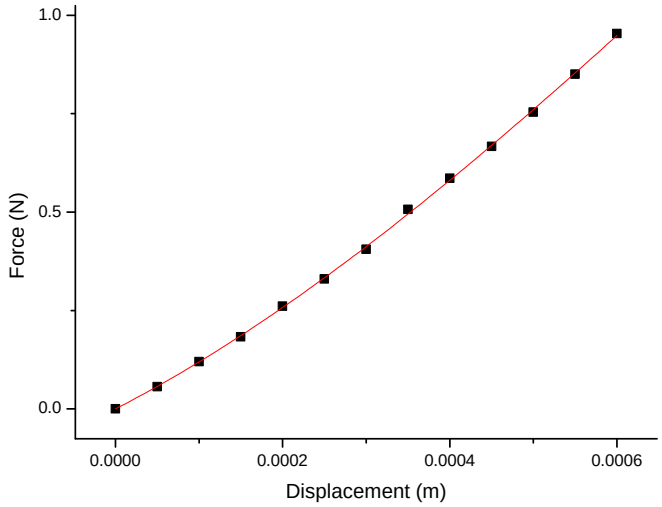

Figure E.31: Stiffness measured at the centre of hub for classic triskelion sample CS2-120 S.No. 1, D.6

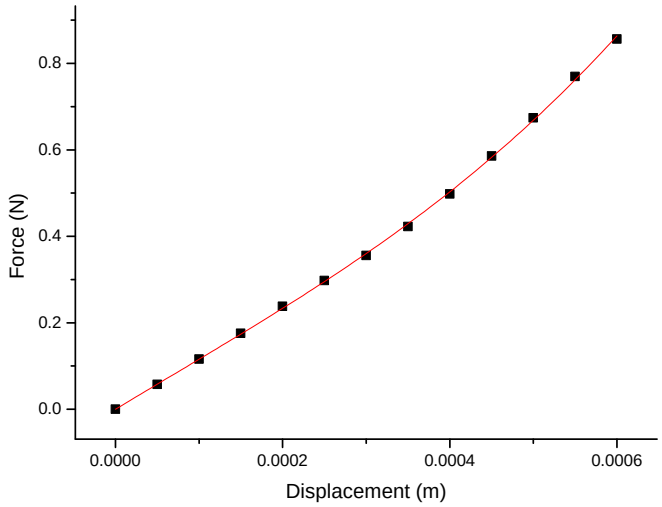

Figure E.32: Stiffness measured at the centre of hub for classic triskelion sample CS2-120 S.No. 2, Table D.6

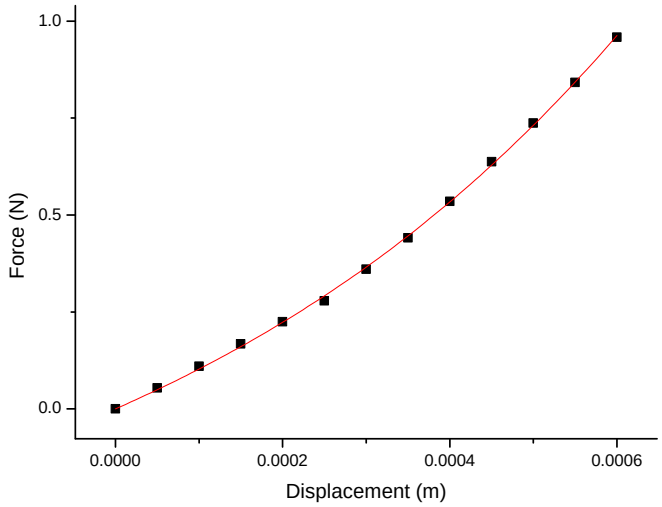

Figure E.33: Stiffness measured at the centre of hub for classic triskelion sample CS2-120 S.No. 3, Table D.6

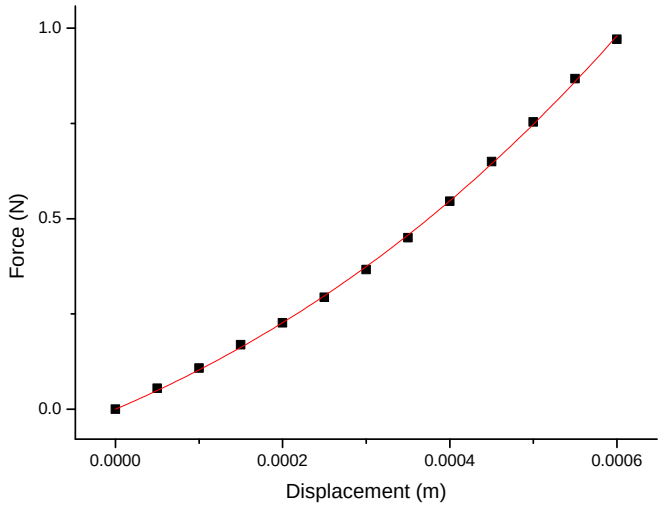

Figure E.34: Stiffness measured at the centre of hub for classic triskelion sample CS2-120 S.No. 4, Table D.6

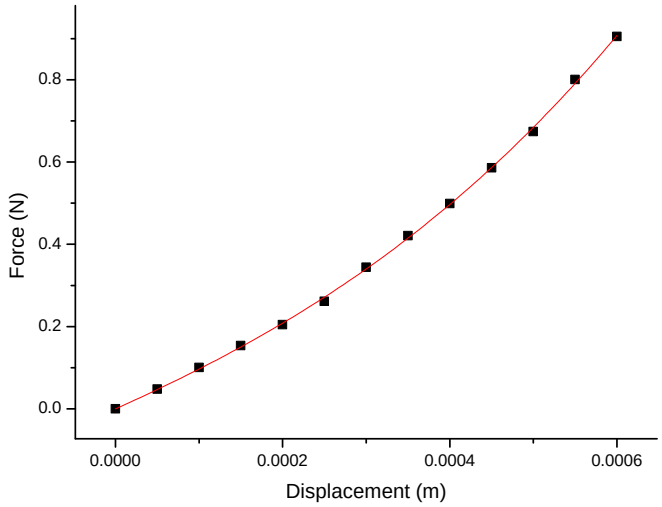

Figure E.35: Stiffness measured at the centre of hub for classic triskelion sample CS2-120 S.No. 5, Table D.6

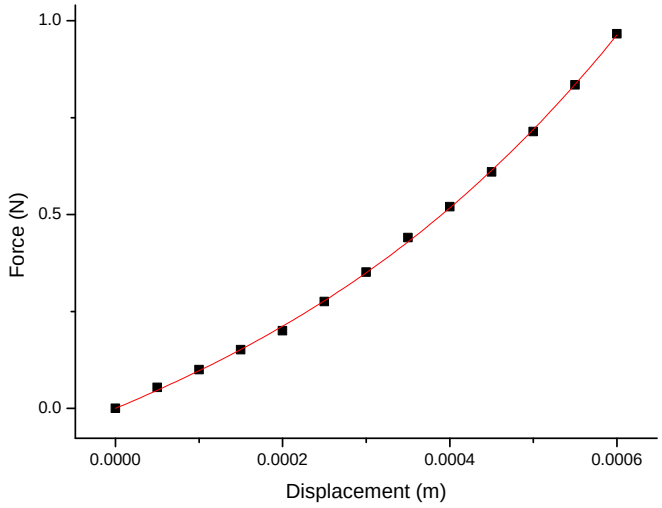

Figure E.36: Stiffness measured at the centre of hub for classic triskelion sample CS2-120 S.No. 6, Table D.6

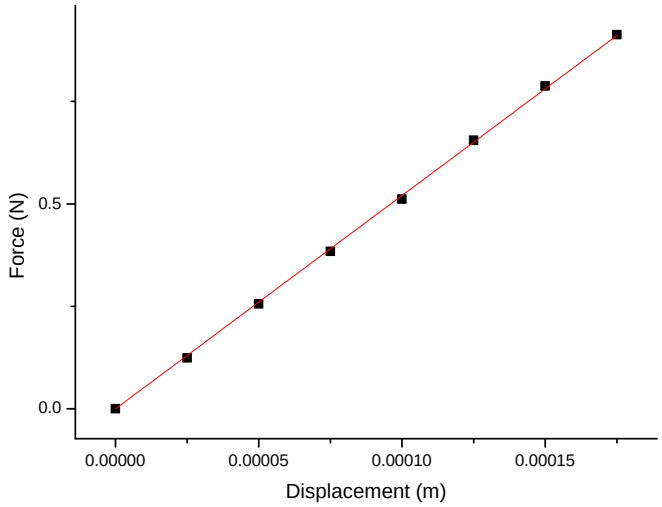

Figure E.37: Stiffness measured at the centre of hub for classic triskelion sample CS1-60 S.No. 1, D.7

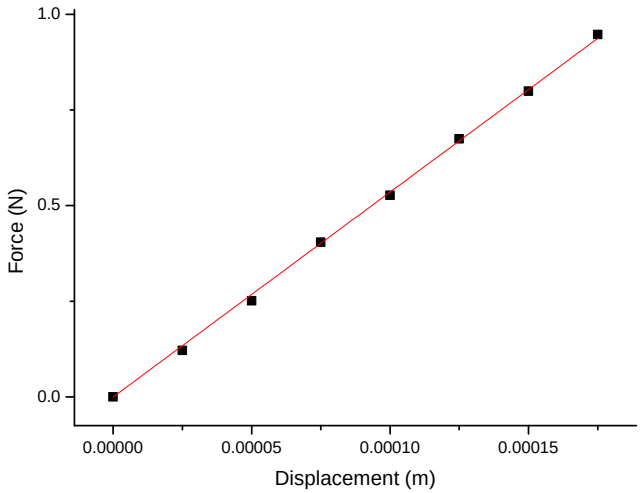

Figure E.38: Stiffness measured at the centre of hub for classic triskelion sample CS1-60 S.No. 2, Table D.7

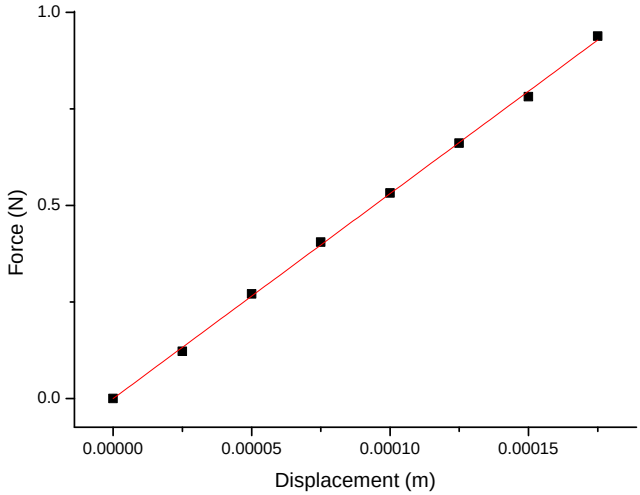

Figure E.39: Stiffness measured at the centre of hub for classic triskelion sample CS1-60 S.No. 3, Table D.7

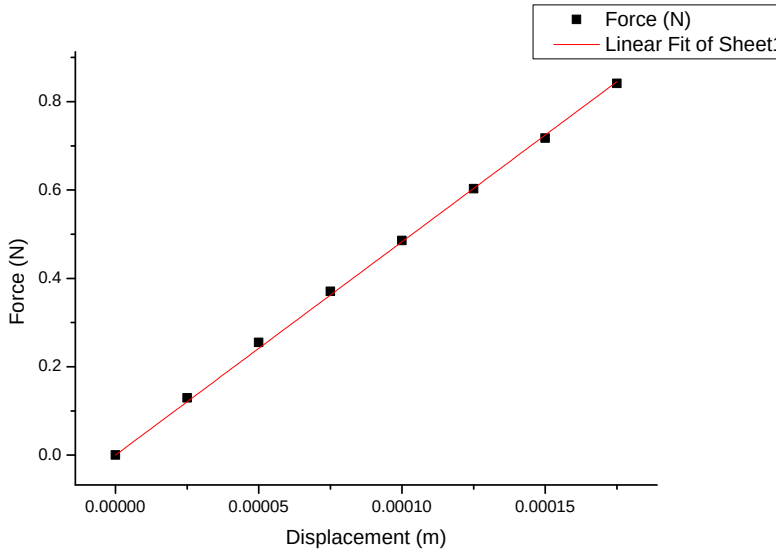

Figure E.40: Stiffness measured at the centre of hub for classic triskelion sample CS1-60 S.No. 4, Table D.7

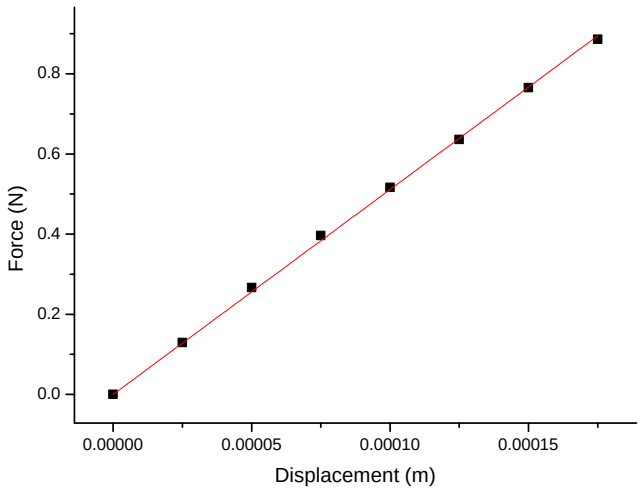

Figure E.41: Stiffness measured at the centre of hub for classic triskelion sample CS1-60 S.No. 5, D.7

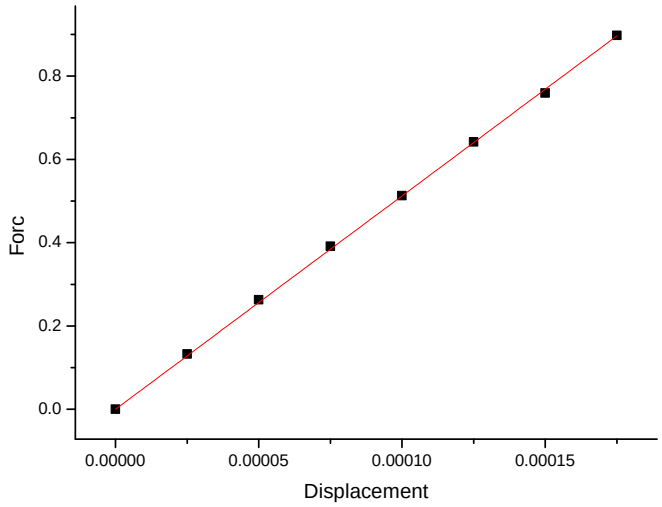

Figure E.42: Stiffness measured at the centre of hub for classic triskelion sample CS1-60 S.No. 6, Table D.7

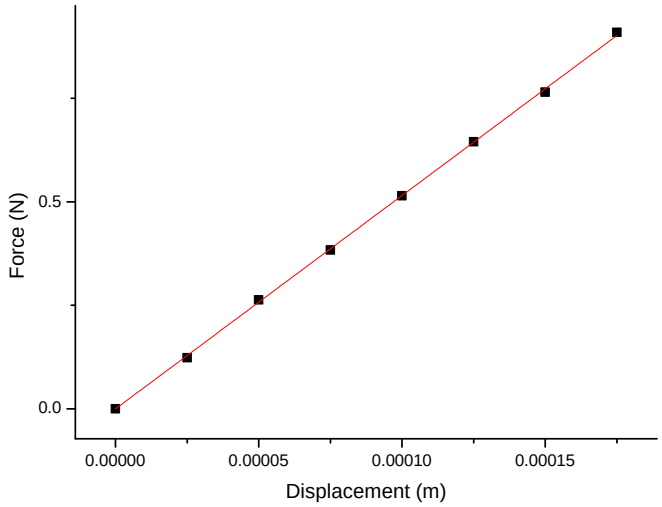

Figure E.43: Stiffness measured at the centre of hub for classic triskelion sample CS1-60 S.No. 1, Table D.8

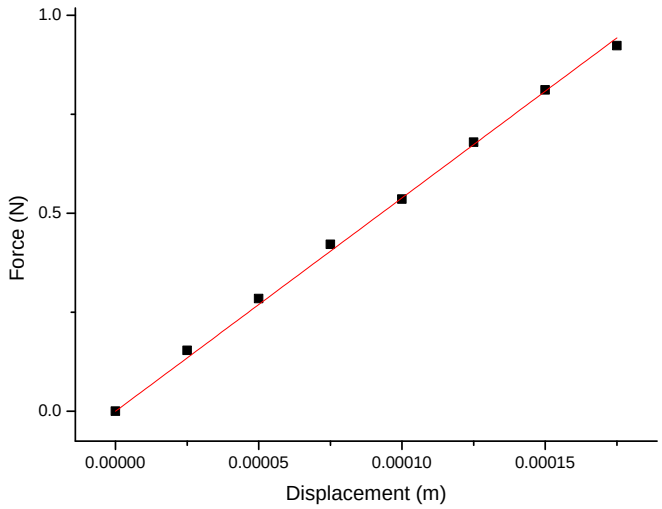

Figure E.44: Stiffness measured at the centre of hub for classic triskelion sample CS1-60 S.No. 2, Table D.8

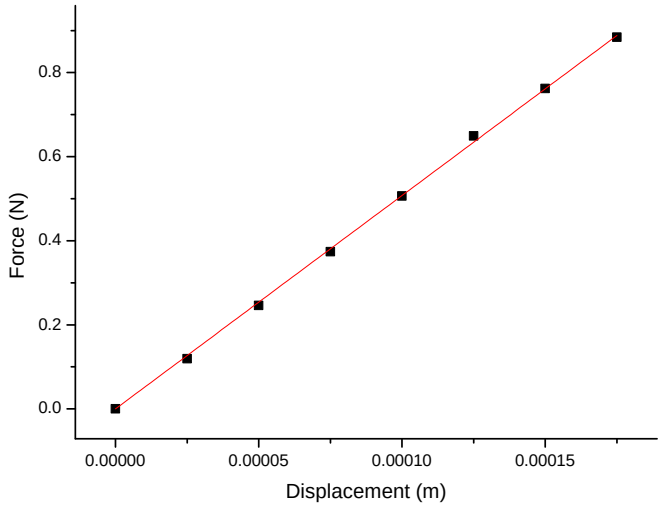

Figure E.45: Stiffness measured at the centre of hub for classic triskelion sample CS1-60 S.No. 3, Table D.8

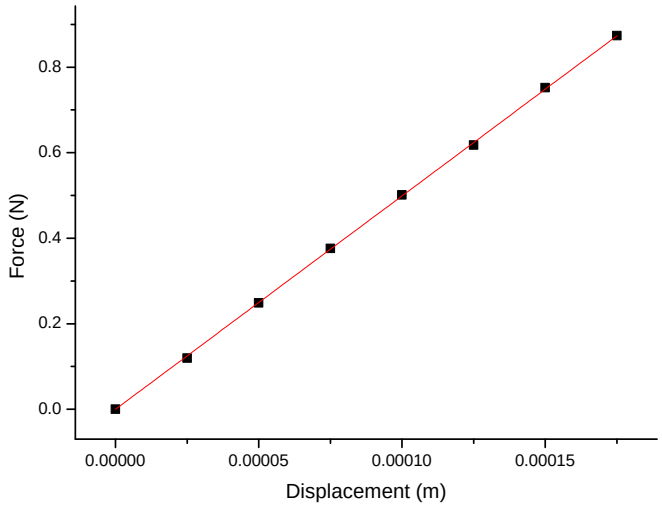

Figure E.46: Stiffness measured at the centre of hub for classic triskelion sample CS1-60 S.No. 4, Table D.8

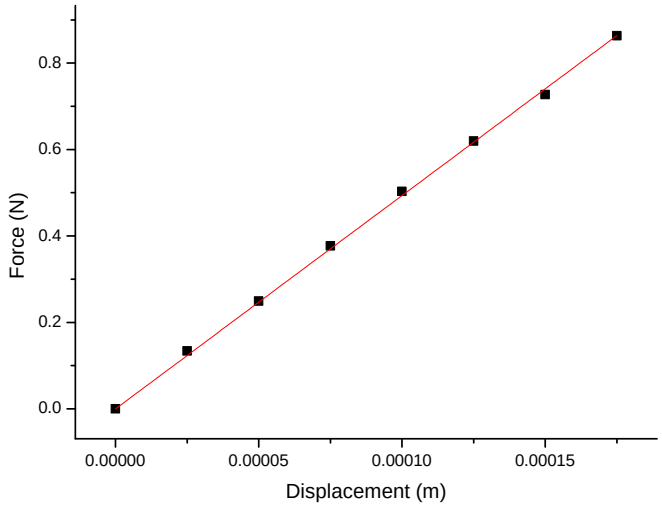

Figure E.47: Stiffness measured at the centre of hub for classic triskelion sample CS1-60 S.No. 5, Table D.8

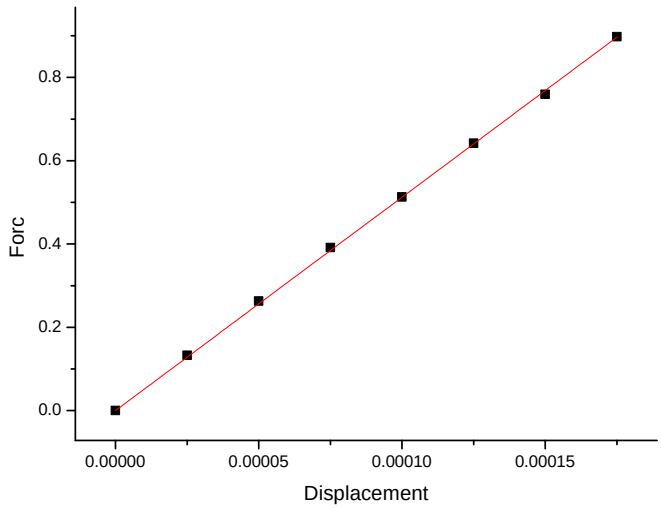

Figure E.48: Stiffness measured at the centre of hub for classic triskelion sample CS1-60 S.No. 6, Table D.8

Appendix F

Tables of cubic coefficients for angle-beam triskelion force arefacts

Table F.1: Coefficients analysis of plotted graph for angle-beam triskelion artefact ABS1-60.

S-No	$\beta_3\ Nm^{-3}$	$\beta_2\ Nm^{-2}$	$\beta_1 = k_{eff}\ Nm^{-1}$	β_0	R^2	*Max range X % mm*
1	3.04264E8	-169329.68918	560.93052	0	0.9999	0.06
2	2.17046E8	-81947.93885	522.25846	0	0.9999	0.06
3	2.54232E8	-93202.19403	527.65616	0	0.9998	0.01
4	8.10788E7	38180.83803	490.58532	0	0.9999	0.04
5	1.35518E8	-45849.54668	500.51806	0	0.9999	0.07
6	2.07642E8	-95344.50455	506.69317	0	0.9999	0.06

Table F.2: Coefficients analysis of plotted graph for classic triskelion artefact ABS2-60.

S-No	$\beta_3\ Nm^{-3}$	$\beta_2\ Nm^{-2}$	$\beta_1 = k_{eff}\ Nm^{-1}$	β_0	R^2	*Max range X % mm*
1	-2.42748E7	164206.51047	475.55183	0	0.9999	0.10
2	-1.29213E7	117716.39681	462.17939	0	0.9998	0.13
3	1.18572E8	16710.98713	497.97089	0	0.9999	0.08
4	-7.16365E6	144250.7681	457.72397	0	0.9998	0.13
5	-1.87916E7	169448.51375	442.75362	0	0.9999	0.11
6	-7.99416E7	173819.53895	416.35389	0	0.9999	0.07

Table F.3: Coefficients analysis of plotted graph for angle-beam triskelion artefact ABS1-90

S-No	$\beta_3\ Nm^{-3}$	$\beta_2\ Nm^{-2}$	$\beta_1 = k_{eff}\ Nm^{-1}$	β_0	R^2	*Max range X % mm*
1	7.96017E8	-581083.21867	902.50281	0	0.9999	0.05
2	6.04933E8	-286536.40699	856.7905	0	0.9999	0.05
3	7.91481E8	342744.65157	859.76599	0	0.9999	0.09
4	7.53794E8	-290361.41217	843.92754	0	0.9998	0.05
5	6.00738E8	-323791.52923	852.28123	0	0.9999	0.13
6	4.40877E8	-167113.64108	802.97021	0	0.9999	0.6

Table F.4: Coefficients analysis of plotted graph for classic triskelion artefact ABAS2-90.

S-No	$\beta_3\ Nm^{-3}$	$\beta_2\ Nm^{-2}$	$\beta_1 = k_{eff}\ Nm^{-1}$	β_0	R^2	*Max range X % mm*
1	7.74111E8	-529464.49777	1157.31141	0	0.9999	0.05
2	1.05567E9	-686804.51624	1195.60135	0	0.9998	0.05
3	1.15192E9	-689852.63793	1287.64663	0	0.9999	0.05
4	6.84177E8	-194601.02162	980.86015	0	0.9999	0.05
5	2.15375E8	131654.15716	965.90122	0	0.9998	0.08
6	3.84234E7	188410.53286	993.46125	0	0.9999	0.13

Table F.5: Coefficients analysis of plotted graph for angle-beam triskelion artefact ABS1-120.

S-No	$\beta_3\ Nm^{-3}$	$\beta_2\ Nm^{-2}$	$\beta_1 = k_{eff}\ Nm^{-1}$	β_0	R^2	*Max range X % mm*
1	1.17265E9	-18905.35879	621.42361	0	0.9998	0.04
2	1.79733E9	-544680.52702	783.00448	0	0.9998	0.03
3	1.19607E9	-181470.90645	799.39845	0	0.9997	0.04
4	6.99111E8	162633.14044	554.89519	0	0.9999	0.09
5	1.28667E9	-217799.29504	635.48953	0	0.9998	0.04
6	1.05704E9	62073.92607	599.41941	0	0.9999	0.04

Table F.6: Coefficients analysis of plotted graph for classic triskelion artefact ABS2-120.

S-No	$\beta_3\ Nm^{-3}$	$\beta_2\ Nm^{-2}$	$\beta_1 = k_{eff}\ Nm^{-1}$	β_0	R^2	*Max range X % mm*
1	9.0106E8	-27639.53028	602.42941	0	0.9997	0.04
2	1.11897E9	40061.37259	597.00420	0	0.9998	0.04
3	7.54334E8	229842.76101	609.54333	0	0.9998	0.04
4	6.27101E8	376377.58468	591.64870	0	0.9995	0.04
5	1.21767E9	-8006.33329	565.17477	0	0.9999	0.03
6	1.10045E9	-10664.80689	573.06067	0	0.9998	0.04

Appendix G

Graphs for angle-beam Triskelion Samples

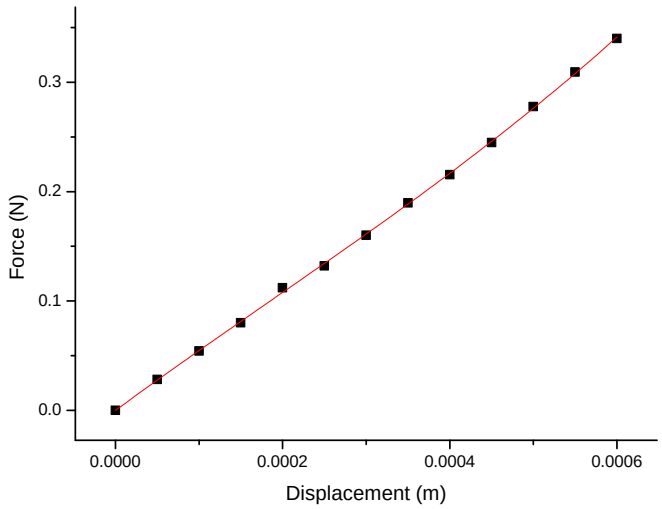

Figure G.1: Stiffness measured at the centre of hub for angle-beam triskelion samples ABS1-60 S.No. 1, Table F.1

.

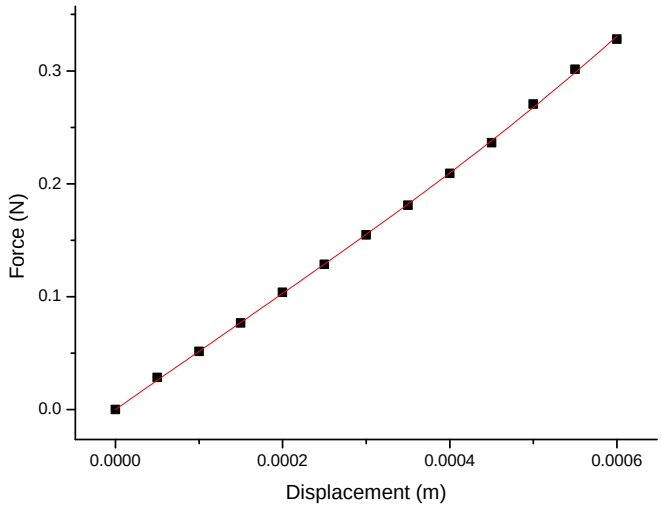

Figure G.2: Stiffness measured at the centre of hub for angle-beam triskelion samples ABS1-60 S.No. 2, Table F.1

.

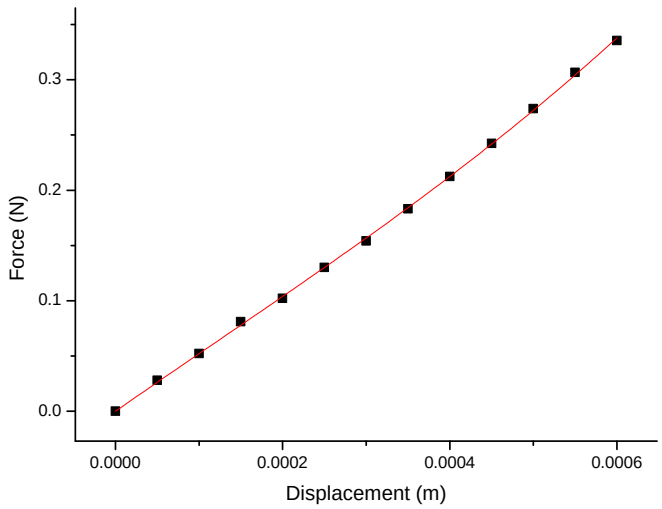

Figure G.3: Stiffness measured at the centre of hub for angle-beam triskelion samples ABS1-60 S.No. 3, Table F.1

.

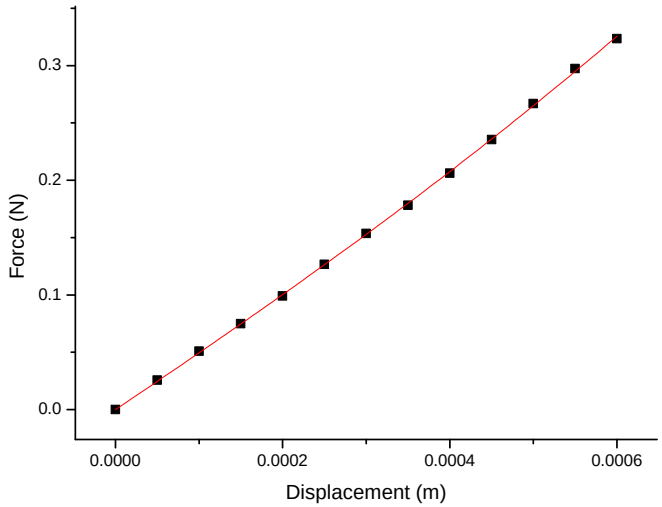

Figure G.4: Stiffness measured at off-centre point for angle-beam triskelion samples ABS1-60 S.No. 4, Table F.1

.

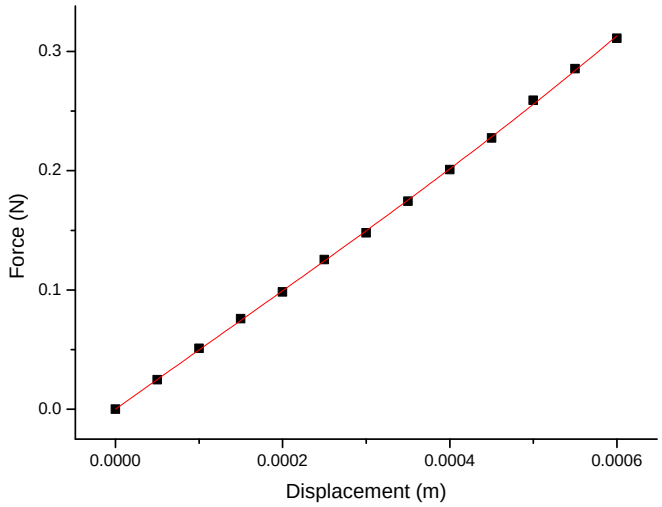

Figure G.5: Stiffness measured at off-centre point for angle-beam triskelion samples ABS1-60 S.No. 5, Table F.1

.

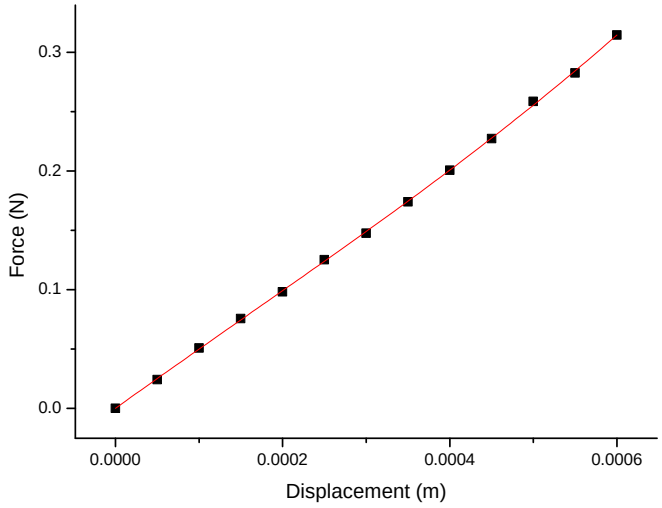

Figure G.6: Stiffness measured at off-centre point for angle-beam triskelion samples ABS1-60 S.No. 6, Table F.1

.

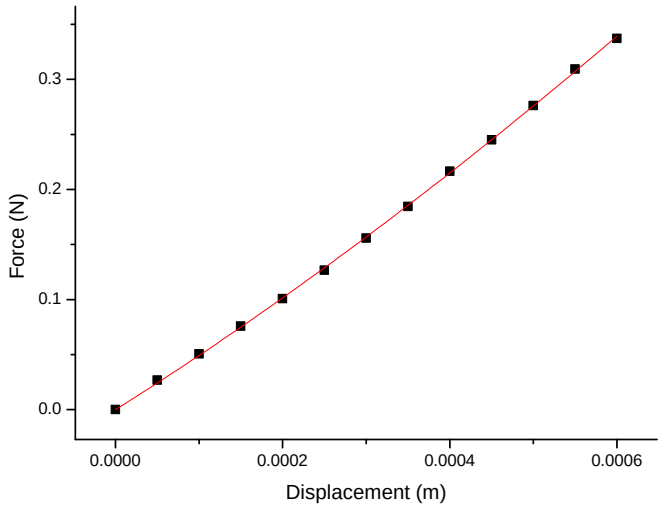

Figure G.7: Stiffness measured at the centre of hub for angle-beam triskelion samples ABS2-60 S.No. 1, Table F.2

.

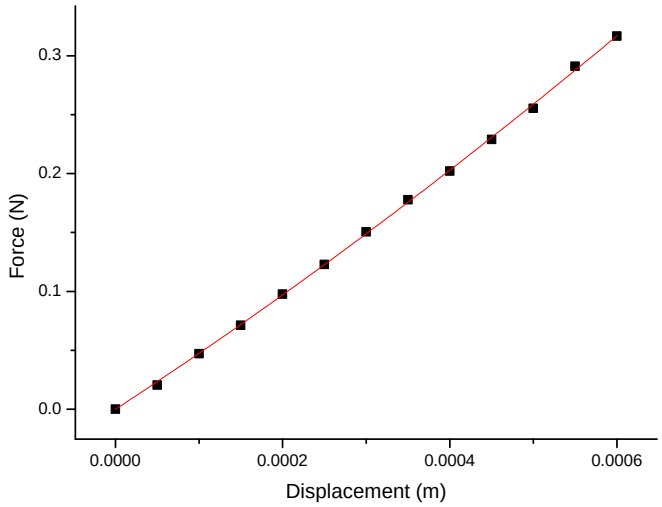

Figure G.8: Stiffness measured at the centre of hub for angle-beam triskelion samples ABS2-60 S.No. 2, Table F.2

.

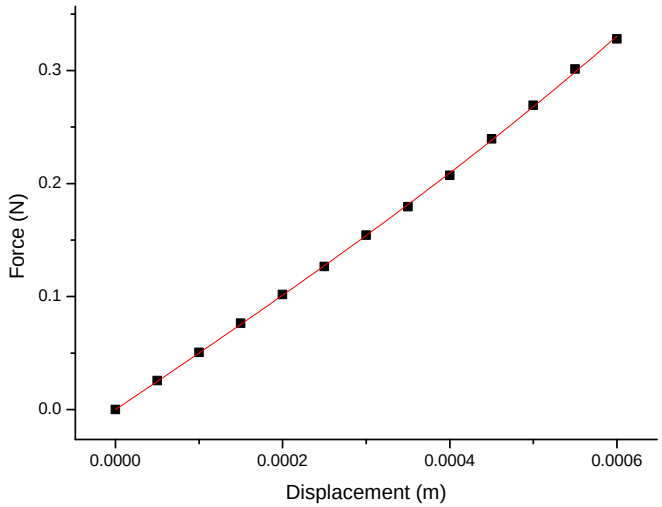

Figure G.9: Stiffness measured at the centre of hub for angle-beam triskelion samples ABS1-60 S.No. 3, Table F.2

.

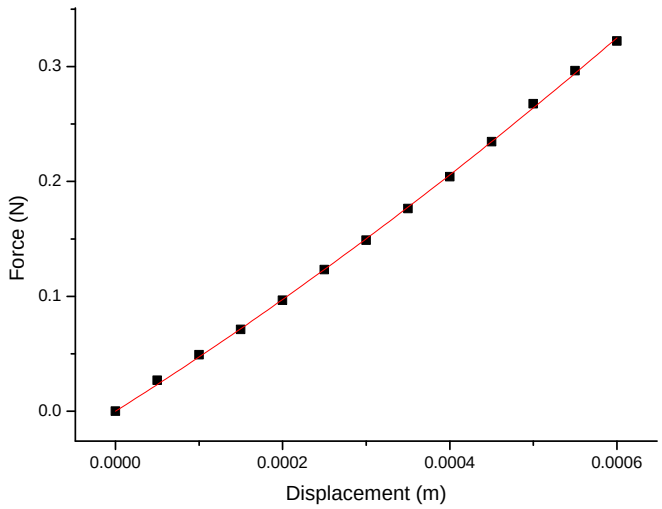

Figure G.10: Stiffness measured at off-centre point for angle-beam triskelion samples ABS1-60 S.No. 4, Table F.2

.

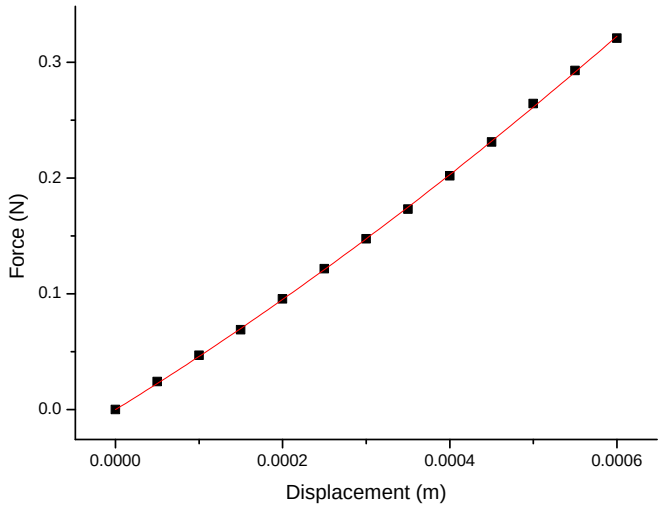

Figure G.11: Stiffness measured at off-centre point for angle-beam triskelion samples ABS2-60 S.No. 5, Table F.2

.

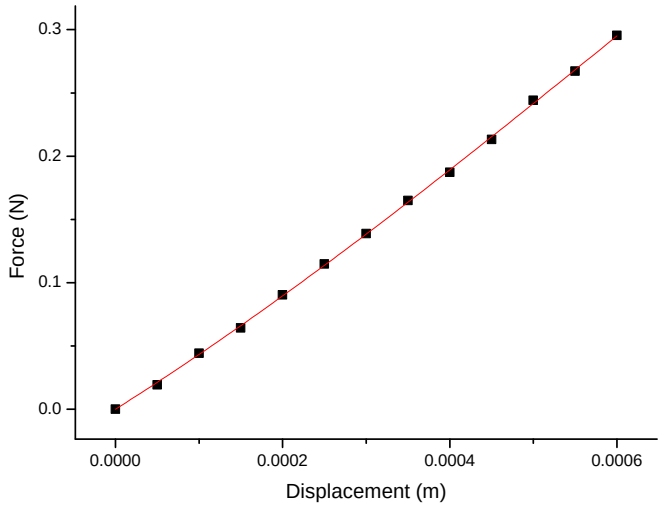

Figure G.12: Stiffness measured at off-centre point for angle-beam triskelion samples ABS2-60 S.No. 6, Table F.2

.

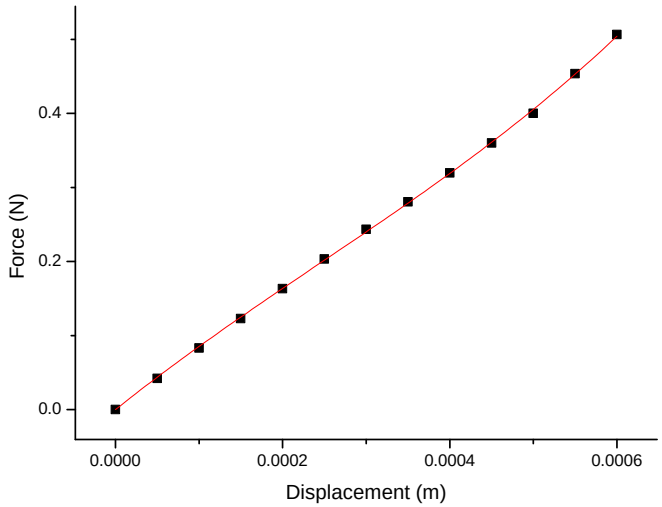

Figure G.13: Stiffness measured at the centre of hub for angle-beam triskelion samples ABS2-90 S.No. 1, Table F.3

.

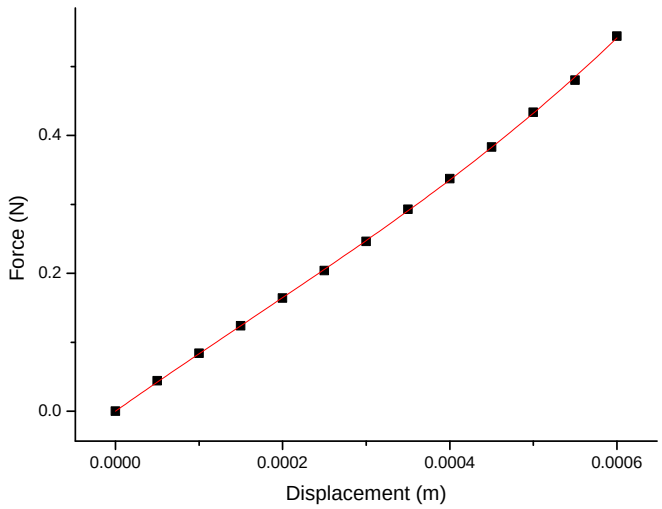

Figure G.14: Stiffness measured at the centre of hub for angle-beam triskelion samples ABS2-90 S.No. 2, Table F.3

.

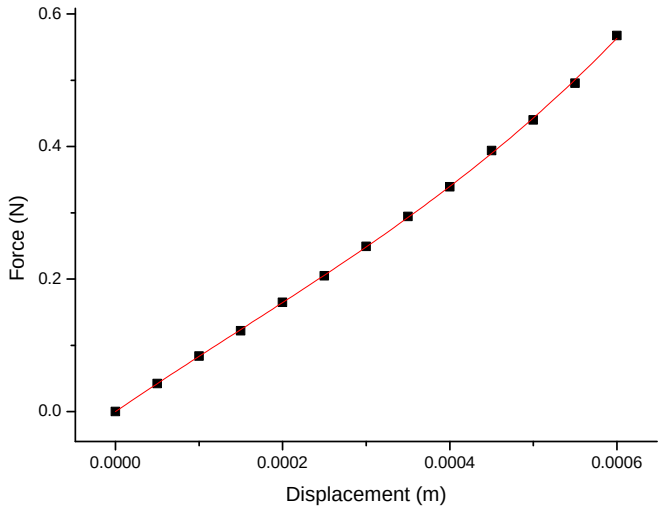

Figure G.15: Stiffness measured at the centre of hub for angle-beam triskelion samples ABS1-90 S.No. 3, Table F.3

.

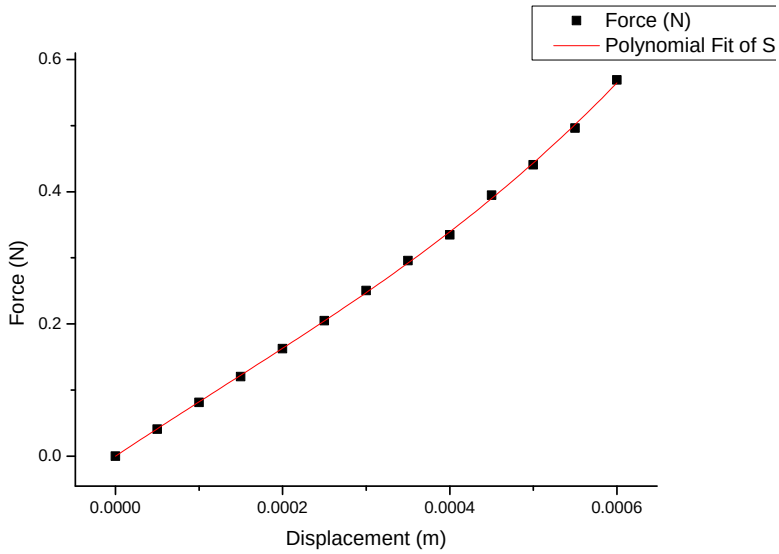

Figure G.16: Stiffness measured at off-centre point for angle-beam triskelion samples ABS1-90 S.No. 4, Table F.3

.

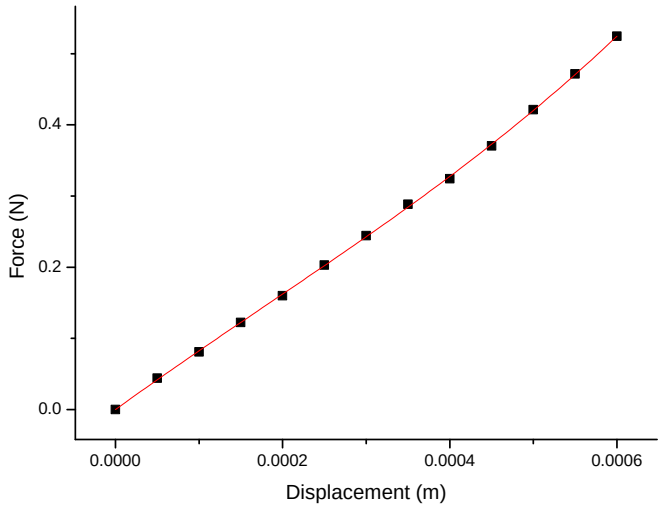

Figure G.17: Stiffness measured at off-centre point for angle-beam triskelion samples ABS2-90 S.No. 5, Table F.3

.

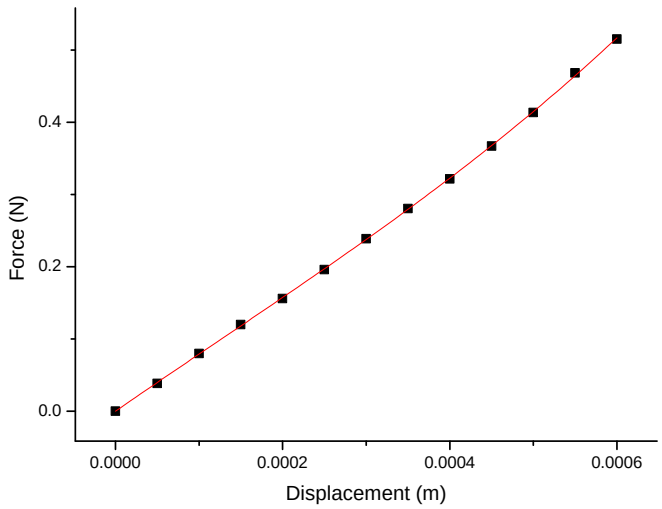

Figure G.18: Stiffness measured at off-centre point for angle-beam triskelion samples ABS2-90 S.No. 6, Table F.3

.

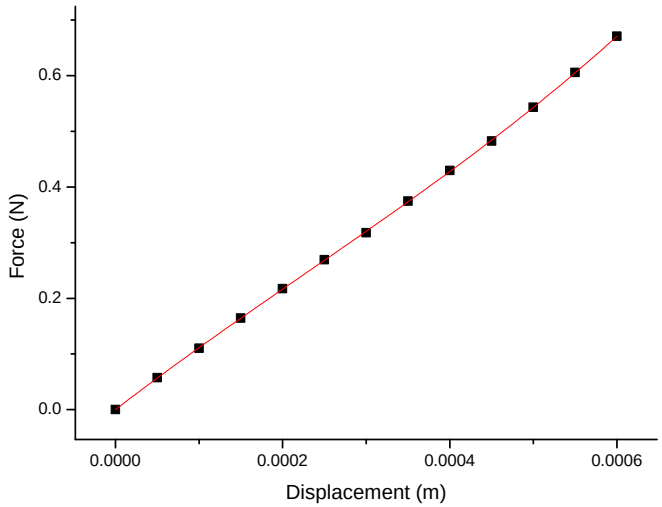

Figure G.19: Stiffness measured at the centre of hub for angle-beam triskelion samples ABS2-90 S.No. 1, Table F.4

.

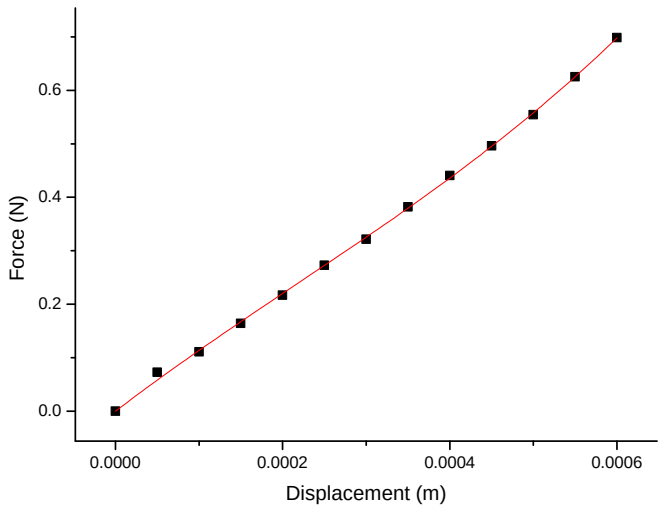

Figure G.20: Stiffness measured at the centre of hub for angle-beam triskelion samples ABS2-90 S.No. 2, Table F.4

.

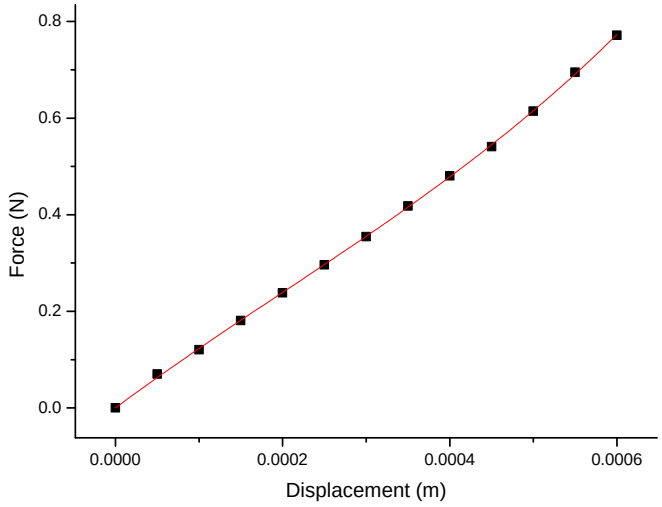

Figure G.21: Stiffness measured at the centre of hub for angle-beam triskelion samples ABS2-90 S.No. 3, Table F.4

.

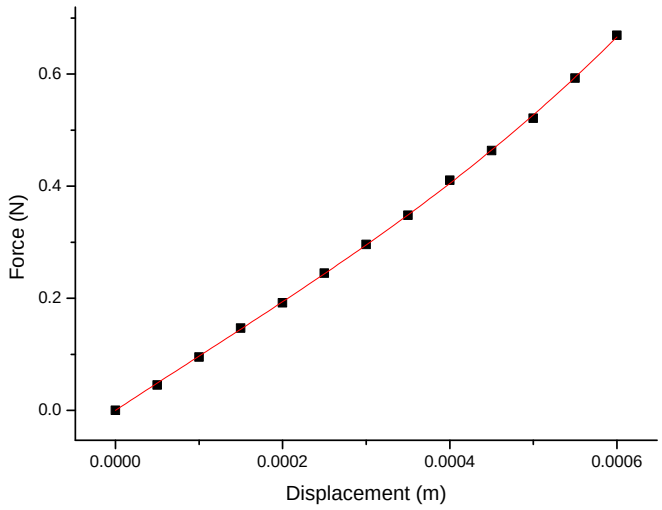

Figure G.22: Stiffness measured at off-centre point for angle-beam triskelion samples ABS2-90 S.No. 4, Table F.4

.

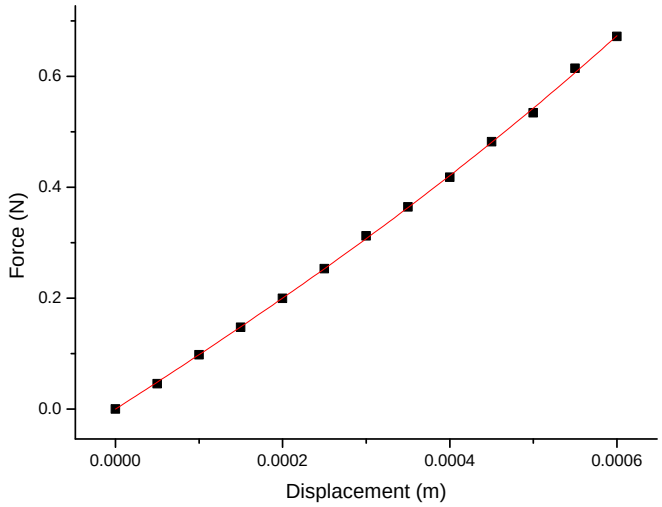

Figure G.23: Stiffness measured at off-centre point for angle-beam triskelion samples ABS2-90 S.No. 5, Table F.4

.

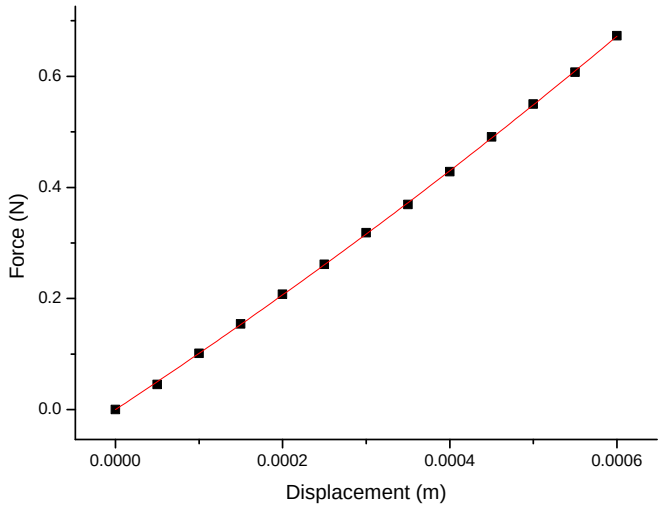

Figure G.24: Stiffness measured at off-centre point for angle-beam triskelion samples ABS2-90 S.No. 6, Table F.4

.

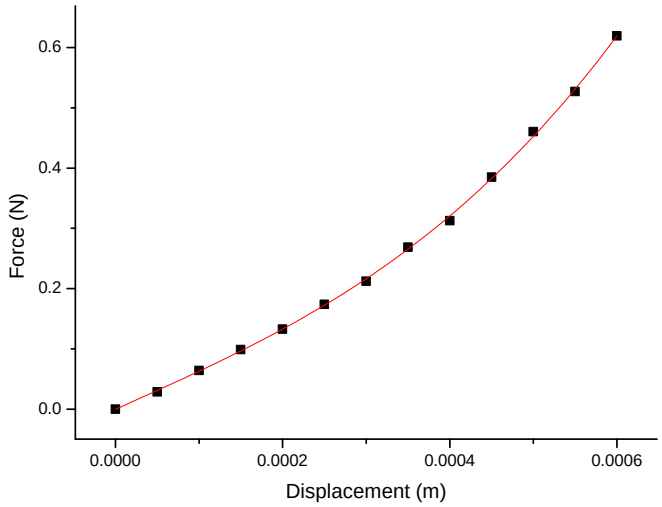

Figure G.25: Stiffness measured at the centre of hub for angle-beam triskelion samples ABS1-120 S.No. 1, Table F.5

.

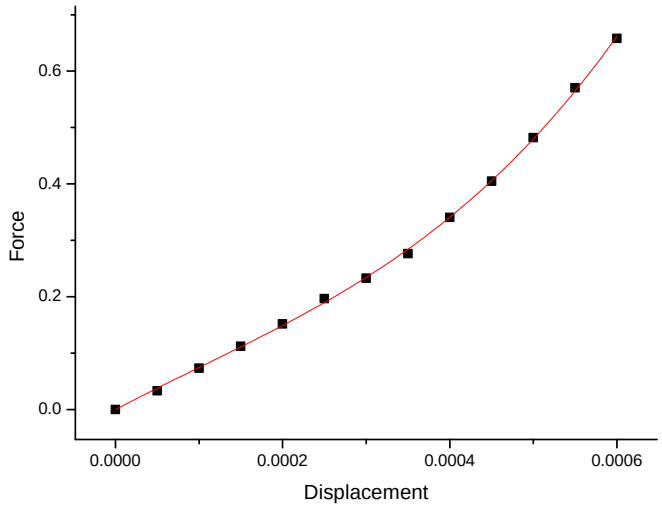

Figure G.26: Stiffness measured at the centre of hub for angle-beam triskelion samples ABS1-120 S.No. 2, Table F.5

.

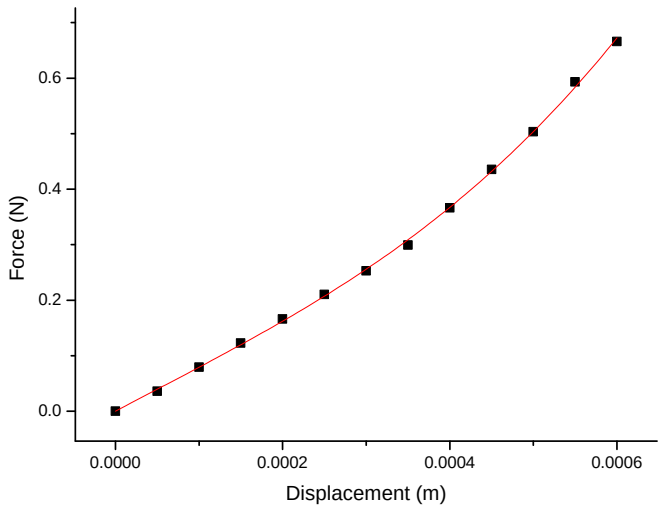

Figure G.27: Stiffness measured at the centre of hub for angle-beam triskelion samples ABS1-120 S.No. 3, Table F.5

.

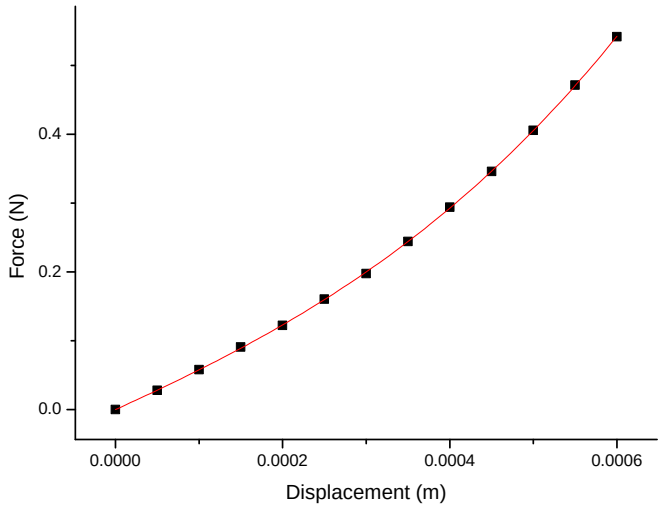

Figure G.28: Stiffness measured at off-centre point for angle-beam triskelion samples ABS1-120 S.No. 4, Table F.5

.

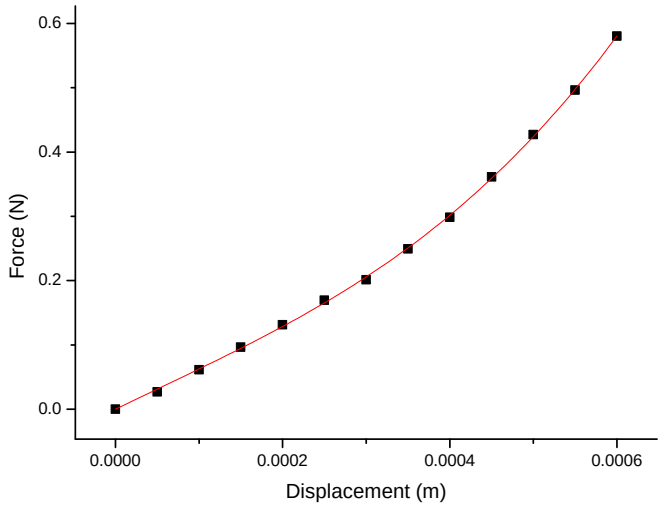

Figure G.29: Stiffness measured at off-centre point for angle-beam triskelion samples ABS1-120 S.No. 5, Table F.5

.

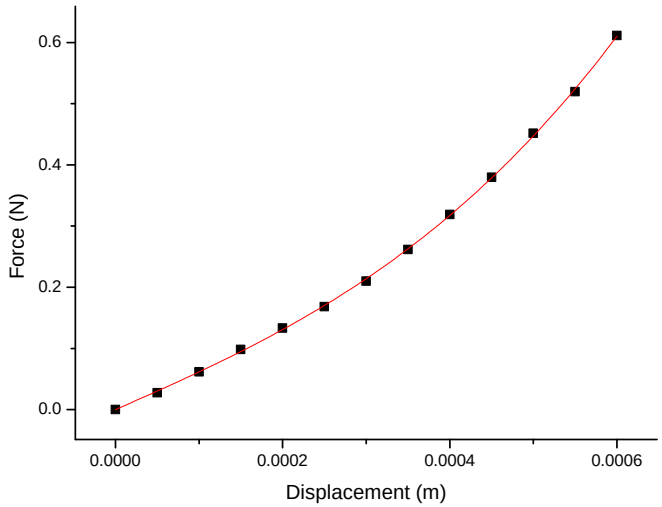

Figure G.30: Stiffness measured at off-centre point for angle-beam triskelion samples ABS1-120 S.No. 6, Table F.5

.

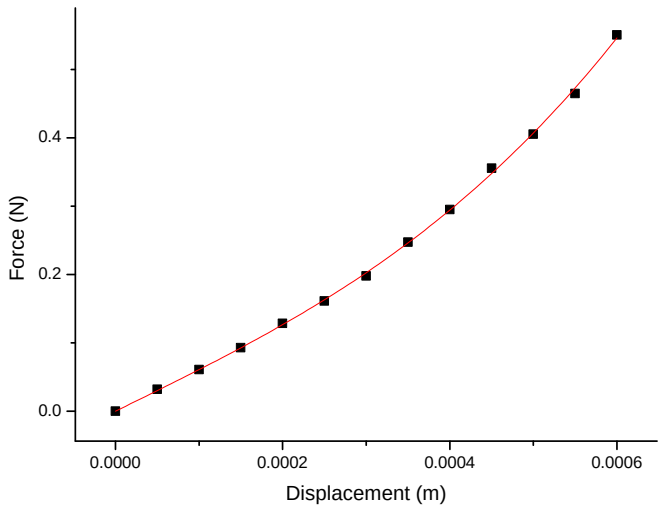

Figure G.31: Stiffness measured at the centre of hub for angle-beam triskelion samples ABS2-120 S.No. 1, Table F.6

.

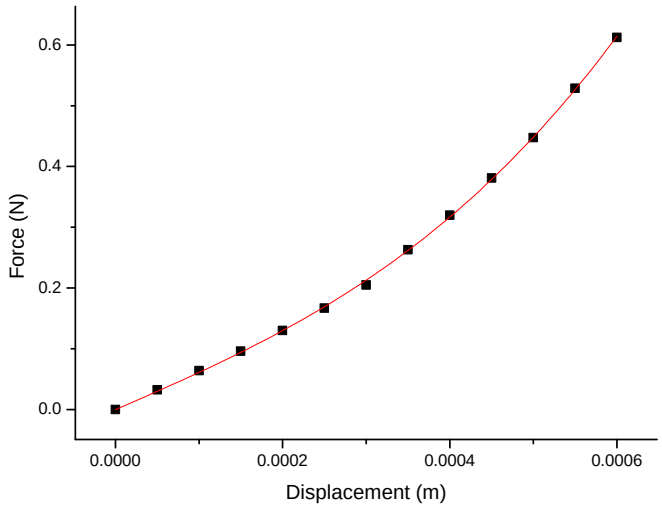

Figure G.32: Stiffness measured at the centre of hub for angle-beam triskelion samples ABS2-1200 S.No. 2, Table F.6

.

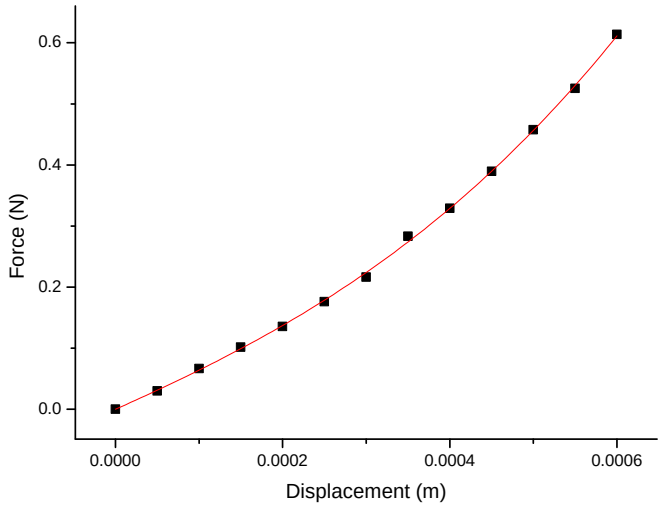

Figure G.33: Stiffness measured at the centre of hub for angle-beam triskelion samples ABS2-120 S.No. 3, Table F.6

.

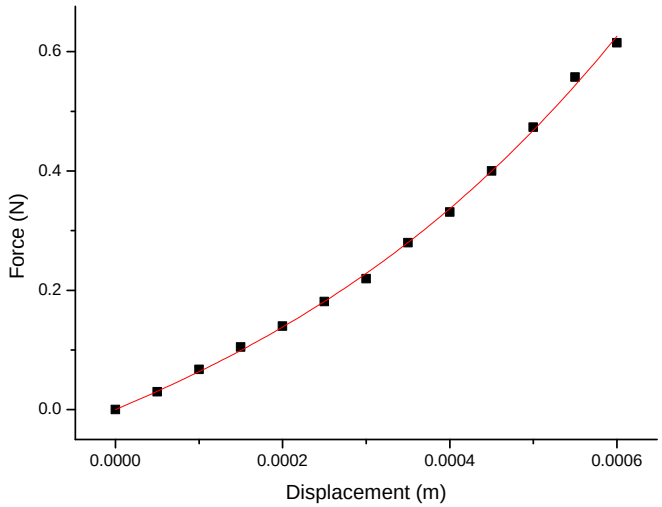

Figure G.34: Stiffness measured at off-centre point for angle-beam triskelion samples ABS2-120 S.No. 4, Table F.6

.

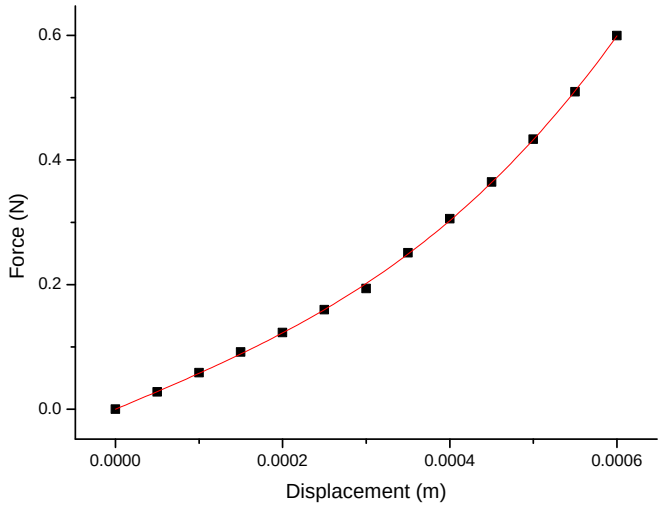

Figure G.35: Stiffness measured at off-centre point for angle-beam triskelion samples ABS2-120 S.No. 5, Table F.6

.

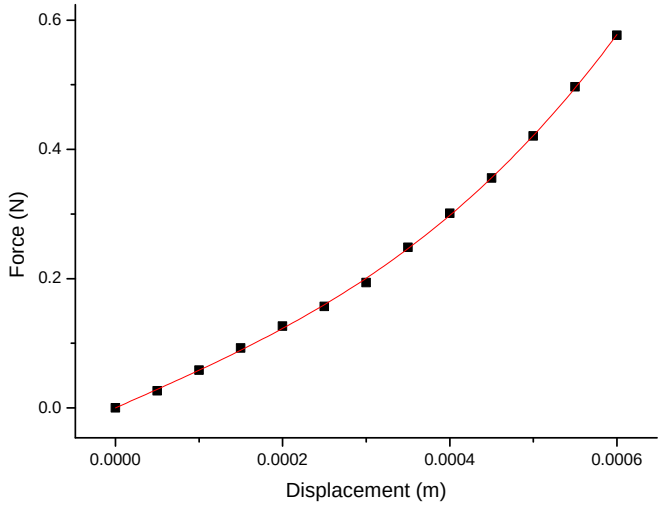

Figure G.36: Stiffness measured at off-centre point for angle-beam triskelion samples ABS2-120 S.No. 6, Table F.6

.

Appendix H

Tables of linear coefficients for classic tetraskelion force artefacts

Table H.1: Coefficients of the best linear fit to graphs for classic tetraskelion centre symmetric sample CS1-CS-90.

S-No	$\beta_1 = k_{eff}\ Nm^{-1}$	β_0	R^2
1	2911.51	0	0.99916
2	2799.84	0	0.99934
3	2815.92	0	0.99904
4	2728.54	0	0.99949
5	2666.03	0	0.99962
6	2658.82	0	0.99956
7	2728.54	0	0.99949

Table H.2: Coefficients of the best linear fit to graphs for classic tetraskelion centre symmetric sample CS2-CS-90.

S-No	$\beta_1 = k_{eff}\ Nm^{-1}$	β_0	R^2
1	2839.92	0	0.99969
2	2885.86	0	0.99968
3	2877.56	0	0.99954
4	2626.50	0	0.99935
5	2679.84	0	0.99954
6	2315.10	0	0.9995
7	2657.10	0	0.9996

Table H.3: Coefficients of the best linear fit to graphs for classic tetraskelion diagonal symmetric sample CS1-DS-90.

S-No	$\beta_1 = k_{eff}\ Nm^{-1}$	β_0	R^2
1	4826.11	0	0.99981
2	4684.39	0	0.99927
3	4623.52	0	0.99979
4	4544.00	0	0.99979
5	4380.78	0	0.99992
6	4380.78	0	0.99996
6	4498.66	0	0.99981

Table H.4: Coefficients of the best linear fit to graphs for classic tetraskelion diagonal symmetric sample CS2-DS-90.

S-No	$\beta_1 = k_{eff}\ Nm^{-1}$	β_0	R^2
1	4513.64	0	0.99954
2	4412.15	0	0.99992
3	4523.92	0	0.99911
4	4028.87	0	0.99953
5	4312.62	0	0.99977
6	4263.96	0	0.99967
7	4131.84	0	0.99972

Table H.5: Coefficients of the best linear fit to graphs for angle-beam tetraskelion centre symmetric sample ABS1-DS-90.

S-No	$\beta_1 = k_{eff}\ Nm^{-1}$	β_0	R^2
1	1256.23	0	0.99921
2	1181.52	0	0.99982
3	1197.90	0	0.99967
4	1101.25	0	0.99942
5	1125.37	0	0.99956
6	1125.52	0	0.99907
7	1166.46	0	0.99978

Table H.6: Coefficients of the best linear fit to graphs for angle-beam tetraskelion diagonal symmetric sample ABS1-DS-90.

S-No	$\beta_1 = k_{eff}\ Nm^{-1}$	β_0	R^2
1	1713.06	0	0.99969
2	1801.88	0	0.99985
3	1724.98	0	0.99916
4	1702.11	0	0.99993
5	1625.94	0	0.99927
6	1646.48	0	0.99991
7	1668.78	0	0.99942

Appendix I

Graphs for classic and angle-beam tetraskelion samples

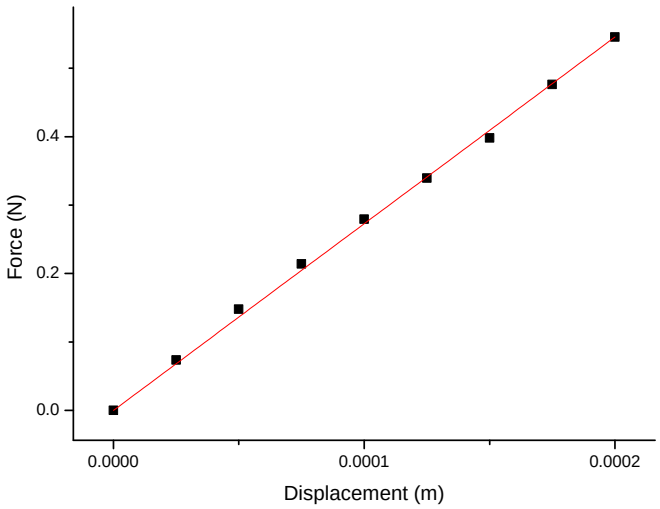

Figure I.1: Stiffness measured at the centre for classic tetraskelion samples CS1-CS-90.No. 1, Table H.1.

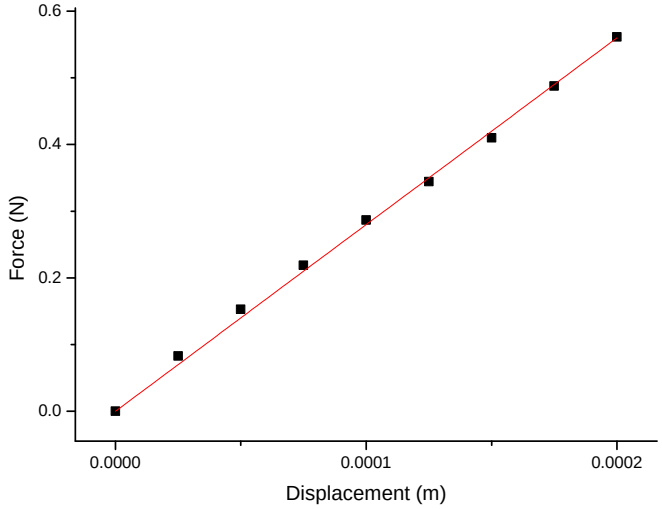

Figure I.2: Stiffness measured at the centre for classic tetraskelion samples CS1-CS-90.No. 2, Table H.1.

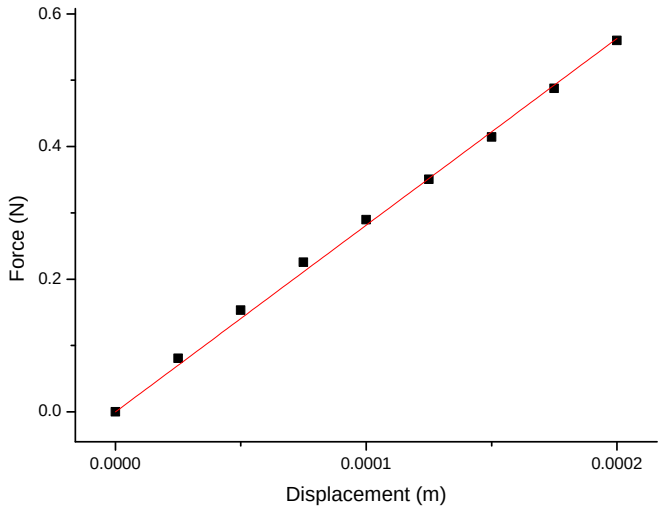

Figure I.3: Stiffness measured at the centre for classic tetraskelion samples CS1-CS-90.No. 3, Table H.1.

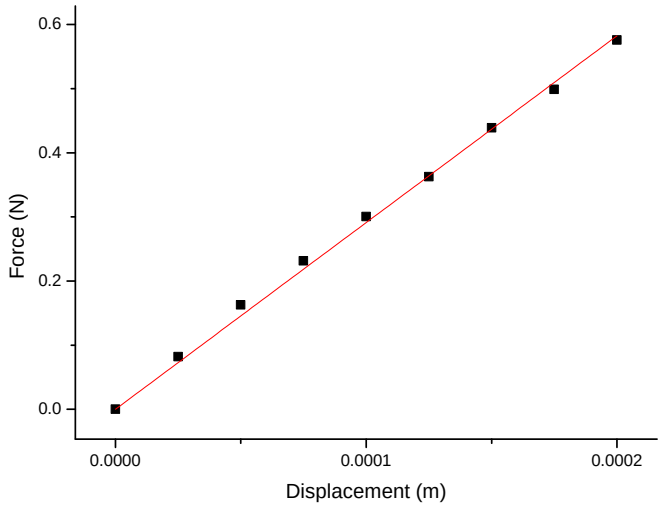

Figure I.4: Stiffness measured at off-centre point of hub for classic tetraskelion samples CS1-CS-90.No. 4, Table H.1.

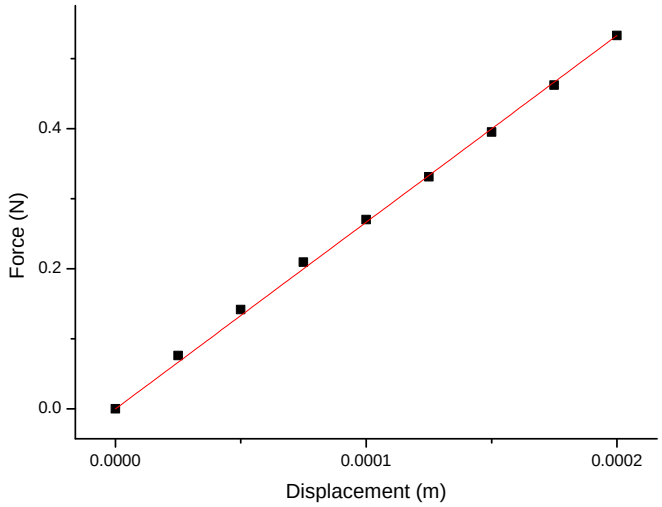

Figure I.5: Stiffness measured at off-centre point for classic tetraskelion samples CS1-CS-90.No. 5, Table H.1.

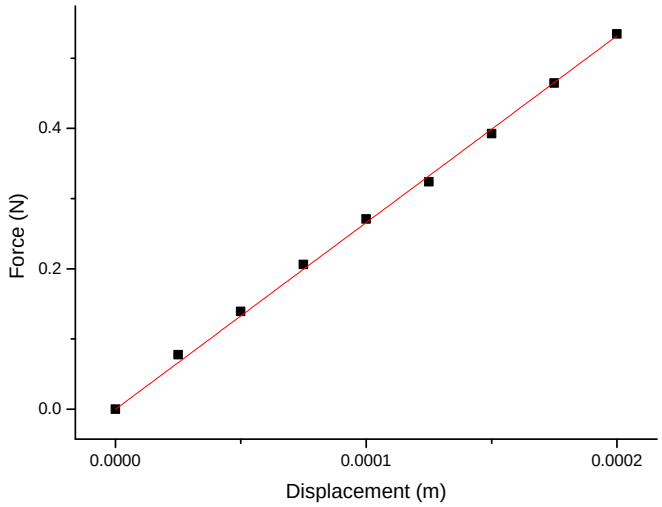

Figure I.6: Stiffness measured at off-centre point for classic tetraskelion samples CS1-CS-90.No. 6, Table H.1.

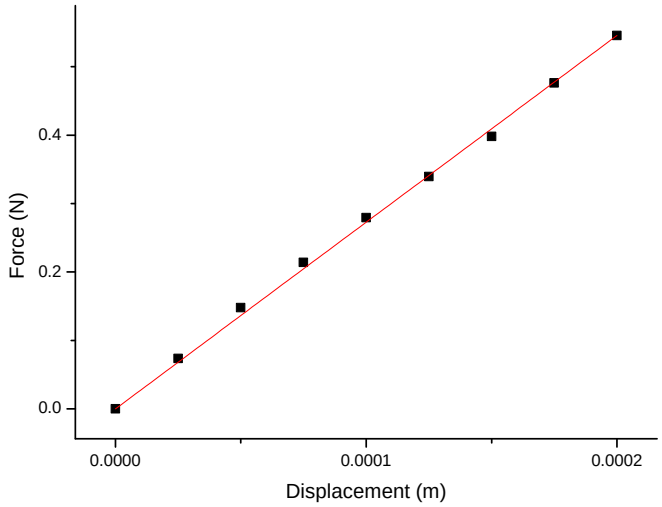

Figure I.7: Stiffness measured at off-centre point for classic tetraskelion samples CS1-CS-90.No. 7, Table H.1.

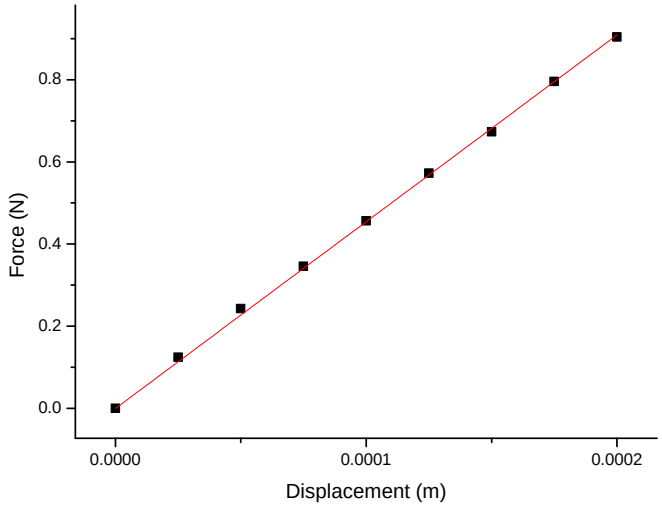

Figure I.8: Stiffness measured at the centre for classic tetraskelion samples CS1-DS-90.No. 1, Table H.3.

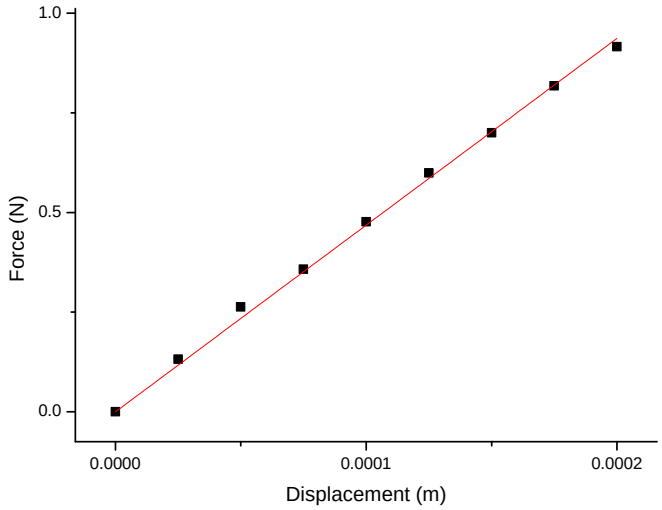

Figure I.9: Stiffness measured at the centre for classic tetraskelion samples CS1-DS-90.No. 2, Table H.3.

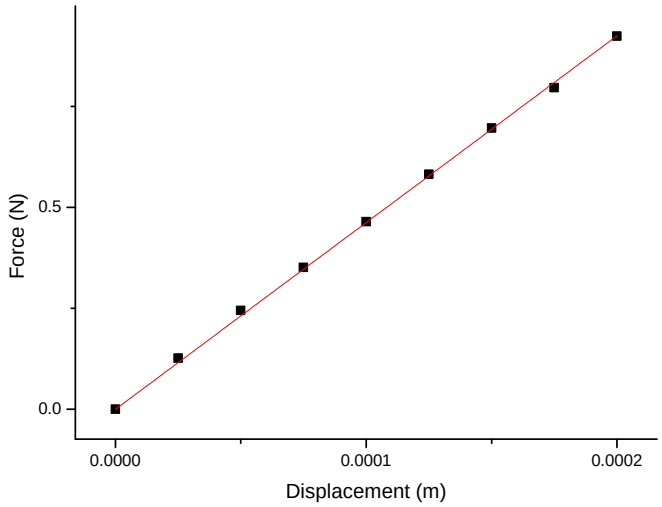

Figure I.10: Stiffness measured at the centre for classic tetraskelion samples CS1-DS-90.No. 3, Table H.3.

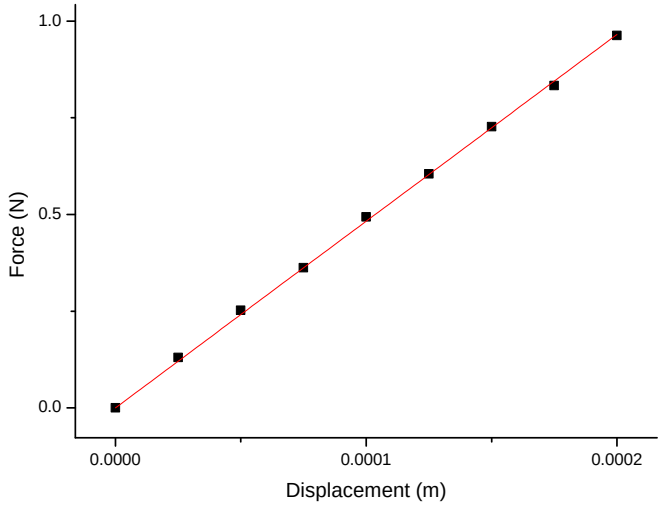

Figure I.11: Stiffness measured at off-centre point of hub for classic tetraskelion samples CS1-DS-90.No. 4, Table H.3.

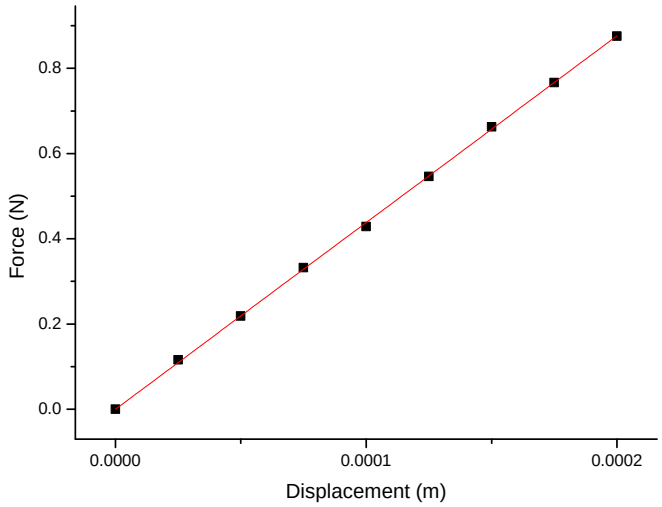

Figure I.12: Stiffness measured at off-centre point for classic tetraskelion samples CS1-DS-90.No. 5, Table H.3.

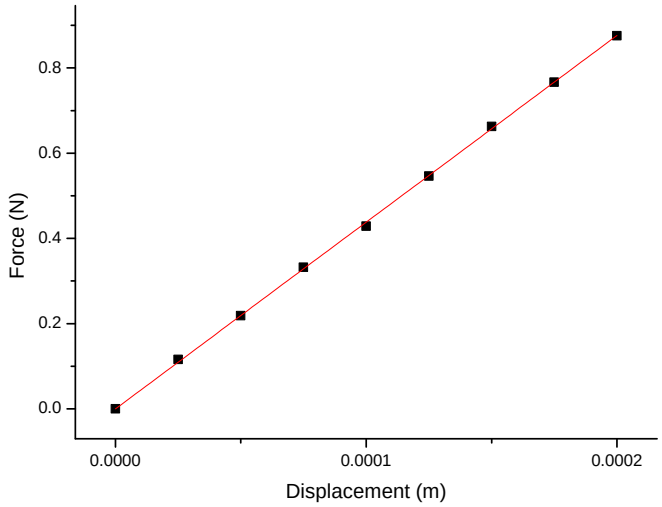

Figure I.13: Stiffness measured at off-centre point for classic tetraskelion samples CS1-DS-90.No. 6, Table H.3.

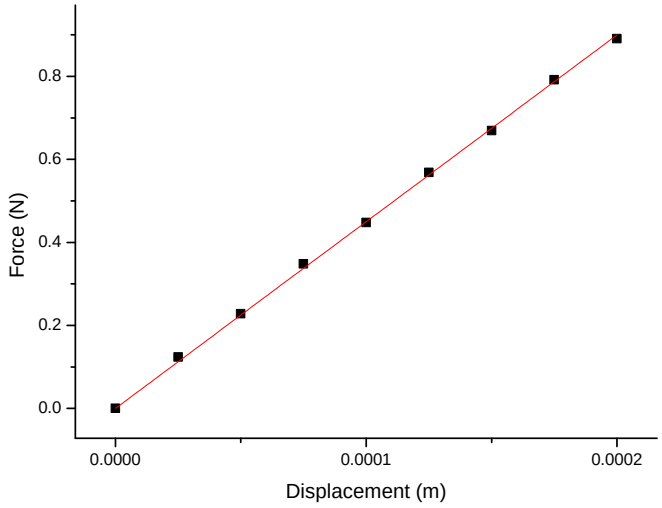

Figure I.14: Stiffness measured at off-centre point for classic tetraskelion samples CS1-DS-90.No. 7, Table H.3.

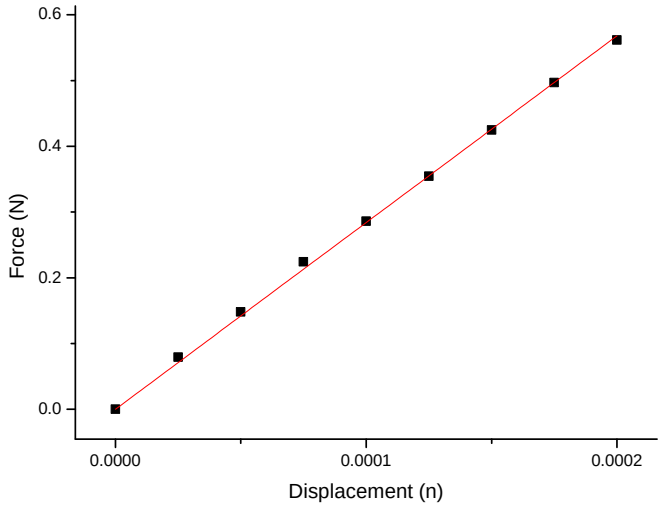

Figure I.15: Stiffness measured at the centre for classic tetraskelion samples CS2-CS-90.No. 1, Table H.2.

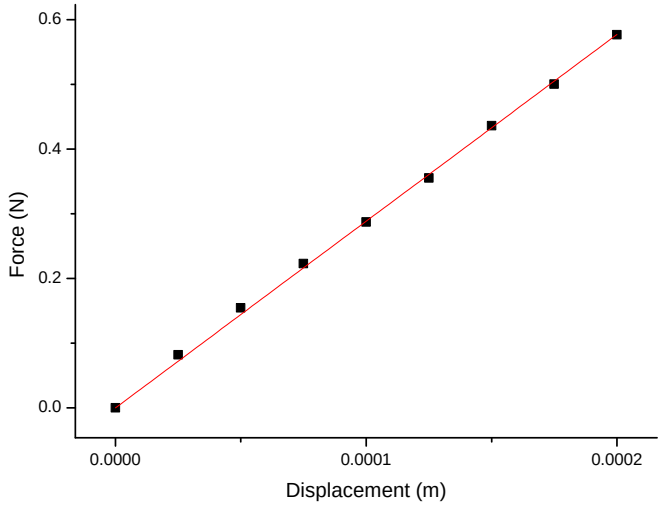

Figure I.16: Stiffness measured at the centre for classic tetraskelion samples CS2-CS-90.No. 2, Table H.2.

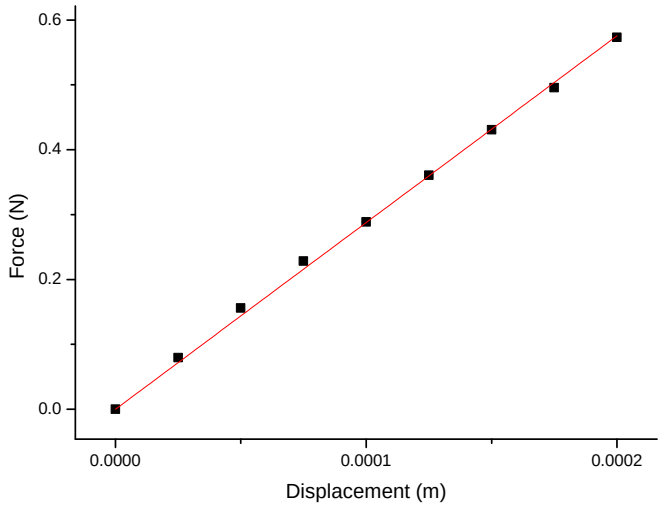

Figure I.17: Stiffness measured at the centre for classic tetraskelion samples CS2-CS-90.No. 3, Table H.2.

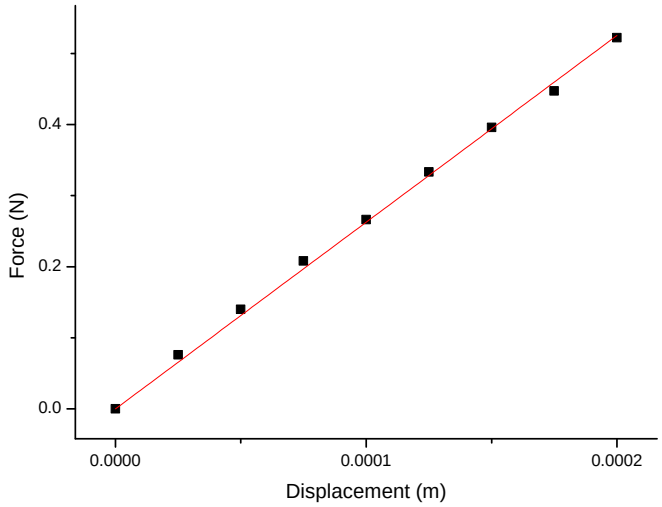

Figure I.18: Stiffness measured at off-centre point of hub for classic tetraskelion samples CS2-CS-90.No. 4, Table H.2.

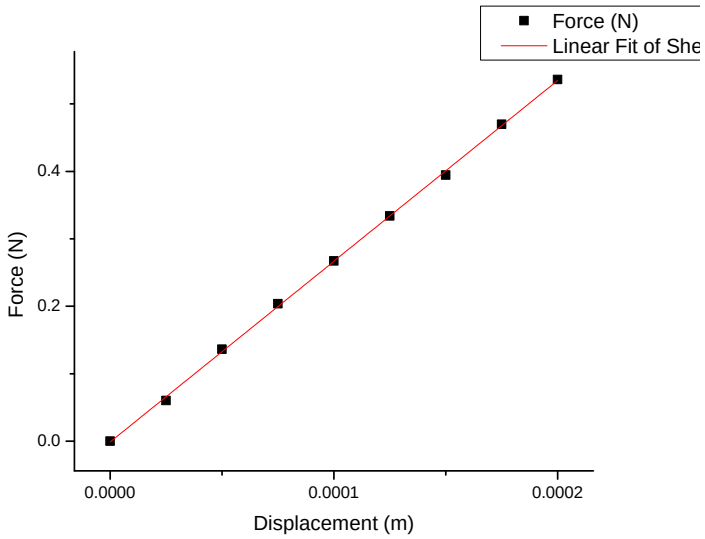

Figure I.19: Stiffness measured at off-centre point for classic tetraskelion samples CS2-CS-90.No. 5, Table H.2.

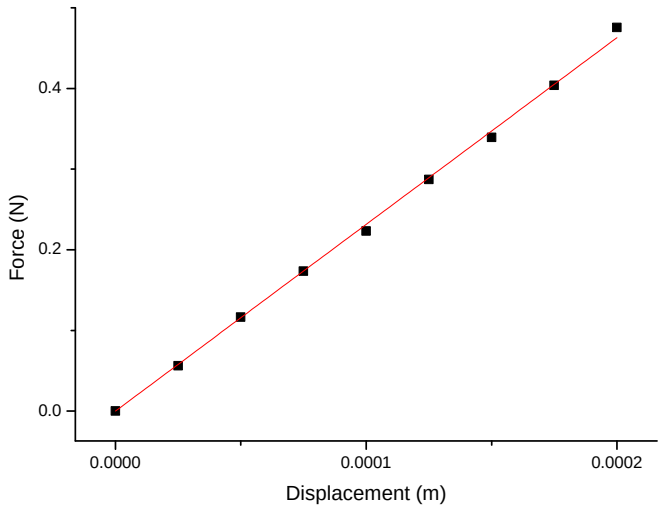

Figure I.20: Stiffness measured at off-centre point for classic tetraskelion samples CS2-CS-90.No. 6, Table H.2.

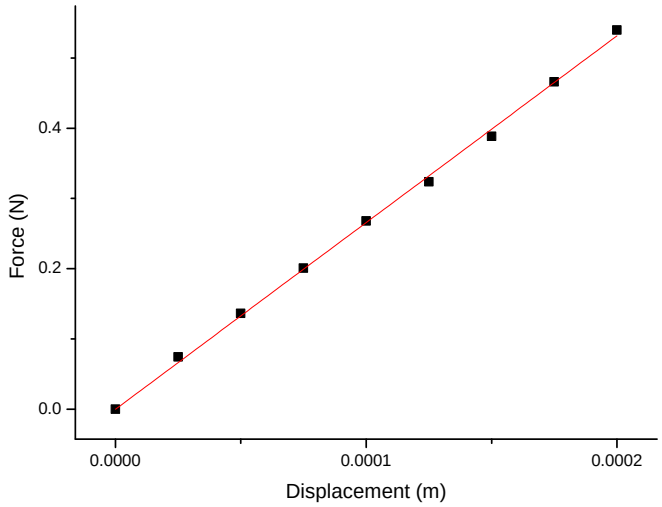

Figure I.21: Stiffness measured at off-centre point for classic tetraskelion samples CS2-CS-90.No. 7, Table H.2.

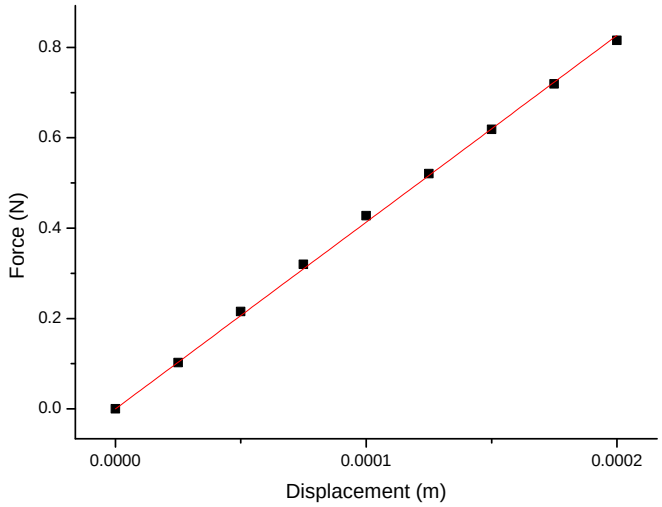

Figure I.22: Stiffness measured at the centre for classic tetraskelion samples CS2-DS-90.No. 1, Table H.4.

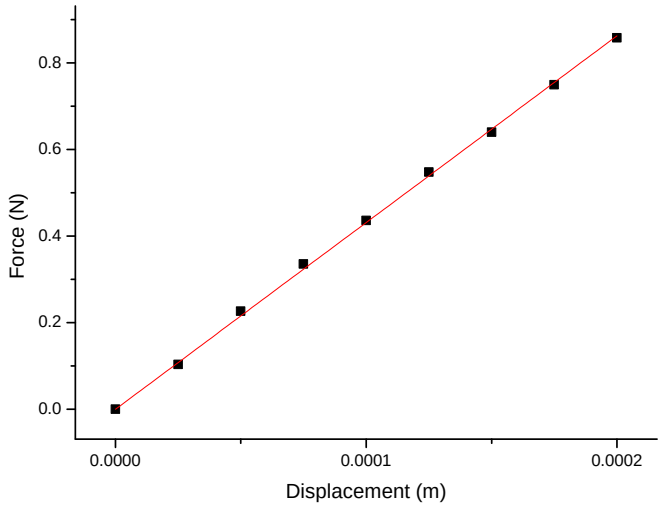

Figure I.23: Stiffness measured at the centre for classic tetraskelion samples CS1-DS-90.No. 2, Table H.4.

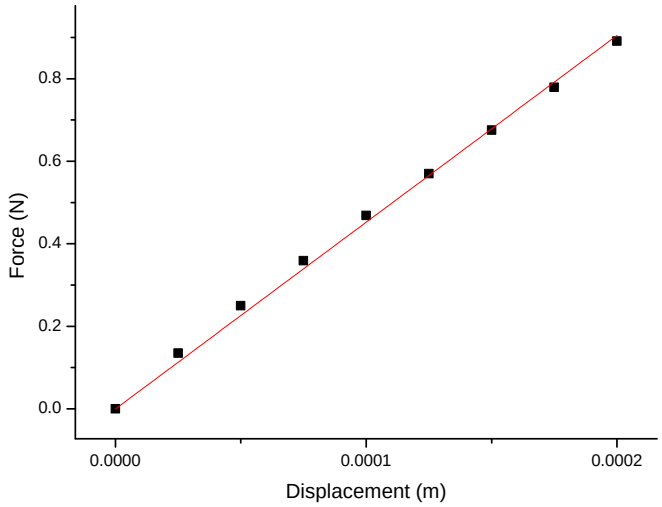

Figure I.24: Stiffness measured at the centre for classic tetraskelion samples CS2-DS-90.No. 3, Table H.4.

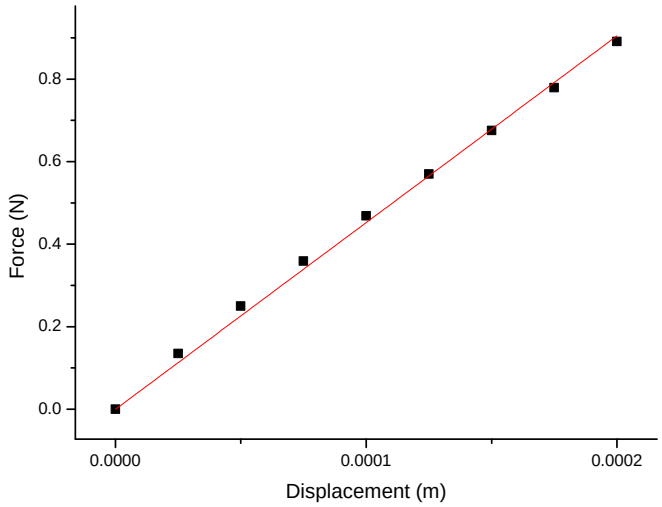

Figure I.25: Stiffness measured at off-centre point of hub for classic tetraskelion samples CS2-DS-90.No. 4, Table H.4.

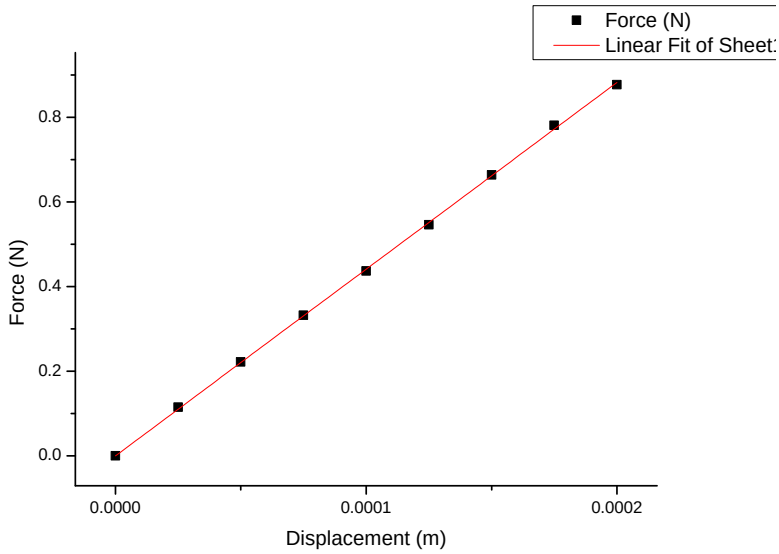

Figure I.26: Stiffness measured at off-centre point for classic tetraskelion samples CS2-DS-90.No. 5, Table H.4.

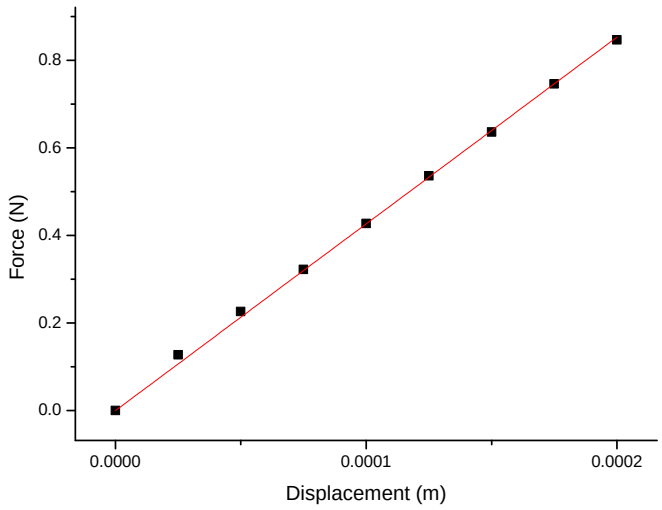

Figure I.27: Stiffness measured at off-centre point for classic tetraskelion samples CS2-DS-90.No. 6, Table H.4.

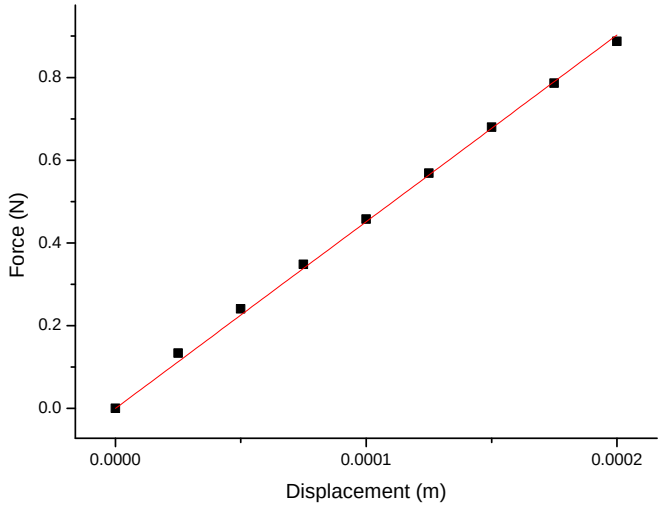

Figure I.28: Stiffness measured at off-centre point for classic tetraskelion samples CS2-DS-90.No. 7, Table H.4.

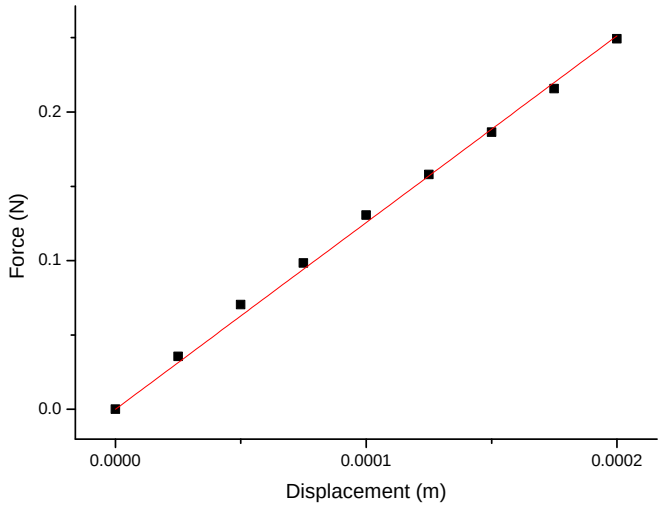

Figure I.29: Stiffness measured at the centre for classic tetraskelion samples ABS1-CS-90.No. 1, Table H.5.

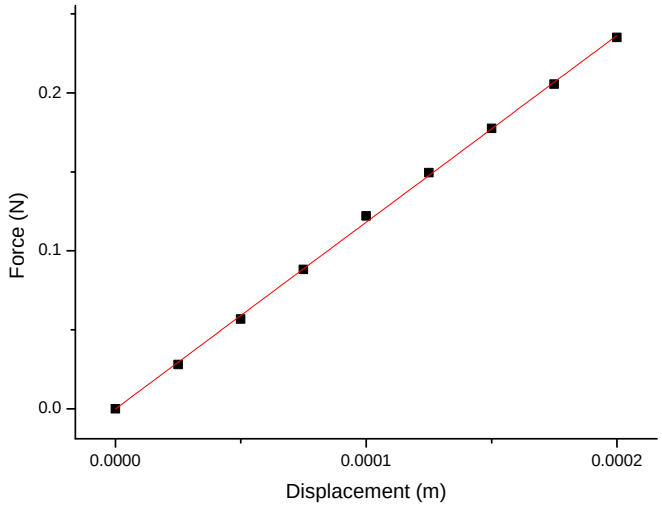

Figure I.30: Stiffness measured at the centre for classic tetraskelion samples ABS1-CS-90.No. 2, Table H.5.

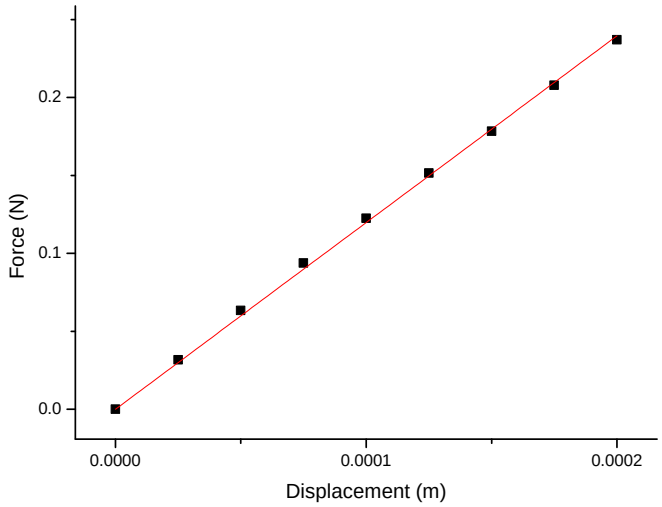

Figure I.31: Stiffness measured at the centre for classic tetraskelion samples ABS1-CS-90.No. 3, Table H.5.

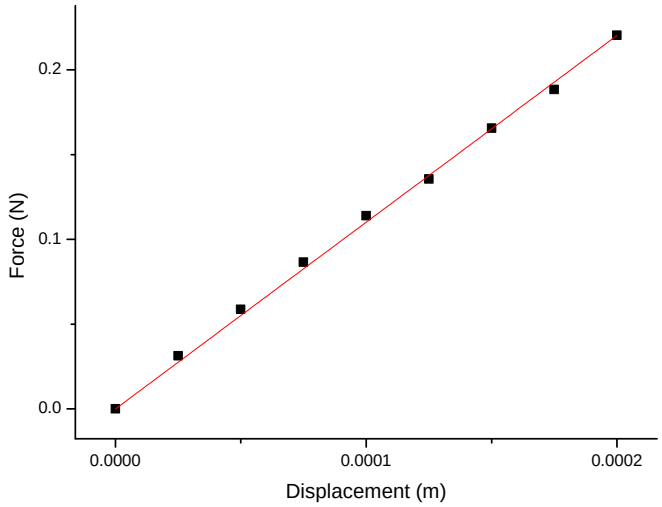

Figure I.32: Stiffness measured at off-centre point of hub for classic tetraskelion samples ABS1-CS-90.No. 4, Table H.5.

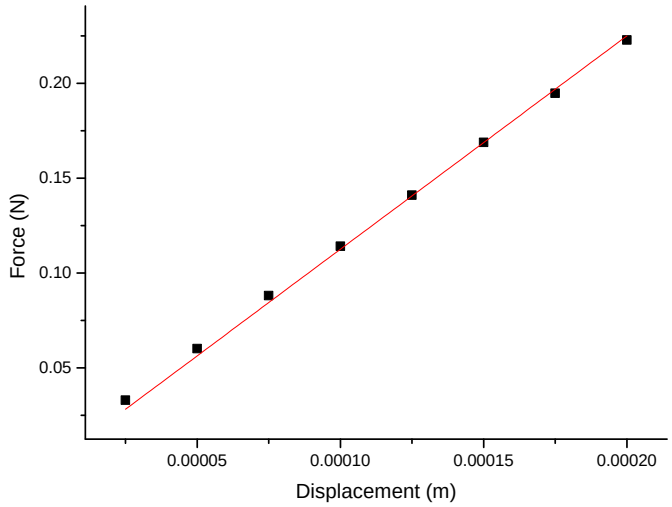

Figure I.33: Stiffness measured at off-centre point for classic tetraskelion samples ABS1-CS-90.No. 5, Table H.5.

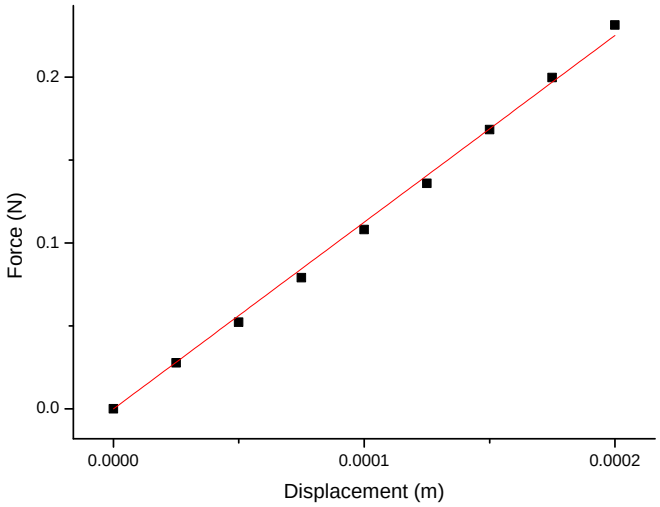

Figure I.34: Stiffness measured at off-centre point for classic tetraskelion samples ABS1-CS-90.No. 6, Table H.5.

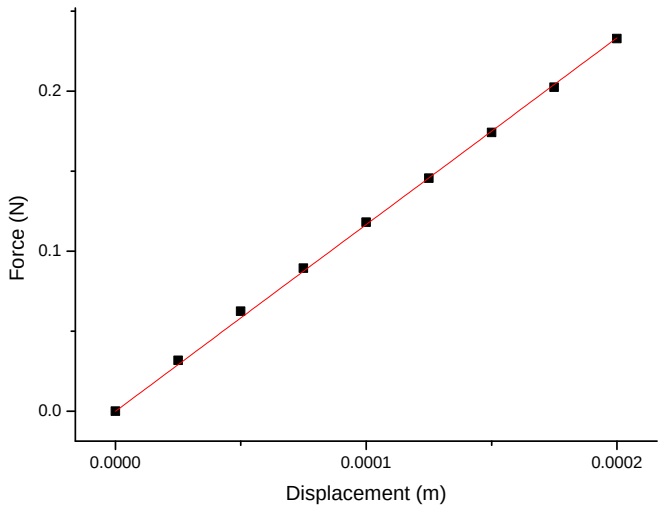

Figure I.35: Stiffness measured at off-centre point for classic tetraskelion samples ABS1-CS-90.No. 7, Table H.5.

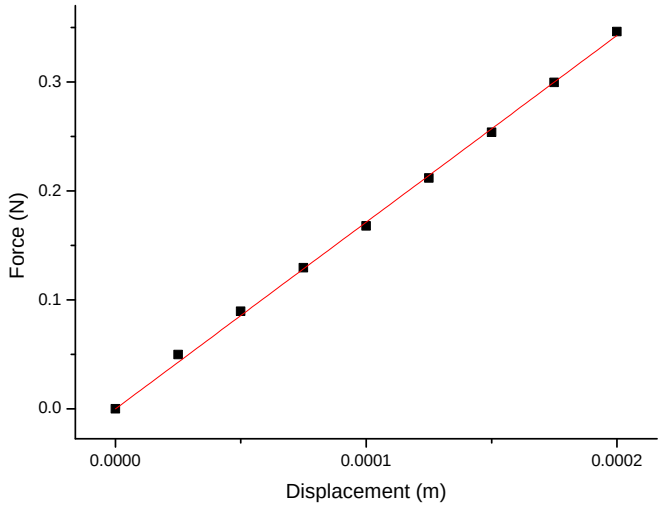

Figure I.36: Stiffness measured at the centre for classic tetraskelion samples ABS1-DS-90.No. 1, Table H.6.

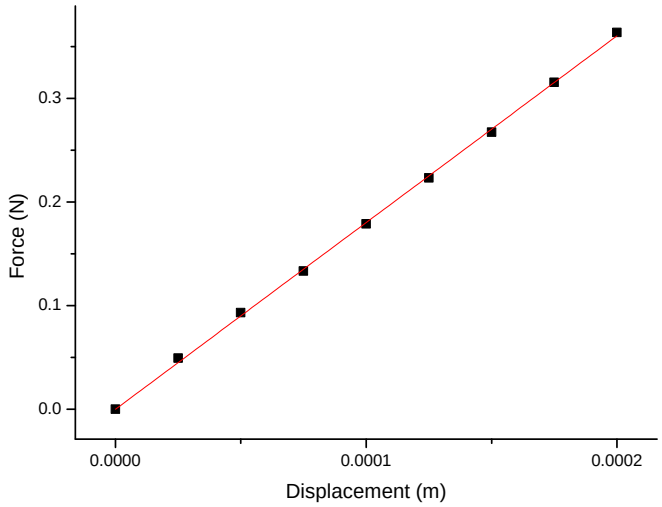

Figure I.37: Stiffness measured at the centre for classic tetraskelion samples ABS1-DS-90.No. 2, Table H.6.

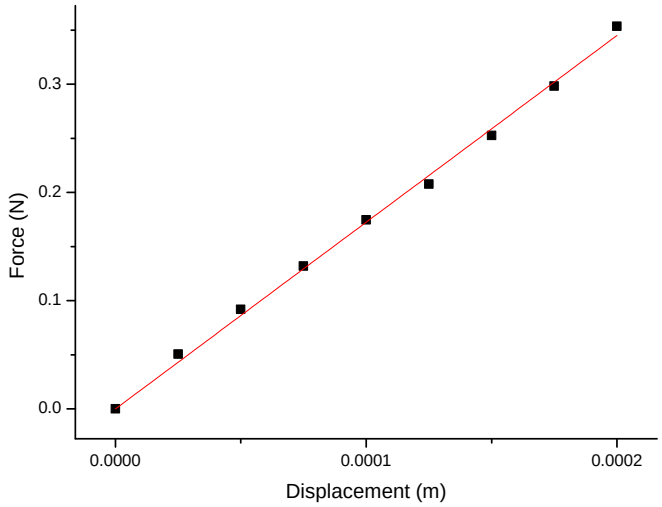

Figure I.38: Stiffness measured at the centre for classic tetraskelion samples ABS1-DS-90.No. 3, Table **??**.

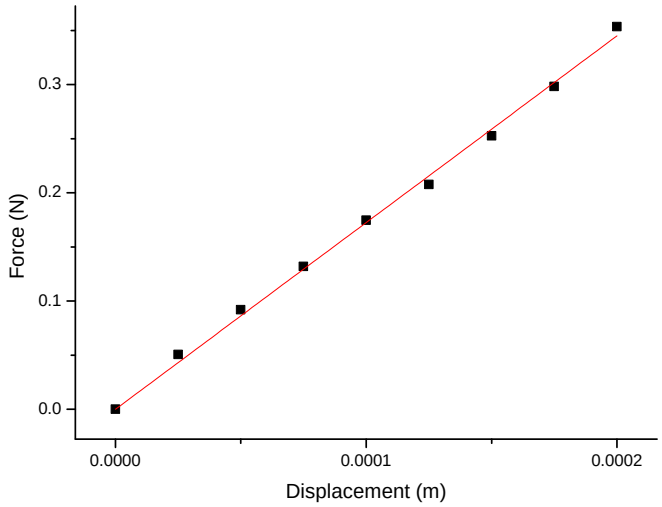

Figure I.39: Stiffness measured at off-centre point of hub for classic tetraskelion samples ABS1-DS-90.No. 4, Table H.6.

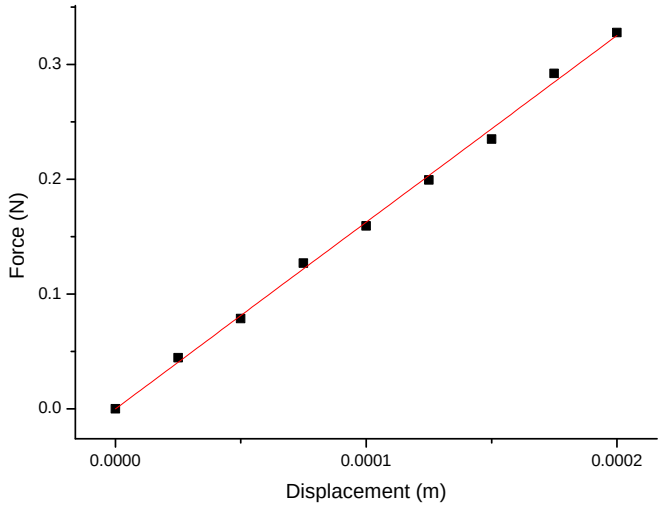

Figure I.40: Stiffness measured at off-centre point for classic tetraskelion samples ABS1-DS-90.No. 5, Table H.6.

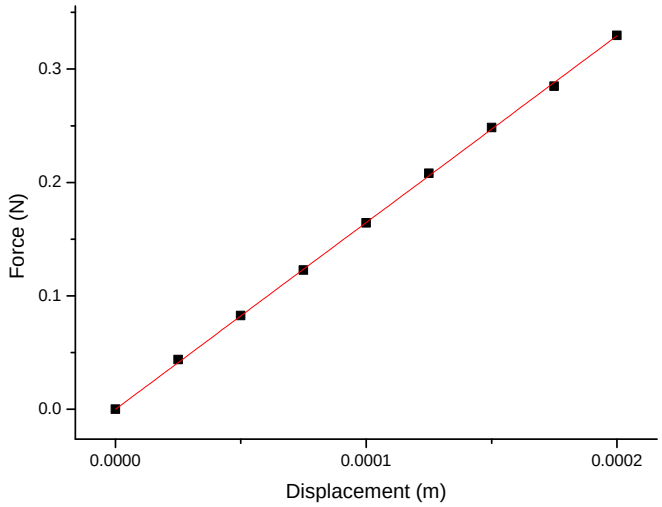

Figure I.41: Stiffness measured at off-centre point for classic tetraskelion samples ABS1-DS-90.No. 6, Table H.6.

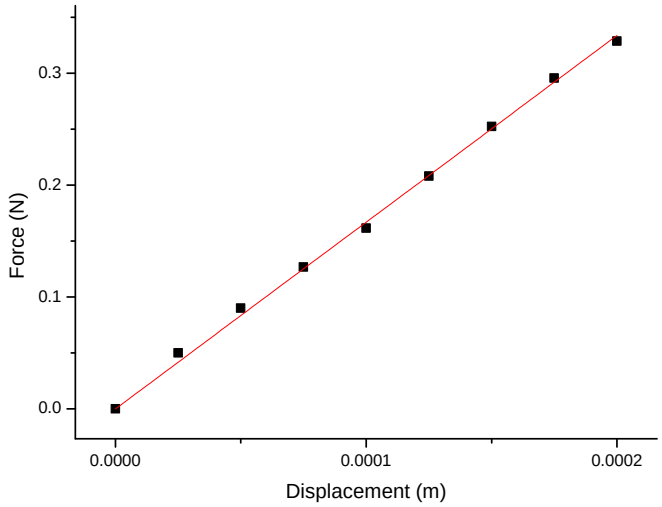

Figure I.42: Stiffness measured at off-centre point for classic tetraskelion samples ABS1-DS-90.No. 6, Table H.6.

Appendix J

Tetraskelion program: MATLAB codes

```
% Aim: Function to generate single coulum matrix from six input vector.

%Pre-Condition:The total inputs are six but three of them
%(dx=dy=dthetaz =0)are set zero locally and remaining three values
%(dz,dthetax, dthetay) user has to enter for executing the function.

%Post-Condtion: Six values are displayed dx,dy,dz, dthetay,
%dthetax, and detheta z.

function Dp= dpl(dz,dthetax,dthetay)
dpl = [ 0; 0; dz; dthetax; dthetay; 0;];
Dp = dpl;
% Aim: Function to compute  at Arm and Defection of the Platform.

%Pre-Condition:
% 8 input values are required for executing this function. Three of them
% are locally set equal to zero and remaining 4 values,  user has to enter
% for execution the function.

%Post-Condtion:Execution of this function generates defection of four
%beams (matric 6x1) in Plat-Coordinates

function Ds= dbp(dz, dthetax, dthetay,a, alpha1, alpha2, alpha3, alpha4)

disp = dpl(dz, dthetax, dthetay);

angl = [alpha1, alpha2, alpha3, alpha4];

%angl = [ -pi/6, pi/2, -5*pi/6];

doa=zeros(6,6,length(angl));

  for i = 1:length(angl)
       doa(:,:,i) = [ 1,  0,   0,   0,   0,    0;
                      0,  1,   0,   0,   0,    0;
```

```
                    0,  0,   1,   (a*sin(angl(i))), - (a*cos(angl(i))),0;
                    0,  0,   0,   1,   0,    0;
                    0,  0,   0,   0,   1,    0;
                    0,  0,   0,   0,   0,    1; ];
  end
      dbp1 = doa(:,:,1)*disp;
      dbp2 = doa(:,:,2)*disp;
      dbp3 = doa(:,:,3)*disp;
      dbp4 = doa(:,:,4)*disp;
dbp = [dbp1, dbp2, dbp3, dbp4];
Ds = dbp;

% Aim:Function to generate stiffness matrix  from reqirement specification
% for suspension beams.

%Pre-Condition: 4 input values are required for this function. i.e. length l
%width w,thickness t and E for three beams.

%Post-Condition: Execution of this function generates a matrix (6x6) for
%each beam.
function C=csa(l,w,t,E)

%G = double(50e+9);
G = double(1e+9);
%E = double(120e+9);


k = ((G*(t^2)/E)*(1/3 - (((0.21*t)/w)*(1 - (t^4)/(12*w^4)))));

csa = [1, 0, 0, 0,0,0;  0,(w/l)^2,0,0,0, (-(w^2)/(2*l));
                   0, 0, (t/l)^2, 0,   ((t^2)/(2*l)), 0;
      0,0,0,k,0, 0; 0, 0, ((t^2)/(2*l)), 0, ((t^2)/3),0;
                    0, (-(w^2)/(2*l)),0,0,0, ((w^2)/3)];
C= ((E*t*w)/l)*csa;

%Aim: Function to Compute, Transformation to the Platform Coordinates.

%Pre-Condition: 4 input values of angles(beta1, beta2,beta3, beat4) are required for
%function ctm.

%Post-Condition: Execution of this function generates four matrices (6x6)
%for end defections of three beams.
function tm = ctm(beta1, beta2,beta3, beta4)

ang2 = [ beta1, beta2, beta3, beta4];


 tpc=zeros(6,6,length(ang2));

  for j = 1:length(ang2)
```

```
       tpc(:,:,j) =  [ cos(ang2(j)), sin(ang2(j)), 0,   0,          0,    0;
             - sin(ang2(j)), cos(ang2(j)), 0,          0,          0,    0;
                          0,          0, 1,            0,          0,    0;
                          0,          0, 0, cos(ang2(j)),sin(ang2(j)),    0;
                          0,          0, 0,-sin(ang2(j)),cos(ang2(j)),    0;
                          0,          0, 0,          0,          0,    1;];
  end
          ctm1 =   tpc(:,:,1);
          ctm2 =   tpc(:,:,2);
          ctm3 =   tpc(:,:,3);
          ctm4 =   tpc(:,:,4);

 ctmp= [ctm1,ctm2, ctm3, ctm4];
tm = ctmp;

Aim: Function to compute Computation for Force(F_x,F_y,F_z) and
%Moment M_x,M_y and M_x.

%Pre-Condition: 16 input values dz, dthetax, dthetay,a,l,w, and t required
%by the user and two functions, csa & dsb  are called.

%Post-Conation: Execution of this function generates the values of force and
%moment for three beams in form of three matrices (6x1)

function p = psb(dz, dthetax, dthetay, a, l, w, t, E, alpha1, alpha2, alpha3,
                                          alpha4, beta1, beta2, beta3, beta4)

sm = csa(l,w,t,E);
q = dsb(dz, dthetax, dthetay, a, alpha1, alpha2, alpha3,alpha4, beta1, beta2,
                                                              beta3, beta4);
psb1 = sm*q(:,1);
psb2 = sm*q(:,2);
psb3 = sm*q(:,3);
psb4 = sm*q(:,4);
p = [psb1, psb2, psb3, psb4];

%Aim: Function to Compute, Force back to Globel Coordintes.

%Pre-Condition: 16 input values are required, two functions psb and tgc are also
%called.

%Post-Condtion: Execution of this function generates four matrices (6x1)
%for end defections of four beams.

function cbg = tgbc(dz, dthetax, dthetay, a, l, w, t, E, alpha1, alpha2,
                               alpha3, alpha4,beta1, beta2, beta3, beta4)
lbf = psb(dz, dthetax, dthetay, a, l, w, t, E, alpha1, alpha2, alpha3,
                                    alpha4,beta1, beta2, beta3, beta4);

tgc = ctm(beta1, beta2, beta3, beta4);
```

```
  gdsb1 = (tgc(:, 1:6)' )*lbf(:,1);
  gdsb2 = (tgc(:, 7:12)')*lbf(:,2);
  gdsb3 = (tgc(:,13:18)')*lbf(:,3);
  gdsb4 = (tgc(:,19:24)')*lbf(:,4);
   sfgc = (gdsb1 + gdsb2 +  gdsb3 + gdsb4);
    tgc = [gdsb1,gdsb2,gdsb3,gdsb4,sfgc];
cbg= tgc;

%Aim: Function to Compute, Force back to Globel Coordintes.

%Pre-Condition: 16 input values are required, the function tgbc is also
%called.

%Post-Condition: Execution of this function generates three matrices (1X3)
%for end defections of three beams.
function sfm = cfmg(dz, dthetax, dthetay, a,l, w, t, E, alpha1, alpha2,
                            alpha3, alpha4, beta1, beta2, beta3, beta4)
           radius = a;
          alpha11 = alpha1;
          alpha22 = alpha2;
          alpha33 = alpha3;
          alpha44 = alpha4;
    csfm = tgbc(dz, dthetax, dthetay, a, l, w, t, E, alpha1, alpha2, alpha3,
                                       alpha4, beta1, beta2, beta3, beta4);

      fb1= csfm(:,1);
      fb2= csfm(:,2);
      fb3= csfm(:,3);
      fb4= csfm(:,4);
     sigfzs = ((-fb1(3)) + (-fb2(3))+ (-fb3(3))  + (-fb4(3)));
     sigmxs = ((-fb1(4)) + (-fb2(4))+ (-fb3(4)) + (-fb4(4)) +
      ((-fb1(3)*radius)*sin(alpha11)) + ((-fb2(3)*radius)*sin(alpha22)) +
      ((-fb3(3)*radius)*sin(alpha33)) + ((-fb4(3)*radius)*sin(alpha44)));
     sigmys = ((-fb1(5)) + (-fb2(5))+ (-fb3(5)) + (-fb4(5)) -
      ((-fb1(3)*radius)*cos(alpha11))  - ((-fb2(3)*radius)*cos(alpha22))-
       ((-fb3(3)*radius)*cos(alpha33))- ((-fb4(3)*radius)*cos(alpha44)));

 fms = [sigfzs, sigmxs, sigmys];
 sfm= fms;

% Aim: Function to computate,  Stress and Strain.


%Pre-Condition: To execute this function, 14 input values, dz, dthetax,
%dthetay,a,l, and w. Function tgbc is also called here.


%Post-Condtion: Execution of this function generates matrix (2x4). The first
```

```
%line indicates values of stress and second for strain of three beams.

function S=sigma(dz, dthetax, dthetay, a, l, w, t, E, alpha1, alpha2,
                            alpha3,alpha4,beta1, beta2, beta3, beta4)

 pg = tgbc(dz, dthetax, dthetay,a, l, w, t, E, alpha1, alpha2,
                     alpha3,alpha4,beta1, beta2, beta3,beta4);

sigma1 = (6*((((pg(3)*l) -  pg(5)))/(w*(t^2))));
sigma2 = (6*((((pg(9)*l) -  pg(11)))/(w*(t^2))));
sigma3 = (6*((((pg(15)*l) - pg(17)))/(w*(t^2))));
sigma4 = (6*((((pg(21)*l) - pg(23)))/(w*(t^2))));

sigma = [sigma1, sigma2, sigma3, sigma4;  sigma1/E, sigma2/E,
                                        sigma3/E, sigma4/E; ];
S = sigma;

%Aim: function to compute values of stiffness.

%Pre-Condition: 16 input valuesdz,dthetax,dthetay,a,l,w, and t are reqired
%to execute this function and two function psg and tfm are called here.

%Post-Condtion: Execution of this function genrates matrix (3x8)i.e.
% (the value of Spring constant K, F_z, Stress/F_z, Strains/F_z,  and
%Lamda_x = M_x/delta_x, Lamda_y = M_y/delta_y, Strain/M_x and Strain/M_y).
function pls = plstiff(dz, dthetax, dthetay, a, l, w, t, E,
 alpha1, alpha2, alpha3,alpha4, beta1, beta2, beta3, beta4)

psg = tgbc(dz, dthetax, dthetay, a ,l, w, t, E, alpha1, alpha2,
                     alpha3,alpha4,beta1, beta2, beta3, beta4);

%ssg= sigma(dz, dthetax, dthetay, a, l, w, t, E, alpha1, alpha2,
                      alpha3,alpha4,beta1, beta2, beta3, beta4);

tfm = cfmg(dz, dthetax, dthetay, a, l, w, t, E, alpha1, alpha2,
                    alpha3, alpha4, beta1, beta2, beta3, beta4);

tfz = tfm(1)/dz;

tmx = tfm(2)/dthetax;

tmy = tfm(3)/dthetay;

plstiff = [tfz, tmx, tmy];
pls = plstiff;

 % Main function to compute Analytical Model of Tri-Skellion Micro Probe
% all results.

% Author: Haroon-Ur-Rashid
```

```
% Date: 15-08-2009
% Date: 31-05-2011
% Date: 14-07-2012
% Date: 10-10-2012
% Supervisor: Professor Derek Chetwynd
% Industrial Supervisor Professor Richard Leach

%Pre-Condition: 16 input valuesdz,dthetax,dthetay,a,l,w,t, E,  are reqired
%alpha1, alpha2, alpha3, beta1, beta2, and  beta3 are reqired to execute this
%function.

%Post-Condition: Execution of main function genrates the computed results
%for Analytical Model of Tri-Skellion Probe thus saving time to execute
%each function one by one.

function mpl(dz,dthetax,dthetay, a, l, w, t, E, alpha1, alpha2, alpha3,
                                    alpha4, beta1, beta2, beta3, beta4)
 disp('Input vectors are generated (6x1 matix) as follows:')
 disp('================================================')
 disp('dx,dy,dz,dthetax,dthetay,dthetaz')
 disp(' ')
 disp(dpl(dz,dthetax,dthetay));
 disp(' ')
 disp('Computation for Deflection of arms at the Platform,6x4 matrix for four arms :')
 disp('============================================================================ ')
 disp('===========arm1==========arm2==========arm3============arm4')
 disp(' ')
 disp(dbp(dz,dthetax,dthetay,a, alpha1, alpha2, alpha3, alpha4 ));
 disp(' ')
 disp('Computation for Deflection of three beams in Platform-Coordinates, 6x1 matrix
                                                                  for each beam :')
 disp('================================================================== ')
 disp(' ')
 disp(ctm(beta1, beta2, beta3, beta4));
 disp('Computation for Deflection of three beams in Platform-Coordinates, 6x1 matrix
                                                               for four beams :')
 disp('================================================================== ')
 disp('==========beam1=======beam2======beam3===========beam4 ')
 disp(dsb(dz,dthetax,dthetay,a, alpha1, alpha2, alpha3,alpha4,beta1, beta2, beta3,
                                                                    beta4 ));
 disp(' ')
 disp('Stiffness matrix 6x6 generted from reqirement specifications:')
 disp('Lenth l, width w, thickness t and Young's modulous E:')
 disp('============================================================ ')
 disp(' ')
 disp(csa(l,w,t, E));
 disp(' ')
 disp('Computation for Force(F_x,F_y,F_z) and Moment M_x,M_y and M_x are')
 disp('done in form of 6x4  Matrix:')
 disp('============================================================== ')
```

```
 disp('==========beam1=======beam2======beam3===============beam4 ')
 disp(' ')
 disp(psb(dz, dthetax, dthetay, a, l ,w, t, E, alpha1, alpha2, alpha3, alpha4, beta1,
                                                              beta2, beta3, beta4));
 disp(' ')
 disp('Computation for Force(F_x, F_y, F_z), Moment M_x, M_y and M_z (6x1) matrix for
                                                                    each beam')
 disp(' and fouth col, their sum in globel-coordinates')
 disp('========beam1=======beam2======beam3========beam4=========Sum-of-four-column')
 disp(' ')
 disp(tgbc(dz, dthetax, dthetay, a, l, w, t, E, alpha1, alpha2, alpha3, alpha4, beta1,
                                                               beta2, beta3, beta4));
 disp(' ')
 disp('Computation for sum of Force(F_x,F_y,F_z), Moment M_x,M_y and M_z  in
                                                         global-coordinates')
 disp('============================================================= ')
 disp(' ')
 disp(cfmg(dz, dthetax, dthetay, a, l, w, t, E, alpha1, alpha2, alpha3, alpha4, beta1,
                                                               beta2, beta3, beta4));
 disp(' ')
 disp('Computation for Stress and Strain, 2x4 matrix for three beams:')
 disp('First Row indicates Stress for three beams:')
 disp('Second Row indicates Strain for three beams:')
 disp('============================================================= ')
 disp(sigma(dz, dthetax, dthetay, a, l, w, t, E, alpha1, alpha2, alpha3, alpha4,
                                                    beta1, beta2, beta3, beta4));
 disp(' ')
 disp('Spring constant K, F_z, Lamda_x = M_x/delta_x, Lamda_y = M_y/delta_y:')
 disp('=========================================================================')
 disp(' ')
 disp(plstiff(dz,dthetax,dthetay, a, l, w, t, E, alpha1, alpha2, alpha3, alpha4,
                                                   beta1, beta2, beta3, beta4));
 disp('=========================================================================')
 disp('All computation done.')
end
```